

https://dspace.org/

Optical and electrical properties of ion beam modified materials

Amolo, George Odhiambo

2008-08-18T13:14:40Z
http://hdl.handle.net/10539/5409

Downloaded from a DSpace repository. https://dspace.org/

Optical and Electrical Properties of Ion Beam Modified Materials

by

George Odhiambo Amolo

A thesis submitted to the Faculty of Science

in fulfillment of the requirements for the degree of

Doctor of Philosophy

School of Physics

2007

I declare that this thesis is my own work. It is being submitted in fulfilment of the requirements for the degree of Doctor of Philosophy at the University of the Witwatersrand, Johannesburg. It has not been submitted before for any degree or examination at any other university.

George Odhiambo Amolo

Date

Abstract

This thesis deals with the optical and certain electrical properties of materials that have been modified by ion implantation and irradiation.

A combination of the optical absorption and near-resonance Raman techniques have been used for the first time, to the best of the author's knowledge, in the study of defect annealing mechanisms and reaction kinetics in proton implanted CsI crystals. From the optical absorption studies, the F_2 and F bands are observed at 1.1 and 1.66 eV, respectively, while several V bands are revealed within an extended absorption envelope including those positively identified at 2.7, 3.4, 4.05, 4.2 and 4.35 eV. The V bands at 2.7 and 3.4 eV are associated with the I_3^- defects. Raman studies show the fundamental peak at 113 cm^{-1} and numerous overtones occurring at spectral positions close to integral multiples of the fundamental. The series of Raman transitions are attributed to I_3^- defects. A comparative analysis, to previous work, shows that similar defects are observed under certain conditions in X- and γ-irradiated KI and RbI suggesting a similar defect creation mechanism. Currently, the results of the isochronal annealing show a simultaneous decay of the F_2 and V bands at 2.7 and 3.4 eV, suggesting an interstitial-vacancy recombination process. The results of the isothermal annealing at 397 K indicate the occurrence of a second order process. Further analysis of the optical and Raman data shows that this recombination process is correlated and consists of a single step. The isochronal annealing data of the decay of the F_2 band or V band (2.7 eV) show that the activation energy for the recombination process is 1.28 eV.

The defect creation mechanism in MgF_2 is known to be excitonic in nature resulting primarily in vacancies and interstitial defects. In the present work, two V bands have been observed in the vacuum ultraviolet region and their behaviour with annealing temperature studied. The observation of the band at the lower photon energy, near 6.5 eV, represents the first report by optical absorption in this spectral region, to the

best of the author's knowledge. The second band is located near 7.8 eV. The technique of difference spectra has been applied to follow the behaviour of the two absorption bands with annealing temperature. The implantation of excess Mg^+ ions into the MgF_2 crystals results in the formation of magnesium colloids (nanoparticles) whose presence is indicated by optical absorption bands in the visible region of the spectrum. The simultaneous growth of the Mg colloids and the annealing of the *V* bands and F_2 centres at lower annealing temperature is a strong indication that the *V* bands themselves are fluorine interstitial aggregates and that an interstitial-vacancy recombination process is taking place. A strong absorption at photon energies lower than the fundamental absorption edge of MgF_2, after annealing at higher temperatures (above 813 K) in air, was observed and suggest a change in the properties of the near surface region of the implanted sample. X-ray photoelectron spectroscopy revealed the presence of oxygen and therefore formation of MgO whose absorption edge is close to that observed for the sample annealed in air. A sample annealed in an argon environment and treated in a similar manner exhibited relatively moderate absorption in the same spectral region compared with the sample annealed in air. It is likely that the decay of the colloid band observed after annealing at 903 K is related to melting of the Mg metal nanoparticles, which is known to occur near 922 K in bulk metal.

Implantation of X-cut lithium niobate (LN) crystals with 100 keV Ag^+ ions to fluences of 1×10^{17} /cm^2 near room and liquid nitrogen temperatures, and at 373 K has been performed. Optical absorption measurements in the visible region reveal the presence of colloid bands in the as-implanted samples. Transmission electron microscopy of a Ag^+ ion implanted X-cut LN sample that was annealed to 513 K, not only confirms the existence of the Ag metal nanoparticles but further indicates the existence of a distribution of particle sizes and various shapes. The Mie theory with the calculated dielectric function of the Ag metal nanoparticles and a fitted host dielectric function (ϵ_h) have been used to estimate the values of the mean particle diameter (*d*) and the

volume fraction (p) of the implanted ions as a function of the annealing temperature. The average particle sizes, obtained from the Mie theory, are in fair agreement with those observed by transmission electron microscopy.

Similarly, implantation of X- and Y-cut LN crystals with 8 MeV Au^{3+} ions to fluences of 1×10^{17} /cm^2 at room temperature has also been carried out. Optical absorption studies following the annealing of the X- and Y-cut faces of LN crystals show differences in the onset temperature of colloid development, which are attributed to the varying diffusion rates in the two crystallographic directions of the LN crystal. The Y-cut and X-cut samples show no absorption bands on heating below 673 and 973 K, respectively. Above the two temperatures the colloid bands grow steadily as the annealing temperature is increased with the peak absorption moving towards the lower photon energy side. Annealing the implanted samples to the highest temperature investigated is shown to remove implantation-induced disorder. Transmission electron microscopy of the X-cut Au^{3+} ion implanted sample, following annealing at 1173 K, reveals near spherical Au metal nanoparticles with a narrow particle size distribution while *in-situ* selected area electron diffraction analysis confirms that the host matrix embedding them is crystalline. The correlation between the average sizes of the Au metal nanoparticles predicted by the Mie theory and a transmission electron micrograph, following annealing at 1173 K, is satisfactory.

Values of ϵ_h less than that of the virgin LN in both cases of implantation with Ag^+ and Au^{3+} ions, observed at lower annealing temperatures, would be consistent with the presence of implantation-induced damage in the host matrix. At the highest annealing temperatures in the range 1273 to 1373 K used for the X-cut samples it is noted that ϵ_h attains values of 5.6 and 5.8, respectively, being higher than that of the virgin crystal. Although full recrystallization has been achieved, the implanted region at these temperatures is subject to the development of oxygen vacancies and the presence of a significant fraction of the previously aggregated Au in a dispersed form in a now crys-

talline but defective host. The decay of the colloid band due to Ag and an onset of average particle size reduction of Au metal nanoparticles predicted by the Mie theory occurred following annealing near 1173 K and 1373 K, respectively. It is likely that melting of the metal nanoparticles takes place as the two temperatures are sufficiently close to the bulk metal values of Ag and Au, known to be near 1235 and 1337 K, respectively.

Irradiation of tin-doped indium oxide (ITO) films using 1 MeV protons to fluences ranging from 1×10^{15} - 250×10^{15} cm^{-2} has been found to induce a reduction in optical transmission leading to observable darkening over a broad spectral region. The increases in the optical absorption coefficient as a function of proton fluence show three stages of development. The first stage involves relatively rapid growth, followed by a near linear second stage and finally a third stage of more rapid growth. The growth processes are temperature dependent and the respective growth rates in each of the stages are reduced with increasing temperature of irradiation of the sample. At the highest fluence of 250×10^{15} cm^{-2} a $1/\lambda$ dependence of the irradiation induced absorption with wavelength is observed being consistent with the presence of defect clusters. A model of defect creation involving the heterogeneous nucleation of defect clusters at pre-existing defects has been developed which satisfactorily accounts for the three stage growth of the optical absorption and its temperature dependence. X-ray diffraction studies show evidence of a strained lattice resulting from the proton bombardment and recovery after long period storage. The effects are attributed to the annealing of the defects produced.

Highly transparent and uniform magnesium fluoride thin films have been prepared by thermal beam evaporation of magnesium fluoride pellets. Attempts to make the films conducting by implantation with Mg^{+} ions, co-deposition with AlF_3 at liquid nitrogen temperature and reduction using suitable gases have not been successful. The effects of sputtering have resulted in highly resistive films.

Dedication

To Alice and Brian Odhiambo and in memory of Ernest, Emily and Dennis Amolo.

Acknowledgements

I would like to thank my supervisors Professors J. D. Comins and D. S. Mclachlan for their guidance and financial support during my stay at the University of Witwatersrand. The advice and kind assistance from Professor T. E. Derry, our main collaborator at the Schonland Research Institute of Nuclear Sciences (Now part of iThemba LABS), Professor A. T. Davidson and Anna Kozakiewicz, our collaborators from University of Zululand is highly appreciated. The financial support from the German Academic Exchange Service (DAAD), the National Research Foundation (NRF) and University of the Witwatersrand is gratefully acknowledged. We also wish to thank Crystran Ltd (UK) for the donation of lithium niobate crystals used in part of this work.

The guidance of Mr. Collin Myburgh of the School of Computational and Applied Mathematics in handling numerical solutions to differential equations is appreciated. The technical support staff of the Physics workshop and in particular Messrs John Augustine, Shaun Rickert, Andrew Carpede, Jerry Germishuizen, Kurt January, Jeff Nyandeni and a former School of Physics driver Mr. Wilson Shezi cannot be forgotten.

I would like to acknowledge friends and fellow students, Nicholas Makau, Ian Korir, Rudolph Erasmus, Lucky Mkhonza, Anna da Costa, George Amulele, Chris Machio, Victor Mofokeng, Godfrey Sauti, Cosmas Chiteme, Bheki Mathe, Erasmus Rammutla, Mary Assiamah, Darryl Rebuli, Ronald Machaka and Denson Dube for support and encouragement.

Contents

Chapter

1 Rationale and General Introduction 1

1.1 Ion Implantation 3

1.1.1 Energy Loss Processes in Matter 4

1.1.2 Energy Dependence of the Stopping Cross Section 6

1.1.3 Damage Distribution and Implanted Ion Profiles 9

1.1.4 Defect Diffusion, Relaxation, Amorphization, Crystallography and Sputtering 11

1.2 Computer Simulations 13

1.3 Introduction to Radiation Induced Defects in Crystals 15

1.3.1 Influence of Lattice Defects on the Electronic Levels 16

1.3.2 Defects Produced by Irradiation of Ionic Crystals 17

1.3.3 The *F* Centre and its Related Charge States 18

1.3.4 *F* Aggregate Centres 19

1.3.5 Hole Centres 20

1.3.6 The V_K Centre (X_2^-) and the Self-Trapped Exciton (STE) 20

1.3.7 The *H* Centre 20

1.3.8 *V* Centres in K and Rb Iodides 21

1.3.9 Models for the di-interstitial Centre 22

1.3.10 Interstitial Aggregates and Dislocation Loops 25

1.3.11 Defect Growth Kinetics 28
1.4 Previous Raman Studies of Iodine and Iodine in Solution 30
1.4.1 Structure of Crystalline Iodine 31
1.4.2 Raman Scattering in Irradiated Alkali Halides 32
1.5 Properties of Metallic Colloids 35
1.5.1 Introduction 35
1.5.2 Colloid Formation and Nucleation kinetics 35
1.5.3 Ripening and Size Distributions of Colloids 38
1.6 Mechanisms of Defect Creation By Irradiation 39
1.7 Review of the Interaction of Electromagnetic Radiation with Small Metal Particles 42
1.7.1 Introduction 42
1.7.2 Mie Theory 44
1.7.3 The Mean Free Path 45
1.7.4 Quantum Size Effects 45
1.8 Plasmon Resonance (PR) Absorption 46
1.9 Review on Properties and Defect Studies of Cesium Iodide 49
1.9.1 Previous Defect Studies on Cesium Iodide 50
1.10 Point Defects in Alkaline Earth Fluorides (AEF) 50
1.10.1 Introduction 50
1.10.2 Fluorite Structured AEF 51
1.10.3 Tetragonal Structured AEF 52
1.10.4 Review of the Irradiation Damage Studies on MgF_2 53
1.11 Defect Studies in Lithium Niobate 55
1.11.1 Introduction and Structural Properties of Lithium Niobate . . . 55
1.11.2 Defect Structure of LN 58
1.11.3 Review on Irradiation Damage Studies in Lithium Niobate . . . 59

1.12 Defect Studies and the Properties of Indium Oxide and Tin-Doped Indium Oxide Films 60
1.12.1 Introduction 60
1.12.2 Structure and Properties of Indium Oxide 61
1.12.3 The Mechanism of Insertion of Tin into the In_2O_3 Lattice 63
1.12.4 Review of Irradiation Damage Studies of ITO Films 68
1.13 Properties of Polycrystalline Magnesium Fluoride Films (PMF) 69
1.13.1 Introduction 69
1.13.2 Structural Properties 70
1.13.3 Optical Properties 70
1.13.4 Electrical Properties 71

2 73

2.1 Theory of Optical Absorption 73
2.1.1 Absorption in Alkali Halide Crystals 73
2.1.2 Theory of Single Particle Absorption 75
2.2 Absorbing Entity in a Solid 76
2.2.1 The Local Field Correction 76
2.2.2 Born-Oppenheimer Approximation and Modified Transition Matrix Element Leading to Smakula's Equation 77
2.2.3 Configuration Co-ordinate Diagram and Absorption Band Shape 79
2.3 Theory of Raman Scattering 81
2.3.1 Introduction 81
2.3.2 Classical Approach 82
2.3.3 Quantum Mechanical Approach 83
2.3.4 The Near Resonance Raman Effect 85
2.4 Annealing Theory 86

2.4.1 Introduction 86
2.4.2 Isochronal Anneal 86
2.4.3 Isothermal Anneal 87
2.4.4 Defect Migration 88
2.4.5 Annealing of Defects from Chemical Rate Theory 89
2.4.6 Determination of γ from Isothermal Anneal Data 91
2.4.7 Determination of E_m from the Isochronal Anneal Data 91
2.5 Theoretical Studies of Resonances Associated With Metal Colloids . . . 92
2.5.1 Introduction 92
2.5.2 Mie Theory 93
2.5.3 Procedure for the Use of the Mie Theory 100
2.6 Determination of the Linear Optical Constants of Thin Film Materials on a Substrate 102
2.6.1 Introduction 102
2.6.2 Bare Substrate and Film-on-Substrate Systems 102
2.6.3 Characterizing the Substrate 105
2.6.4 Characterizing the Film. 106
2.7 The Rutherford Backscattering Technique 108
2.7.1 Introduction 108

3 Experimental Techniques 111
3.1 General Introduction 111
3.2 The Cockcroft-Walton Accelerator 111
3.2.1 Production of a Proton Beam 115
3.3 Higher Energy Accelerators 116
3.3.1 The Van de Graaff Generator and Accelerator 116
3.3.2 The Tandem Accelerator 117

3.3.3 Beam Transport 119
3.3.4 Target Chamber 121
3.4 The Ion Implanter 122
3.5 Laue X-ray Orientation of the Crystals 123
3.5.1 Crystal Sawing 124
3.5.2 Crystal Polishing 125
3.6 Furnaces Used for Annealing 125
3.7 Optical Absorption Measurements 127
3.7.1 Introduction 127
3.7.2 The Principle of Optical Absorption 128
3.7.3 The Cary 500 Spectrophotometer 129
3.7.4 The Vacuum UV Spectrophotometer 130
3.8 Experimental Setup for the Raman Study 131
3.8.1 Introduction 131
3.8.2 The Exciting Laser 132
3.8.3 The Raman Spectrograph 132
3.8.4 The Monochromators 132
3.8.5 Gratings 134
3.8.6 Scanning Mechanisms and Spectral Range 135
3.8.7 Detectors 135
3.8.8 Photon Counting 135
3.8.9 Oxford Micro-cryostat 136
3.9 The Principles of the X-ray Photoelectron Spectroscopy (XPS) 137
3.10 Transmission Electron Microscopy 138
3.10.1 Introduction and Principles of Operation 138

4 Optical Properties of Proton Implanted Cesium Iodide Crystals 142

4.1 Motivation and Scope of Work 142

4.1.1 Preparation of the CsI Crystals 142

4.1.2 Implantation and Storage of the Crystals 143

4.1.3 Annealing of the Crystals 144

4.1.4 Optical Absorption and near-Resonance Raman Studies 145

4.2 Discussion of the Results 146

4.2.1 Typical Optical Absorption and Raman Spectra 146

4.3 Isochronal Anneal 152

4.4 Isothermal Anneal 155

4.4.1 Comparison With Defects Produced in Irradiated KI and RbI . . 158

4.5 Summary and Discussion 160

5 Mg Colloids in Magnesium Fluoride Single Crystals 163

5.1 Motivation and Scope of Work 163

5.2 Sample Preparation and Implantation of Mg^+ ions into MgF_2 163

5.3 Optical Absorption Measurements and Annealing of the Samples 164

5.4 Surface Studies of Mg^+ Ion Implanted MgF_2 Sample 165

5.5 Discussion of Results 165

5.5.1 A SRIM2003 Simulation of Ion Implantation in MgF_2 Crystals . 165

5.5.2 Optical Band Features Observed before Annealing 168

5.5.3 Air Annealed Samples 168

5.5.4 Results of Use of the Mie Theory (MT) and Characteristics Emerging from the Variation of the Fit Parameters 173

5.5.5 Effects at Higher Annealing Temperatures 177

5.5.6 Argon Annealed Samples 180

5.6 Summary and Discussion 181

6 Optical Studies of Ag and Au Metal Nanoparticles Embedded in Lithium Niobate 184

6.1 Motivation and Scope of Work 184

6.2 Preparation and Implantation of LN Samples 185

6.2.1 Introduction 185

6.2.2 Implantation of LN Using Ag^{+} Ion Beam 185

6.2.3 Implantation of LN Crystals Using Au^{3+} Ion Beam 185

6.2.4 Optical Absorption Measurements and Annealing of the Samples 186

6.2.5 Rutherford Backscattering Study of the Au^{3+} Implanted LN Sample 186

6.2.6 TEM Specimen Preparation 187

6.2.7 Identity of Implanted Samples 188

6.3 Results and Discussion I: Optical Absorption Effects of Annealing on the Host Matrix 189

6.4 Results and Discussion II: Ag^{+} Ion Implanted LN 190

6.4.1 Optical Absorption Studies of Ag^{+} Ion Implanted LN Samples . 190

6.4.2 Correlation between the MT-Fit and the Experimental Data - Ag^{+} Implanted LN 195

6.5 Results and Discussion III: Au^{3+} Ion Implanted LN 200

6.5.1 Results of RBS Studies of Unannealed Au^{3+} Ion Implanted LN Sample 200

6.5.2 Optical Absorption Studies of Au^{3+} Ion Implanted LN 203

6.5.3 Correlation Between the MT-Fit and the Experimental Data - Au^{3+} Ion Implanted LN 206

6.6 Summary and Discussion 211

7 Proton Irradiation of Tin Doped Indium Oxide (ITO) Films 215

7.1 Motivation and Scope of Work 215
7.2 The Irradiation of the ITO Films 215
7.2.1 Measurement of the Sheet Resistance 216
7.3 Results and Discussion 220
7.3.1 Simulations of the Proton Bombardment of ITO Films 220
7.3.2 X-ray Diffraction Studies 221
7.3.3 Optical Properties of the Substrate 223
7.3.4 Optical Properties of the ITO Films 225
7.3.5 Model of Defect Growth Behaviour 229
7.3.6 Results of the Resistance-Temperature Measurements 233
7.3.7 Correlation between the Optical, Structural and Electrical Properties 234
7.4 Summary and Discussion 236

8 Studies of the Properties of Polycrystalline Magnesium Fluoride Films 239
8.1 Motivation and Scope of Work 239
8.2 Preparation of PMF Films 240
8.2.1 Substrate Preparation 240
8.2.2 Thermal Evaporation Unit 240
8.2.3 Resistance Measurements 243
8.2.4 Ion Implantation of the Films 243
8.2.5 Ion Milling of the Films 244
8.2.6 Reduction of the Films 245
8.3 Results and Discussion 246
8.3.1 Summary of Prepared Selected Samples and Their Identities . . 246
8.3.2 Results of SRIM2003 Simulations of the Mean Depth of Ions Implanted into PMF Films 247

8.3.3 Results of the Structural Analysis 247
8.3.4 Results of the Annealing Studies in a Slightly Reducing Atmosphere 249
8.3.5 Results of the Optical Studies 251
8.3.6 Results of the Resistivity Measurements 254
8.4 Summary and Correlation with Optical Properties 256

9 Summary and Discussion, and Outlook for Further Work 258
9.1 Optical Studies of Proton Implanted CsI 258
9.1.1 Summary and Discussion 258
9.1.2 Outlook for Further Work 259
9.2 Mg Colloids in Magnesium Fluoride Single Crystals 260
9.2.1 Summary and Discussion 260
9.2.2 Outlook for Further Work 262
9.3 Studies of Ag and Au Metal Nanoparticles Embedded in Lithium Niobate 262
9.3.1 Summary and Discussion 262
9.3.2 Outlook for Further Work 265
9.4 Comparison of the Optical Behaviour of Mg MNP in MgF_2 and Ag or Au MNP in LN Systems 265
9.5 Proton Irradiation of Tin Doped Indium Oxide (ITO) Films 267
9.5.1 Summary and Discussion 267
9.5.2 Outlook for Further Work 269
9.6 Studies of the Properties of Polycrystalline Magnesium Fluoride Films . 269
9.6.1 Summary and Discussion 269
9.6.2 Outlook for Further Work 270

Bibliography 272

Appendix

A 289

A.1 Expansion of Some Higher Order Terms of the Mie Equation 289

A.2 Mie Theory Simulations Using Originlab 6.1 291

B 294

B.1 Solving Defect Growth Kinetic Equations Using Micromath Scientist . 294

C 298

C.1 Published Refereed Articles and International Conference Proceedings . 298

C.2 Articles in Preparation for Publication 299

C.3 International Conference Presentations 299

Tables

Table

1.1 Previously observed optical absorption of *V* bands in irradiated K and Rb iodides. 22

1.2 Raman transitions due to iodine and iodide ions in solution and solid matrices. 34

1.3 Colour centres and colloids in AEF. The colloids in the spectral regions indicated in this table are due to the same cation as the one forming the AEF. 52

2.1 Details of the values of the mean free path, l, Fermi velocity, v_F, and the plasma frequency, ω_p, used in the calculations. 102

5.1 Details of the parameters used to fit the experimental data using MT shown in rows 2 - 4. The data after the double line shows the experimental values of the FWHM ($\triangle\omega_{1/2}$) used to calculate d. The Fermi velocity v_F (Mg) $\approx 1.58\times10^6$ m/s. 176

6.1 Details of the LN sample identity, implantation conditions and subsequent analysis after implantation. Ion implantation was performed by the implanter for the case of Ag^+ ions, while the tandem accelerator was used for the higher energy implantation of Au^{3+} ions in LN crystals. . . 188

6.2 Details of the fit parameters used to correlate the experimental data to the theory for the Ag^+ ion implanted X-cut LN sample (see rows 2 - 4). For comparison purposes, the data in the row immediately after the double line shows the experimental values of the FWHM ($\triangle\omega_{1/2}$) which can also be used to estimate the values of d. 197

6.3 Details of the fit parameters used to correlate the experimental data to the theory for the Au^{3+} ion implanted Y-cut LN sample. 207

6.4 Details of the fit parameters used to correlate the experimental data to the theory for the Au^{3+} ion implanted X-cut LN sample. 208

7.1 Details of the peak position, in degrees, arising from X-ray reflections of characteristic crystallographic planes associated with the In_2O_3 lattice before, immediately after and one month following the irradiation of sample 5 (to a fluence of 250×10^{15} protons/cm^2). 222

8.1 Details of selected PMF film samples as-grown, ion implanted, and co-deposited with AlF_3 at LNT. Samples 10 - 13, 15 - 16 and 18 - 20 (deposited during a single evaporation run) were implanted with Mg^+ ions to a fluence of 100×10^{15} ions/cm^2. 246

8.2 Results of resistivity measurements at RT of samples implanted with various fluences of Mg^+ ions at 100 keV at LNT. Samples 13, 15, 16 and 18 - 20 were prepared during a single evaporation run. Values of the resistivity in brackets, unbracketed and in square brackets were measured before, after ion implantation and annealing at standard conditions, respectively. 254

9.1 PR peak position as a function of the annealing temperature. Bulk metal melting points (m.p) and the observed MNP colloid band decay temperature are also shown. 266

Figures

Figure

1.1 The relationship between the projected range R_p and the total ion path R as the ion is scattered from the forward direction [1]. 5

1.2 Typical dependences of electronic (S_e) and nuclear (S_n) contributions to the stopping power (S) as a function of the incident particle energy. E_c is the critical energy. S is in reduced units and hence dimensionless [5]. 7

1.3 Calculations of lattice disorder generated by 2.5 MeV alpha particles implanted into crystalline quartz. The fluences range from 0.5×10^{16} to 12×10^{16} ions/cm^2 [1]. 10

1.4 The dependence of sputtering yield on incident angle, θ [1]. 12

1.5 Range and damage simulations of 2 MeV alpha particles implanted into lithium niobate (LN). EP, NP and RA represent profiles of the electronic damage processes, nuclear collisions and the ion range, respectively [1]. 14

1.6 Optical absorption band diagram of an alkali halide crystal. The subscripts e and g stand for the excited and ground states respectively [15]. 17

1.7 Diagram showing several common defects in alkali halide crystals [16]. 18

1.8 The possible configurations of the halogen interstitial (a) Loosely bound di-interstitial centre (b) Interstitial X_2 molecule (c) X_3^- defect (d) molecule-vacancy pair complex (e) X_3^--trivacancy complex : squares enclosing negative sign represents an anion vacancy, while those enclosing a positive sign represents a cation vacancy. Taken from Catlow et al. [59] . . 23

1.9 Perfect interstitial dislocation loop in alkali halides (a) and (d) edges of loop ; (b) and (c) possible ways of accommodating halogen molecules [78]. 27

1.10 Schematic diagram of the structure of crystalline iodine. (a) Packing drawing of solid iodine (b) The orthorhombic structure projected onto the $b-c$ plane. Molecules labelled as 00 are in the $b-c$ plane, molecules labelled 1/2 1/2 are displaced by $\pm\, a/2$ from the a plane. a = 7.14 $\overset{0}{\text{A}}$, b = 9.78 $\overset{0}{\text{A}}$, c = 4.69 $\overset{0}{\text{A}}$ [107]. 31

1.11 Schematic diagram of the centre to colloid transformation in alkali halides. (a) Perfect crystal; (b) A region of aggregated F centres; (c) Formation of metal atoms after electron transfer from F centres to cations [79]. 36

1.12 Illustration of adiabatic potential surfaces connecting the various states of the STE. The total energy is plotted against the transitional co-ordinate Q_2 of the STE. Q_2=0 represents the on-centre STE corresponding to a maximum on the potential surface. The off-centre STE (FH_{nn}) may undergo radiative decay or migrate to successive minima along the Q_2 axis, corresponding to H centre migration as depicted in the lower diagram [156]. 41

1.13 Light wave incident on a metal particle. Displacement of negative and positive charges occurs on interaction with the light wave. Adapted from Kreibig and Vollmer [116]. 43

1.14 Schematic diagram of the structure of cesium iodide. The dark and light circles represent the Cs cations and iodide anion, respectively. . . . 49

1.15 Diagram showing the lattice structure of MgF_2. The Mg and F ions are represented by the shaded and open circles, respectively. The labels D_{2h}, C_{2v}, C_{2h} and C_1 refer to the four non-equivalent pairs of fluoride ions. The lattice constants a and c are 4.64 and 3.06 $\overset{0}{\text{A}}$, respectively [156]. 53

1.16 Diagram showing (a) the crystal structure of LN and a projection onto the c-axis [221], which is perpendicular to the plane of the paper; (b) the x and y directions from which the X- and Y-crystal cuts are obtained. 57

1.17 Schematic diagram of the structure of indium oxide showing the two different sites of the In, namely In1 and In2. Shaded circles at occupied corners represent oxygen atoms. Unoccupied corners represent oxygen vacancies. Adapted from Parent et al. [254]. 61

1.18 Schematic energy band diagram illustrating the doping of In_2O_3 with Sn [251]. 63

1.19 Simulated curves of the transmittance as a function of wavelength for different values of electron density starting from 1×10^{20} - 30×10^{20} cm^{-3} [251]. 67

2.1 Electronic energy, E, versus nuclear co-ordinates, $\boldsymbol{R}$, for an electronic ground state l and excited state m, also illustrating the nuclear state η and γ for each of the electronics states, respectively. $\boldsymbol{R_G}$ and $\boldsymbol{R_E}$ are the nuclear co-ordinates for the ground and excited states respectively [295]. 80

2.2 Raman spectrum of liquid CCl_4 excited by an argon ion laser. A central intense line associated with the Rayleigh line and two sets of a series of lines to its left and right are observed [311]. 81

2.3 Representation of the Rayleigh and Raman scattering as a two-photon process. The broken lines denote virtual states. 84

2.4 (a) Isochronal anneal: step-like temperature pulses of constant duration $\triangle t_f$ at successively higher temperatures T_i. (b) Isothermal anneal : increasing duration $\triangle t_i$ at fixed temperature T_a. 87

2.5 Schematic diagrams of (a) isochronal anneal showing decrease in the absorption coefficient over the possible anneal component stages (b) isothermal anneal of a single stage process. 88

2.6 The incoming electromagnetic wave, directed along the +z-axis and the outgoing spherical wave, which is scattered by a particle at position P. . 94

2.7 Schematic diagram of transmission ($\mathcal{T}$) and reflection (R) of a film-on-substrate system. L_1 and L_2 are the thickness of the film and substrate, respectively. 103

2.8 Schematic diagram showing interference spectra and the smooth envelopes $\mathcal{T}_+$ and $\mathcal{T}_-$ [331]. 105

2.9 The geometry and typical backscattered energy spectrum of a heavy thin film on a lighter substrate. The peaks are due to scattering of the incident ions by the two different elements that constitute the material under investigation. Taken from the Materials Research Society Handbook, 1995 [334]. 109

3.1 Circuit diagram of a voltage multiplier. 112

3.2 Schematic diagram of the Cockcroft-Walton high voltage transformer. . 112

3.3 Block diagram of main features of the Cockcroft-Walton accelerator (DP stands for diffusion pump). 114

3.4 Schematic diagram of a Van de Graaff generator and accelerator. 116

3.5 Schematic diagram of the main features of the tandem accelerator. . . . 118

3.6 Schematic diagram illustrating the attraction and repulsion mechanism at the centre terminal of the tandem accelerator. 119
3.7 Schematic diagram of a quadrupole lens. 120
3.8 A cross-sectional diagram of the sample holder employed in the Au ion implantation using the tandem accelerator. 121
3.9 Block diagram of the main features of the ion implanter. 123
3.10 (a) Resistance heated tube furnace used in the isochronal annealing process in air. (b) Block diagram of the enclosed Carbolite furnace used in the isochronal anneal under argon gas flow. 126
3.11 Cross-sectional diagram of a RF-heated fused silica tube furnace used in the isochronal sample annealing under gentle argon flow [337]. . . . 127
3.12 Schematic diagram of the main features and the beam path of the Cary 500 Spectrophotometer [338]. 129
3.13 Schematic diagram of the monochromator in the VUV Spectrophotometer [339]. 131
3.14 Optical diagram of the Jobin Yvon T64000 spectrometer. 133
3.15 The triple subtractive monochromator spectrograph mode. Taken from the manual of the Jobin Yvon model T64000 spectrometer. 134
3.16 Cross-sectional view of the Oxford micro-cryostat. Taken from Oxford Instruments manual. 136
3.17 (a) Schematic diagram illustrating the removal of a core electron by X-ray photons. (b) Typical XPS technique configuration. 138
3.18 Diagram of incident electron-matter interaction. 140
3.19 Schematic cross-section diagram of the optics used to display an image in a TEM facility [343]. 141

4.1 Optical absorption spectrum of a CsI sample implanted to a fluence of 6×10^{16} ions/cm^2 at room temperature measured at 77 K. The spectral positions of the F, F_2 and V bands are shown. 146

4.2 Optical absorption spectra in the V band region of KI [81] and RbI [112] samples taken near 77 K after annealing at the temperatures indicated. These crystals were subjected to γ-irradiation near room temperature and are shown for comparison purposes to indicate the position of the V bands. 147

4.3 (a) Development of the optical absorption features with increasing proton implantation fluence ($1 : 5\times10^{15}$, $2 : 1\times10^{16}$, $3 : 3\times10^{16}$, $4 : 6\times10^{16}$ ions/cm^2). (b) Growth of the F_2 band at 1.1 eV (triangles), V bands at 2.7 eV (circles), 3.4 eV (squares) and at 4.2 eV (plus sign) with increasing implantation time. All the implantations and optical absorption measurements (within 30 minutes of the former) were performed near 300 K. 148

4.4 Raman spectra of (a) a proton implanted CsI irradiated at 300 K, (b) γ-irradiated RbI [112] and (c) KI [81] samples, shown for comparison purposes. The irradiation of the latter two samples was performed at 295 K. All spectra are measured near 77 K. The Raman excitation wavelength was the 488 nm argon laser line in all cases. 150

4.5 The evolution of very weak Raman features between 130 and 210 cm^{-1} that may be associated with the presence of I_n^- and the I_2 monomer, which are known to occur near 173 and 201 cm^{-1}, respectively. These features are observed following annealing between (a) room temperature - 380 K and (b) 400 - 420 K. 151

4.6 (a) Optical absorption spectra measured at 77 K temperature following 30 minutes isochronal annealing cycles (1 : unannealed, 2 : 340 , 3 : 350, 4 : 360, 5 : 370, 6 : 380, 7 : 390, 8 : 400, 9 : 410, 10 : 420 and 11 : 430 K). (b) Similar optical absorption spectra (1-8) as in (a) above shifted to show the development around the *V* band near 4.2 eV. Sample was implanted with 1 MeV protons to a fluence of 6×10^{16} ion/cm^2 near 300 K. 153

4.7 (a) Correlation of the F_2 (triangles) and *V* bands (circles : 2.7 eV, squares : 3.4 eV and plus sign : 4.2 eV) and Raman intensity (asterisk) with increasing annealing temperature, obtained from the isochronal cycles. The absorbance values for the *V* band at 4.2 eV are reduced by a factor of 0.5. 154

4.8 Linear plot used for the determination of the activation energy for the interstitial-vacancy recombination from the isochronal annealing of the F_2 or *V* band (2.7 eV). This plot, as discussed in section 2.4, yields a straight line for $\gamma = 2$ from which the activation energy of 1.28 eV is obtained for the reaction. 154

4.9 Optical absorption spectra measured at 77 K following isothermal annealing at 397 K for the respective total durations (10, 20, 40, 80, 160, 320 minutes). The solid line represents the spectrum obtained from the as-implanted sample, which was implanted with 1 MeV protons to a fluence of 6×10^{16} ions/cm^2 near 300 K. 155

4.10 (a) Correlation between the rate of decay of the F_2 and *V* bands and the Raman intensity obtained from the isothermal annealing performed at 397 K. (b) The associated chemical reaction kinetics graph (see section 2.4) for the determination of the order of the recombination process. The reaction order is 2. 157

5.1 Results of a SRIM2003 simulation showing the distribution of the implanted 100 keV Mg^+ ions in a MgF_2 crystal as a function of depth measured from the implanted surface. 166

5.2 Simulations of the (a) energy loss via ionization and (b) vacancy creation as a function of penetration depth following ion implantation with 100 keV Mg^+ ions and the generated recoils in MgF_2 crystals using a SRIM2003 program. 167

5.3 I. Optical absorption spectra for VIS and UV photon energy range between 2.0 and 6.5 eV for MgF_2 crystals implanted with 100 keV Mg^+ ions using a dose rate of $2\mu A/cm^2$ at ambient temperature and not actively cooled. The curves correspond to different fluences of implanted ions. (a) 6×10^{15}; (b) 1×10^{16} ; (c) 3×10^{16} ions/cm^2 [123]. II. Optical absorption spectra for (d) a virgin crystal in which the spectrum was measured with air as reference, (e) and (f) after implantation with 100 keV Mg^+ ions to a fluence of 10^{17} ions/cm^2 at LNT and warmed to RT. The spectra for samples (e) and (f) were measured using a virgin crystal as reference. All measurements were done at RT. 169

5.4 (a) Annealing behaviour in air of a MgF_2 crystal after ion implantation with 100 keV Mg^+ ions to a fluence of $10^{17}/cm^2$ at LNT and warmed to RT. The curves show successive optical absorption spectra over the VIS and UV photon energy range (2.0 - 6.5 eV) during an isochronal anneal with annealing stages each of duration 30 minutes (1 : RT, 2 : 373, 3 : 463, 4 : 543, 5 : 633, 6 : 813, 7 : 903, 8 : 973 K). The spectra were measured at RT. (b) Peak absorbance of the various features in (a) above as a function of annealing temperature. Inverted triangles - F_2 band (unresolved combination of the $F_2(1)$ and $F_2(3)$ bands at 3.36 eV (369 nm); triangles - Mg-colloid at 4.43 eV (282 nm); circles - *V* band at 6.5 eV (191 nm); squares - *V* band at 7.8 eV (159 nm). 171

5.5 (a) Optical absorption spectra in the UV and VUV photon energy range between 5.5 and 11.5 eV for the same MgF_2 crystal as reported in figure 5.4. The spectra were measured at RT and have the same numbering for each annealing temperature as in figure 5.4a (2 : 373, 3 : 463, 4 : 543, 5 : 633 K). (b) - (d) Difference spectra for the UV and VUV photon energy range between 5.5 and 11 eV obtained from the data presented in figure 5.4. The figure identifies two absorption bands peaking at 7.8 eV (159 nm) and near 6.5 eV (191 nm). Spectra b, c and d in this figure represent the difference between spectra 2 and 3, 3 and 4, 4 and 5 in a above, respectively. 172

5.6 Theoretical fitting of the MT to the experimental data after the 723 K anneal. The open circles represent the experimental data while the theoretical curves are drawn in solid and dashed lines. Comparison between experimental data and theoretical spectra when (a) the best fit (ϵ_h = 2.45, d = 1.5 nm, p = 0.08) values, referred to as MT-fit in the text, are used (b) the ϵ_h is changed from the best fit value to 2.0, the real part of the linear dielectric constant of the unimplanted MgF_2, then to 3.5. (c) d is changed from the best fit to 0.9 and 2.0 nm. (d) p is changed from best fit value to 0.03 and 0.25. Note the scale difference in subfigure d. 174

5.7 MT fit to the experimental data after annealing at a : 543, b : 633, c : 723 and d : 813 K. 175

5.8 High temperature annealing behaviour in air for a MgF_2 crystal after ion implantation with 100 keV Mg^+ ions to a fluence of $10^{17}/cm^2$ at LNT and warmed to RT. The curves show successive optical absorption spectra over the UV and VUV photon energy range (3.8 - 11 eV) during an isochronal anneal consisting of stages each of duration 30 minutes. The spectra were measured at RT. The numbering of the spectra corresponds to that of figure 5.4 (6 : 813, 7 : 903, 8 : 973 K). 177

5.9 Near surface analysis of a MgF_2 sample after implantation of 100 keV Mg^+ ions to a fluence of $10^{17}/cm^2$ at LNT, warmed to RT and subjected to high temperature annealing in air to a temperature of 973 K. The analysis was carried out using XPS and shows the elemental concentration as a function of depth from the implanted surface. 179

5.10 High temperature annealing behaviour in argon for a complementary MgF_2 crystal after implantation with 100 keV Mg^+ ions to a fluence of 10^{17}ions/cm^2 at LNT and warmed to RT. The curves show successive optical absorption spectra over the UV and VUV photon energy range (3.8 - 11.5 eV) during an isochronal anneal consisting of stages each of duration 30 minutes The spectra were measured at RT. The numbering of the spectra corresponds to that of figure 5.4 (6 : 813, 7 : 903 K). . . . 180

6.1 Schematic diagram of the main stages of the TEM sample preparation. (a) Two sample slices with the implanted surfaces facing each other sandwiched between silicon crystal slices using epoxy. (b) Cross-sectional view of the cylindrical brass tube and sandwich-like structure. 188

6.2 Optical absorption spectra of unimplanted (a) X-cut LN (1: unannealed, 2: 973, 3: 1073, 4: 1173, 5: 1273, 6: 1373 K) and (b) Y-cut LN (6: unannealed, 7: 973, 8: 1073, 9: 1173, 10: 1273, 11: 1373 K) following annealing under argon flow. All measurements were performed at RT with a similar virgin and unannealed X- and Y-cut LN crystal, respectively, as reference. 190

6.3 Absorption spectra of similar X-cut LN samples implanted at various temperatures with 100 keV Ag^+ ions to a fluence of 10^{17}/cm^2 : 1 (LNT), 2 (RT) and 3 (373 K). All measurements were performed at RT immediately after ion implantation. 191

6.4 Ion distribution versus depth profile obtained from a SRIM2003 simulation of implantation into LN crystals of Ag^+ ions using energies of 100 keV. 193

6.5 Absorption spectra of sample 3 (X-cut LN face), implanted with 100 keV Ag^+ ions to fluence of $1\times10^{17}/cm^2$ at 373 K, obtained at 300 K and after the annealing temperatures indicated. The optical absorption measurements were performed at RT. 194

6.6 Comparison between the experimental data and the MT model, discussed in subsection 2.5.3, of the optical extinction spectra for sample 3 (see Table 6.1) after annealing at 573, 773 and 973 K and labelled a, b, and c, respectively. The X-cut LN sample was implanted with 100 keV Ag^+ ions at 373 K to a fluence of 10^{17} ions/cm^2. The open circles represent the experimental data, while the theory is shown by the solid line. 196

6.7 (a) Pictorial results of the TEM cross-section studies of a complementary X-cut LN sample (2, Table 6.1) showing Ag MNP within the embedding host. Lower picture shows a magnified section of the upper one. Ag MNP labelled A appears spherical, while B may be two particles sticking together. (b) EDX spectrum obtained from the implanted region of the TEM section. 198

6.8 RBS spectrum of unannealed Au^{3+} ion implanted X-cut LN sample (7, Table 6.1, section 6.2.7) performed at RT using a 6 MeV Li^{2+} ion beam. 200

6.9 Ion distribution versus depth profile obtained from a SRIM2003 simulation of implantation into LN crystals with (a) 8 MeV Au^{3+} ions (open diamonds). (b) 6 MeV Au^{2+} (open squares) and 10 MeV Au^{4+} (open circles). The latter two are included since there is a possibility of these ions finding their way into the target due to lack of use of the analyzer magnet. 202

6.10 The results of a SRIM2003 simulation of implantation into LN crystals with 8 MeV Au^{3+} ions showing the (a) energy loss profile (by primary ions - squares; recoils - circles) and (b) distribution of vacancies (created by primary ions - triangles; recoils - diamonds) as a function of penetration depth. 203

6.11 Optical absorption spectra after isochronal annealing for 30 minutes for (a) Y-cut sample (1 : 673, 2 : 773, 3 : 973, and 4 : 1073 K). (b) X-cut sample (5 : 973, 6 : 1073, 7 : 1173, and 8 : 1273 and 9: 1373 K). Both the X- and Y-cut LN samples (see Table 6.1) were implanted with Au^{3+} ions at a beam energy of 8 MeV to a fluence of 10^{17} ions/cm^2 at RT. All optical absorption measurements were performed at RT. 205

6.12 Results of the MT fit of the FWHM, PR peak position and intensity of the intensity of the experimental data for the 8 MeV Au^{3+} ion implanted Y-cut LN sample annealed at 773, 973 and 1073 K and labelled a, b, c, and d, respectively. Open circles represent the experimental data and the solid line describes the theory. The implantation done at RT to a fluence of 10^{17} ions/cm^2. 207

6.13 Results of the MT fit of the FWHM, PR peak position and intensity of the experimental data for the Au^{3+} ion implanted X-cut LN sample annealed at 1073, 1173, 1273 and 1373 K and labelled a, b, c, and d, respectively. Open circles represent the experimental data and the solid line describes the theory. The X-cut LN sample was implanted with 8 MeV Au^{3+} ions at RT to a fluence of 10^{17} ions/cm^2. 208

6.14 (a) Pictorial results of the TEM cross-section studies of a complementary X-cut LN sample (8, Table 6.1) showing Au MNP within the embedding host following annealing at 1173 K. Lower picture shows a magnified section of the upper one. (b) EDX spectrum obtained from the implanted region of the TEM section. This sample was implanted at RT with 8 MeV Au^{3+} ions to a fluence of $1\times10^{17}/cm^2$. 210

6.15 Representative selected area electron diffraction pattern of various positions around the Au MNP within the implanted region. The X-cut LN sample investigated was annealed at 1173 K. The electron diffraction pattern shows hexagonal symmetry associated with the LN structure. . . 211

7.1 Schematic of the cryogenic probe and a cross-sectional diagram of the copper sample holder. 218

7.2 Measurement circuit diagrams used for the determination of the resistance of (a) the sample and (b) the thermometer. 219

7.3 Graphical results a of SRIM2003 simulation showing (a) the electronic energy loss profile with distance and (b) the ion range distribution for 1 MeV protons accelerated into an ITO thin film on float glass. The thickness of the film (610 nm) is indicated. 220

7.4 Graphs showing the results of room temperature X-ray spectra of selected samples (a) immediately after proton irradiation. They are samples 1, which was unirradiated and 2, 3, 4 and 5 which were irradiated to a fluence of 1, 6, 40 and 250×10^{15} protons/cm^2 at a beam energy of 1 MeV, respectively; (b) after storage for a month. 222

7.5 (a) Transmittance (T) and reflectance (R) spectra of a 2.5 mm thick floatglass substrate. (b) Calculated values of the real part (n_2) and imaginary part (κ_2) of the refractive index and the absorption coefficient as a function of wavelength from measurement of the transmittance and reflectance of the float glass substrate spectra shown in figure 7.5a. . . . 224

7.6 Transmission spectra of selected ITO samples with varying proton fluence after irradiation with 1 MeV protons at: I - near RT (a: unirradiated, b: 1×10^{15}, c: 6×10^{15}, d: 40×10^{15}, e: 190×10^{15}, f: 215×10^{15}, g: 250×10^{15} ions/cm^2); II - 373 K (h: unirradiated, i: 6×10^{15}, j: 40×10^{15} k: 120×10^{15}, l: 190×10^{15}, m: 215×10^{15}, n: 250×10^{15} ions/cm^2). Optical spectra measured at RT. The spectrum between that for the unirradiated sample (h) and that for sample i has been omitted in II for better clarity. 226

7.7 (a) The optical transmittance of irradiated ITO thin films after storage for about a month (a : unirradiated, b : 1×10^{15}, c : 6×10^{15}, d : 40×10^{15}, e : 250×10^{15} ions/cm^2). (b) The real (n_1) and imaginary (κ_1) parts of the refractive index as a function of wavelength for selected samples 1 : unirradiated, 2 : 1×10^{15}, 3 : 6×10^{15}, 4 : 40×10^{15} and 5 : 250×10^{15} ions/cm^2. The calculations were performed using the data from I in figure 7.6. The curves for both optical indices are represented by the same type of lines. 228

7.8 The variation of the absorption coefficient in the middle of the visible region (at 550 nm) with irradiation time obtained for two similar samples near RT and at 373 K, represented by circles and squares, respectively. 229

7.9 Simulation of the variation of the defect concentration of x centres with irradiation time at different temperatures, near RT (solid line) and 373 K (dashed line). The following parameter values have been used in the simulation: $\sigma = 1.6 \times 10^{-13}\exp(-E_m/K_BT)$ cm^3 s^{-1}, $E_m = 75$ meV; $g = 10^{16}$cm^{-3} s^{-1}; $\sigma_d = 7.1\times10^5\exp(-E_d/K_BT)$ s^{-1}, where $E_d = 0.12$ eV; $\sigma_1/\sigma = 1.0$, $\sigma_2/\sigma = 0.02$; $s_0(0) = 3\times10^{15}$cm^{-3}, where $s_0(0)$ stands for the density of pre-existing defects at time ($t = 0$). 231

7.10 Relationship between the irradiation induced absorbance difference (A) and wavelength for various irradiation fluences: 6, 40 and 250×10^{15} protons/cm^2. The $1/\lambda$ dependence is associated with cluster absorption. 232

7.11 Graph showing resistance-temperature behaviour of selected ITO film samples after irradiation. it000 is unirradiated, while it115, it416, it2516 are irradiated with proton fluences of 1, 40 and 250×10^{15}/cm^2, respectively. 233

8.1 (a) Diagram of the flame polishing process applied to the substrates used in PMF film deposition. (b) Top-view diagram of PMF film on pyrex glass/fused silica substrate with palladium electrodes. 241

8.2 Schematic cross-sectional diagram of the thermal evaporation unit used for the deposition of the PMF films on to pyrex and fused silica glass substrates. 242

8.3 Schematic cross-sectional diagram of the resistance measurement setup. 244

8.4 Schematic cross-section diagram of the argon gas mill. 245

8.5 Graphical SRIM2003 simulations showing the range of 50, 75 and 100 keV Mg^+ ions used in the implantation of the PMF films plotted on the same scale. 247

8.6 (a) X-ray diffraction spectrum of a 500 nm (sample 4, Table 8.1) thick PMF film deposited on a pyrex glass substrate at LNT. The symbols t and c stand for tetragonal and cubic phases present in the polycrystalline sample. Measurements were performed at RT. (b) Photograph of a 375×375 μm^2 region of the surface of the PMF film sample on pyrex glass substrate taken at RT using a camera attached to an optical microscope. This is the same sample whose X-ray diffraction spectrum appears in (a) above (1 cm : 34 μm). 248

8.7 Graph showing the variation of resistivity with annealing temperature for a 500 nm thick as-grown PMF film sample (sample 5, Table 8.1). The resistivity measurements were performed around RT. 250

8.8 Graph of variation of the log of the resistivity with annealing time in a slightly reducing atmosphere (96% nitrogen and 4% hydrogen) performed at 748 K of samples 6, 7 and 8 of thickness 300, 200 and 1000 nm respectively. All resistance measurements were performed between 291 and 298 K. 251

8.9 Transmission spectra of samples 18, 19 and 20 with thickness of 250, 500 and 1000 nm respectively (a) before and (b) after ion implantation with 100 keV Mg^+ ions to fluences of 10^{17} ions/cm^2 at LNT (see Table 8.1). The transmittance measurements were carried out at RT. 252

8.10 Graph showing the changes in transmittance after the 24 hour annealing period for samples (a) 18 and (b) 19 at the temperatures indicated. The transmittance measurements were carried out at RT. 253

8.11 Graph showing the logarithm of the resistivity for samples doped with different concentrations of AlF_3. Open squares : thickness 200 nm; open circle : thickness 500 nm. 256

Chapter 1

Rationale and General Introduction

This thesis deals mainly with the optical and certain electrical effects of materials modified by radiation, including bombardment with protons and implantation with light and heavy ions. Various materials of interest have been investigated including single crystals of ionically bonded compounds such as CsI, MgF_2, $LiNbO_3$, and thin films of tin-doped indium oxide (ITO). Work has also been carried out on MgF_2 thin films doped with Al by thermal co-evaporation. An ion implanter capable of providing scanned ion beams with energies varying from 20 - 200 keV was used for shallow implants. This involved implantation of 100 keV Mg^+ and Ag^+ ions into MgF_2 and $LiNbO_3$, respectively. A Cockcroft-Walton accelerator was used to provide 1 MeV proton beams for use in performing low mass ion irradiation of tin-doped indium oxide thin films on glass substrates and creation of damage in CsI crystals. A 6 MeV tandem accelerator was used when it was necessary to implant ions, specifically Au^{3+}, deeper into $LiNbO_3$ to minimize ion diffusion out of the implanted layer by lowering the concentration gradient.

This chapter provides a general introduction to topics that are immediately relevant and associated with the theme of this thesis. Some of the topics discussed include, the mechanisms of energy loss during ion implantation, ion range and damage distributions, use and limitations of computer codes available in modelling the events that occur on ion bombardment of matter. The structure and properties of some of the defects that emerge including simple and extended defects, their characteristics and the mechanisms involved in defect creation are also presented. The well-studied alkali

halides are discussed where appropriate, in sections 1.1 - 1.6, since they provide a basis for the understanding of the properties of CsI as well as other materials studied in this work.

Much interest in what are today called metal nanoparticles has led to large resources being put in place to study how their properties may be put to use in miniaturized devices. These metal particles are alternatively known as colloids and have been studied in the past. Some discussion on colloid development and formation and an updated historical perspective on the area are presented. A descriptive introduction to chapter 2, describing the physical concepts of extinction of light by small metal particles and their response under illumination with light is also provided in sections 1.7 and 1.8.

A summarized review of the properties of the materials whose results are discussed in chapters 4, 5, 6, 7 and 8 are presented in sections 1.9, 1.10, 1.11, 1.12 and 1.13, respectively.

Chapter 2 deals with the theoretical principles relevant to this thesis including optical absorption, Raman scattering, annealing and Mie absorption and scattering. The theory of the determination of the linear optical constants of substrates, film-on-substrate and a metal-host composite is discussed.

Chapter 3 describes the equipment used in this work including the principles of operation. More specific details may be found in the references cited in the text.

In chapter 4 the optical properties of defects produced in CsI by implantation with protons having energy of 1 MeV, subjected to a series of annealing cycles and studied by both Raman spectroscopy and optical absorption techniques are presented.

Chapter 5 deals with the ion implantation of 100 keV Mg^{+} ions in MgF_2 crystals. The evolution of the optical properties with annealing temperature is discussed.

Chapter 6 discusses the effects of the implantation of lithium niobate (LN) with Ag^{+} and Au^{3+} metal ions using the ion implanter and the tandem accelerator, respec-

tively, and the emerging optical properties on annealing.

Chapter 7 discusses the results of the optical and some electrical properties of proton irradiated tin doped indium oxide (ITO) thin films.

As a follow up from chapter 5, attempts were made to produce conducting polycrystalline magnesium fluoride (PMF) thin films prepared by thermal beam evaporation and subsequent ion implantation and annealing. These results are reported in chapter 8.

A summary and discussion of the main results of the thesis and suggestions for further work are presented in chapter 9.

1.1 Ion Implantation

The following discussion on ion implantation is based on the texts of Townsend et al. [1] and Carter and Grant [2] with emphasis on issues relevant to this thesis.

Ion implantation is a process where ions are introduced into a solid sample by ion bombardment usually in the keV to MeV energy range. The solid-state effects are extensive because of the range of physical properties that are sensitive to the presence of a trace of foreign atoms. Optical, mechanical, magnetic, electrical and superconducting properties are all affected and indeed may even be dominated by the presence of such foreign atomic species. In contrast to diffusion processes in which the number of dopant ions introduced into the lattice is largely controlled by the physical properties of the sample, ion implantation provides an alternative method where the number of ions introduced is controlled by the external system. For example in the semiconductor industry, dopants can be implanted at temperatures at which normal diffusion would be negligible and the dopant concentration is not limited by ordinary solubility considerations. Thus a wider variety of dopant elements may be utilized.

The possibility of implanting insulating materials and in particular wide bandgap materials using various ions has generated a great deal of interest. The materials implanted range from items as large as glass windows to exotic and costly crystals used

in solid state tuneable lasers and opto-electronics [1]. Having mentioned several advantages of ion implantation, it is worth noting that the technique has some undesirable effects. The most common effect is the formation of radiation damage which will be discussed in section 1.1.3.

1.1.1 Energy Loss Processes in Matter

There are two main processes that contribute to the energy loss of an energetic ion implanted in a solid target [1, 2]. They are electronic and nuclear stopping. The rate of energy transfer from each process depends on the nuclear charge Z_1, mass M_1 and energy E_1 of the incoming ion and the nuclear charge Z_2 and mass M_2 of the target atoms. When the ion velocity is high, electronic stopping is predominant in the beginning of the impinging ion's path into the implanted material. There are several possible origins of electronic stopping. They mainly involve exchange interactions, excitations and ionization of the target and projectile electrons.

As the ion penetrates further into the solid, reaching lower energies, nuclear stopping starts to dominate and eventually forms the major part of the energy loss process. Here the ion experiences a number of violent collisions with the atoms of the solid displacing them from their lattice positions. The higher energy transfer to target atoms during nuclear interactions will result in the slowing down of the penetrating ion to occur faster. The large momentum transfer on the other hand will cause increased scattering thereby enhancing the lateral spread of a beam of incident ions.

The total loss of energy with penetration depth in a medium of unit atomic density, $S(E)$, is defined as the stopping power. $S(E)$ may be expressed as a combination of the nuclear, electronic and other interactions' stopping powers in the form

$$S(E) = -\frac{dE}{dx} = \left(\frac{dE}{dx}\right)_{nucl.} + \left(\frac{dE}{dx}\right)_{elec.} + \left(\frac{dE}{dx}\right)_{other}. \qquad (1.1)$$

The units of $S(E)$ are eV cm^2/atom among several other units used in the literature. By

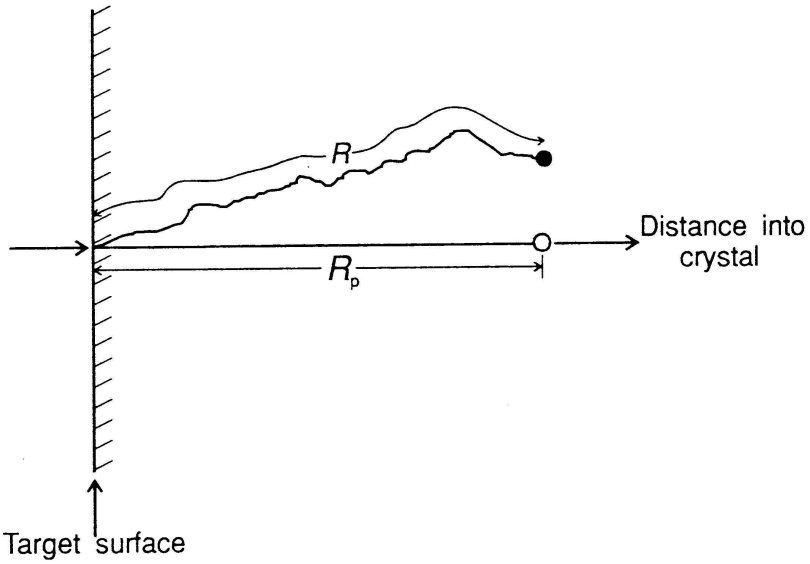


Figure 1.1: The relationship between the projected range R_p and the total ion path R as the ion is scattered from the forward direction [1].

integrating equation 1.1, the mean distance, $R(E)$, an ion travels before coming to rest from an initial energy E_0 is estimated by

$$R(E) = \int_0^{E_0} \frac{dE}{NS(E)} \tag{1.2}$$

where N is the number of target atoms per unit volume. Generally, from predicted functions of the components of $S(E)$, which depend on the mass and velocity of the incoming ion and target atom, it is possible to calculate the total path length for a given ion and target. Figure 1.1 indicates the difference between the mean projected range $R_p(E)$, being the ion range normal to the surface, and $R(E)$ the total ion path. $R_p(E)$ is normally smaller than $R(E)$ by a factor which depends on the scattering angles, mean path, and, thus the specific path of an individual ion. Moreover, because of multiple collisions, the ions will be deviated from their original direction leading to a lateral spreading, $R_\perp$(straggling effect) of the ion beam in the target. In the case of a single element target, the ratio $R_p/R \ll 1$ for $M_1 \ll M_2$, and close to 1 for $M_1 \gg M_2$. For a compound target material, the determination of the ion range is more complicated by

the need to consider the combination of interactions between the ion and the constituent atoms of the compound.

In reality, statistical fluctuations in the actual stopping mechanism will give a spread to the range R and hence contribute to the spread $\triangle R_p$. The extent of spreading, which shows dependence on the mass ratio M_2/M_1, will increase with larger penetration depths into the target. However, a small deviation is observed for heavy ions incident on a light atom target ; for $M_2/M_1 \simeq 0.1$, $\triangle R_p \simeq 0.2R_p$. The spreading increases with an increasing M_2/M_1 ratio and is about $0.5R_p$ for $M_2 = M_1$. The straggling effect results in an ion distribution which is approximately Gaussian in form and hence a typical range distribution in an amorphous or even polycrystalline substrate may be characterized with a mean range and a straggling about this mean. Initial calculations of such range spreading, both along the projected range direction, and laterally, were discussed by Schiott [3].

When using low energies, the concentration $C(x)$, of implanted ions at a depth x, for an incident fluence D (ions/cm^2) in a target of atomic density N characterized by R_p and $\triangle R_p$ [4], is given by

$$C(x) = \frac{D}{(2\pi)^{1/2} N \triangle R_p} \exp\left[\frac{-(x - R_p)^2}{2\pi \triangle R_p}\right]. \tag{1.3}$$

An estimate of the average impurity concentration within the implant region assuming a Gaussian distribution is

$$C(x) = (\text{Total Fluence})/2.5\triangle R_p. \tag{1.4}$$

1.1.2 Energy Dependence of the Stopping Cross Section

Figure 1.2 [5] schematically illustrates how electronic and nuclear contributions to the stopping cross section depend on the incident ion energy. The critical energy,

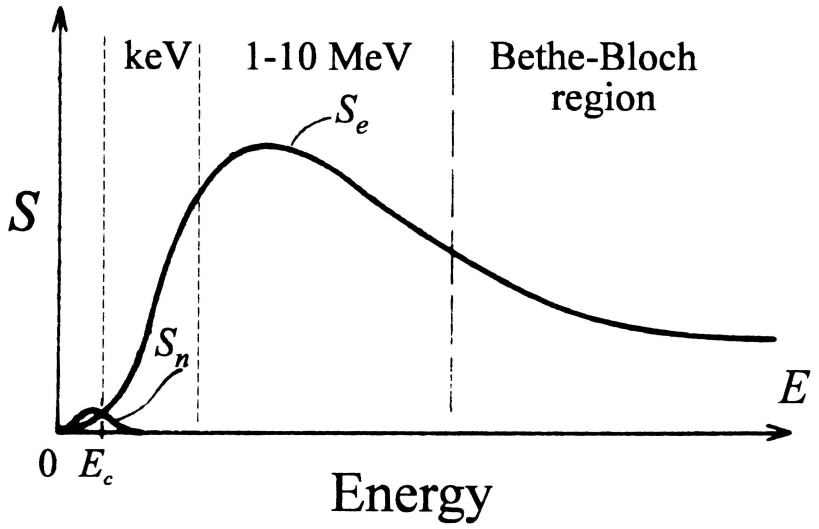


Figure 1.2: Typical dependences of electronic (S_e) and nuclear (S_n) contributions to the stopping power (S) as a function of the incident particle energy. E_c is the critical energy. S is in reduced units and hence dimensionless [5].

E_c, is defined as the energy below which the nuclear ($S_n = (dE/dx)_{nucl}$) and electronic ($S_e = (dE/dx)_{elec}$) stopping are comparable as shown in figure 1.2. In the range 1 - 10 MeV, electronic stopping reaches a maximum value before decreasing as the incident energy is raised further. In this energy regime, the velocities of the incident ions are similar to those of the orbital electrons in the target atoms which leads to exchange of electrons between the two and hence an enhancement in electronic energy loss. For higher energy, E >10 MeV, stopping is well described by the Bethe-Bloch formalism [6]. The electronic stopping decreases when moving to higher energies in the Bethe-Bloch region. This is due to the fact that the higher the velocity of the incident ion, the less time it has to interact with each target atom it encounters. The Bethe-Bloch formulation for electronic stopping (S_e) in the region where E > 10 MeV is given by

$$S_e = \frac{4\pi e^4 Z_1^2 Z_2}{m_e \mathrm{v}^2} \mathcal{L}(\mathrm{v}), \tag{1.5}$$

in which Bethe's stopping number is expressed as

$$\mathcal{L}(\mathrm{v}) = \ln\left(\frac{2m_e\mathrm{v}^2}{\mathcal{I}_e}\right) - \ln\left(1 - \frac{\mathrm{v}^2}{c^2}\right) - \frac{\mathrm{v}^2}{c^2} - \frac{C}{Z_2} - \frac{\xi}{2}. \tag{1.6}$$

$\mathcal{I}_e$ is the mean excitation potential of the target, e is the electronic charge, m_e is the mass of the electron, c is the speed of light, v is the velocity of the incident ion and C/Z_2 the shell correction, where C is a constant that varies between 1.5 - 2. ξ is an ultra-relativistic density correction which can be neglected [6]. The mean excitation potential is defined as

$$\ln \mathcal{I}_e = \sum f_n \ln E_n, \tag{1.7}$$

where E_n are all possible energy transitions of the target atom and f_n the corresponding dipole oscillator strengths. The calculations of $\mathcal{I}_e$ are usually based on a statistical model of the target atoms. The shell correction accounts for the deviations from the requirement in Bethe's derivation that the projectile velocity should be much larger than that of bound electrons [1]. Bethe's calculation is based on a first order quantum mechanical perturbation treatment. In practice, equation 1.7 is too complicated to use except for the case of the simplest target atoms. Usually arguments of a Thomas-Fermi screening [2] nature are used to estimate $\mathcal{I}_e$ [7] which in its simplest form is given by Bloch's rule namely $\mathcal{I}_e = \mathcal{I}_0 Z_2$ where $\mathcal{I}_0$ is approximately 10 eV [8]. The most substantial change is that Z_1 enters into the stopping number, and thus, that the position of the maximum depends on atomic number of the projectile ion. The charge state of the penetrating ions is normally not clearly known. However, a general rule states that projectile electrons having speeds exceeding the projectile velocity will stick to the projectile while the slower ones, belonging to the outer shells, will be stripped [1].

There are two regions in figure 1.2 that are of importance in the present study. The low and medium energy regions which vary from 1 - 1000 keV and 1 - 10 MeV, respectively. The 100 keV Ag^+ and Mg^+ ion implants fall within the low energy region while the 1 MeV protons and 8 MeV Au^{3+} ion implants fall within the medium energy

region. Figure 1.2 also indicates that electronic stopping is the dominant energy loss mechanism as the accelerated ions move through the target. Nuclear stopping becomes significant as the ions are brought to rest. This occurs at relatively lower energies which are less or near the critical energy, E_c. Because the implantation of Ag^+, Mg^+ and Au^{3+} ions into the various samples was deliberately performed in such a manner that these ions were largely to remain within the implanted region, the effects of both the electronic and nuclear stopping need to be considered.

1.1.3 Damage Distribution and Implanted Ion Profiles

Damage production is *inter alia* a function of the temperature of the sample at which the implantation is performed and the original state of the lattice. Relatively more defects are created and retained when the ion implantation is done at low temperatures because of reduced diffusion rates. Although the displacement energy may be about 25 eV for a dynamic displacement in which an atom is forced through the neighbouring sites of an unperturbed lattice, electronic processes that involve a long-lived excited state allow lattice relaxation and hence greatly reduce the barrier to atomic motion. An effective displacement threshold may thus fall to 5 or 10 eV. At lower fluences, mainly point defects exist, but once sufficient disorder is formed by damage, impurities or stress, then the rate of defect production increases rapidly. In part this may reflect a lowering of the displacement threshold energy. At the highest fluence levels a near amorphous layer may develop and so the rate of formation of damage saturates.

Damage distributions and implanted ion profiles may appear to be similar. However, closer examination reveals that the peak due to the former occurs closer to the surface. This is because energy is transferred to target ions throughout the ion range; hence displacements will occur even near the surface while the distribution of implanted ions will be peaked at greater depths. In a crystalline target, the displacement energy will be direction sensitive, and may decrease with increasing disorder in the lattice. Figure

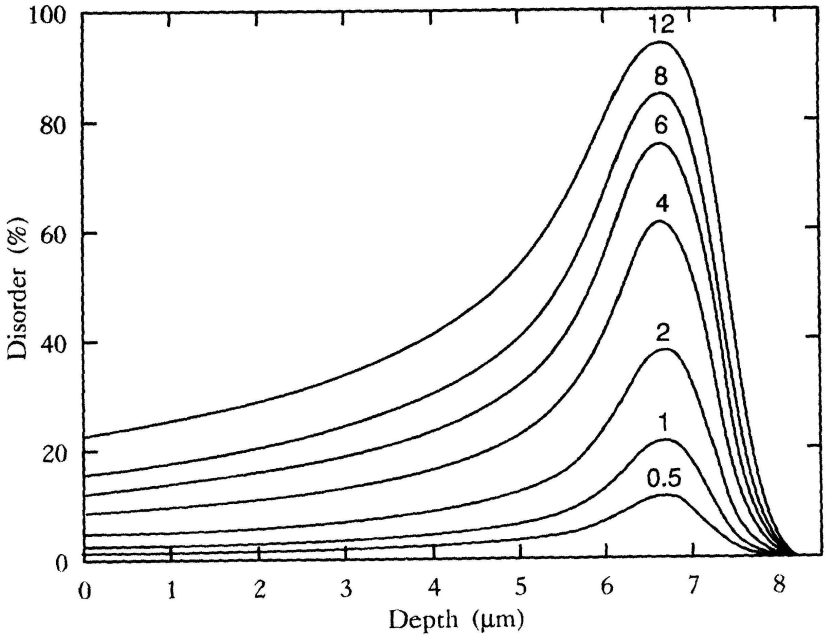


Figure 1.3: Calculations of lattice disorder generated by 2.5 MeV alpha particles implanted into crystalline quartz. The fluences range from 0.5×10^{16} to 12×10^{16} ions/cm^2 [1].

1.3 shows an example of calculated damage distributions for different fluence for alpha particles implanted into crystalline quartz. The damage creation profile shown in this figure is only an estimate referring to the initial damage situation during the entry of the ion into the sample. There could well be a complete recovery after the passage of several incident ions. Computer simulations predict that the core of the cascade will be vacancy rich whereas interstitials will predominantly appear at the outer parts of the track. However the separation of vacancies and interstitials is insufficient to stabilize them and a very large percentage of the damage recovers within nanoseconds.

1.1.4 Defect Diffusion, Relaxation, Amorphization, Crystallography and Sputtering

The point defects and lattice disorder created during ion implantation are not in thermal equilibrium resulting in a high probability of migration within the implantation layer. These two entities will eventually tend toward thermal equilibrium with defects which require an activation energy, E_a, being formed with a probability proportional to $\exp(-E_a/K_BT)$, where T is the effective temperature and K_B is the Boltzmann's constant. This includes defect clusters with E_a values of perhaps 10 eV which would have been totally inhibited by any normal thermal treatment. The net effect of this is that in insulators implanted with energetic light ions there will be regions of point defects, near the surface, and more complex structures near the end of the ion track. Without sufficient recovery of damage in the implanted region, the continued production of local disorder may lead to the development of an amorphous region. With increasing fluence, damage tracks will overlap and thus help in the stabilization of the amorphous region. The presence of amorphous regions will affect a property of crystalline material such as the refractive index which has been observed to decrease in certain cases [1].

The development of stress may also influence the diffusion, relaxation and amorphization. Typically stress builds up to a critical level and is followed by a collapse with consequent plastic flow, precipitation of defects and relaxation. Diffusion of defects in crystalline materials is not isotropic and therefore ion implantation in different crystallographic directions will not be identical in as far as defect retention is concerned. If the direction of rapid diffusion coincides with that of damage production, defect retention will be less and hence there will be a dependence on crystal cut [9].

The process of ejection of target atoms from the surface by incident ions during ion implantation is referred to as sputtering. The number of ejected atoms per incident ion, the sputtering yield, is a function of the incoming ion energy E_0 and the masses

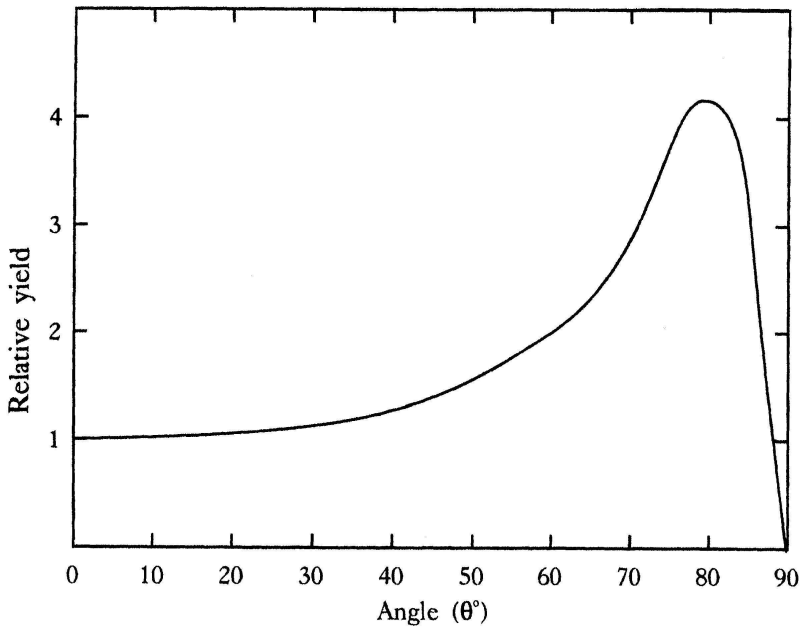


Figure 1.4: The dependence of sputtering yield on incident angle, θ [1].

of the ion and target atom M_1, M_2. The yield is also a function of the depth of the energy deposition so the yield varies strongly with angle of incidence θ, as shown in figure 1.4. The relative sputtering yield is defined as the ratio of the sputtering at an angle θ to the sputtering at 0^0. The original theoretical descriptions of sputtering such as those of Thompson [10] and Sigmund [11] were made in terms of single element targets. The predictions were for idealized systems and describe the initial sputtering yields from perfect amorphous solids caused by the deposition of energy via nuclear collision processes. This approach leads to some apparent conflict with experimental data since for experimental reasons it is normally simpler to measure the steady state or large fluence sputtering yields. In compounds, the sputtering yield is not the same for all elements. Assuming that the sputtering cascade is in thermal equilibrium, the lighter ions are travelling faster and so are more likely to escape from the surface. Hence, compounds are most likely to be depleted of the lighter elements. The situation

becomes more complicated as gaseous elements, such as oxygen or nitrogen, tend to be lost more readily than metallic elements of comparable mass.

1.2 Computer Simulations

Estimates of the ion range and damage distribution profiles are important parameters for ion implantation processes and numerous computer simulation programmes have been developed in this regard. The incorporation of all the events that take place as an energetic ion enters a target until it comes to rest is a complex task. Besides the processes involving electronic and nuclear stopping, other events include :

a) sputtering from the surface of the target,

b) the possibility of annealing of damage created,

c) stabilization of defects and creation of new compounds and

d) diffusion of simple or clustered defects among others.

The discussion in the first paragraph within this section assumes that the target is amorphous. When dealing with a crystal lattice, not only will the ion trajectories be steered by the planes and channels of the lattice (channeling), but, additionally, the separation of vacancies and interstitials will be sensitive to the diffusion rates along different crystalline directions. Integrating all these events in the simulations has yet to be achieved. However, estimates of the range distribution and initial damage creation are still useful.

Many of the simulations are well refined and widely used but are only a guide since the final damage distribution may look totally different from initial picture provided. Some of the widely used programs, have been upgraded continuously over the years from their original versions, e.g. the TRIM (TRansport of Ions in Matter) of Biersack and Haggmark [12], has been modified both by Biersack, Ziegler and by owners of copies of the program to produce several versions that have appeared almost yearly. Recently the simulation program was modified to SRIM (Stopping and Range of Ions

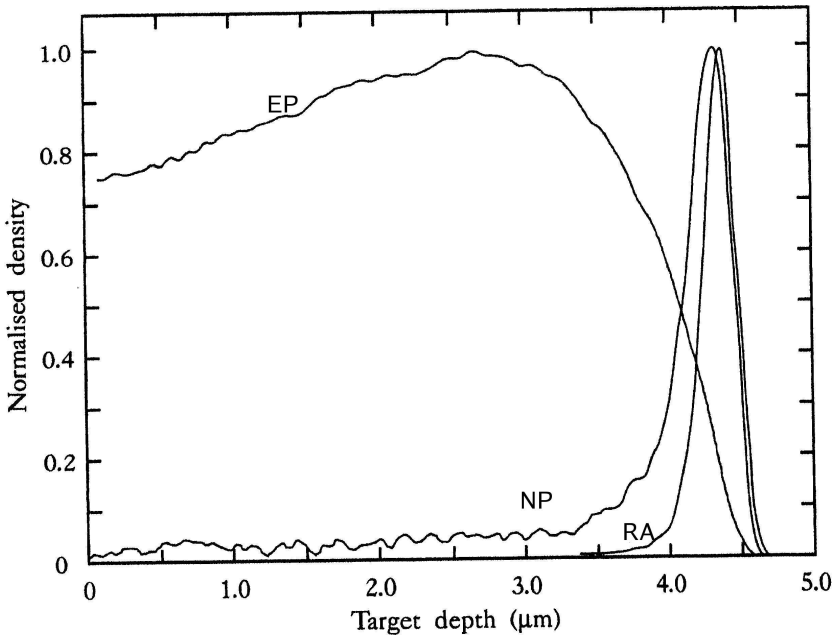


Figure 1.5: Range and damage simulations of 2 MeV alpha particles implanted into lithium niobate (LN). EP, NP and RA represent profiles of the electronic damage processes, nuclear collisions and the ion range, respectively [1].

in Matter) [13]. Stating the version of TRIM used is important, or else the simulation may lead to apparent anomalies in range and lateral distributions of the implanted ions which far exceed the normal 10% accuracy expected from a modern version. Variants of TRIM include codes for sputtering, high dose damage estimates and formation of new compounds. A different binary-type code which is designed for crystalline targets is named MARLOWE [14] and others are under development. Examples of electronic, nuclear damage distributions and the ion range profile which are obtained from TRIM98 simulations are shown in figure 1.5 for the case of alpha particles with energy of 2 MeV implanted into LN. From this simulation, it is clear that most of the energy of the ion is lost in electronic processes (profile represented by curve EP). The total number of target vacancies created by nuclear collisions is distributed in a peak near the end of the track (profile represented by curve NP). The centre of this distribution is at about 4.2 μm. The energy loss mechanism below this value is dominated by ion-

ization. The ion range (profile represented by curve RA) is also distributed in a peak, the centre of which is slightly deeper than the nuclear damage distribution centre. This example shows that the simulations can be successfully used at quite high energies, despite being initially designed for low energy ion implantation of semiconductors.

1.3 Introduction to Radiation Induced Defects in Crystals

In terms of ionic crystals the alkali halides are the most widely studied materials in as far as radiation induced defects are concerned and many of the examples quoted in this section will refer to them. This will form a basis for the study of the optical behaviour of implantation induced defects in CsI and the other irradiated materials in the present work. Studies of defects in other crystals such as the alkaline earth fluorides to which MgF_2 belongs will also be presented. Although there are reports in the literature on studies of irradiation of oxides performed over periods spanning a few decades, those involving defect studies in ternary oxides, particularly In_2O_3 and $LiNbO_3$ (LN), are relatively few. The study of oxides can be interesting especially due to the existence or creation of oxygen vacancies which can be neutral, singly or doubly charged. A summarized review of the defect studies and properties of the two oxides will be presented in separate sections that follow. The italic *F* is used to represent the *F* centre, being an electron trapped in a negative ion vacancy, rather than F which is used to represent the fluorine ion.

A general description of the nature of bonding and optical response to photon energy is first discussed. Alkali halides are strongly ionic in character and with the cations and anions occupying the lattice points of two interpenetrating face centred cubic lattices in the majority of cases. Each alkali metal ion is surrounded by six nearest neighbour halide ions and vice versa. Assuming that the crystals are of ideal stoichiometric composition then the energy band scheme will be that of a completely filled valence band and empty conduction band. In the ionically-bonded salt form, the cations

and anions have the rare gas electronic configuration. The energies of the outermost p orbital electrons of the halide ions are of the order of several electron volts higher than those of the alkali ions, and so constitute the highest valence band. The band gap lies in the range 6 - 10 eV [15]. As a result of the large forbidden gap intrinsic alkali halides and indeed many other wide bandgap crystals are transparent between the ultraviolet and near infrared (IR) region of the spectrum. Absorption in the far IR is associated with lattice vibrations of the ionic constituents, whereas absorption in the ultraviolet (UV) arises from electronic transitions. The latter correspond to the removal of an outer p electron from the halide ion and its promotion into the conduction band. However, if the photon energy corresponds to the long wavelength tail of the UV absorption, a bound electron-hole pair is created: the valence electron is raised to an energy level below the conduction band, corresponding to the promotion of the halide electron to a higher excited state though maintaining a Coulomb bond with its complementary hole. This bound electron-hole pair is called an exciton and the corresponding energy levels are called exciton bands.

1.3.1 Influence of Lattice Defects on the Electronic Levels

The idealized energy level scheme suggested above, wherein the energy gap between the valence and conduction band contains only the exciton levels, does not occur in practice. All crystals no matter how pure contain some structural defects (mainly vacancies and interstitials) and trace impurities that introduce localized energy levels into the forbidden band. Thus new absorption bands present in the optically transparent region of the pure crystal result from the presence of such imperfections; accordingly optical absorption techniques may be used to study them. As an example an energy band scheme of an alkali halide crystal is shown in figure 1.6 [15]. Defects which reduce the bonding energy of the halide electrons introduce occupied electronic levels above the valence band; defects which cause an increased electron affinity over and

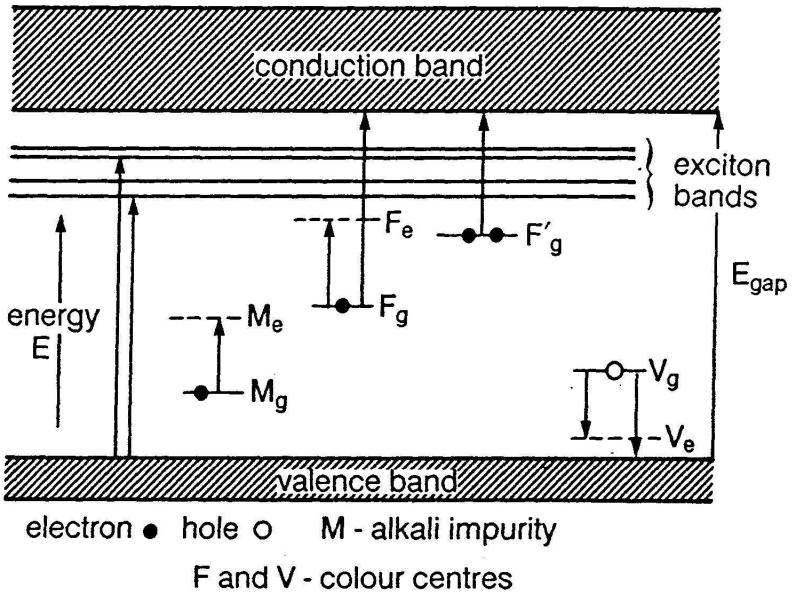


Figure 1.6: Optical absorption band diagram of an alkali halide crystal. The subscripts e and g stand for the excited and ground states respectively [15].

above that of the regular lattice cations introduce unoccupied states below the conduction band. The resulting absorption, often in the visible region of the spectrum accounts for the naming of responsible defects as *colour centres*.

1.3.2 Defects Produced by Irradiation of Ionic Crystals

Defects created by irradiation can be classified as electron or hole centres. The spectrum of the defects created in a given crystal is a function of the crystal itself, the type of radiation used, the irradiation temperature, the fluence, dose rate, as well as the pre-existing defects and impurities in the crystal. Although several types of defects occurring in crystals will be discussed, more emphasis will be placed on the processes of defect aggregation, extended defects and colloid formation. Again work on alkali halides is emphasized, since it provides a relatively complete picture of the types of processes involved. Figure 1.7 [16] shows a schematic diagram of some of the defects.

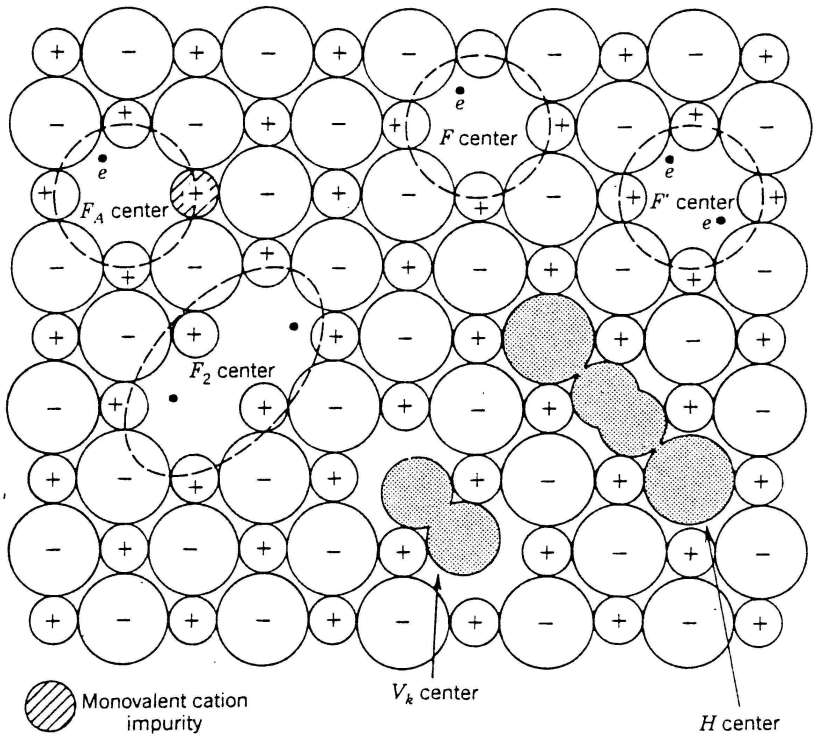


Figure 1.7: Diagram showing several common defects in alkali halide crystals [16].

1.3.3 The *F* Centre and its Related Charge States

There are several electron centres that arise from a vacant site or sites in the lattice. The vacancies are generally, but not always, occupied by an electron or electrons. In alkali halides, intrinsic vacancy centres include not only the F centre but also the F^+ and F^- (F') centres derived from alteration of the charge state of the F centre, and the F_2, and F_3 centres derived from the aggregation of F centres. Alteration of the charge state of aggregate centres can also occur. Selected centres are discussed briefly within this subsection while the aggregate centres are treated separately.

The F centre in alkali halides [17] consists of an electron trapped at a negative ion vacancy and is an electrically neutral entity. A 3-D particle-in-a-box model has proved quite successful in explaining the properties of F centre absorption [18, 19]. EPR studies [20] have been applied to this paramagnetic centre establishing the degree

of localization of the electron. The large width of the *F* band and the temperature dependence of its peak position arises from the interaction of the trapped electrons with lattice vibrations. Absorption bands on the high energy side of *F* band are due to transitions of the trapped electrons to higher excited states.

When an *F* centre captures an electron, a new centre, the F^- centre is formed which is thermally unstable at ambient temperature. The centre is formed during irradiation at sufficiently low temperatures or by low temperature ($\approx$ 100 K) bleaching of coloured crystals by *F*-band light, resulting in the transfer of an *F* centre electron to another *F* centre [21, 22, 23, 24, 25, 26]. The process yields an F^- centre and an empty anion vacancy known as an F^+ or an α centre [27]. The F^+ centre absorption band arises from a perturbed exciton transition in the vicinity of an F^+ centre.

The F_A centre is a perturbed *F* centre having one of its nearest neighbour as a foreign cation with a smaller ionic radius than the host cation [28].

1.3.4 *F* Aggregate Centres

In crystals irradiated at room temperature or at somewhat lower temperatures and warmed to room temperature, there are bands that appear on the low energy side of the *F* band. These are due to small aggregates of *F* centres; two such centres comprise F_2, or *M* centre, while three centres result in an F_3, or *R* centre. This discussion is immediately relevant to the work in MgF_2 where similar structures have been reported and will be discussed in chapter 5.

The mechanism of the production of such aggregates has been and is still the subject of controversy. The proposed mechanisms include those in which the F^+ centre is the mobile entity [23, 29, 30, 31, 32, 33] and those favouring an excited state of F^* of the *F* centre as the mobile entity [34]. Further aggregation of *F* centres in alkali halides leads to the formation of metallic colloids formed from the host cations. This process is discussed further in section 1.5.

1.3.5 Hole Centres

Several of the trapped hole centres in alkali halides are known as *V* centres and include the variety of defects complementary to the anion vacancy centres. Early studies of these centres were presented by Schulman and Compton [15]. Intrinsic hole centres include the V_K centre, the self-trapped exciton, the *H* centre and the *I* centre [35]. A summarized discussion of the first three hole centres is given in the sections that follow and the centres are shown schematically in figure 1.7.

1.3.6 The V_K Centre (X_2^-) and the Self-Trapped Exciton (STE)

First identified by EPR studies of Castner and Kanzig [17], the V_K centre (or the self-trapped hole) consists of two adjacent halide ions which have trapped a hole resulting in a bonding state. It can be represented by molecule ion $[X_2^-]$ oriented along a $< 110 >$ direction (see figure 1.7) in which the intermolecular separation is slightly reduced from that of the free X_2^- ion. The square brackets imply that it is an integral part of the lattice. The V_K centre is a very efficient electron trap thus creating an exciton-like structure whose role in the production of Frenkel defects will be explored in Section 1.6.

The identity and structure of the self-trapped exciton (STE) was determined via a number of studies [36, 37, 38, 39, 40, 41, 42, 43] ultimately leading to the modern view of an off-centre STE of considerable importance in the excitonic mechanism of defect creation (section 1.6).

1.3.7 The *H* Centre

This is the major complementary defect (see figure 1.7) of the *F* centre at sufficiently low irradiation temperatures ($\simeq$ 4 - 20 K). The *H* centre consists of an interstitial halogen atom bound to a halide lattice ion. In structure it resembles the V_K centre being

described by a X_2^- molecule ion orientated along a $< 110 >$ direction in most alkali halides. However in this case there are two halogen atoms per one halide ion lattice site such as in the split interstitial configuration [35, 44, 45].

There are a number of perturbed *H* centres associated with cation and anion impurities [46]. The H_A centre is formed when an *H* centre is trapped close to a substitutional impurity such as Na^+ or Li^+, the configuration depending on the specific alkali halide and the dopant.

When the dopant species are divalent cations, charge compensation comes into effect resulting in the incorporation of cation vacancies in the lattice. Below room temperature, these vacancies exist mainly in the form of impurity-vacancy (IV) dipoles [46, 47]. The H_D centre is thus identified as an interstitial halogen trapped at a IV dipole [48, 49, 50, 51, 52, 53].

1.3.8 *V* Centres in K and Rb Iodides

There is general confusion in the assignment of *V* bands as a result of comparisons between crystals coloured by a variety of methods. The *V* bands were originally named from ultraviolet absorption spectra produced by the effect of ionising radiation on alkali halides but the same nomenclature has been applied to bands arising from other methods, occurring in different positions and from different species [54, 55]. This discussion will, however, be restricted to the optical properties of *V* bands in pure iodide crystals of K and Rb. Table 1.1, taken from the work of Winter et al. [56], summarises some of the observations in the two iodides. Winter and co-workers noted that the V_2 and V_3 could also be produced by thermal bleaching of V_4 and V_2, respectively near and above the production temperature. Konitzer and Hersh [57] had earlier reported a *V* band near 275 nm which was produced at 195 K. It was assigned to a composite V_2V_3 band. They made similar observations, to Winter and co-workers, with the spectral location of the V_2 and V_3 bands being 335 nm and 310 nm, respectively. The

Iodide	V_4 (100 K)	V_2 (200 K)	V_3 (300 K)
K	355 nm (3.50 eV)	325 nm (3.82 eV)	310 nm (4.0 eV)
Rb	360 nm (3.44 eV)	355 nm (3.50 eV)	345 nm (3.60 eV)

Table 1.1: Previously observed optical absorption of V bands in irradiated K and Rb iodides.

former was produced at a larger temperature range, while the latter at a similar temperature. The observations of Lefrant and Rzepka [58] concur with the two discussed earlier in terms of the spectral location of the V_2 and V_3 bands and the temperature of their production.

1.3.9 Models for the di-interstitial Centre

A substantial effort was made by Catlow et al. [59] to explain defect reactions leading to the initial clustering of interstitial species using the method of computational lattice simulations in alkali halides. Using the HADES program of colleagues Lidiard and Norgett [60] they developed a set of lattice potentials which faithfully generated a wide class of halide crystal properties yielding values of defect energies, proposed viable structures and possible stabilization and aggregation dynamics. They started with the $< 110 >$ configuration of the X_2^- molecule of the single H centre. As the H centre migrates it recombines with F centres or may be stabilized by impurity traps, in which the binding energy is supplied by the interaction of the elastic strain field of the impurity trap and the H centre. They had considerable success [61, 46] and made predictions that agreed with EPR results of Delbecq and co-workers [62]. Apart from looking at models of a possible range of impurity traps, they extended the calculations to the problem of H centre clustering. In the context of the current work only the model for intrinsic di-interstitials defects are discussed. The complex consisting of two neighbouring H centres shown in figure 1.8a was found to be bound [59]. This complex can show composite structure due to a range of weakly bound di-interstitial

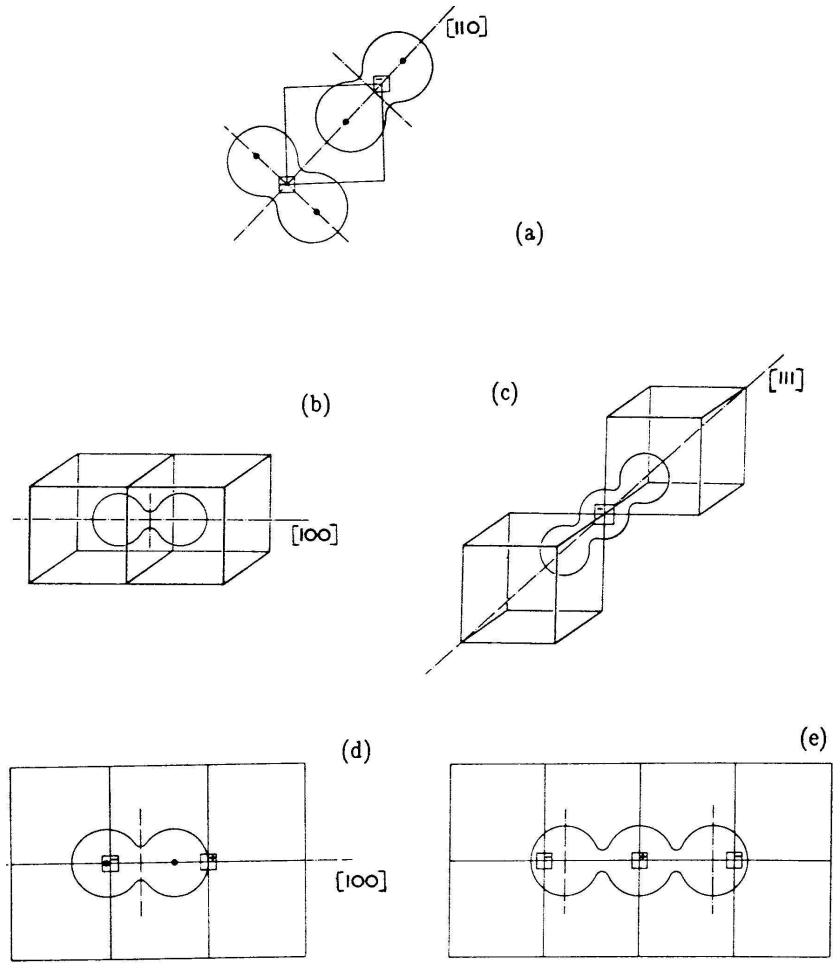


Figure 1.8: The possible configurations of the halogen interstitial (a) Loosely bound di-interstitial centre (b) Interstitial X_2 molecule (c) X_3^- defect (d) molecule-vacancy pair complex (e) X_3^--trivacancy complex : squares enclosing negative sign represents an anion vacancy, while those enclosing a positive sign represents a cation vacancy. Taken from Catlow et al. [59]

aggregates with configurations varying about their lowest-energy geometry [63, 59]. The collapse of such a structure into halogen molecular aggregates was also investigated by considering likely halogen atom displacements. Although the emerging two end products, the X_2 neutral molecule adopting the cube-centre configuration (figure 1.8b) and the $< 111 >$ oriented X_3^- molecular ion (figure 1.8c), were found have similar binding energies, the former was favoured. The reason being that the formation of

the X_3^- molecular ion includes a kinetic barrier to motion of the aggregating H centres which could limit its formation at higher temperatures. Because the magnitude of the barrier was not known there is a possibility that either of the interstitial complexes could be responsible for the V_4 absorption band [35] created by irradiation near 77 K in KCl and KBr and the V_2 band in KI. These latter conclusions are not sustained by Raman spectroscopy studies (see the discussion below).

Catlow and co-workers [59] also investigated the energy reduction in accommodating these di-interstitial types in anion-cation vacancy pairs. Figure 1.8d shows an X_2 molecule in an anion-cation vacancy pair, while figure 1.8e shows a defect formed by the interaction of such a molecule-vacancy defect with a neighbouring lattice ion to form a X_3^- molecule along a $< 100 >$ orientation. The formation of such defects in conjunction with a proposed mechanism of dislocation loop formation (section 1.3.10) would result in a substantial reduction in energy. An interesting aspect of the structure in figure 1.8e is that a linear X_3^- molecule had been proposed earlier by Christy and Phelps [64].

The absorption spectrum of I_3^- molecular ion has been very well defined. Hersh [65] studied the absorption spectrum of iodine dissolved in aqueous iodide solutions and observed bands peaking near 3.8 eV and 4.4 eV which were attributed to this molecular ion. Hersh [66] proposed that this molecular ion was a linear array of iodine molecule and an iodide ion. Similar bands were reportedly observed in a number of iodide crystals coloured by irradiation or additive methods [64, 57]. The latter workers observed that the ratio of the intensity of the band at 4.4 eV to that at 3.8 eV was a constant in their growth or decay suggesting that they were related to the same defect.

Other suggestions for the model of the I_3^- complex includes one by Okuda et al. [67] who proposed it to be a linear symmetrical molecular ion oriented along $< 100 >$ direction and bound to a cation vacancy. This model explained the photochemical behaviour of interstitial centres above 77 K and agreed with the results of ionic conduc-

tivity from the work of Forbes and Lynch [68].

Subsequent studies of photochemical conversions in electrolytically and additively coloured KI undertaken by Okada [54, 55] provided evidence for at least four different structures of an I_3^- molecular centre in KI below 100 K, which differed in the configurations of the I_3^- centre around a cation vacancy. This study gave strong indications that at low temperatures the molecular ion centre is optically sensitive, the molecular axes can orientate in different directions, giving rise to a range of structures and absorption spectra for two associated *H* centres. Each spectrum consists of a peak in the 340 to 360 nm range accompanied by another peak in the 288 to 303 nm spectral region. The ratio of the peak heights may vary from one type of configuration to another.

1.3.10 Interstitial Aggregates and Dislocation Loops

Interstitial aggregates are produced in alkali halides and other wide band gap crystals by irradiation at room temperature or by low temperature irradiation with subsequent warming of the crystal. They give rise to optical absorption bands in the UV and, as discussed previously, known generally as *V* bands. Early attempts to identify these centres were based mainly on observation of the behaviour of the *V* bands under various conditions of irradiation and bleaching, and gave rise to a large variety of proposals : The first models, due to Seitz [69, 70], proposed an arrangement of holes in association with a positive ion vacancy or cluster of vacancies. Later Varley [71] suggested that the centres comprised interstitial metal ions and halogens atoms. It was not until much later that a consistent picture emerged. Comins [72] and Sonder et al. [73] were among the first researchers to suggest that two or more interstitial halogen atoms may be stabilized together. Evidence for di-interstitials came from work by Itoh and Saidoh [74, 75] and gradually the concept of interstitials clusters, nucleated homogeneously or at impurity traps, emerged. It was only later with increased interest in the

evolution of defects to the macroscopic damage stage [76] that the identity of some of these interstitial aggregate species was conclusively established. Agullo-Lopez et al. [77] have presented these developments and have drawn together and clarified the wide range of reported centres in their comprehensive review.

It is now appropriate to discuss the nature of the defects which supersede the above mentioned *cluster* stage. At some point beyond this defect stage these clusters develop into perfect dislocation loops detected by Hobbs and co-workers, in an electron microscope [78, 79], who made a detailed study of interstitial clusters at different temperatures and produced in various ways in alkali halides. Crystal specimens irradiated by an external source could be mounted on a low temperature (10 K) microscope stage for observation of damage for the order of minutes (e.g. KI) before *in situ* damage of the sample by the beam would occur. The major complementary structures to the *F* centres in a wide range of alkali halides after high dose of irradiation (corresponding to the *F* centre concentration of 10^{17}cm^{-3} and upward) were observed in the electron microscope to be large clustered defects. Increasing the irradiation dose had the effect of increasing the cluster size. A detailed study of the size and morphology of the clusters formed in KI irradiated at room temperature, led to the conclusion that these large scale clusters exhibited the characteristics of planar interstitial dislocation loops. The correlation between halogen atom mobility and loop growth on the one hand and the correlation between centre concentration and the number of halogen sites involved in the loops, on the other, led Hobbs et al. [78] to propose that the perfect interstitial dislocation loops arose from halogen interstitial aggregation together with displacement on the cation sublattice. Figure 1.9, taken from Hobbs and co-workers, shows their proposed model for the dislocation loops. Other proposals for the formation for the dislocation loops include that of Catlow et al [59], which is presented in figure 1.8d in subsection 1.3.9. This group studied the energies involved in loop formation through a process of displacement of lattice ions onto a dislocation loop by an

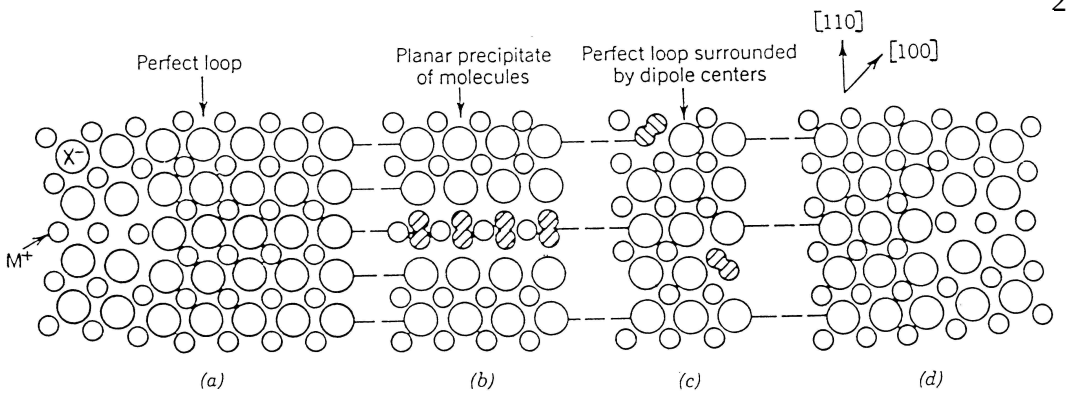


Figure 1.9: Perfect interstitial dislocation loop in alkali halides (a) and (d) edges of loop ; (b) and (c) possible ways of accommodating halogen molecules [78].

interstitial halogen molecule which would then occupy the cation-anion vacancy created. Such a process is favoured thermodynamically and may be indirectly related to the molecule-in-a-vacancy pair suggested by Stott and Crawford in their study of dipolar defects [80]. Other proposals for the molecule-vacancy defect involve its interaction with a lattice anion producing a linear X_3^- molecule ion that is shown in figure 1.8e. Thus another possible model for the dislocation loops is a perfect loop surrounded by the X_3^--trivacancy complexes.

The work on the use of Raman spectroscopy to study defects in crystals was pioneered by Lefrant and Rzepka [58, 81] and by Allen, Comins and co-workers [82, 83] and was employed to study the stage between the primary damage and the formation of large interstitial defects considered to lead ultimately to dislocation loops. This technique contributed significantly to the clarification of the structure of the interstitial aggregates beyond the use of optical absorption and electron microscopy [79]. The study of interstitial aggregates in KI is one good example where the Raman technique was used to systematically follow the evolution of the I_3^- molecule to a higher aggregation form by trapping of single iodine interstitials. Even fine details such as a change of the lattice environment could be detected in the form of a shift of a few wavenumbers in the

Raman peak associated with the I_3^- molecular defect in doped crystals [83, 84]. Higher order aggregates of iodine defects are discussed in section 1.4 to follow.

1.3.11 Defect Growth Kinetics

The general shape of the growth curve of *F* centre concentration as a function of irradiation fluence in alkali halides near room temperature consists of three stages which depend on temperature, dose rate, chemical impurity and thermal history [85]. The characteristics of this curve will be used as a reference for the proton irradiation of thin films of ITO on float glass in the present work which shows similar features. In an attempt to explain the shape of the *F* centre colouring curves in alkali halides, various theoretical models for defect production and stabilization emerged. Impurities in the crystals were found to alter the shape of the colouring curves. For instance, monovalent cation impurities with radii smaller than cations of the host crystal would trap interstitials to form H_A centres while those with cations whose radii was larger had no significant effect [86, 87]. Introduction of divalent cation impurities causes the creation of cation vacancies of the host crystal for charge neutrality in the lattice. These isolated vacancies were initially thought to act as saturable traps for interstitials and therefore to result in the enhancement of the early stage of the *F* centre colouring curve at room temperature [88, 89] and the proportionality between the early stage growth and the square root of impurity concentration. The earliest models developed by Farge [90] and Sonder [73] considered that impurities act as saturable traps, and appeared to reproduce very well the stage I growth plus a saturable pattern. However, low temperature ESR studies by Shoemaker [46] and the use of an ionic thermocurrent technique (ITC) by Marat-Mendes and Comins [52, 91, 92] established that the IV dipoles acted as the major trap for the halogen interstitials.

This new revelation on the role of the IV dipoles formed in the presence of di-valent impurities was the key to disproving that the stage I was truly saturable because

it could be altered by changing the temperature of the sample. By using a system of kinetic equations, it was demonstrated in a model by Comins and Carragher [48, 49] that the first stage is a dynamic process involving stabilization of interstitial defects at IV traps and radiation-induced detrapping of interstitials. This model satisfactorily accounted for the dynamic temperature dependence of the first saturation stage and provided a new explanation of the square root relation on divalent cation impurity concentration discussed earlier. It thereby changed the interpretation of the exhaustion of pre-existing defects and the isolated vacancy approach as an explanation of the shape of stage I [48, 49].

Agullo-Lopez and Jaque [85, 93] had earlier developed a set of rate equations describing the intrinsic production of defects, the effects of interstitial clustering, the effect of trapping at impurities and of interstitial *F* centre recombination. Though the computer solutions to these equations agreed remarkably well with the experimental data on dose rate and impurity effects, the model assumed homogeneous nucleation of interstitial clusters which was clearly in contradiction to the observations of Hobbs et al. [76]. This model was later modified to include heterogeneous nucleation by impurities [94, 95]. Other models along these lines were proposed by Itoh and Goto [96] and Guillot and Nouailhat [97] and the computer simulated growth curves reproduced satisfactorily the characteristics of the experimental growth curves.

Ramos et al. [98] extended the model for *F* centre colouring in alkali halides doped with divalent impurity cations which change their valence state during irradiation. Their model incorporated all three stages of *F* centre colouring : the first stage being interpreted as the heterogeneous nucleation of single *H* centres at IV dipoles, the second less stable stage associated with the trapping of di-interstitials at such dipoles, and the third being the formation of large interstitial clusters. Their numerical solutions showed good qualitative agreement with experimentally determined patterns. Increasing the intensity of the radiation shortened stage II and enhances the colouring rate of

stage III.

On the other hand, for very pure samples, the structure of the colouring curve is lost and the *F* centre concentration is observed to grow monotonously with fluence, reaching a higher level of colouration than the impure sample [99]. The presence of impurities delay the *H* centre aggregation process by stabilizing the early interstitial species. A detailed review of impurity-related processes in irradiated alkali halides is well presented by Agullo-Lopez et al. [77].

1.4 Previous Raman Studies of Iodine and Iodine in Solution

There are numerous Raman scattering studies on iodine in matrices and solution reported in the literature. This section will summarize the main results and focus on immediate relevance to the present work and hence not all references are cited here. The first documented Raman spectra of halogens are attributed to Stammreich and colleagues [100, 101]. Thereafter several other workers [102, 103] reported results of Raman spectra of iodine species in various environment and specifically noted features near 114 cm^{-1} and 143 cm^{-1}. The 114 cm^{-1} Raman band, attributed earlier to a symmetric stretching mode of I_3^- [102], was studied [75] in more detail by newly emerging techniques such the near resonance Raman effect which showed the peak at 114 cm^{-1} and concomitant progressive overtones. The weaker band observed near 143 cm^{-1} was attributed to an antisymmetric stretching mode of I_3^-. It was also found that the peak position of the Raman band of the I_3^- symmetric stretching mode in aqueous iodide solutions of K, Li, Na and Cs all yielded the same 114 cm^{-1} Raman shift. Loos and Jones [104] observed a band at 155 cm^{-1} which showed behaviour independent of the 114 cm^{-1} and attributed it to a higher polyiodide, I_n^-. Indications of dissociation [103] of iodine clusters in solution have also been noted with a shift in wavenumbers from 202 cm^{-1} to 114 cm^{-1} and 143 cm^{-1}. It was well established that the observation of Raman bands in solid matrices agreed well with those in solution [105, 106]. In par-

ticular a band at 180 cm^{-1} was attributed to molecular iodine in aggregated form, $(I_2)_n$. A broad feature at 170 cm^{-1} was attributed to a higher order polyiodide of the type I_5^- and a shoulder on this band at 145 cm^{-1} was assigned to the antisymmetric I_3^- mode, in agreement with the work on ions in solution.

1.4.1 Structure of Crystalline Iodine

Figure 1.10a shows a diagram of the orthorhombic unit cell of crystalline iodine, whose symmetry is of the space group D_{2h}^{18}, and contains 8 atoms (4 molecules) [107]. In part (b) of the same figure the position of the atoms in the $b - c$ projection is shown. The I-I bond length in the crystalline iodine molecule is 2.72 $\overset{0}{\text{A}}$, which is longer than in the gaseous molecule. Each iodine atom is also involved in a charge sharing type of bond with the two nearest neighbours at 3.50 $\overset{0}{\text{A}}$ [108].

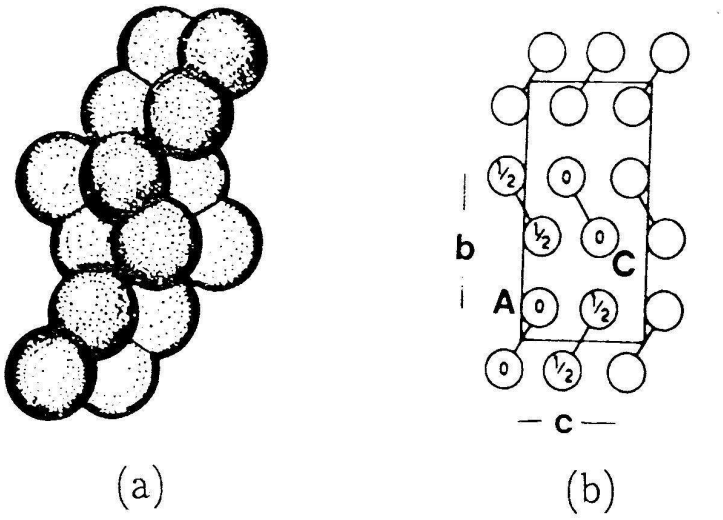


Figure 1.10: Schematic diagram of the structure of crystalline iodine. (a) Packing drawing of solid iodine (b) The orthorhombic structure projected onto the $b - c$ plane. Molecules labelled as 00 are in the $b - c$ plane, molecules labelled 1/2 1/2 are displaced by $\pm\, a/2$ from the a plane. a = 7.14 $\overset{0}{\text{A}}$, b = 9.78 $\overset{0}{\text{A}}$, c = 4.69 $\overset{0}{\text{A}}$ [107].

1.4.2 Raman Scattering in Irradiated Alkali Halides

Lefrant and Rzepka [58, 81] were instrumental in the use of the Raman scattering technique in an organized study of crystal defects. Using both Raman scattering as well as optical absorption techniques they studied X-irradiated KI crystals at 190 and 273 K. At the lower temperature they observed an absorption band at 335 nm (3.7 eV), while the Raman spectra showed two peaks located at 113 cm^{-1} and 173 cm^{-1}, with the one located at the latter wavenumber being weaker. They associated these Raman peaks observations to the I_3^- molecule. A shoulder at 275 nm (4.5 eV) observed in the optical absorption measurement for the I_3^- in solution had earlier [109] been also attributed to the same molecule. The I_3^- molecular complex was proposed to be the product of the first stage of stabilization of iodine interstitials resulting from the trapping of two interstitial atoms at a halide ion site or the capture of a further interstitial by an already trapped single interstitial:

$2I^0 + I^-_{lattice} \rightarrow I_3^-$ or $I^0 + I_2^- \rightarrow I_3^-$.

At 273 K there was a reduction in the optical absorption band at 335 nm and a new unresolved band emerged at about 310 nm (4 eV). There was also a corresponding reversal in the intensities of the Raman features at 113 cm^{-1} and 173 cm^{-1}. The latter feature grew and the former decayed. The Raman peak at 173 cm^{-1} was associated with I_n^- polyiodide clusters.

Irradiation of KI crystals [58, 81] at room temperature resulted in a broad optical absorption band extending from 300 nm to 500 nm. The associated Raman spectrum revealed two sharp peaks observed at 180 and 189 cm^{-1} which were similar to those assigned to aggregated iodine molecules by Andrews et al. [110] and Shanabrook and Lannin [111]. It was established that the observed large iodine molecular structures were products of the evolution of the cluster types, from the smaller I_3^- and I_n^- aggregates at lower temperatures to the large $(I_2)_n$ aggregate at room temperature [81].

Comins and co-workers [83, 84, 112, 113] reported results of several experiments involving X- and γ-irradiation of pure and doped KI at 198 K and near room temperature, and pure RbI at similar temperatures. These results are summarised in the current and next three paragraphs. The behaviour of defects formed by irradiation in these two iodides is immediately relevant to the present work since the cations belong to the same group, 1 of the periodic table. Irradiation of a KI sample below room temperature formed I_3^- and traces of I_n^- centres observed by Raman spectroscopy as features occurring at 113 cm^{-1} and 173 cm^{-1}, respectively. Optical absorption studies showed that the *V* bands at 3.8 and 4.4 eV are related to the Raman feature at 113 cm^{-1}. Subsequent work performed on γ-irradiated KI below room temperature gave a clearer picture. An annealing stage at 338 K for both the Raman features at 113 cm^{-1} and 173 cm^{-1} was revealed. An isothermal anneal carried out at this temperature was found to be consistent with second order reaction kinetics and an activation energy of 1.4 eV. An unresolved residual *V* band absorption observed in earlier work [84] was subsequently explained [114]. It was established that the remaining *V* band absorption above the 338 K annealing stage was due the presence of a small number of $(I_2)_n$ defects.

Room temperature γ-irradiations and subsequent annealing of a similar KI sample show that the main optical absorption bands are the *F* and a broad *V* band at 4.0 eV. The Raman spectrum showed features at 180 and 189 cm^{-1} associated with large interstitial iodine aggregates. The concurrent presence of small concentrations of I_3^- and I_n^- ions indicated that they are initially formed but are not the final form of the aggregating *H* centres. Simultaneous *F, V* band and Raman intensity reductions which began at 380 K, in the initial stage, indicated that the Raman intensity and a large part of the *V* band are due to the large iodine aggregates. An isothermal anneal performed at this stage of the anneal showed that first order kinetics were obeyed. Part of the *F* centre reduction in the initial stage was accompanied by the formation of potassium colloids, which together with the remainder of the *V* band annealed in the second stage,

at a higher temperature, beginning at 430 K.

The results of γ-irradiation of a RbI sample at 195 K largely indicated the presence of I_3^- complexes which annealed near 338 K via a second order reaction and an activation energy of 1.2 eV. Irradiation of a RbI sample near room temperature revealed that some interstitial halogen existed in the form of I_2^0 neutral molecules and is associated with a Raman band at 201 cm^{-1}. Subsequent annealing indicated the presence of a significant concentration of Raman-inactive halogen interstitial halogens which had a major annealing stage near 433 K with first order kinetics and an activation energy of 1.6 eV [113].

One clear difference between the products of irradiation of the iodides of the two metals is that whereas the large molecular iodine aggregates $(I_2)_n$ are formed in KI near room temperature, in RbI the dominant defect is the I_3^- both at 195 K and near room temperature. There is however the formation of the I_2^0 neutral molecules in RbI which are not observed in irradiated KI.

Table 1.2 summarises the documented Raman signals and their possible origin.

Preparation	Raman Signals (cm^{-1})	Origin
I_2 in solution	201 - 212	$I-I$ stretching of I_2^0 monomer
$I_2 - M^+I^-$ in solution	113, 143 155, 160 173	Symmetric/antisymmetric stretch I_n^- (n=5,...) I_n^-
Alkali metal-Iodine	113	I_3^-
Matrix reaction products	170 180, 189 212	I_n^- $(I_2)_n$ I_2
Thin films of crystalline iodine	180 50 - 100	$(I_2)_n$ in- and out of phase stretch of the two I_2 units of the primitive cell of an iodine crystal Crystalline iodine lattice modes

Table 1.2: Raman transitions due to iodine and iodide ions in solution and solid matrices.

1.5 Properties of Metallic Colloids

1.5.1 Introduction

The following discussion on colloids will serve as a general introduction on this subject which forms part of the present work. A colloid is a particle whose size is sufficiently small that its physical and chemical properties differ from those of the bulk material. A particle would normally be referred to as colloid when its dimensions are of the order of 1 - 100 nm. It may therefore contain a few tens to several thousands of atoms, so that at the one extreme the properties approach those of a large molecular cluster and at the other extreme those of bulk condensed matter. The contemporary terminology for colloids is now nanoparticles. Although most of the work in the recent past has involved colloids of noble metal particles, reference in some instances will be made to alkali metal colloids which have been studied for many years.

1.5.2 Colloid Formation and Nucleation kinetics

A major review article of the production and properties of metal colloids in ionic crystals has been presented by Hughes and Jain [115] and recently by Kreibig and Vollmer [116]. Part of the discussion in this subsection and those that follow have been adapted from this article. Colloids may be formed by annealing a crystal which has been irradiated at room temperature or by using crystals containing an excess of cations [117] so that *F* centres are converted into colloids. The process of colloid formation also occurs by irradiating a crystal at a temperature where *F* centres are mobile [118, 119, 120]. An electron transfer to the cations results in the formation of a metallic inclusion. Figure 1.11 [79] shows a schematic representation of this transformation. The early stages of nucleation of colloids and the structure of the embryonic colloid are not well understood. However it is well established that colloids are nucleated inhomogeneously near dislocation lines and impurities [76, 121, 122]. It should be pointed out that when

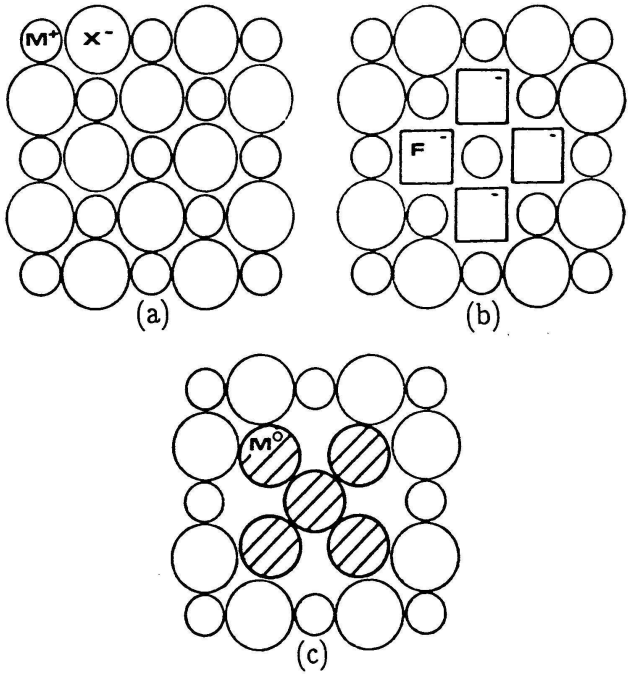


Figure 1.11: Schematic diagram of the centre to colloid transformation in alkali halides. (a) Perfect crystal; (b) A region of aggregated F centres; (c) Formation of metal atoms after electron transfer from F centres to cations [79].

using high fluences of implanted metallic ions, colloid formation may proceed via the direct agglomeration of the implanted ions [123].

Colloids in alkali halides crystals give rise to a broad extinction band in the visible region on the low energy side of the F band. Colloid bands in the visible spectral region are also observed in other ionic crystals and transparent insulators. The shape and width of the colloid band is understood from application of the Mie theory of extinction of small particles [115, 124, 125] which exhibit surface plasmon modes within a bounded conduction volume. The position and width of the band is a function of the particle size distribution. Jain and Arora [126] have used the quantum mechanical Kawabata-Kubo theory to compute theoretical extinction curves using appropriate particle size distribution functions. The composite curve for a specific particle size range

can then be easily obtained and agrees well with experiment. Given a resultant colloid band representing a range of particle sizes, the band parameters were found to be virtually independent of temperature [115, 127, 128, 126, 129].

Jain and Lidiard [125] have drawn parallels between the growth of colloids in irradiated alkali halides and void growth in metals. Adapting the rate equation for void growth, Lidiard [130] developed a formulation of interstitial growth to the dislocation loop stage proceeding alongside the aggregation of *F* centres. The predicted dose and temperature dependence of colloid radius which this analysis yielded, fitted very well with experimentally determined values. Implicit in the formulation was the assumption of a stronger interaction between interstitials and dislocations for the mobile interstitials that would result in an excess concentration of *F* centres over that of free interstitials. This excess concentration would reduce the probability of competing recombination processes and allow for the aggregation of *F* centres into colloids. The blocking of the recombination path may be because electron transfer from the *F* centre to the interstitial is rendered inefficient by the mobility of the *F* centres, or by the aggregation of the *H* centres. This interpretation is supported by the observation of Hobbs et al. [76] that dislocation climb is complimentary to the growth of colloids during irradiation of alkali halides. In the analogous process of void growth in metals, it is accepted that the stronger attraction of the dislocation to the interstitial defect is the driving force for the growth of voids [131, 132].

It is noted that in a departure from the mechanism that has generally been accepted for the formation of dislocations loops and voids developed by Hobbs et al. [76], Dubinko and co-workers [133] have proposed an alternative model that accounts for the effects observed for extremely high irradiation doses. Although the Hobbs et al. model does not explain all experimental observations, this latest model by Dubinko and his colleagues is interesting and provides valuable information but does not include the presence of *V* centres in the formulation.

Another view on colloid growth in irradiated crystals is that the mechanism may in part be similar to that which operates in additively coloured crystals viz. the aggregation of *F* centres due to thermally induced motion or due to the dislocation strain field [134]. Hughes and Jain [115] have examined the evidence for nucleation centres in colloid particles predicted in colloid growth in additively coloured crystals. The large size of colloidal particles predicted from nucleation kinetics is not achieved in practice and this they ascribed to the fact that advanced homogeneous nucleation is blocked by the lack of stability of an aggregation product. They concluded that dislocations and vacancy clusters provided nucleation sites for the stabilization of the smaller species observed.

1.5.3 Ripening and Size Distributions of Colloids

The theory of Ostwald ripening by solute transport from small particles to large particles was developed by Lifshitz and Slezov [115, 135, 136, 137] and Wagner [138]. Reviews and a discussion of the techniques and approximations involved have been given by Greenwood [139], Kahlweit [140, 141] and Jain and Hughes [142, 143]. The main objective of the theory was to describe the time variation of the particle size distribution function at any given time after the start of the ripening process. The time variation of the mean colloid radius has been studied by Calleja and Agullo-Lopez [144] in KCl. Their results were obtained using the peak position of the colloid extinction band to measure the most probable radius, which is close to the mean radius and the critical radius R_c, defined as the radius of a particle which is instantaneously fixed.

Attempts by Kreibig [124] to fit measured size distribution of Ag colloids in glass using electron microscopy to a prescribed size distribution function assuming a single ripening mechanism showed a large disparity with experimental data. Jain and Hughes [145, 146] obtained a reasonable fit to Kreibig's data by suggesting that several more or less independently ripening systems may exist in a sample where there is an

inhomogeneous distribution of nucleation sites. Jain and Arora [126] have measured the size distribution of Ag colloids in KCl by dissolving the crystal and collecting the precipitates on an electron microscope specimen grid. A good correlation for the observed size distribution was obtained when the prescribed distribution function was fitted to theoretical curves [142].

These two cases, the results of Krebig and Jain and Arora, offer examples where ripening theory has successfully explained the observed distribution sizes. However, several cases exist [145, 147] where no satisfactory explanation could be found. Jain and Hughes [145, 146] have discussed the results and concluded that the presence of some anomalously large particles can result from the rapid ripening of groups of very closely packed particles. The Lifshitz-Slezov-Wagner theory breaks down under these conditions (λ not $\ll R$) and no satisfactory alternative theory has been developed [148, 149]. Another possibility is that ripening does not only proceed by transport of solute from small particles to large particles through the matrix, but that motion of the particles themselves leads to binary collisions and coalescence [150, 151]. The qualitative behaviour of colloids has been found to be consistent with theory, but the quantitative agreement is generally lacking. The inhomogeneous distributions of colloids nucleated at dislocation sites makes the single crystal systems even more complicated for simple analysis.

1.6 Mechanisms of Defect Creation By Irradiation

A brief mention has been made under section 1.1.1 of nuclear collision (elastic) and electronic (inelastic) energy loss processes which essentially lead to damage in crystals and hence defect creation. These two processes will be referred to as defect creation mechanisms under this subsection with emphasis on the excitonic mechanism.

The nuclear mechanism involves transfer of momentum and energy from the primary ions resulting in displacement of target atoms from their lattice site hence the

creation of Frenkel defects. Further displacement of atoms occurs, either directly or indirectly, via secondary collisions by atoms of the target material. However, the largest effect of nuclear collisions is experienced at the end of the track when all the remaining kinetic energy of the accelerated ion is passed on to the target atoms. The probability of creating defects by this mechanism increases as the ion mass of the projectile becomes larger.

The process of radiolysis covers the range of mechanisms whereby ionizing radiation produces electronic excitation of such form that can be converted into energy for mass transport of the lattice ions to produce Frenkel defects [57, 152, 153, 154].

Electronic processes involve the direct kinetic energy transfer via electron-electron interactions; excitation, ionization or electron capture of the incident ion; excitation or ionization of the core electrons of the target atom and excitation of the weakly bound or unlocalized target atom electrons. If the incident energy merely excites a valence electron to a higher state, the resulting mobile exciton may be trapped at an impurity or defect site.

The production of F and H centres in alkali halides and certain other materials proceeds via an electronic mechanism in which a self-trapped exciton (STE) decays non-radiatively. The process is commonly referred to in the literature as the excitonic mechanism. The latest description of this mechanism that follows, summarized from the texts of Itoh and Stoneham [155] and Song and Williams [156], mainly relates to alkali halides but could be applied to many other halides in which self-trapping occurs (see chapter 4 of Itoh and Stoneham [155]). It is now considered that the transformation of an exciton into a defect pair occurs by the system following an adiabatic potential energy surface for the excited state via an off-centre configuration as illustrated in figure 1.12 [156]. A central maximum corresponding to the on-centre STE is considered to be unstable to the interaction of the excited electron with the molecular ion. The energy is lowered by the removal of the X_2^- molecular ion past the cation gap to reduce strain. The

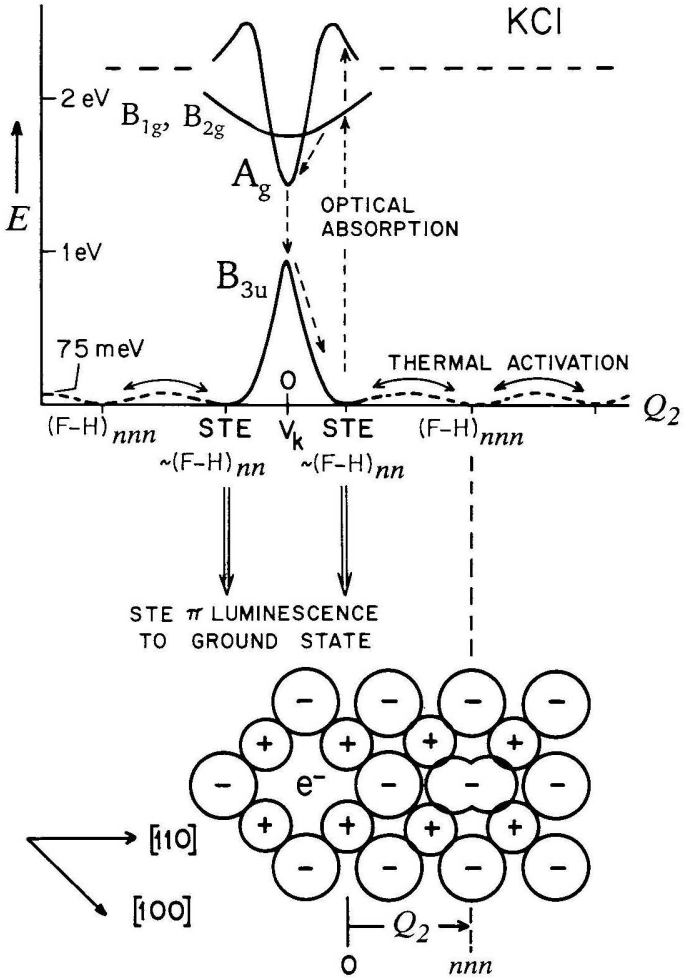


Figure 1.12: Illustration of adiabatic potential surfaces connecting the various states of the STE. The total energy is plotted against the transitional co-ordinate Q_2 of the STE. Q_2=0 represents the on-centre STE corresponding to a maximum on the potential surface. The off-centre STE (FH_{nn}) may undergo radiative decay or migrate to successive minima along the Q_2 axis, corresponding to *H* centre migration as depicted in the lower diagram [156].

stable STE is the same as $(FH)_{nn}$ and displacement corresponds to *H* centre diffusion to successively larger separations denoted by the flanking minima. Since the stable STE is already equivalent to an $F-H$ pair the barriers to further halogen movement are essentially equal to the activation energy for *H* centre migration. This model not only accounts for the thermally activated primary $F-H$ production, common to all alkali

halides at sufficiently high temperatures, but also for the low temperature process of F centre formation in the Group II alkali halides. It is possible that the low temperature F centre formation may only be found in the relaxation of higher STE excited states. The on- to off-centre transition in Group II alkali halides could release about 1 eV, which is enough to displace the halogen beyond the $(F - H)_{nn}$ site and thus generate stable defects.

The excitonic mechanism is not operative in all materials. There are a number of factors that must be fulfilled. The excitons must first self-trap. Secondly, the energy of the exciton must be larger than that of the defect pair. Lastly, the potential barrier between the self-trapped exciton and the defect pair should be much lower than that of the exciton.

1.7 Review of the Interaction of Electromagnetic Radiation with Small Metal Particles

1.7.1 Introduction

This discussion is a summary from a recent review by Kreibig and Vollmer [116] among other articles. It has been limited to optical properties of small metal particles embedded in a transparent matrix.

To build a realistic picture of what occurs during the passage of an electromagnetic wave in a matrix consisting of a collection of small isolated metallic particles with a size distribution, two simplifications are made. The lattice structure of the metal particles is ignored to a first approximation and the existence of a high density of electrons is assumed. Figure 1.13 [116] shows a schematic diagram in which an incident electromagnetic wave creates an uncompensated charge on the surfaces of the various metal particles by displacing the electrons from their equilibrium positions thus leading to polarization. The net result will be a restoring force that causes electrons to oscillate.

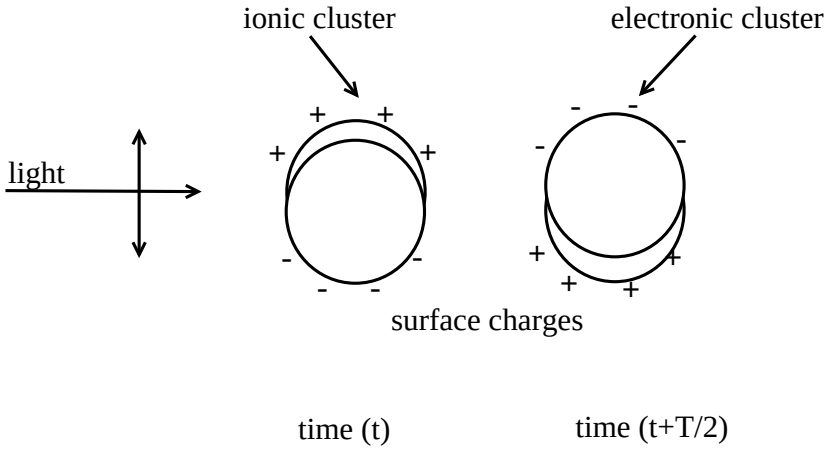


Figure 1.13: Light wave incident on a metal particle. Displacement of negative and positive charges occurs on interaction with the light wave. Adapted from Kreibig and Vollmer [116].

This excitation of small metallic particles in optical experiments also produces oscillating dipoles , which interact with each other forming collective optical excitations of the whole system generally termed as plasmon resonance in the literature. There is also the possibility of excitation of multipoles superimposed on the dipolar interaction between the metal particles. The oscillations may propagate on the surface of a metal, being surface plasmons, or into the bulk to produce volume plasmons [157]. The plasmon resonance depends on the restoring force resulting from a non-compensated surface charge and this force in turn depends on the shape of a particle. The plasmon resonance may therefore be regarded as a geometrical resonance, with the resonance frequency depending on the particle shape.

Several theories have been applied to explain the interaction of small metal particles with electromagnetic radiation, the most common and widely used being the Mie theory. Some properties of the plasmon resonance extinction may also be explained by the free electron theory if the theory provides a valid description of the metal [158]. A summary of the mathematical derivation of the Mie theory is presented in chapter 2.

1.7.2 Mie Theory

A particle exposed to electromagnetic radiation will reduce the intensity of the incident beam either by scattering or absorption or by both processes. The term extinction is commonly used in the literature and applies to the existence of the two processes. This problem was analyzed in the last century in terms of the classical electromagnetic theory by Mie [159]. It should be noted that although the theory is generally known as Mie theory, the problem was independently studied by several researchers [160, 161, 162]. The discussion of this problem is simplified by the fact that the dimensions of the submicroscopic particles of interest are much smaller than the wavelength of the incoming electromagnetic wave, the so called quasi-static approximation. The applied field may then be assumed to be homogeneous over the entire volume of the particle. For the case of a spherical particle the full solution of the boundary problem derived by Mie is presented in chapter 2. The dielectric constant of the metal and of the surrounding medium are the only material properties which enter the calculation thus extending the applicability of this theory to metals, ionic and covalent crystals among other materials. The Mie theory has been applied to ellipsoidal and other particle geometries whose solutions may be found elsewhere [163]. Normally one is interested in the properties of a collection of more or less identical particles, reasonably well separated from each other, and embedded in a medium with well defined dielectric constant: an appreciable fraction of the volume of the embedding medium will be occupied by small particles.

A number of the parameters predicted by the Mie theory may also be determined by the theory of Maxwell Garnett [164] which gives a prescription of how to calculate the effective dielectric constant of a medium containing a small volume fraction of particles. When the particles occupy a large fraction of the total volume, as in some composite materials, the Maxwell Garnett theory fails. The evaluation of the effective

dielectric constant is then possible only in so far as it is possible to characterize the material explicitly. The Mie theory does not account for all experimental features observed such as the shift in the plasma resonance frequency with increasing particle size, broadening of the resonance peaks and quantum size effects. This led to modifications that are described in the two subsections that immediately follow.

1.7.3 The Mean Free Path

The interpretation of the optical properties of small metal particles should take into account the limited mean free path of electrons which essentially modifies the optical constants of finely dispersed metal [165, 166, 167]. The mean free path for diffuse scattering at the surface of a spherical particle is $0.5d$ [116], where d is the particle diameter, will be smaller than the bulk mean free path for sufficiently small crystallites. The corresponding reduction of the life time of the electrons leads to a broadening of the resonance inversely proportional to the particle diameter. It is generally accepted that a good approximation to the dielectric constant in small particles is easily obtained from the bulk optical constants : The contribution due to interband transitions is mostly believed to remain unchanged, but the Drude-like free electron part should be modified using a size limited scattering time [168].

1.7.4 Quantum Size Effects

For very small particles the phenomenon called Quantum Size Effect (QSE) comes into play. Due to size quantization, the conduction band breaks up into discrete levels with an average separation large compared to thermal energies [169]. Several attempts have been made to derive a dielectric function relevant for this situation quantum mechanically [170, 171]. In particular Kawabata and Kubo [172] have argued that the classical interpretation of mean free path limitation by scattering at the surface is not correct: the surface of particles in this size range does not really scatter the elec-

trons, it rather manifests itself as a boundary condition for electron states bound to the finite volume of the particle. However, the quantum mechanical calculations predict an effective mean free path for a spherical particle of approximately twice the value of the classical estimate leading to a line width which is considerably smaller than the one observed.

It seems that the classical interpretation of the results of the Mie theory compares better with experiment than the quantum mechanical calculations which take into account the quantum size effects. It should be noted, however, that anomalously short scattering times can result from lattice defects in small metallic particles [173]. In addition, the size distribution in samples containing larger particles tends to broaden the resonance peak. The situation is even more controversial concerning the position of the peak of the plasma resonance. For small particles, higher order terms of the Mie theory may be neglected and the position of the peak will be fixed, unless some size dependence of the dielectric constant comes into play. This is illustrated by model calculations for small sodium particles of Smithard and Tran [117].

1.8 Plasmon Resonance (PR) Absorption

This discussion of the physics of absorption of light by metal particles closely follows an article by Yang and co-workers [174] that has explained a number of fundamental aspects regarding Plasmon Resonance (PR) absorption. Several models have been suggested to explain the PR absorption of Metal NanoParticles (MNP). However, there are none that are applicable to all cases of MNP irrespective of the medium in which they are embedded. Persson's [175] electron transfer and Hovel's [176], chemical interface damping models have successfully explained the properties of Ag MNP in silica and rare solid gas systems but are unable to appropriately account for the case of vacuum as a medium. PR absorption is basically an intrinsic property of the MNP and therefore is observed whether they are embedded in a transparent dielectric medium or

in vacuum.

According to the Hovel model, excited electrons reside in an affinity level of the embedding matrix for a duration of the order of 10^{-14} s on collision with the interface and back again. This time duration is sufficient to disrupt the phase coherence of the collective plasmon excitation. The surrounding medium absorbs the excess electron energy rendering the process an inelastic electron scattering event.

Yang and co-workers assert [174] that the plasmon oscillations in MNP are excited by light because of the their band structure. Termination of the lattice structure by a surface creates electronic states with wavefunctions on the surface decaying exponentially into the matrix. An electron outside but in the locality of such a metal surface may be trapped into the vacuum well produced by the self-interaction of the electron and the polarization charge it induces in the surface [177]. Further into the vacuum, this potential well approaches a classical image potential, and the resulting quantized electronic states form Rydberg-like states (these are states of an atom in which one of the electrons has been excited to a high principal quantum number) that converge towards the vacuum energy [178, 179]. These Rydberg-like states are coupled to a continuum of final states [180] named the surface resonance state (SRS). Upon excitation by photons, the electron in the vicinity of the Fermi level may absorb enough energy to be transferred to the surface resonance state. This excitation state of the MNP may lose its energy through inelastic electron-electron scattering, or decay via Auger and other secondary processes until the ground state is reached again.

The movement of the PR peak to longer wavelengths, the red shift, with increasing particle size may be summarized as follows. The surfaces of the MNP are not sharp since theory [116] has shown that the electron wavefunctions extend well beyond the physical boundaries (electron spill-out effect). This has two consequences. Assuming the particles to be metal spheres in vacuum, the first consequence is that effectively the particles have a larger radius which would increase the classical static polarizability

defined by

$$\alpha_{cl} = 4\pi\epsilon_0 R^3, \tag{1.8}$$

where R is the particle radius and hence a corresponding frequency given by

$$\omega = \left(\frac{Ne^2}{m_e\alpha_{cl}}\right)^{1/2}, \tag{1.9}$$

where the symbols have their usual meaning. From equation 1.9 it is clear that the plasmon frequency will decrease with larger R leading to a PR peak shift toward the longer wavelength. Secondly, the volume averaged-mean electron density, N, is reduced which also results in lower plasmon frequency.

When embedded in different matrices, the reasons for the shift of the position of the PR absorption is still a subject of a great deal of debate. Different matrices may obviously have different work functions and refractive indices and hence it expected that the position of the PR peak will vary. The electronic effect of the matrix on the metal particles is summarized as follows. In the case where occupied MNP states have different energy from the electronic states of the matrix, a situation that is representative of the MNP in transparent, dielectric and chemically inert matrices, the behaviour is not predicted by the Mie theory and may be observed due to the electron spill-out effect. If the energy of the occupied MNP states are close to the electronic states of the matrix, the electron wavefunctions of the MNP will be exponentially damped away from the particle leading to a red shift. In the event that the occupied MNP states have similar energy to those of the surrounding matrix, at resonance, the conduction electrons of the MNP will be transmitted through the interface and will no longer be confined to the MNP resulting in the removal of the plasmons. Therefore the shift of the peak position of the plasmon resonance results from a competition of these three mechanisms. Others mechanisms that affect the position of the PR peak are related to thermal contraction of the lattice and changes of the optical band transitions [181].

1.9 Review on Properties and Defect Studies of Cesium Iodide

The mechanism of irradiation damage in alkali halide crystals and the resulting defects have been subject to a large number of studies but in almost all cases have been restricted to those with the f.c.c. NaCl structure. Extremely few studies have been made on the s.c. alkali halides. Since the structural aspects have a bearing on both the primary excitonic defect production mechanism and the resulting defects it is of value to carry out complementary studies on these neglected compounds.

A brief mention of some structural properties of this material and a review of work done is necessary at this stage to serve as an introduction for chapter 4 to follow. Cesium Iodide (CsI) has a simple cubic structure similar to that of cesium chloride with a basis of Cs ion at (0,0,0) and iodine ion at (0.5,0.5,0.5). The lattice constant of CsI is 4.56 $\overset{0}{A}$. Figure 1.14 shows a schematic diagram of such as structure which is different from most of the other alkali halide crystals that have the NaCl structure. The constituent atoms making up CsI have almost similar atomic number, 53 (I) and (55) Cs, though their ionic radii for a single charge state differ, I (2.16 $\overset{0}{A}$) and Cs (1.69 $\overset{0}{A}$).

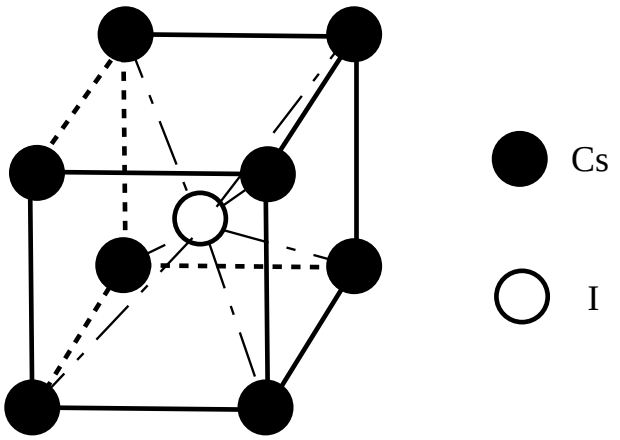


Figure 1.14: Schematic diagram of the structure of cesium iodide. The dark and light circles represent the Cs cations and iodide anion, respectively.

1.9.1 Previous Defect Studies on Cesium Iodide

Little work on irradiation damage studies of this alkali halide exist for reasons that have to do with the difficulty of colouration. Apart from the work of Avakian and Smakula [182] and Lynch et al. [183], optical absorption studies of irradiated CsI are almost non-existent. Avakian and Smakula used a high temperature electrolytic method to create colour centres in CsI since other conventional irradiation methods had failed. They identified several bands in the near infrared, visible and ultraviolet regions. Lynch et al. used the additive colouration method to create defects in CsI and performed studies of the properties of F and F aggregate centres in this and other cesium halide crystals. Martin [184, 185] also used additive colouration of CsI grown in a melt from HI. He performed Raman scattering studies at 150 K and 8 K in which he observed the 113 cm^{-1} peak and a large number of overtones associated with the I_3^- defect. Rzepka et al. [186] and Bernard et al. [187] have reported similar kind of Raman spectra from heavily γ-irradiated crystals and X-ray irradiation of pressed powder of CsI. Both irradiations were performed at room temperature. In these two cases no optical absorption studies appear to have been performed in order to link the Raman spectra to optical absorption studies of the defects created. Intrinsic emissions near 290 nm (4.27 eV) and 338 nm (3.7 eV) at low temperatures from what are believed to be self-trapped excitons in CsI have been studied theoretically, experimentally and reported in 1980 by a group of collaborators [188, 189, 190]. There is, however, uncertainty as to whether, for instance, the emission near 4.1 eV is intrinsic or extrinsic [191].

1.10 Point Defects in Alkaline Earth Fluorides (AEF)

1.10.1 Introduction

MgF_2, having a rutile structure, falls in the category of the alkaline earth fluorides (AEF) of the group IIA of the periodic table which form highly ionic salts with the flu-

oride ions in the combination MF_2, where the symbol M stands for the various possible metal cations. The other common cations of the AEF in this group are Ca^{2+}, Sr^{2+} and Ba^{2+}. These last three cations form AEF that have the fluorite structure and their properties are briefly summarized in the next subsection, while rutile structured MgF_2 is discussed separately in a following subsection. Both subsections are summarised from the text by Hayes [192].

1.10.2 Fluorite Structured AEF

It is not easy to colour nominally pure fluorite structured AEF crystals using ionizing radiation at room temperature. This difficulty is increased as the purity is enhanced. The nature of the *F* centre, created by additive colouring, in the fluorite structured CaF_2 [193], SrF_2 [194] and BaF_2 [195], has been established using magnetic resonance investigations as a single electron trapped in a fluorine ion vacancy. The nearest neighbours are four cations at the corners of a regular tetrahedron and the point symmetry of the *F* centre is T_d in contrast with O_h symmetry in the alkali halides. The second nearest neighbours are six fluorines at the corners of a regular octahedron. A detailed theory of the *F* centre in the fluorite structured AEF may be found elsewhere [192].

The F_2 centre, the simplest aggregate, is formed by aggregation of *F* centres in additively-coloured AEF crystals. It has been shown [196, 197, 198] that two types of F_2 centres can exist in CaF_2 and SrF_2. The first type consists of two nearest *F* centres located on a crystal cube edge in the $< 100 >$ direction. The second type has the two nearest *F* centre on a face diagonal in the $< 110 >$ direction. Investigations of the F_2 centre in BaF_2 have also been performed [196] but the study is less detailed compared with those on CaF_2 and SrF_2.

Self-trapped hole centres have been observed and studied in nominally pure CaF_2 by Hayes and Twidell [199] who produced them using X-ray irradiation at 77 K. Similar

centres have been studied in SrF_2 [200, 201] and BaF_2 [202]. Electron paramagnetic resonance showed that these centres were of a molecular-type with their principal axis aligned along the < 100 >. The hole centres have been observed to give rise to strong optical absorption in the ultraviolet and the near infrared spectral regions [196].

H centres have been produced by X-ray irradiation of CaF_2 by Hall et al. [203], and in CaF_2, SrF_2 and BaF_2 by Beaumont et al. [201]. Hayes et al. [197] have reported *H* centres, produced in undoped fluorite structured AEF, using 1 MeV electrons at 77 K. Table 1.3 [192] shows several colour centres of the fluorite structured AEF and includes some observed in MgF_2 [123].

Material and Peak wavelength (nm)				
Centre	MgF_2	CaF_2	SrF_2	BaF_2
F	260	375	449	606
F_2	370, 400	366	427	550
V_k		320	326	336
H		314, 285	325	364
colloid		540 - 550	550 - 600	400 - 450

Table 1.3: Colour centres and colloids in AEF. The colloids in the spectral regions indicated in this table are due to the same cation as the one forming the AEF.

1.10.3 Tetragonal Structured AEF

In MgF_2, the smaller metal ion leads to stability in a rutile structure shown in figure 1.15. The rutile structure of MgF_2 provides different possible geometries for defect structures from those observed in the alkali halides or the fluorite-structured AEF. The unit cell of MgF_2 consists of 2 Mg^{2+} and 4 F^- ions. The space group is D_{4h}^{14}. Each magnesium ion occupies a site of symmetry D_{2h}, while each fluorine ion occupies a site of symmetry C_{2v}. There are four non-equivalent pairs of fluoride ions labelled D_{2h}, C_{2v}, C_{2h} and C_1. The band structure of MgF_2 has been theoretically calculated by Harker [204] who found the peak energy for the *F* centre absorption to be 4.8 eV, a

value which is reasonably close to that observed in experiments.

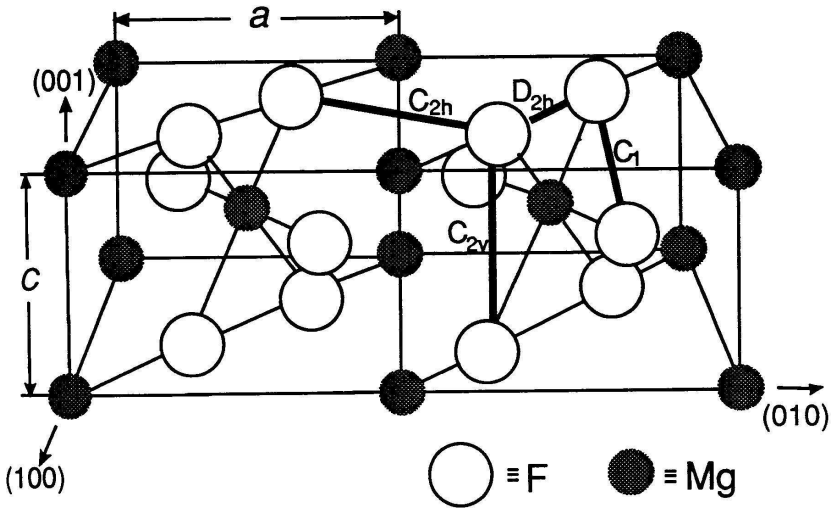


Figure 1.15: Diagram showing the lattice structure of MgF_2. The Mg and F ions are represented by the shaded and open circles, respectively. The labels D_{2h}, C_{2v}, C_{2h} and C_1 refer to the four non-equivalent pairs of fluoride ions. The lattice constants a and c are 4.64 and 3.06 $\overset{0}{\text{A}}$, respectively [156].

1.10.4 Review of the Irradiation Damage Studies on MgF_2

Magnesium fluoride has attracted the attention of a number of researchers in the context of irradiation-induced defects and radiation damage mechanisms. Various types of radiation have been used to induce colour centres in pure MgF_2 crystals using 1.7 MeV electrons and ^{60}Co γ rays [205] , 50 kV x-rays [206], 400 keV electrons and 50 kV x-rays [207], high energy protons [208], 100 keV [123] and GeV [209] heavy ions and VUV [210] irradiation. It is now accepted that the defect production mechanism in MgF_2 proceeds via an excitonic mechanism [211, 212, 213], being related to that observed in the alkali halides (see section 1.6) and thus leading to separated anion vacancy type defects (*F* and *F* aggregate centres) and their complementary fluorine interstitial defects.

It is believed that recombination luminescence in fluorite structured AEF occurs

when the *F* centre electron recombines with the *H* centre hole. This is supported by transient absorption spectra, observed during illumination of the crystals by an electron pulse, corresponding to transitions from the self-trapped exciton triplet state to higher states. Williams et al. [214] assert that the spectra of the identifiable well-separated *F* and *H* centres in AEF are only observable in transient absorption since the yield of stable defects produced by ionizing radiation in pure samples is negligible. There is, however, a single absorption band for MgF_2 which the authors attribute to spectral overlap of the electron and hole transitions. The conclusion by Williams et al. is at variance with those discussed in the previous paragraph also using pure MgF_2 crystals in which substantial numbers of stable *F* and *H* aggregate centres are observed, and an excitonic mechanism inferred.

Owing to the large bandgap of MgF_2 and the need for VUV optical absorption studies, the fluorine interstitial defects have received very little attention previously. Preliminary studies of a band in the region of 7.5 eV (165 nm) was reported by Davidson et al. [123] for high fluence sodium and krypton ion bombardments and tentatively assigned to fluorine-based defects. An *H* centre-like defect in MgF_2 has been identified by the EPR method in crystals irradiated by neutrons at low temperatures by Ueda [215]. The centre has been described as an interstitial fluorine atom bonded to a lattice fluoride ion, with hole asymmetry corresponding to the charge states $F^{-0.4}$ - $F^{-0.6}$ for the interstitial and substitutional sites, respectively. Ueda concluded that since this *H* centre was stable up to 560 K, it was probably stabilized by a nearby defect. V_k-like centres have also been observed in the same experiments by Ueda. EPR shows them to be nearly-$< 011 >$ oriented F_2^- molecular ions sharing the hole charge equally. These V_k centres have been observed for both neutron and gamma irradiated samples. However the centre in gamma irradiated samples were tilted by a few degrees from the $< 011 >$ direction. The fluoride pair site on which the self-trapped hole localizes with greatest probability was shown to be the C_1 site on the MgF_2 (see figure 1.15). Although Ueda

seems to have identified the *H* centre in MgF_2 many decades ago, there are no published confirmatory reports of its observation by optical absorption spectroscopy. Table 1.3, appearing in section 1.10.3, shows a summary of the colour centres and colloids in AEF.

Absorption bands due to three out of the four F_2 centres of different symmetry, predicted by Facey and Sibley [216], have been identified experimentally [123, 216] and a probable candidate for the fourth pointed out by Davidson et al. [123]. In the same article [123] studies of intrinsic and extrinsic Mg colloid formation using Mg^+ and Kr^+ ion bombardment at high fluences were carried out, showing the presence of an associated optical extinction band peaking near 4.43 eV (280 nm). No work on ion implantation of excess Mg into MgF_2 appears to have been reported before 1993 and Davidson et al. [123] seems to be the first case.

1.11 Defect Studies in Lithium Niobate

This section provides a literature survey on the properties and previous work on lithium niobate and thus serves as a background to chapter 6.

1.11.1 Introduction and Structural Properties of Lithium Niobate

Lithium Niobate (LN) is classified among the perovskite family [217] of ternary oxides which have been studied in the past mainly because nonlinear optical properties and hence possible applications in electro-optic and photorefractive devices. LN is already used in second and third harmonic frequency generation devices. The origin of the observed photorefractive effects [218] in this material is related to light-induced charge transfer between Fe^{2+} and Fe^{3+} impurity centres which act as donor and acceptor states respectively [4]. Investigations of the photorefractive effects of LN in a two-wave mixing experiment have indicated that nonstoichiometric defect control was vital as properties such as photoconductivity, diffraction gain and buildup time could be

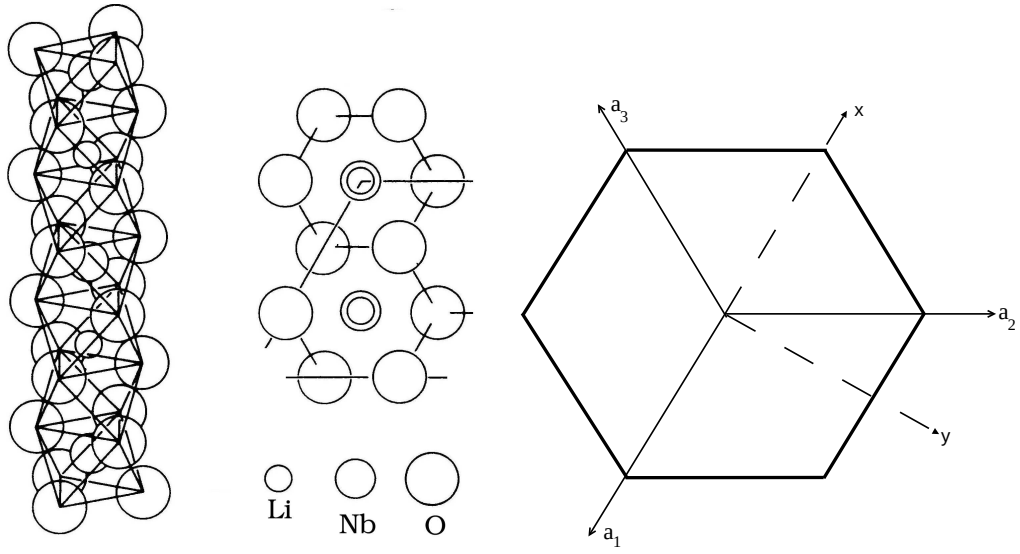
improved [218]. These photorefractive properties are useful in applications for holographic storage devices [219]. Other impurities and lattice defects such as oxygen vacancies may also have a role to play in the photorefractive phenomenon displayed by LN. An excellent review article by Abouelliel and co-workers [220] focusing on the applications of LN in the field of opto-electronic is in the literature. Other properties of LN crystals such as the birefringence, Curie and phase matching temperatures have been studied as a function of stoichiometry by Abrahams et al. [221] and Bergman et al. [222].

Malovichko et al. [223, 224] have in the recent past studied several impurity centres in congruent, stoichiometric and regularly ordered LN crystals. The highlights of the work of this group includes studies of intrinsic and extrinsic defects in these three types of LN crystals. A common approach that can be used to address the issue of a large number of experimental results published by various groups working on LN crystals obtained from different crystal growers has been introduced by Malovichko et al. [223]. They have also elaborately studied axial and low-symmetry centres of Cr^{3+} and resolved eight satellite Cr centres using optical absorption and EPR methods.

LN belongs to the R3c space group and has a rhombohedrally-centred hexagonal lattice structure with a = 5.148 and c = 13.684 $\overset{0}{\text{A}}$. A schematic diagram [221] of the structure of this material is shown in figure 1.16 (a). On the top right of figure 1.16 (a) the ions Li, Nb and O are shown with their relative sizes and a projection onto the c-axis. In part (b) of the same figure the concept of the x- and y-crystal cuts is illustrated. The x- and y-cut faces are perpendicular to the x and y directions, respectively.

The refractive index of a ferroelectric crystal like LN originates from electronic polarization [225]. A generalized Lorentz-Lorenz formula describing the refractive index is written as

$$\frac{(n^2-1)}{(n^2+2)} = (1+\Upsilon)\sum_i \frac{\zeta_i}{3\epsilon_0 V}, \tag{1.10}$$



(a) (b)

Figure 1.16: Diagram showing (a) the crystal structure of LN and a projection onto the c-axis [221], which is perpendicular to the plane of the paper; (b) the x and y directions from which the X- and Y-crystal cuts are obtained.

where Υ is the specific correction factor for the crystal, ζ_i is the electronic polarizability of the *i*th ion in a primitive cell, V is the cell volume, and the summation is over the ions in a molecule. Υ is zero if the solid changes to an amorphous state or has a cubic structure. In the case of a hexagonal structure such as LN, Υ becomes positive for a number of reasons. First the interaction between the noncubic dipole arrays leads to a larger Lorentz correction for the local field than the ordinary $\zeta_i/3\epsilon_0$ and second, the ferroelectric spontaneous polarization deforms both the electronic shells and the ionic lattice varying Υ. Lastly the volume of the material decreases since closer packing is attained when the crystal becomes amorphous [226].

1.11.2 Defect Structure of LN

Three possible defect structure models have been proposed for LN in the literature. They are the oxygen and the cation substitution models. The latter consists of the Li- and Nb-site vacancy models. Peterson and Carnevale [227] initially proposed the Nb cation substitution model based on their nuclear magnetic resonance study, which was later superseded by other suggestions. Charge neutrality was thought to be achieved by oxygen and lithium vacancies [228, 229, 230]. However, theoretical and experimental studies of the density of LN as a function of composition ruled out the oxygen vacancy model [231, 232]. Lerner et al. [233] explained the increase in the density of Nb enriched LN in terms of the occupation of the Li site by the excess Nb ions. The Li cation substitution model proposed by Lerner and co-workers was later supported by electrical conductivity studies [234, 235].

The first defect structure studies of LN were performed by Abraham and Marsh [231] using a single crystal X-ray diffraction technique. The result of their work was in excellent agreement with the Nb-site vacancy model which was accepted and the effects of dopants were discussed on the basis of this model. However, energy calculation results on isolated defects in the LN structure later showed that the Nb-site vacancy was more unfavourable than the Li-site vacancy [236]. Further questions arose from diffusion studies of the resulting crystals of different nonstoichiometries on the Nb-site vacancy model. Kitamura et al. [237] observed that the diffusion rates of Ti^{4+} which was thought to occupy the Nb site showed no correlation on the degree of nonstoichiometry which was inconsistent with the accepted idea of the vacancy at the Nb site.

Iyi et al. [238] have used X-ray and neutron diffraction analysis backed with a structure refinement technique on LN samples having four different compositions to resolve the defect structure model for LN. Their results are consistent with the Li-site

vacancy model initially proposed by Lerner et al. [233] and the energy calculations by Donnerberg et al. [236].

1.11.3 Review on Irradiation Damage Studies in Lithium Niobate

There is no clear evidence of the formation of *F* centres in this material after heavy ion irradiation. However, the use of fast electrons with energy above 300 keV has produced broad bands in the visible region of the spectrum which could be due to *F* centres [239, 240]. It is interesting to note that irradiation of oxides such MgO and Al_2O_3 produces *F* centres using both electron and ion irradiation. The reason for this difference in the efficiency of formation of point defects has been attributed to ionization-induced annealing of the vacancy-interstitial Frenkel pairs by Popov and Balanzat [241]. They emphasise the role of electronic excitations of the oxides, where *F* centres are created by elastic collisions, as being vital since it leads to radiation-enhanced diffusion of the point defects created. In cases where the point defects have low activation energies for diffusion, ionization-induced annealing would be relatively effective. As an example, in MgO, intrinsic diffusion of both *F* centres and oxygen vacancies begins above 1273 K, with corresponding migration energies of 2.5 - 3.3 eV compared to the low migration energy of the oxygen vacancy of 0.7 eV [242] in $KNbO_3$ (the value of the migration energy of the oxygen vacancy in $LiNbO_3$ (LN) is considered to be similar).

The implantation of inert gases, Ar^+ and Ne^+, to fluences of 1 - 4×10^{16} ions/cm^2 have been reportedly used to produce buried layers in LN crystals by Wei et al. [226]. They found that the implantation-induced changes in the refractive index, determined by the Abeles method [243], were independent of the fluence and ion species indicating the possibility of the creation of an amorphous layer.

It has been observed that the reduction in nonlinearity in this material is linked to localized defects rather than the total destruction of its crystalline state during ion

implantation [244]. A large amount of work has been performed by several groups [245, 246, 247, 248, 249, 250] on ion implantation of this material to tailor its properties. Malovichko et al [223, 224] have studied several impurity centres in congruent, stoichiometric and regularly ordered LN crystals.

1.12 Defect Studies and the Properties of Indium Oxide and Tin-Doped Indium Oxide Films

1.12.1 Introduction

This section, which serves as a background to chapter 7, provides a summary of the properties of indium oxide and indium oxide doped with tin largely follows a review article by Hamberg and Granqvist [251] who have discussed the optical and electronic properties of these materials in depth. Reports on the optical and electrical properties of single crystals of indium oxide are rare [252, 253] and as such the discussion on the sections that follow discuss only thin films. Indium oxide has technological importance when doped with tin to form the material commonly known as tin-doped indium oxide (ITO). ITO thin films are currently being used commercially as transparent conducting electrodes. Some of the applications include use as coatings on solar cells, vehicle windscreens and on efficient energy windows on buildings among others. This is because ITO films show interesting and technologically important combinations of properties; they have high optical transmittance and infrared reflectance, good electrical conductivity, excellent substrate adherence, hardness and chemical inertness. A well optimized ITO sample, for solar energy efficiency, would have a transmittance of 75 - 85% in the visible region of the spectrum. Such a sample is characterized by two transmittance edges, the fundamental interband transition edge in the short wavelength side, while the other is on the long wavelength end and is dependent on the concentration of free carriers in the film. By varying the free carrier density the latter edge can

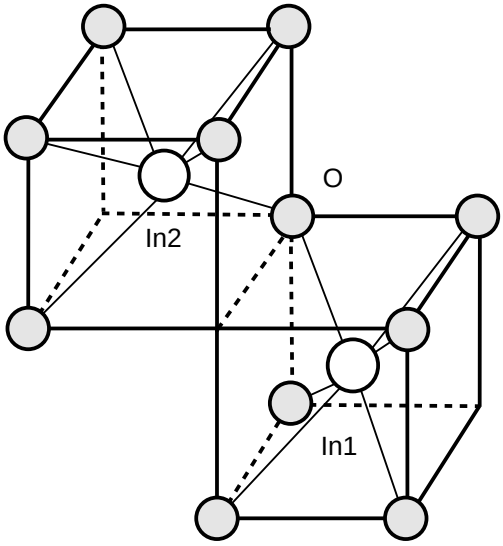


Figure 1.17: Schematic diagram of the structure of indium oxide showing the two different sites of the In, namely In1 and In2. Shaded circles at occupied corners represent oxygen atoms. Unoccupied corners represent oxygen vacancies. Adapted from Parent et al. [254].

be moved within the visible and near infrared spectral regions.

1.12.2 Structure and Properties of Indium Oxide

In_2O_3 is a nonstoichiometric compound under various conditions, having an indium-oxygen ratio larger than 2/3 and containing oxygen vacancies. The nonstoichiometry in the In_2O_3 structure leads to n-type conductivity. Under normal conditions, it crystallizes into a cubic structure (see figure 1.17 [254]) of the bixbyite Mn_2O_3 type (space group T^{7h} Ia3), with a body centred cubic unit cell having 80 atoms and a lattice constant of 10.12 $\overset{0}{\text{A}}$ [255]. This structure is closely related to the fluorite structure but in In_2O_3 every fourth anion is missing, so that small positional shifts of the ions take place. The coordination is sixfold for indium ions and fourfold for the oxygen ions. There are two crystallographically nonequivalent indium sites. One of these is associated with an indium-oxygen separation of 2.18 $\overset{0}{\text{A}}$ with the oxygen ions lying nearly at the corners

of the cube with two body-diagonally opposite corners unoccupied (In1); the other is associated with non-equal indium-oxygen separation being 2.13, 2.19 and 2.23 $\mathring{A}$ and the oxygen ions lying nearly at the corners of a cube with two face-diagonally opposite corners unoccupied (In2). A hexagonal structure of In_2O_3 occurs at high pressure and is generally not detectable in thin films [251]. Fairly recent results of calculations of the electronic structure of undoped In_2O_3 from first principles by Tanaka and co-workers [256] show that the presence of an oxygen vacancy creates a vacancy level in the band gap. According to this group, the occupation of this level which is attributed to the localization of electrons to the oxygen vacancy was found to result in a stronger In-In bond and is suggested to be the electronic mechanism for the stability of oxygen vacancies in In_2O_3. Hall effect measurements by de Wit et al. [257, 258, 259] showed that electron concentrations of sintered pellets of In_2O_3 were strongly influenced by oxygen partial pressure at room and higher temperatures. These researchers proposed that conduction was from grain to grain, perturbed by surface barriers strongly influenced by chemisorbed oxygen.

Some of the properties mentioned above may vary slightly depending on sample history and method of preparation. Higuchi et al. [260] have attempted to relate the microstructure and electronic characteristics of ITO. They found that surface roughness did not relate to resistivity in a simple way. It was, however, clear that films exhibiting low resistivity were composed of domains and had lower values of roughness. Other researchers indicate that highly oriented films have lower resistance [261].

ITO films grown by various methods have been found to be textured with the $< 100 >$ and $< 111 >$ preferred orientations perpendicular to the film plane [262, 263]. Parent et al. [262] observed that the occurrence of the $< 100 >$ texture was a function of the concentration of tin, disappearing as the content was increased. On the other hand Hamberg and Granqvist [251] have found no evidence of existence of the suggested preferred orientations and cited the differences in the deposition parameters as the cause

of the conflicting reports.

1.12.3 The Mechanism of Insertion of Tin into the In_2O_3 Lattice

The mechanism of insertion of tin into the In_2O_3 structure has not been widely studied. The discussion that follows is a summary of the work by Hamberg and Granqvist [251]. Some work of Quaas et al. [264] who used the Rietveld method, a form of refined grazing angle X-ray diffractometry, to study the structure ITO films and Parent et al. [262, 254] who employed an extended X-ray absorption fine structure analysis to study this material is included. A good pictorial illustration of the effect of Sn doping, In_2O_3 being the host matrix with the valence and conduction bands, is shown in figure 1.18 [251]. E_{go} and E_g stand for the energy gaps of the undoped and doped In_2O_3, respectively. The direct band gap for undoped In_2O_3 is quoted to be about 3.75 eV. W stands for the separation between the bottom of the valence and the top of the conduction bands as a result of narrowing due to many body effects [251]. In the undoped state,

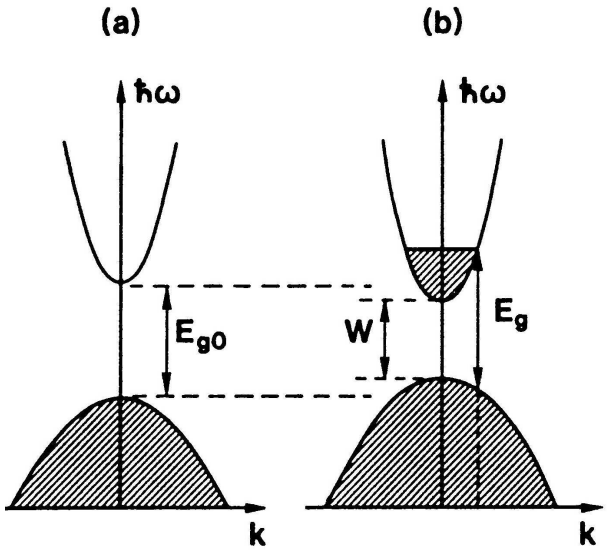


Figure 1.18: Schematic energy band diagram illustrating the doping of In_2O_3 with Sn [251].

the Fermi energy (E_F) lies between the two bands. With introduction of the dopant a small number of energy levels of the donor electrons lie between E_F and the bottom of the conduction band. For heavy doping these donor levels merge with the conduction band. The low lying states in the bottom of the conduction band are therefore occupied.

Hamberg and Granqvist [251] have estimated the donor density, N_c, at this doping level by invoking Mott's criterion [265]

$$N_c^{1/3} a_0^* \approx 0.25 \tag{1.11}$$

where a_0^* is the effective Bohr radius given by

$$a_0^* = h^2 \epsilon_0 \epsilon^M / \pi e^2 m_c^* \tag{1.12}$$

ϵ^M and m_c^* are the static dielectric constant and the effective mass in the conduction band, respectively. According to the arguments above combined with known values of ϵ^M and m_c^* a_0^* $\approx$ 1.3 nm, N_c was found to be 6×10^{18} cm^{-3}. The value of the critical density is based on the assumption that each donor provides one electron. Free electron properties would therefore be expected above the N_c.

Experimentally, the effect of heavy doping of In_2O_3 and subsequently the increase in the direct band gap is observed when the ITO films are deposited on substrates that have an fundamental absorption edge that occurs at wavelengths much lower than of ITO itself. With the levels at the bottom of the conduction band filled, electrons excited across the band gap at the onset of interband transitions have to occupy higher levels. This phenomenon is referred to as the Burstein-Moss shift [266, 267] in the literature. The introduction of tetravalent cations should enhance the electron concentration and ideally, the Sn^{4+} ions are generally thought to replace In^{3+} ions providing one free electron for each tin atom [262]. The free carrier concentration increases over the range 0 to 6 - 10 atom % Sn doping, depending on the preparation technique. At higher tin content, the free carrier concentration reduces as an increasing number of

the dopant ions are neutralized. Assuming that with increasing tin content, a larger proportion of the Sn ions occupy nearest-neighbour sites, two Sn^{4+} ions close to each other may compensate their donor action. This means that the Sn^{4+} ion pair may attract additional oxygen atoms forming a complex whose neutral equivalent is a $(SnO_2)_2$ cluster. In such clusters, the additional oxygen ions have been reported to act as electron traps [268]. This conclusion is supported by the complicated oxygen partial pressure dependence of conduction electron concentration. Such an influence of oxygen pressure on the electrical properties of the ITO films may result from complex processes of adsorption and desorption of oxygen atoms on the film surface and diffusion of these atoms from the surface into the film interior [269]. If the complete thermodynamic equilibrium between the interior of the ITO samples is not achieved, the charge carrier concentration would depend on the history of the samples, oxygen pressure, heating as well as ambient gases. As such ITO films may be considered to be only metastable.

It has been reported that the size of the grains in the films remains reasonably large as the dopant concentration is increased. However, the intensity of the X-ray reflections decreases with increasing tin concentration and there are small shifts of the peaks to lower angles [262]. This is because increasing the concentration of tin enhances disorder in the local structure of In_2O_3. It is known that tin has a solubility in ITO films that is larger than 60% [270, 271]. Therefore, the local strain induced by the tin atoms must be relaxed. The oxygen vacancies within the In_2O_3 structure may allow non-negligible displacements of the cation positions, so that indium oxide is able to undergo local disorder without a total collapse of its lattice structure. The detailed work on ITO films by Parent et al. [254] using extended X-ray absorption fine structure did not however reveal the presence of the $(SnO_2)_2$ clusters which have normally been associated with electronic compensation during increased tin content when on In_2O_3.

The role of oxygen in ITO is more complex and unlike the situation in In_2O_3, oxygen vacancies are now minority defects and the electrical properties may described

in terms of interstitial oxygen ions introduced by the dopant tin. The oxygen vacancies are associated with the tin ions, and at low dopant levels they act as a source of electrons. Thus commercial ITO films are usually annealed in a reducing atmosphere to optimize their electrical performance [262]. The annealing removes adsorbed gases and water vapour, while the reducing atmosphere maximizes oxygen vacancies.

The optical properties of ITO are influenced by several physical mechanisms. These mechanisms may be expressed in terms of the dielectric constant of a heavily doped semiconductor by separate elementary excitations as

$$\epsilon = 1 + \chi^{VE} + \chi^{FC} + \chi^{PH} \tag{1.13}$$

where χ is a complex susceptibility and the superscripts denote valence electrons (VE) , free carriers (FC) and polar optical phonons (PH). In undoped In_2O_3 only χ^{VE} and χ^{PH} are taken into account. χ^{VE} originates from intraband transitions by valence electrons, χ^{FC} is due to the contribution by free carriers, while χ^{PH} is caused by polar optical phonons which couple to the transverse field in the far infrared.

Hamberg and Granqvist have, in a detailed review article [251] partially summarised in the current and following paragraph, outlined several electron scattering mechanisms that affect the optical properties of ITO films. These mechanisms can generally be grouped into three separate cases, some of which may be classified further. The first case occurs due to electron-defect interactions which includes scattering by grain boundaries, external surfaces, neutral and ionized point defects, dislocations, precipitates and clusters. The second case deals with electron-lattice scattering where an effect such as local deformation potential occurs, while the third mechanism involves electron-electron scattering. The review article looks at the optical, structural and electric properties of the films from previous work of the authors and several other researchers reported over many years.

Hamberg and Granqvist have developed a quantitative model, whose results of

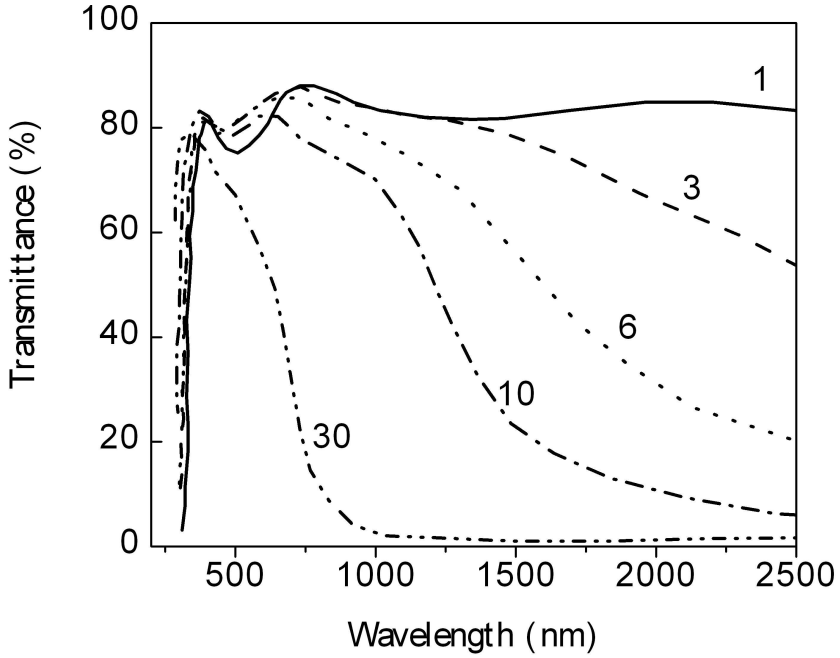


Figure 1.19: Simulated curves of the transmittance as a function of wavelength for different values of electron density starting from 1×10^{20} - 30×10^{20} cm^{-3} [251].

the variation of the transmittance as a function of the free electron density are shown in figure 1.19 [251], which takes into account the susceptibility of phonons and valence electrons in the band-edge range, free carrier scattering and a numerical factor indicating the quality of the films. An increase in the free electron density was not only found to have the effect of moving the free carrier absorption edge towards the visible region of the spectrum but it was also established that singly ionised tin ions were the most efficient scatterers for the free electrons. The influence of lattice defects on the resistivity of the films was found to be small in their highly crystalline films. The composition of the ITO films (10% wt $Sn0_2$ and 90% wt In_2O_3) used in the present work is considered to fall in the category of a heavily doped semiconductor [251] and has a transmission spectrum similar to the sample with a free electron density of 10×10^{20} cm^{-3}.

1.12.4 Review of Irradiation Damage Studies of ITO Films

There are several reports of irradiation damage studies, using different ions, that have been carried out on ITO films prepared by a variety of methods. Protons [272, 273, 274], oxygen [273, 274, 275] and argon ions [275, 274] with energies ranging from 15 to 120 keV have been used on samples that had film thickness below 200 nm. SRIM2003 simulations show that most of the accelerated ions would be embedded within the material itself. All these research groups have investigated the changes in the resistivity of the films as a function of the ion fluence. A few cases of investigation on the effects of irradiation damage on the optical properties of the films have been reported [272, 274] where it was indicated that the transmittance of the films decreased as the fluence was increased. The former group, using 15 keV protons, also found that the resistivity of ITO films increased at large fluences but were able to recover most of the optical and electrical properties on annealing at 773 K in a nitrogen atmosphere. The mechanism for the change in the resistivity of the films is, however, not mentioned by these authors. Studies of the optical properties resulting from the effects of irradiation on ITO films are therefore still largely lacking.

A comparison of the conductivity of amorphous and polycrystalline films in a similar growth environment has shown that the Sn dopant is sensitive to the crystal structure and is thus not active in amorphous films. The contribution of the oxygen vacancies is insensitive to the crystal structure and remains intact even in amorphous ITO films. Thus implant induced crystal damage can be expected to deactivate the Sn dopant in crystalline ITO film preferentially and leaves the contribution of the oxygen unchanged. The exact nature of the implant-induced defects in ITO has not yet been clearly established [274]. They have suggested that at a fluence of 1×10^{16} O^{+} cm^{-2}, a chemical effect occurs which is responsible for removal of the electrically active oxygen vacancies and hence a decrease in the carrier density. This was justified by comparison

with an implant of the same fluence of Ar^+ where only a moderate effect was observed.

The results of ITO implantation with H_2^+ and O^+ carried out Shigesato et al. [273] suggest that the effect of ion implantation on transmittance, Hall effect, carrier density and mobility was determined by the number of atomic displacements created irrespective of the chemical species of the ion. No evidence of a chemical effect associated with either oxidation of the ITO by the O^+ or reduction by H_2^+ implant could be deduced. Contrary to previous research [275] that implantation of H^+ reduced the resistively of sputter deposited ITO, Shigesato et al. [273] assert that the change could have been due to an improvement in the as-deposited film quality as a result of dynamic annealing effects during the irradiation process. They did find however, that in the case where the electronic properties of the material are limited by the crystalline quality, ion implantation improved the crystallinity by *in situ* dynamic annealing [273].

1.13 Properties of Polycrystalline Magnesium Fluoride Films (PMF)

1.13.1 Introduction

This subsection presents a background discussion and a summarized review of polycrystalline magnesium fluoride films (PMF) relevant to chapter 8. Epitaxially grown magnesium fluoride films are used as anti-reflection coatings on transparent conducting oxides and optical windows [251]. The property of these films that make them attractive for this application is the high optical transmittance in the visible and near infrared regions of the electromagnetic spectrum. If it were possible to lower the resistance of the polycrystalline magnesium fluoride (PMF) films by introducing free carriers into the magnesium fluoride matrix, without altering its optical transmittance too drastically, one would then achieve what has previously been performed by both transparent conducting oxide and magnesium fluoride films with a single coating of conducting magnesium fluoride films. It is noted that previous work has been carried

out on co-deposition of Au, Ag and magnesium fluoride films in which optical extinction bands resulting from the agglomeration of these two metal ions were observed [276, 277].

1.13.2 Structural Properties

The structure of PMF films will vary depending on the preparation conditions [278, 279]. Bauer [280] has reported that thicker films had some degree of preferred orientation and were always found to be polycrystalline. Coleman et al. [281] have noted that thick films, grown on substrates maintained at higher temperatures, exhibit preferred orientation but the orientation varies with the substrate temperature and the crystallite sizes were larger than those prepared at lower substrate temperatures [282]. Evidence from transmission electron microscopy studies suggests that evaporated PMF films have an appreciable concentration of voids present as defects [283, 284]. No direct evidence of aggregation, such as occurs in polycrystalline metal films, has been observed [282]. This is possibly due to electrostatic attraction between the ions of the film and ions of the substrate and in this case the adhesion would be considerably greater than for metallic films leading to suppression of aggregation [282, 285]. Dislocations and extended other defects may be formed because of point-defect aggregation during growth, provided that the vacancies are relatively mobile. Deposition at very high rates and onto sufficiently low temperature substrates might cause many vacancies to become trapped, and these could aggregate slowly [286, 287].

1.13.3 Optical Properties

The transmittance (normally thickness dependent) of PMF films grown by various techniques is high, ranging from 80 - 95% in the visible and infrared regions of the spectrum [251, 288]. The absorption edge of the PMF films should occur at lower energies than for single crystals of magnesium fluoride, which is near 10.4 eV. This is

because of the existence of intrinsic defects in PMF films that arise as a result of the method of preparation, namely vapour quenching on low temperature substrates.

The results of the refractive index of PMF films reported in the literature show a dependence on the method of measurement. Those found by the Brewster angle method on thin films have shown the refractive index to be above 1.39 [279, 289] while an increase in the value of the refractive index has been observed on aging [279]. Values of the refractive index obtained from reflectivity or transmission methods, which depend upon interference effects in the films and therefore involve the film thickness, have always been found to be lower [279]. Morita [290] has reported that films grown under a vacuum better of than 5×10^{-5} mm Hg had the same values of refractive index as the bulk and showed no aging effects.

A detailed study of the refractive index and packing density of PMF films, as a result of water sorption and subsequent temperature dependence, has been carried out by Ogura and others [291]. They noted that about 10% of the total volume of the films was occupied with water molecules before exposure to air. This has a large effect on the refractive index of the films when taken through various heat treatments. The refractive index of the PMF material, after most of the water vapour filling the voids had been removed, was found to vary from 1.40 at about 303 K to 1.38 at 573 K [291].

1.13.4 Electrical Properties

Insulators are characterized by a filled valence band, an empty conduction band and a forbidden band gap of several eV. Conduction cannot therefore take place in either of the two bands except if extra charge carriers are created. For the case of an insulator sandwiched between two electrodes a number of processes responsible for charge transport have been discussed elsewhere [285]. The situation relevant to present work is one in which metal electrodes have been deposited at the ends of the film and carriers has to traverse the entire length of the film. Charge carriers are introduced into

the conduction (or valence) band of the insulator by thermionic or Schottky emission over the metal-insulator barrier. They are then transported to the other electrode with their mobility limited by scattering from structural and other defects. Scattering of the charge carriers by grain boundaries in polycrystalline films is significant because these boundaries reduce the electron mean free path. Growth in the grain size, for films deposited at low temperatures leading to the removal of boundaries, is a major factor in the decrease of the resistivity when the films are subjected to thermal annealing.

There are a number of reports in the literature where attempts have been made to measure the d.c resistivity of PMF films co-evaporated with other metals such as Mn and Co [292, 293]. These reports indicate that the value of the resistivity of a freshly prepared vacuum deposited thin film depends on a number of factors such as the deposition rate, residual gases in the deposition chamber, nature and temperature of substrate. Some of these factors are responsible for the wide range of resistivity values obtained by different groups using similar source material [294].

Chapter 2

2.1 Theory of Optical Absorption

In the following sections an outline of the theory of optical absorption will be presented. Since the full quantum-mechanical treatment of this subject is lengthy and involved, only the major points relevant to this work, summarised from an article by Fowler [295], will be discussed. The more detailed derivations may be found in the same article, references therein and other references cited in the current text. In subsection 2.1.1 the characteristics of the absorption spectrum of pure alkali halides are discussed. A qualitative explanation of band edge properties is given. A quantum mechanical treatment of absorption by an isolated atom is outlined and important definitions of the oscillator strength and absorption coefficient given in subsection 2.1.2. Section 2.2 deals with the effect of the environment on an absorbing centre in a solid. The results of the Born-Oppenheimer approximation are employed to explain the features of the optical absorption bands.

2.1.1 Absorption in Alkali Halide Crystals

Optical absorption occurs in systems which have electronic energy levels separated from each other by a gap corresponding to the energy of an optical photon. With increase in frequency, these pure insulating crystals are transparent until the threshold for interband transitions is reached. Because of the relatively loose binding in the case of the alkali ions, the outer electrons of the halides are higher in energy than those of the alkali. Hence the valence band in alkali halides is populated by p-shell electrons of

the halide ions. The lowest conduction band, on the other hand is mainly characteristic of the lowest s-band unfilled state of the alkali ion. Interband transitions involve the ionization of the halide ion.

There are a number of transitions called exciton transitions on the low energy side of the band edge. These arise from excitation of the electron of the halide ion to a higher excited state without its removal from the ion. This results in the creation of a bound electron-hole pair. Such a bound electron-hole pair is termed an exciton and its energy levels lie just below the conduction band. The onset of absorption as the energy is increased into the UV region is due to the long wavelength side of the first exciton transition. The photons create bound electron-hole pairs of increasingly large radius until a series limit is reached and then band-to-band transitions occur as free pairs are created. The optical absorption spectra of a range of alkali halides exhibit this effect [296] i.e. the absorption edge is characterized by a sharp peak or peaks, and at higher energies a step occurs in the spectrum where interband transitions commence.

The transition width of the absorption edge at room temperature is broadened and different from that measured at low temperature which includes clear absorption features due to exciton absorption [156]. This is because at higher temperatures exciton-phonon interactions tend to smear out the effects leading to an exponential variation of the absorption coefficient in the low energy side as we approach the onset of interband transitions commonly known as the Urbach tail phenomenon [297]. (There have been several other mechanisms such as electric microfields due to ionized defects [298, 299] and thermal fluctuation [300] of the bandgap, which also give rise to logarithmic band edges but the dominant mechanism depends on the material under investigation).

Optical transitions observed in the far infrared region are attributed to absorption resulting from lattice vibrations. The major coupling mechanism between the incident photon and the lattice phonon is produced by a change of state in the electric dipole moment of the crystal. (Detailed studies reveal that three different coupling mechanisms

exist. The first is the Restrahl absorption which occurs in ionic crystals and is caused by the creation of single phonons in the lattice. The second is multiphonon absorption, which occurs when two or more phonons simultaneously interact and produce an electric moment with which the incident radiation may couple. The third mechanism is defect induced phonon absorption by the existence of a lattice defect or impurity that may aid the coupling mechanism).

Defects introduced into a crystal have their own associated optical absorption bands. For the alkali halides the presence of impurities, vacancy and interstitial type defects introduces absorption bands into the forbidden gap region. For this reason optical absorption is an effective technique in the study of colour centres.

2.1.2 Theory of Single Particle Absorption

To develop the theory of optical absorption, a *free particle* model is assumed. The quantum mechanical Hamiltonian in the Coulomb gauge is

$$\frac{-\hbar^2}{2m^2}\nabla^2 + \frac{i\hbar e}{mc}\boldsymbol{A}\cdot\nabla, \tag{2.1}$$

where the symbols have their usual meaning. Perturbation theory can be employed to derive an expression for the transition probability. The expression for transition probability attained by this treatment is the same as that presented by Fowler [295] whose notation will be used in this section and that following.

$$W_{lm} = \frac{4\pi^2}{\hbar} \mid E_m - E_l \mid N_p \mid \boldsymbol{\eta}\cdot\boldsymbol{r} \mid^2 \delta[\mid E_m - E_l \mid -\hbar w], \tag{2.2}$$

where W_{lm} is the transition probability per unit time for a particle initially in state l to absorb energy from the radiation field of density N_p (photons per unit volume) and change to state m. $\boldsymbol{\eta}$ is the unit vector denoting the polarization of the incident radiation and $\boldsymbol{r}$ is the electric dipole matrix element defined as follows

$$\boldsymbol{r}_{lm} = \int \phi_m^{0^*} \boldsymbol{e}\boldsymbol{r}\phi_l^0 d\tau, \tag{2.3}$$

where ϕ_m and ϕ_l are solutions of the time-dependent Schrödinger equation with energies E_m and E_l respectively. For unpolarized radiation equation 2.2 becomes

$$W_{lm} = \frac{4\pi^2}{3\hbar} \mid E_m - E_l \mid N_p \mid \boldsymbol{r}_{lm} \mid^2 \delta\left[\mid E_m - E_l \mid -\hbar w\right]. \tag{2.4}$$

The absorption cross-section, ε_{lm}, is the transition probability divided by the photon flux and integrated over the energy delta function [301]

$$\varepsilon_{lm} = \frac{4\pi^2 \hbar \omega_{lm}}{3\hbar c} \mid \boldsymbol{r}_{lm} \mid^2, \tag{2.5}$$

where $\hbar\omega_{lm} =\mid E_m - E_l \mid$. The oscillator strength is

$$f_{lm} = \left[\frac{2m}{3\hbar e^2}\right] \omega_{lm} \mid \boldsymbol{r}_{lm} \mid^2 . \tag{2.6}$$

The absorption coefficient, α, defined as the fractional change in intensity per unit thickness of absorber ($dI = -\alpha dx$) can also be expressed as the energy removed per unit time per unit volume from a beam intensity

$$\alpha_{lm} = \frac{W_{lm} N_A}{c N_p} = \frac{4\pi^2 N_A \hbar \omega_{lm}}{3\hbar c} \mid \boldsymbol{r}_{lm} \mid^2 \delta\left[\mid E_m - E_l \mid -\hbar\omega\right], \tag{2.7}$$

where N_A is the number of atoms per unit volume. The oscillator strength, f, and the integrated absorption coefficient α are related by

$$N_A f_{lm} = \frac{mc}{2\pi^2 e^2 \hbar} \int \alpha_{lm}(E) dE. \tag{2.8}$$

2.2 Absorbing Entity in a Solid

2.2.1 The Local Field Correction

If the applied radiation field, $\mathcal{E}_0$, is modified by the environment surrounding the absorbing particle to a local value, $\mathcal{E}_{eff}$. The transition probability, W_{lm}, should

corrected by a multiplicative factor $(\mathcal{E}_{eff}/\mathcal{E}_0)^2$. The value of $\mathcal{E}_{eff}$ is dependent on the nature of the absorbing centre but can be related to $\mathcal{E}_0$, for compact centres [295] by

$$\left[\frac{\mathcal{E}_{eff}}{\mathcal{E}_0}\right]^2 = 1 + \frac{1}{3}(n^2 - 1), \tag{2.9}$$

where n is the refractive index of the medium. The absorption cross section, ε, requires correction by additional factors and is obtained by dividing the total transition probability by the energy density, which in a medium is proportional to n^2; where the speed of light (c) is replaced by c/n. Hence the total correction factor for the absorption cross-section is $\left[1/n(\mathcal{E}_{eff}/\mathcal{E}_0)^2\right]$.

2.2.2 Born-Oppenheimer Approximation and Modified Transition Matrix Element Leading to Smakula's Equation

According to the Born-Oppenheimer approximation, electrons respond to the instantaneous positions of the nuclei, whereas the lattice responds to the average positions of the electrons. It may be assumed that the nuclei are essentially stationary when calculating the electron wavefunctions. Following Fowler's [295] summary of this approximation, the wave equation for the system consisting of electrons plus lattice is given by,

$$[E_{ke} + E_{kn} + U(\boldsymbol{r}, \boldsymbol{R})]\,\psi(\boldsymbol{r}, \boldsymbol{R}) = E\psi(\boldsymbol{r}, \boldsymbol{R}) \tag{2.10}$$

where $\boldsymbol{r}$ are electron co-ordinates, $\boldsymbol{R}$ nuclear co-ordinates, E_{ke} and E_{kn} are the total kinetic energy of electrons and nuclei respectively. $U(\boldsymbol{r}, \boldsymbol{R})$ is the total potential energy term for electron-electron, electron-nucleus and nucleus-nucleus interactions. The wavefunction $\psi(\boldsymbol{r}, \boldsymbol{R})$ is more explicitly described by defining a set of electronic quantum numbers n and nuclear quantum numbers η such that

$$\psi_{n\eta}(\boldsymbol{r}, \boldsymbol{R}) = \phi_{n,\boldsymbol{R}}(\boldsymbol{r})\theta_{n\eta}(\boldsymbol{R}). \tag{2.11}$$

Solving for these wavefunctions is a difficult exercise. Approximations may be used involving simplified models of the electron-phonon interaction. The dipole moment

matrix element $\boldsymbol{r}_{lm}$, (equation 2.3) becomes

$$\boldsymbol{r}_{l_\eta,m_\gamma} = d\boldsymbol{R}\theta^*_{l\eta}(\boldsymbol{R})\boldsymbol{r}_{lm}(\boldsymbol{R})\theta m_\gamma(\boldsymbol{R}) \tag{2.12}$$

where

$$\boldsymbol{r}_{lm}(\boldsymbol{R}) = \int d\boldsymbol{r}\phi^*_{l\boldsymbol{R}}(\boldsymbol{r})\boldsymbol{r}\phi_{m\boldsymbol{R}}(\boldsymbol{r}). \tag{2.13}$$

The oscillator strength now becomes

$$f_{lm} = \frac{2m}{3\hbar e^2}\omega_{lm} \mid \boldsymbol{r}_{lm}(\boldsymbol{R}_G) \mid^2, \tag{2.14}$$

where the Condon approximation has been used and $\boldsymbol{r}_{lm}$ assumed to depend on an equilibrium nuclear co-ordinate, $\boldsymbol{R_G}$. This is discussed further in the next subsection. The absorption coefficient is now

$$\alpha_{lm}(E) = \left[\frac{1}{n}\left[\frac{\mathcal{E}_{eff}}{\mathcal{E}_0}\right]^2\right]\frac{4\pi^2}{3\hbar c}\hbar\omega_{lm}N_A \mid \boldsymbol{r}_{lm} \mid^2 I_{lm}(E), \tag{2.15}$$

where

$$I_{lm}(E) = a\nu_\eta \sum_\gamma \mid \int d\boldsymbol{R}\theta^*_{l_\eta}(\boldsymbol{R})\theta_{\boldsymbol{m\gamma}}(\boldsymbol{R}) \mid^2 \delta(\mid Em - E_l \mid -\hbar\omega) \tag{2.16}$$

and

$$\int I_{lm}(E)dE = 1. \tag{2.17}$$

By comparing $f_{lm}(E)$ and $\alpha_{lm}(E)$ and using the Lorentz approximation, equation 2.9, for the local field then

$$N_A f_{lm} = 8.21 \times 10^{16} cm^{-3}\frac{n}{(n^2+2)^2}\int \alpha_{lm}(E)dE, \tag{2.18}$$

where α is in cm^{-1} and E is in electron volts. $\int \alpha_{lm}(E)dE = \frac{1}{2}\pi\alpha_{lm}(\mathrm{max})W$ for a Lorentzian function, where W is the full width of the absorption band at half maximum. Substituting this, one obtains the Smakula equation [302]

$$N_A f_{lm} = 1.29 \times 10^{17} cm^{-3}\frac{n}{(n^2+2)^2}\alpha_{lm}(\mathrm{max})W. \tag{2.19}$$

For a Gaussian function, the integral above is reduced by the factor $(\pi \ln 2)^{\frac{1}{2}}$ and the constant becomes 0.87. The F centre absorption band has the characteristics of an approximately Gaussian band, hence the concentration of defects is given by

$$N(cm^{-3}) = \frac{0.87 \times 10^{17}}{f} \frac{n}{(n^2+2)^2} \alpha(max) W. \tag{2.20}$$

This expression is used to calculate the defect concentration provided that the oscillator strength (f) is known. It has therefore been included for completeness sake in the present case where the value of f is unknown.

2.2.3 Configuration Co-ordinate Diagram and Absorption Band Shape

The separation of electron and nuclear states, according to Born-Oppenheimer approximation can be represented in a simple model called the configuration co-ordinate diagram [301, 303, 304, 305]. Such a diagram taken from Fowler [295] is presented in figure 2.1. The response of the electrons to the instantaneous positions of the nuclei is represented by the parabolic curves of electronic energy versus nuclear co-ordinate. This energy dependence is illustrated for a ground electronic state l and an excited state m. The quantum states of the lattice are represented by $\eta_0, \eta_1, ...$ and $\gamma_0, \gamma_1, ...$ etc in the ground and excited electronic states, respectively. If the Franck-Condon principle (which states that during electronic transitions the nuclear co-ordinate do not change) is invoked, this simple diagram can account qualitatively for the finite width of absorption bands. The Born-Oppenheimer approximation predicts Gaussian shaped bands giving a relationship between the width of the band at half-maximum (W) and the temperature of the form

$$W = W_0 \left[\coth \left(\frac{\hbar\omega}{2KT} \right) \right]^{\frac{1}{2}}, \tag{2.21}$$

where W_0 is the width of the band at half-maximum at 0 K and ω is the angular frequency. The validity of the Franck-Condon principle can be illustrated quantum mechanically. The most probable transitions (figure 2.1) will be those that reach the vi-

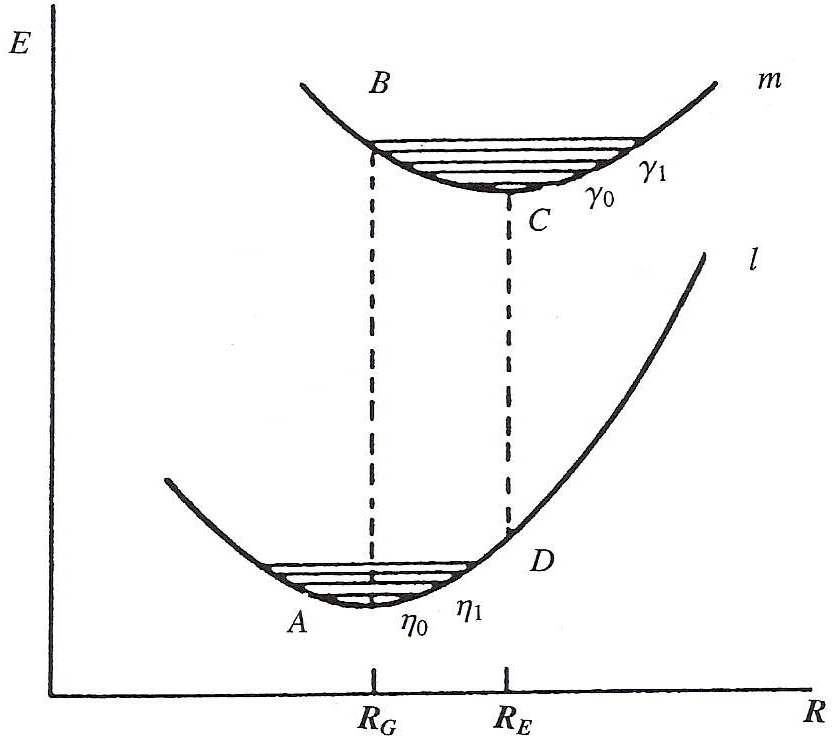


Figure 2.1: Electronic energy, E, versus nuclear co-ordinates, $\boldsymbol{R}$, for an electronic ground state l and excited state m, also illustrating the nuclear state η and γ for each of the electronics states, respectively. $\boldsymbol{R_G}$ and $\boldsymbol{R_E}$ are the nuclear co-ordinates for the ground and excited states respectively [295].

brational states of the excited electronic state that have high probability functions at the internuclear separation equal to that of the ground state. This principle emphasizes that only these transitions need be considered and hence the use of $\boldsymbol{R_G}$ in equation 2.14 [16, 306, 307].

The basic underlying theory of optical absorption, which is a major experimental technique in the present work has been presented. Examination of the fundamental aspects of the theory can help to predict the form of absorption bands due to defects in solids, and the essential properties of such bands.

2.3 Theory of Raman Scattering

2.3.1 Introduction

The name Raman effect originates from the work of Raman and Krishan [308], who reported the phenomenon in 1928, following studies on molecular light scattering. However, the effect had theoretically been suggested earlier in 1923 by Smekal [309] and also observed in quartz by Landsberg and Mandelstam [310] on the same year that Raman and Krishan reported the results of their work. It was observed that when monochromatic light of known frequency was used to illuminate certain media, the resulting spectrum consisted of a pattern of lines of shifted frequencies (Raman shifts) relative to the unscattered line (Rayleigh line). Figure 2.2 [311] shows a representative Raman spectrum of liquid CCl_4 obtained using an argon ion laser. The centrally located line corresponds to the Rayleigh line, the three features to its left are the Raman

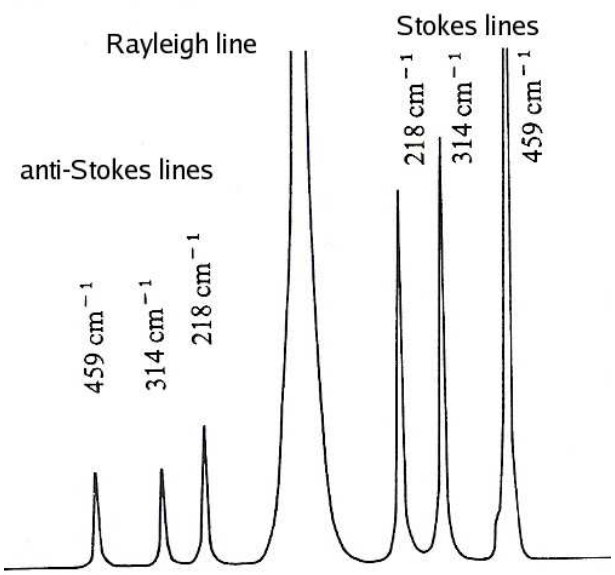


Figure 2.2: Raman spectrum of liquid CCl_4 excited by an argon ion laser. A central intense line associated with the Rayleigh line and two sets of a series of lines to its left and right are observed [311].

anti-Stokes lines, while the more intense lines to the right are the Raman Stokes lines. The Raman shifts, which are more commonly used, are independent of the exciting frequency and characteristic of the species giving rise to the scattering. The Raman effect may generally occur due to the inelastic scattering of light by phonons, plasmons, polaritons, magnons in a medium. In a restricted sense Raman scattering describes the light scattering caused by the spatial variation of the electronic polarizability of a system by the nuclear vibrations and rotations only. The current discussion will use the latter definition. Raman spectroscopy is an excellent tool in studying the nature of molecular defect clusters formed in crystals and can be applied successfully to the study of defects in crystals of the alkali halide type. First order Raman scattering is forbidden in pure alkali halides crystals due to symmetry considerations. However, Raman transitions due to defects in the crystal are often localised modes which are clearly distinguishable above the weak background of this lattice scattering. Alkali halides thus exhibit a second order continuous Raman spectrum.

Since this technique is only used in the study of proton implanted CsI crystals, whose results are discussed in chapter 4, the theoretical description is summarised and more details may be found in references cited in the text. The two subsections that immediately follow provide a brief discussion of the Raman effect from both classical and quantum mechanical treatments. Near resonance Raman effect, which can be employed to provide enhanced signals, thus making it possible to study scattering species in low concentrations, will be discussed in a following subsection.

2.3.2 Classical Approach

An incident light photon interacting with a molecule in a material may be inelastically or elastically scattered. Consider an incident electric field described by

$$\mathcal{E} = \mathcal{E}_0 cos(2\pi\nu_0 t), \tag{2.22}$$

where $\mathcal{E}_0$ is the amplitude and ν_0 the associated frequency. The molecule will vibrate in normal coordinates given by

$$X_k(t) = X_k^0 cos(2\pi\nu_0 t), \tag{2.23}$$

where $X_k(t)$ is the displacement from the equilibrium position X_k^0 in time, t, during the motion that is approximated to be harmonic. These molecular vibrations will consequently induce a variation in the electronic polarization given by

$$\alpha = \alpha_0 + \sum_k \left(\frac{d\alpha}{dX_k}\right)_0 X_k + \cdots. \tag{2.24}$$

Since the induced dipole moment is obtained by the product of the polarization and the electric field

$$P = \alpha_0\mathcal{E}_0 cos(2\pi\nu_0 t) + \frac{1}{2}\sum_k \left(\frac{d\alpha}{dX_k}\right)_0 X_k.[cos(2(\pi(\nu_0-\nu_k)t+\phi_k)+cos(2(\pi(\nu_0+\nu_k)t+\phi_k)]+\cdots. \tag{2.25}$$

The first term in equation 2.25 corresponds to the elastically scattered wave associated with the Rayleigh mode. The two terms in square brackets with different frequencies, $\nu_0-\nu_k$ and $\nu_0+\nu_k$ are the inelastically scattered waves associated with the Raman Stokes and anti-Stokes lines, respectively. The classical theory clearly identifies the existence of the three scattered components but not the relative intensity between the Stokes and anti-Stokes lines, which is taken up in the quantum treatment to follow.

2.3.3 Quantum Mechanical Approach

The quantum mechanical treatment involves a two-photon process schematically illustrated in figure 2.3. The occurrence of the sidebands at frequencies $\nu_0 \pm \nu_k$ can be explained in terms of an energy transfer between the incident radiation and the scattering system. ν_k is associated with the transitions in the vibrational energy levels in the scattering system under study. The system stimulated by the incident radiation may absorb energy for an internal excitation. The scattered light will then contain photons

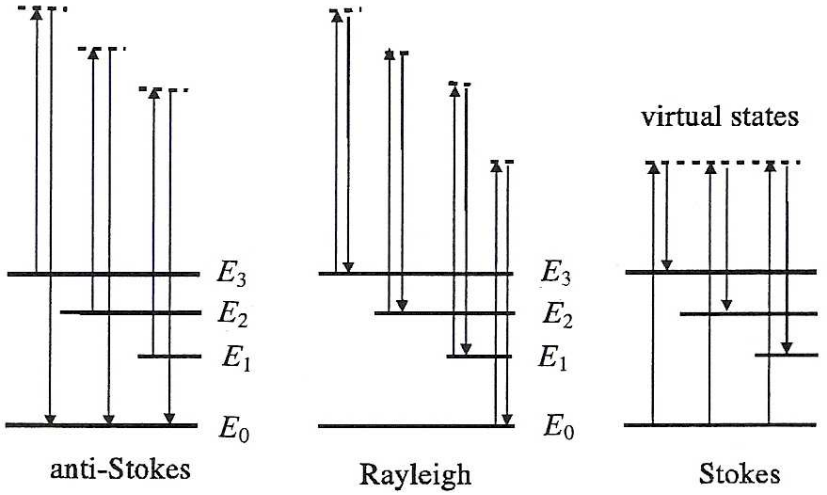


Figure 2.3: Representation of the Rayleigh and Raman scattering as a two-photon process. The broken lines denote virtual states.

of energy $h(\nu_0 - \nu_k)$. Alternatively if the system is already in an excited state, it may make a downward transition in the presence of the exciting excitation, thus contributing to the creation of photons of energy $h(\nu_0 + \nu_k)$. Thus the occurrence of scattered radiation of frequencies $\nu_0 \pm \nu_k$ depend on the energy levels of the scattering system and the transitions permitted between them. The concept of the virtual states is adopted to describe the intermediate levels prior to a final transition involving a different vibrational state and hence their role is purely imaginary. The scattered radiation at lower wavenumbers is termed Stokes scattering, and that at higher wavenumbers anti-Stokes scattering. Since anti-Stokes scattering corresponds to a transition in the system from a populated upper state to a lower state, this sideband will be much weaker in intensity than the Stokes sideband. The thermal population of such upper states decreases as their energy above the lower states becomes large.

2.3.4 The Near Resonance Raman Effect

One of the earliest reviews of the quantum mechanical treatment explaining the Raman effect was published by Placzek [312]. Part of the results, relevant to the current subsection, are presented without proof. Placzek's treatment considers the perturbation of the wave-functions of the scattering molecule by the electric field ($\mathcal{E}$) of the incident light having frequency ν_0 and gives an expression of the induced electric moment matrix element P_{mn} (also known as the induced transition moment) as

$$P_{mn} = \frac{1}{h} \sum_r \left(\frac{M_{nr} M_{rm}}{\nu_{rn} - \nu_0} + \frac{M_{nr} M_{rm}}{\nu_{rm} + \nu_0} \right) \mathcal{E}, \tag{2.26}$$

where h is Planck's constant, r denotes any level of the complete set belonging to the unperturbed molecule, ν_{rn} and ν_{rm} are the frequencies corresponding to the differences between the states denoted by the subscripts, M_{nr} and M_{rm} are the respective transition moments. The square of P_{mn} determines the scattering intensity of the line involving the induced transition from n to m. If the exciting frequency, ν_0, is chosen to lie close to a particular absorption frequency, ν_{rn}, the term in the denominator with the factor $1/(\nu_{rn} - \nu_0)$ will become significant in the determination of the intensity.

Thus the near resonance Raman effect is described as the increase in the intensity of the scattered light as the wavelength of the exciting radiation is made to approach the absorption frequency of the scattering system. The usefulness of the near resonance Raman effect can be appreciated when scattering entities, such as defects in the crystals are present in low concentrations and the regular Raman scattering too weak to monitor. The symmetric stretching overtones of the vibration appear under near resonance conditions as will be shown in the present work on molecular defects produced by the proton implantation of CsI.

2.4 Annealing Theory

2.4.1 Introduction

The defects created by irradiation of crystals reach a thermodynamic equilibrium when the source of irradiation is removed. The temperature of the crystal determines the equilibrium concentration of defects. If the temperature is dropped below the threshold temperature for mobility of any of the defects species then the defect profile produced by the irradiation can be *frozen in*. If the temperature is raised sufficiently then the defects become mobile and their thermally activated motion may result in a variety of effects [313, 314]: they may encounter traps (e.g. impurities) where they become immobilized, they may be absorbed by sinks (e.g. surfaces, dislocations, grain boundaries), an interstitial defect may encounter its complementary vacancy and become annihilated, and defects may themselves act as traps for similar defects producing defect clusters. As well as the elimination of a defect type by any of the processes listed above, defects may be liberated from clusters or traps. The possible fate of defects is not limited to those mentioned above, but whatever the processes induced by the temperature rise, when there is reduction in the original type of defects, this is called annealing. The two commonly used types of annealing procedures are isochronal and isothermal which are discussed below.

2.4.2 Isochronal Anneal

Figure 2.4a illustrates the procedure for this type of anneal. The temperature of the crystal is raised in a step-like manner from some base or reference temperature to T_i for the i^{th} anneal step. The temperature is maintained at T_i for a fixed time $\triangle t_f$ (30 minutes in the present work). Between each temperature step the crystal is brought back to a reference temperature for measurement of the property (e.g. absorption) indicating the defect concentration. A series of such steps at successively higher temperatures T_i,

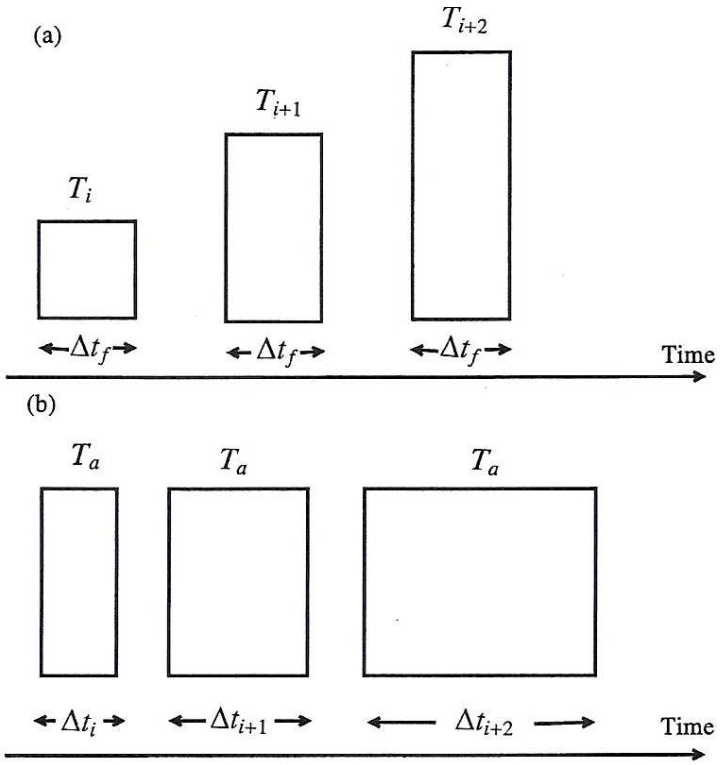


Figure 2.4: (a) Isochronal anneal: step-like temperature pulses of constant duration $\triangle t_f$ at successively higher temperatures T_i. (b) Isothermal anneal : increasing duration $\triangle t_i$ at fixed temperature T_a.

T_{i+1}, T_{i+2}... constitutes an isochronal anneal. Figure 2.5a illustrates a schematic diagram of an isochronal anneal curve showing the variation of the absorption coefficient with temperature. The presence of different defects which anneal out by independent mechanisms at different temperatures is indicated by separate stages for each process.

2.4.3 Isothermal Anneal

In an isothermal anneal a fixed temperature (T_a in figure 2.4b) corresponding approximately to the middle of the isochronal anneal step is selected (see figure 2.5a). The sample is annealed at this temperature for sequentially increasing total time t_i. As in the isochronal cycle, the sample is cooled to the reference temperature between the

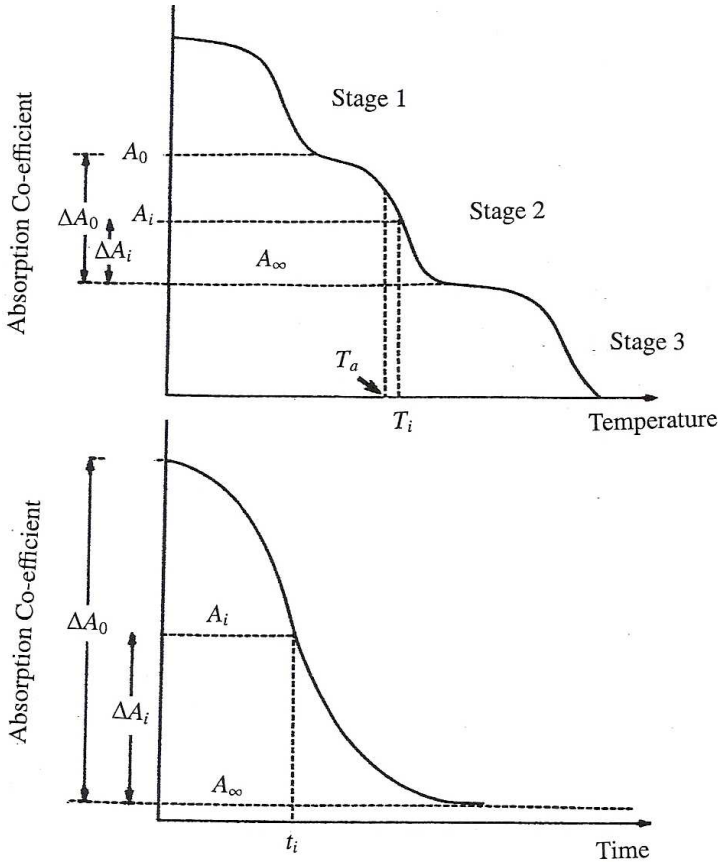


Figure 2.5: Schematic diagrams of (a) isochronal anneal showing decrease in the absorption coefficient over the possible anneal component stages (b) isothermal anneal of a single stage process.

annealing steps and the necessary measurement taken. In the present work the additional anneal time $\Delta t_{i+1} = 2\Delta t_i$, with Δt_0=10 minutes. Figure 2.5b shows the isothermal annealing characteristics due to the presence of a single type of defect where the absorption coefficient goes close to zero in one stage.

2.4.4 Defect Migration

The motion of defects through a crystal is usually treated by the application of the absolute rate theory, where the main factor dictating the change in position of the defect is the potential barrier which must be overcome. Howard and Lidiard [315]

have shown, using statistical mechanics, that migrating atoms have a jump frequency associated with the vibration of the atom between its original position and the saddle point for migration, of the form

$$\nu = \nu_0 e^{-E_m/K_B T}, \tag{2.27}$$

where E_m is the energy barrier for migration, K_B the Boltzmann constant and ν_0 the effective frequency of vibration of the defect toward the saddle point. This type of expression is termed as the Arrhenius equation which also applies to chemical reactions. The chemical rate theory is therefore applicable to defect migration and annealing.

2.4.5 Annealing of Defects from Chemical Rate Theory

Consider a crystal containing a particular kind of defect whose concentration is N at a time t. The defect concentration obeys a differential equation of the form

$$-\frac{dN}{dt} = \nu \mathcal{K}(N), \tag{2.28}$$

where ν is the rate constant defined by equation 2.27 and $\mathcal{K}(N)$ is a monotonically decreasing function of N. As the temperature is raised during annealing, dN/dt initially remains small, since ν varies exponentially with temperature, and as the characteristic annealing temperature, T_a, is approached and ν tends to unity, then dN/dt increases substantially. This rate drops rapidly again as the defects anneal out. The function $\mathcal{K}(N)$ may be given a specific form for an anneal involving the decay of one species at a time. Therefore in this case equation 2.28 can be written as

$$-\frac{dN}{dt} = \nu \mathcal{Z} N^{\gamma}. \tag{2.29}$$

The term $\mathcal{Z}$ incorporates an entropy factor, sink or trap distribution factors and the co-ordination of the defect site and γ indicates the order of the reaction. If $\gamma = 1$ the annealing reaction is called first order and if $\gamma = 2$, second order. The conditions required for the annealing process to be assigned as first or second order are discussed

in more detail elsewhere [313]. In the case where defects migrate to unsaturable sinks, for example, the reaction would be expected to be first order. For the mutual annihilation between two complementary defect types distributed randomly throughout the crystal and which are therefore uncorrelated, a second order type of reaction would be expected.

The data obtained from annealing procedures described in subsections 2.4.2 and 2.4.3 can be used to determine the order of the reaction (γ) and the activation energy (E_m). Some property of the crystal, independent of the temperature and time which monitors the defect concentration, must be recorded during the annealing cycle. One such property is the absorbance of the band produced by the decaying defects. Since the optical absorption is defect specific it is possible to study the decay of particular type of defects and the growth of reaction products independently of other defects. Even when different defects types absorb in the same spectral region the components of the resulting composite absorption band due to the individual species can often be identified by careful subtraction and difference analysis techniques. The use of Raman scattering, which is also defect-specific, in conjunction with optical absorption is helpful in such circumstances. The decay of the Raman peaks due to certain defects can be correlated to the decay of the constituent overlapping components of a composite absorption band.

The absorbance, $A = L\alpha/2.303$ (α : absorption coefficient, L : sample thickness), is related to the defect concentration by the Smakula equation 2.20 which can be rewritten as

$$Nf = cWA, \tag{2.30}$$

where f is the oscillator strength and c is a constant. The width at half maximum, W, of the absorption band is temperature dependent. If the crystal is, however, returned to the reference temperature for measurement of the absorbance (A) after each annealing pulse, then W will be fixed, independent of temperature. From figure 2.5a Smakula's

equation for the i^{th} anneal step can be rewritten as

$$N_i f = cW\Delta A_i, \tag{2.31}$$

where N_i is the concentration of defects remaining and $\Delta A_1 = A_i - A_\infty$ is the incremental absorbance increase for the i^{th} anneal step. The change in the absorbance for the whole anneal step is $\Delta A_0 = A_0 - A_\infty$. Equation 2.31 can be written in a more compact form as

$$N_i = c'\Delta A_i, \tag{2.32}$$

where c' is a constant. Methods of analysis on the rate equation 2.29 adapted for use with isothermal and isochronal data are presented in the following two subsections.

2.4.6 Determination of γ from Isothermal Anneal Data

If equation 2.29 is integrated and a substitution made for the concentration, N, in terms of ΔA_i, the following expressions result :

$$ln\frac{\Delta A_0}{\Delta A_i} = \nu\mathcal{Z}t. \tag{2.33}$$

Therefore a plot of $ln(\Delta A_0/\Delta A_i)$ versus t yields a straight line in the case where $\gamma = 1$. If $\gamma > 1$,

$$\Delta A_i^{1-\gamma} - \Delta A_0^{1-\gamma} = \nu\mathcal{Z}(\gamma - 1)tc^{\gamma-1}. \tag{2.34}$$

γ can be chosen so that a plot of $\Delta A_i^{1-\gamma}$ versus t results in a straight line.

2.4.7 Determination of E_m from the Isochronal Anneal Data

It is assumed in this case that the anneal is characterised by a single process with a unique activation energy, E_m. Equation 2.29 is integrated and a substitution made for N in terms of ΔA as before. Substituting for ν from equation 2.27 gives

$$ln\frac{\Delta A_0}{\Delta A_i} = Bte^{-E_m/K_BT}, \tag{2.35}$$

for $\gamma = 1$ and

$$\Delta A_i^{1-\gamma} - \Delta A_0^{1-\gamma} = Bc^{\gamma-1}(\gamma - 1)te^{-E_m/K_BT} \tag{2.36}$$

if $\gamma > 1$, where $B = \nu_0 \mathcal{Z}$.

By examining one temperature step of the isochronal anneal for which the step duration Δt is fixed, it follows that for $\gamma = 1$

$$ln\frac{\Delta A_{i-1}}{\Delta A_i} = B\Delta te^{-E_m/K_BT_i}. \tag{2.37}$$

A plot of $ln[ln(\Delta A_{i-1})/\Delta A_i]$ versus $1/T_i$ yields a straight line with a slope of E_m/K_B. For $\gamma > 1$,

$$\Delta A_i^{1-\gamma} - \Delta A_{i-1}^{1-\gamma} = Bc^{\gamma-1}(\gamma - 1)\Delta te^{-E_m/K_BT_i}. \tag{2.38}$$

A plot of $ln[\Delta A_i^{1-\gamma} - \Delta A_{i-1}^{1-\gamma}]$ versus $1/T_i$ yields a straight line with a slope of E_m/K_B. The general procedure is to determine γ first, and then use the appropriate equation to obtain the activation energy.

2.5 Theoretical Studies of Resonances Associated With Metal Colloids

2.5.1 Introduction

There are a number of methods reported in the literature that are used to describe resonances associated with metal particles embedded in materials. The first one is the *ab initio* quantum theoretical approach [316] that provides a sufficient description of the plasmon resonance peak for very small clusters and may be extended to larger sizes. The second, commonly known as the jellium model, yields multiple line structure in the spectra, some of which have been related to collective electron resonances [317, 318]. Both methods can predict the plasmon resonance peaks but have problems providing the shapes or widths. The Mie theory which is the third method applies classical electrodynamics to clusters whose shapes may be approximated to be spherical but may have other geometrical forms. The Mie resonances predicted by the

third approach cause selective optical extinction bands, which are generally observed in the visible spectral region for both the noble and alkali metals, whose characteristics are dependent on the cluster diameter, the refractive index of the host medium and the metal volume fraction among other factors. The Mie theory therefore has an advantage of being conceptually simple and has been used in the present work in which Mg^+ and Ag^+ or Au^{3+} ions have been implanted in magnesium fluoride and lithium niobate single crystals, respectively.

2.5.2 Mie Theory

The calculation of interaction of the small spherical particles with electromagnetic radiation, commonly known as the Mie theory (MT) [159] has been repeatedly elaborated by many workers [162, 319, 320]. A summarized outline of the procedure to calculate the attenuation of an unpolarized monochromatic light beam after it has passed through a medium containing spherical particles is presented from an article by Pereenboom and co-workers [168], and selected texts [320, 321]. This summary begins with an assumption that the volume concentration of particles is so low that the particles act as independent scattering centres with no multiple scattering taking place. The extinction of the beam is then given by:

$$I(z) = I_0 e^{-\Gamma z}, \tag{2.39}$$

where $I(z)$ is the intensity of the incoming beam after a distance z. The extinction coefficient, Γ, is therefore a product of the number of scattering centres per unit volume (N/V) and the extinction cross section of a single particle, C_{ext}. The extinction cross section is the sum of both the scattering cross section, C_{sca}, and the absorption cross section, C_{abs}:

$$\Gamma = \frac{N}{V} C_{ext} = \frac{N}{V}(C_{sca} + C_{abs}). \tag{2.40}$$

This extinction cross section may now be calculated from the MT by applying Maxwell's

equations. Consider the case of a monochromatic, linearly polarized plane wave of electric and magnetic field amplitudes $\mathcal{E}$ and B incident onto a particle at position P (see figure 2.6). From Maxwell's equations, $\mathcal{E}$ and B are not independent: $B = (n/c)\mathcal{E}$, where $n = \sqrt{[\varepsilon\mu]}$, is the refractive index of the medium and ε and μ denote the relative permittivity and permeability, respectively. The incoming field expressed in polar coordinates is written as:

$$\begin{aligned} \mathcal{E}_r &= \sin\theta\cos\phi e^{ikr\cos\theta}e^{-i\omega t} \\ \mathcal{E}_\theta &= \cos\theta\cos\phi e^{ikr\cos\theta}e^{-i\omega t} \\ \mathcal{E}_\phi &= -\sin\phi e^{ikr\cos\theta}e^{-i\omega t} \end{aligned} \tag{2.41}$$

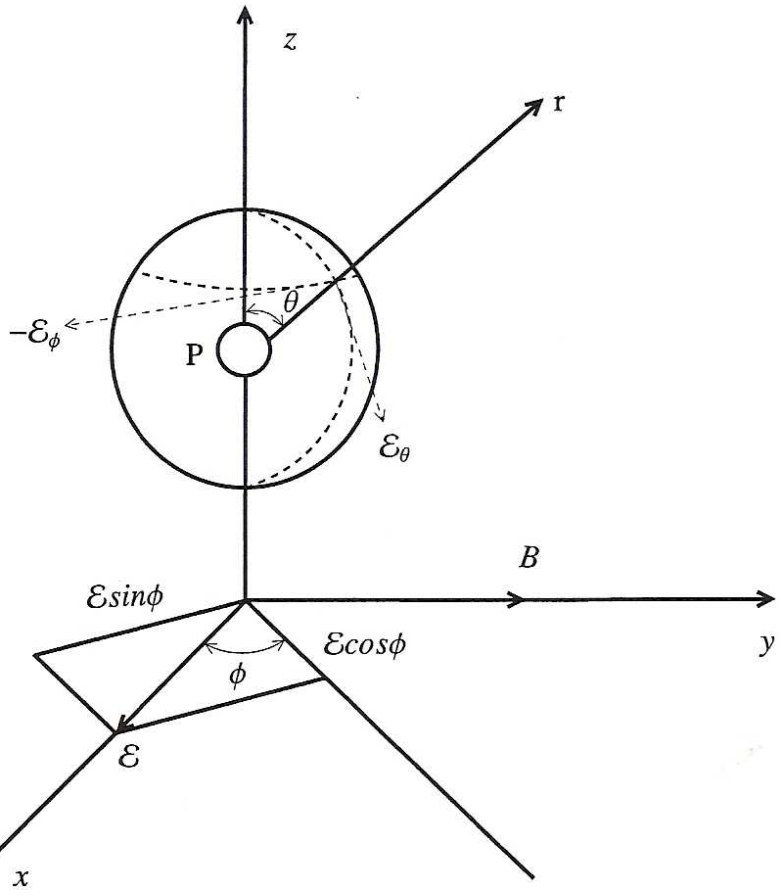


Figure 2.6: The incoming electromagnetic wave, directed along the +z-axis and the outgoing spherical wave, which is scattered by a particle at position P.

$$
\begin{aligned}
B_r &= (n/c)\sin\theta\sin\phi e^{ikr\cos\theta}e^{-i\omega t} \\
B_\theta &= (n/c)\cos\theta\sin\phi e^{ikr\cos\theta}e^{-i\omega t} \\
B_\phi &= (n/c)\cos\phi e^{-ikr\cos\theta}e^{-i\omega t}. \qquad (2.42)
\end{aligned}
$$

It was noted by Debye [162] that this problem was solvable on realization that the vectors $\vec{\mathcal{E}}$ and $\vec{B}$ could be derived from a scalar field $\mathcal{V}$ which satisfies the same wave equation as the Cartesian components of $\vec{\mathcal{E}}$ and $\vec{B}$, i.e. : $\nabla^2\mathcal{V} + k^2\mathcal{V} = 0$. All possible solutions are obtained by considering two different functions $\mathcal{V}_1$ and $\mathcal{V}_2$; the first corresponds to the case where the radial part of $\vec{B}$ vanishes and electrical waves are generated while the second represents the magnetic waves with vanishing $\mathcal{E}_r$. A superposition of the fields derived from the two potentials would represent the complete solution. For the electrical waves the components of $\vec{\mathcal{E}}$ may be found as derivatives of the function $(\partial/\partial r)r\mathcal{V}_1$ (see equation 2.43) and the contribution of $r\mathcal{V}_1$ to the magnetic field is obtained subsequently by using Maxwell's equations. Similarly for the magnetic waves, the components of $\vec{B}$ are obtained directly from the differentiation of $(\partial/\partial r)r\mathcal{V}_2$, and the contribution to the electric field is found again from the corresponding Maxwell equation.

Therefore

$$
\begin{aligned}
\mathcal{E}_r &= \frac{\partial^2}{\partial r^2}r\mathcal{V}_1 + k^2 r\mathcal{V}_1 \\
\mathcal{E}_\theta &= \frac{1}{r}\frac{\partial^2}{\partial r\partial\theta}r\mathcal{V}_1 + \frac{ick}{nr\sin\theta}\frac{\partial}{\partial\phi}r\mathcal{V}_2 \\
\mathcal{E}_\phi &= \frac{1}{r\sin\theta}\frac{\partial^2}{\partial r\partial\theta}r\mathcal{V}_1 - \frac{ick}{nr}\frac{\partial}{\partial\theta}r\mathcal{V}_2 \qquad (2.43)
\end{aligned}
$$

$$
\begin{aligned}
B_r &= \frac{\partial^2}{\partial r^2}r\mathcal{V}_2 + k^2 r\mathcal{V}_2 \\
B_\theta &= \frac{1}{r}\frac{\partial^2}{\partial r\partial\theta}r\mathcal{V}_2 - \frac{ink}{cr\sin\theta}\frac{\partial}{\partial\phi}r\mathcal{V}_1 \\
B_\phi &= \frac{1}{r\sin\theta}\frac{\partial^2}{\partial r\partial\theta}r\mathcal{V}_2 + \frac{ink}{cr}\frac{\partial}{\partial\theta}r\mathcal{V}_1. \qquad (2.44)
\end{aligned}
$$

The expressions for $\mathcal{E}_r$ and B_r may be used to obtain $r\mathcal{V}_1$ and $r\mathcal{V}_2$, respectively. The solutions may be written as a series expansion in spherical harmonics:

$$\begin{aligned} r\mathcal{V}_1^{(1)} &= \frac{1}{k_1^2} e^{-i\omega t} \cos\phi \sum_{l=1}^{\infty} i^{l-1} \frac{2l+1}{l(l+1)} \alpha_l \psi_l(k_1 r) P_l^{(1)}(cos\theta) \\ r\mathcal{V}_2^{(1)} &= \frac{n}{ck_1^2} e^{-i\omega t} \sin\phi \sum_{l=1}^{\infty} i^{l-1} \frac{2l+1}{l(l+1)} \beta_l \psi_l(k_1 r) P_l^{(1)}(cos\theta). \end{aligned} \tag{2.45}$$

$k = nw/c$ is the modulus of the wavevector and n the complex index of refraction of the medium; $\psi_l(Z)$ [162] is a Ricatti-Bessel function of the type $(\pi z/2)^{1/2} J_{l+I/2}(Z)$, where $J_{l/+I/2}(Z)$ is a half integral Bessel function, and $P_l^{(1)}(cos\theta)$ is an associated Legendre polynomial. For $\alpha_l = \beta_l = 1$, solution 2.45 will generate the incoming wave whose components are given by equations 2.43 and 2.44. For the field inside the particle, an ansatz of the form given in solution 2.45 is appropriate. For the scattered wave outside the particle, a decomposition must be made with functions $\eta_l(kr)$ [162] instead of $\psi_l(kr)$. $\eta_l(z)$ is a Ricatti-Bessel function of the type $(\pi z)^{1/2} H_{l+1/2}^{(1)}(z)$ where $H_{l+1/2}^{(1)}$ is half integral Hankel function of the first kind. The asymptotic form of $\eta_l(kr)$ for $kr \gg 1$ is $\eta_l(kr) = (-1)^{l+1} e^{ikr}$, representing an outgoing wave. The ansatz for the scattered wave is therefore:

$$\begin{aligned} r\mathcal{V}_1^{(2)} &= \frac{1}{k_2^2} e^{-i\omega t} \cos\phi \sum_{l=1}^{\infty} i^{l-1} \frac{2l+1}{l(l+1)} a_l \eta_l(k_2 r) P_l^{(1)}(cos\theta) \\ r\mathcal{V}_2^{(2)} &= \frac{n_0}{ck_2^2} e^{-i\omega t} \sin\phi \sum_{l=1}^{\infty} i^{l-1} \frac{2l+1}{l(l+1)} b_l \eta_l(k_2 r) P_l^{(1)}(\cos\theta). \end{aligned} \tag{2.46}$$

The indices (1) and (2) refer to the particle and the embedding medium, respectively. The coefficients α_l, β_l, a_l and b_l may be obtained from the boundary conditions at the surface of the particle: -

$$\mathcal{E}_{tang.}^{(1)} = \mathcal{E}_{tang.}^{(i)} + \mathcal{E}_{tang.}^{(2)} \tag{2.47}$$

$$B_{tang.}^{(1)} = B_{tang.}^{(i)} + B_{tang.}^{(2)}, \tag{2.48}$$

where index (i) refers to the incoming wave. The continuity of $\mathcal{E}_\theta$ and $\mathcal{E}_\phi$ implies the continuity of the functions $(\partial/\partial r) r\mathcal{V}_1$ and $r\mathcal{V}_2$ at $r = 0.5d$, where d is the particle

diameter. Similarly, the continuity of $k^2 r\mathcal{V}_1$ and $(\partial/\partial r) r\mathcal{V}_2$ follows from the continuity of both B_θ and B_ϕ at the particle surface. The coefficients a_l and b_l for the scattered wave determined from the boundary conditions are:

$$a_l = -\frac{n\psi_l(n_0 x)\psi_l'(n_0 x) - n_0\psi_l'(nx)\psi_l(n_0 x)}{n\psi_l(nx)\eta_l'(n_0 x) - n_0\psi_l'(nx)\eta_l(n_0 x)} \tag{2.49}$$

$$b_l = -\frac{n_0\psi_l(nx)\psi_l'(n_0 x) - n\psi_l'(nx)\psi_l(n_0 x)}{n_0\psi_l(nx)\eta_l'(n_0 x) - n\psi_l'(nx)\eta_l(n_0 x)}. \tag{2.50}$$

Equations 2.49 and 2.50 contain the Mie-parameter $x = 0.5 k_0 d$, with the modulus of the vacuum wavevector $k_0 = 2\pi/\lambda_0$, the index of refraction of the embedding medium $n_0 = \sqrt{\epsilon_h}$, where ϵ_h is the real part of the dielectric constant of the nonabsorbing host, assumed to remain constant in the visible region. n is the complex refractive index of the metal particle defined by

$$n = \sqrt{\epsilon} = \sqrt{\epsilon_1 - i\epsilon_2}. \tag{2.51}$$

ϵ_1 and ϵ_2 are the real and imaginary parts of the metal particle dielectric function, ϵ.

Far away from the particle, $r \gg \lambda_0$, the asymptotic form of the function $\eta_l(k_2 r)$ may be substituted. By defining the functions $S_1(\theta)$ and $S_2(\theta)$ as:

$$S_1(\theta) = \sum_{l=1}^{\infty} \frac{2l+1}{l(l+1)} \left[a_l \frac{P_l^{(1)}(\cos\theta)}{\sin\theta} + b_l \frac{dP_l^{(1)}(\cos\theta)}{d\theta} \right] \tag{2.52}$$

$$S_2(\theta) = \sum_{l=1}^{\infty} \frac{2l+1}{l(l+1)} \left[a_l \frac{dP_l^{(1)}(\cos\theta)}{d\theta} + b_l \frac{P_l^{(1)}(\cos\theta)}{\sin\theta} \right], \tag{2.53}$$

the components of the electric and magnetic fields may be expressed conveniently as:

$$\begin{pmatrix} \mathcal{E}_\phi \\ -B_\theta \end{pmatrix} = \frac{iexp(ik_2 r) - i\omega t}{k_2 r} \sin\phi S_1(\theta) \begin{pmatrix} \mathcal{E} \\ B \end{pmatrix} \tag{2.54}$$

$$\begin{pmatrix} \mathcal{E}_\theta \\ B_\phi \end{pmatrix} = -\frac{iexp(ik_2 r) - i\omega t}{k_2 r} \cos\phi S_1(\theta) \begin{pmatrix} \mathcal{E} \\ B \end{pmatrix} \tag{2.55}$$

$$\mathcal{E}_r = B_r = 0. \tag{2.56}$$

If the condition $r \gg \lambda_0$ is still satisfied the scattered wave has the form of an outgoing transverse spherical wave. The forward scattered beam ($\theta = 0$) determines the

extinction cross section. Because of the fact that

$$\frac{1}{\sin\theta}P_l^{(1)}(\cos\theta)\,|_{\theta=0} \;=\; \frac{d}{d\theta}P_l^{(1)}(\cos\theta)\,|_{\theta=0} \;=\; \frac{1}{2}l(l+1), \tag{2.57}$$

the functions $S_1(0)$ and $S_2(0)$ are equal and the extinction cross section is independent of the state of polarization of the incident radiation. The extinction and scattering cross sections are then obtained from the amplitude function $S(0)$ giving :

$$C_{ext} = -\frac{\pi d^2}{(n_0 x)^2} ReS(0) = -\frac{2\pi}{n_0^2 k_0^2}\sum_{l=1}^{\infty}(2l+1)Re\,[a_l + b_l] \tag{2.58}$$

and

$$C_{sca} = \frac{2\pi}{n_0^2 k_0^2}\sum_{l=1}^{\infty}(2l+1)\left[|\,a_l\,|^2 + |\,b_l\,|^2\right]. \tag{2.59}$$

The cross sections may then be evaluated by a series expansion in powers of x of the functions by substituting equations 2.49 and 2.50. The lowest order term in C_{ext} is proportional to x^3 and originates from a_1 written fully in equation 2.60 (see appendix A for a more detailed derivation and the expansion to include higher order terms) as

$$a_1 = -\frac{2}{3}i\left(\frac{n^2-n_0^2}{n^2+2n_0^2}\right)x^3 + -\frac{2}{5}i\frac{(n^2-n_0^2)(n^2-2n_0^2)}{(n^2+2n_0^2)^2}x^5 + \frac{4}{9}\left(\frac{n^2-n_0^2}{n^2+2n_0^2}\right)^2 x^6. \tag{2.60}$$

The third term in the expansion of a_1 is proportional to x^6 and is related with the first term in the power series for C_{sca}. For very small particles, only the first order electric wave will contribute, and the extinction will be mainly due to absorption. Applying the definition of the extinction coefficient in equation 2.40, stated at the beginning of the current section, to the lowest order term of a_1 the result obtained is

$$\Gamma = \frac{18\pi p\epsilon_h^{3/2}}{\lambda_0}\left\{\frac{\epsilon_2}{(\epsilon_1+2\epsilon_h)^2+\epsilon_2^2}\right\}. \tag{2.61}$$

p is the volume fraction of Au in the metal particles, which is defined as the product between the average volume (V_0) of a metal particle and their number per unit volume (N/V). λ_0, ϵ_h, ϵ_1 and ϵ_2 are the wavelength of light in vacuum, the real part of the dielectric constant of the nonabsorbing embedding medium, and the real and imaginary

parts of the dielectric function of the metal particles, respectively. The range of validity of equation 2.61 has to be checked in each case by comparison with the full extinction and scattering cross-sections defined by equations 2.58 and 2.59. However, in the optical frequency range and for very small particles, $d \leq \lambda_0/10$, only the electric dipole contribution needs to be taken into account [168]. d here is the mean particle diameter.

When considering a case of free electrons or free electron-like metals and using the definitions

$$\epsilon_1 = 1 - \frac{\omega_p^2}{\omega^2 + \omega_0^2} \tag{2.62}$$

and

$$\epsilon_2 = \frac{\omega_p^2 \omega_0}{(\omega^2 + \omega_0^2)\omega}, \tag{2.63}$$

where the collision frequency $\omega_0 \ll \omega_p$, it can be shown that the absorption maximum occurs when

$$\omega^2 = \frac{\omega_p^2}{\omega(1 + 2\epsilon_h)^{1/2}}. \tag{2.64}$$

The maximum absorption would occur at a wavelength (λ_{0m}) given by

$$\lambda_{0m} = \frac{2\pi c}{\omega_p}(1 + 2\epsilon_h)^{1/2}, \tag{2.65}$$

where ϵ_h is the real part of the dielectric constant of the host medium [165, 322]. However, in most realistic metals modifications are made to include the contribution due to core electrons and interband transitions as will be outlined in the following subsection.

A similar expression as equation 2.61 may also be obtained using the Maxwell-Garnett theory [160, 161] of a composite medium when the volume fraction of the metal spherical particles, p, is small [170, 323]. According to Maxwell-Garnett theory [160, 161, 164] the effective linear dielectric function $\epsilon_{eff}(\omega)$ is given by

$$\epsilon_{eff}(\omega) = \epsilon_h \frac{(1 + 2p)\epsilon'(\omega) + 2(1 - p)\epsilon_h}{(1 - p)\epsilon'(\omega) + (2 + p)\epsilon_h}. \tag{2.66}$$

where $\epsilon'(\omega) = \epsilon_1'(\omega) - i\epsilon_2'(\omega)$ is the dielectric constant of the bulk metal and p the metal volume fraction.

2.5.3 Procedure for the Use of the Mie Theory

It is necessary to study the characteristics of the Mie theory (MT) simulation curves as the parameters describing the properties of the metal nanoparticles (MNP) and the host matrix are varied. Studying such simulations will help interpret the results that follow in sections to be discussed later. It should be pointed out that the substitution of equations 2.69 and 2.70 assumes the particles are spherical and are distributed over the mean particle diameter. It is also assumed that the implanted metal ions are converted into colloids.

The MNP dielectric function is assumed to be size dependent and is modified to take into account the diffuse scattering of electrons by the surface of the MNP. This modification is necessary when the size of the particles is less than the electron mean free path in the bulk material. Therefore the effective electron scattering time τ_f is given by a formula involving the scattering time in the bulk τ_0 and a term associated with surface scattering by the particles as

$$\tau_f = 1/\left(\frac{1}{\tau_0} + \frac{2G\mathrm{v_F}}{d}\right), \tag{2.67}$$

where d, $\mathrm{v_F}$ and G are the mean particle diameter, the Fermi velocity of the electrons and a scaling constant, respectively [115]. It has been shown from early work [124] that a good correlation between experiment and theory was realised when the scaling constant, G, was set equal to 1 and has been applied in the present work.

The size dependent particle dielectric function is thus given by

$$\epsilon(\omega, d) = \epsilon_{core} - \frac{\omega_p^2}{\omega^2 + i\omega/\tau_f}, \tag{2.68}$$

where ω_p and τ_f are the free electron plasmon frequency and effective electron scattering time, respectively. ϵ_{core} includes the contribution of the core electrons to the dielectric function, regarded to remain unchanged in the Mie resonance neighbourhood [168, 324, 325]. The real and imaginary parts of the metal particle dielectric function

incorporating the effective electron scattering time are, respectively, given by

$$\epsilon_1(\omega, d) = \epsilon_{core} - \left[\frac{\omega_p^2}{\omega^2 + 1/\tau_f^2}\right] \tag{2.69}$$

and

$$\epsilon_2(\omega, d) = \frac{\omega_p^2}{\omega}\left[\frac{1}{\omega^2 + 1/\tau_f^2}\left(\frac{1}{\tau_0} + \frac{2\mathrm{v_f}}{d}\right)\right]. \tag{2.70}$$

The optical absorption spectra of Au MNP implanted in several transparent materials [249, 326] have been observed to have a large absorption background that rises toward the shorter wavelength. It is very likely that this background originates from defect induced absorption. To take into account a background arising from a wide range of defects absorbing in the same spectral region an expression of the form

$$\frac{k_1}{\lambda_0} + \frac{k_2}{\lambda_0^2} + \frac{k_3}{\lambda_0^3}, \tag{2.71}$$

where k_1, k_2 and k_3 are fit parameters, is added directly to equation 2.61, which describes the extinction due to the MNP in a host medium. Equation 2.71 provides an appropriate baseline and hence an accurate fitting to the FWHM of the colloid band. From the experimental data the MT is used predict the MNP mean diameter (d) and the metal ion volume fraction (p) in the implanted layer. A value for the host dielectric constant (ϵ_h) also emerges from the fitting process. All these fit parameters change with annealing temperature and are obtained when the experimental data and the theory have the best correlation. To attain a good match between the theory and the experimental data higher order terms in the Mie theory (see equations A.16, A.17, A.19 and A.20 in appendix A) may at times be included. The actual procedure of obtaining the best fit parameters is done by a standard least squares fit method and begins with simulations using reasonable physical values to a point where the experimental features are almost attained. This is repeated until the deviation function of the standard least squares method and hence the incremental change in the best fit parameters is negligible. Table 2.1 shows the numerical values of the bulk metal properties used in the fitting process.

The values of the mean free path, l, for Au and Ag have been obtained from published literature values [327, 328, 329] of their effective electron masses [327, 330]. Values of ϵ_{core} for Ag and Au used are 5.0 [324] and 9.9 [325], respectively.

Element	l (nm) (273 K)	$v_F \times 10^8$ cm/s	$\omega_p \times 10^{16}$ s^{-1}
Ag	42	1.38	1.3
Au	13	1.39	1.3
Mg	17	1.58	1.63

Table 2.1: Details of the values of the mean free path, l, Fermi velocity, v_F, and the plasma frequency, ω_p, used in the calculations.

2.6 Determination of the Linear Optical Constants of Thin Film Materials on a Substrate

2.6.1 Introduction

The systems of a bare substrate and a film-on-substrate are discussed. For the case of a multilayer system and others the text by Heavens and Smith [279] may be consulted. Measurement of transmittance has traditionally been used in studying the optical behaviour of thin film materials in general in the field of opto-electronics and will be used in the present work.

2.6.2 Bare Substrate and Film-on-Substrate Systems

This discussion is a summary from the work presented by Swanepoel [331] in which the film and the substrate are assumed to be uniform, homogeneous, isotropic and have finite dimensions. It is also assumed that the incident light has negligible bandwidth and it impinges normally on the system with the surrounding medium as air whose real part of the refractive index n_0 is 1. The general case of an absorbing film with thickness L_1 on an absorbing substrate of thickness L_2 is depicted in figure 2.7.

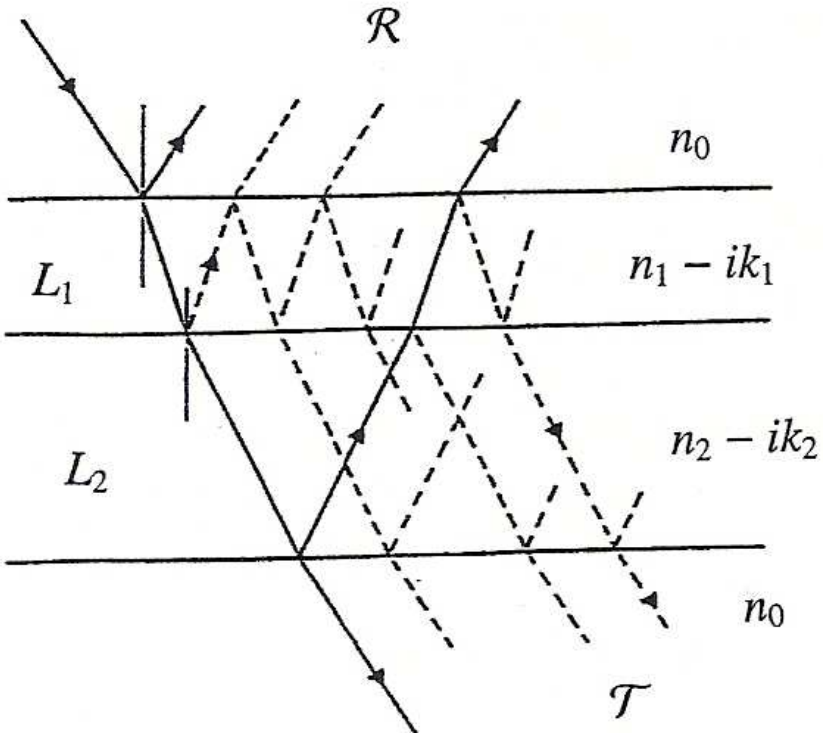


Figure 2.7: Schematic diagram of transmission ($\mathcal{T}$) and reflection (R) of a film-on-substrate system. L_1 and L_2 are the thickness of the film and substrate, respectively.

The layers are optically characterized by their respective complex indices of refraction

$$\begin{aligned} \boldsymbol{n_1} &= n_1 - \boldsymbol{i}\kappa_1 \\ \boldsymbol{n_2} &= n_2 - \boldsymbol{i}\kappa_2. \end{aligned} \tag{2.72}$$

The reflection at interfaces are determined by the complex Fresnel coefficients $\boldsymbol{r}$ and reflectances $\mathcal{R}$, which for normal incidence are given by [332]

$$\begin{aligned} \boldsymbol{r_{ij}} &= \frac{\boldsymbol{n_i} - \boldsymbol{n_j}}{\boldsymbol{n_i} + \boldsymbol{n_j}} = r_{ij} + \boldsymbol{i}r'_{ij}, \\ r_{ij} &= \frac{(n_i^2 - n_j^2) + (\kappa_i^2 - \kappa_j^2)}{(n_i + n_j)^2 + (\kappa_i + \kappa_j)^2}, \\ r'_{ij} &= \frac{2(n_i\kappa_j - n_j\kappa_i)}{(n_i + n_j)^2 + (\kappa_i + \kappa_j)^2}, \\ \mathcal{R}_{ij} &= r_{ij}^2 + {r'_{ij}}^2. \end{aligned} \tag{2.73}$$

The propagation of an electromagnetic wave with wavelength λ through layer j with thickness L_j is characterized by its complex phase angle, Θ_j. It is convenient to define a real phase angle δ_j, absorption coefficient α_j and the quantity $\mathcal{A}$ which measures the absorption as follows :

$$\begin{aligned} \widetilde{\Theta}_j &= \delta_j/2 + i\alpha_j L_j/2, \\ \delta_j &= 4\pi n_j L_j/\lambda, \\ \alpha_j &= 4\pi\kappa_j/\lambda, \\ \mathcal{A}_j &= \exp(-\alpha_j L_j). \end{aligned} \tag{2.74}$$

The determination of the optical constants involves solving the appropriate equations from the experimental values of transmittance and reflectance. Because these equations are generally nonlinear, computer programmes such as Newton iteration may be employed. The formulation of the expressions is such that the layer thicknesses, L, are embedded as products (nL) and (κL), in the quantities δ and $\mathcal{A}$ respectively in the equations. Here, n and κ are the real and imaginary parts of the refractive index, respectively. The equations should thus be solved for n and $\mathcal{A}$ while the determination of L requires special treatment.

In the field of opto-electronics, films usually have thicknesses $L_1 > \lambda/n_1$ and if the substrate is thick and non-uniform thus minimizing the effects of multiple reflections, the transmission and reflection spectra have a sinusoidal nature with one fundamental frequency $2n_1L_1$ in wave number space. Smooth envelopes may be constructed around the extrema of these spectra [333]. Figure 2.8 [331] shows these extrema which represent the loci of points on the spectra where δ_1 is an integer multiple of π. In this case where $n_1 > n_2$, $\mathcal{T}_+$ and $\mathcal{T}_-$ represent maximum and minimum transmittance respectively. The use of the envelopes ($\mathcal{T}_+$ and $\mathcal{T}_-$) and their expressions are particularly useful since they are smooth curves and the periodic behaviour has been eliminated. The appropriate experimental procedure is to obtain the transmission spectrum of the

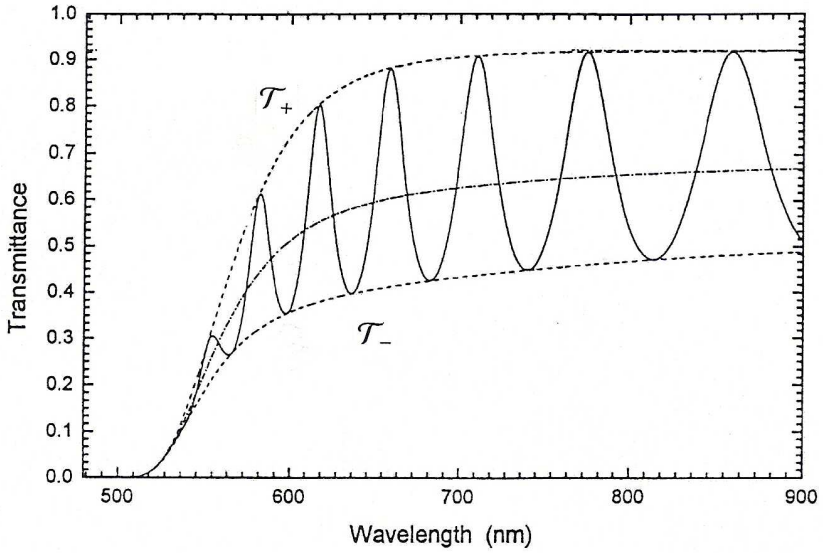


Figure 2.8: Schematic diagram showing interference spectra and the smooth envelopes $\mathcal{T}_+$ and $\mathcal{T}_-$ [331].

substrate alone and then calculate $n_2(\lambda)$ and $\mathcal{A}_2(\lambda)$ which are the refractive index and a measure of the absorption in the substrate, respectively. The values of L_1, $n_1(\lambda)$ and $\mathcal{A}_1(\lambda)$ are then determined from the transmission spectrum of the film-on-substrate, using the predetermined values of $n_2(\lambda)$ and $\mathcal{A}_2(\lambda)$ [331].

2.6.3 Characterizing the Substrate

In the transparent region ($\mathcal{A}_2$=1), $n_2(\lambda)$ may be solved directly from the transmittance of the substrate [331], $\mathcal{T}_2$, using

$$n_2(\lambda) = \left[1 + (1 - \mathcal{T}_2^2)^{1/2}\right] / \mathcal{T}_2, \tag{2.75}$$

else $n_2(\lambda)$ is solved from the following expression

$$\mathcal{T}_2 = \frac{(1 - \mathcal{R}_{02})^2 \mathcal{A}_2}{1 - \mathcal{R}_{02}^2 \mathcal{A}_2^2}, \tag{2.76}$$

where

$$\mathcal{R}_{02} = \frac{1 - n_2}{1 + n_2}. \tag{2.77}$$

The values of $n_2(\lambda)$ may be calculated over a range of values of λ where the substrate is transparent and the values fitted to the Cauchy relation for extrapolation to other regions. The Cauchy relation is written as :

$$n_2(\lambda) = b_4/\lambda^4 + b_2/\lambda^2 + b_0, \tag{2.78}$$

where b_0, b_2 and b_4 are fit parameters. In the region where the substrate becomes absorbing the values of $\mathcal{A}_2(\lambda)$ can be calculated by solving equation 2.76 to yield:

$$\mathcal{A}_2 = -\frac{(1-\mathcal{R}_{20})^2}{2\mathcal{T}_2\mathcal{R}_{20}^2} + \left[\left(\frac{(1-\mathcal{R}_{20})^2}{2_{\mathcal{T}}2\mathcal{R}_{20}^2}\right) + \frac{1}{\mathcal{R}_{20}^2}\right]^{1/2}, \tag{2.79}$$

where

$$\mathcal{R}_{20} = \frac{n_2 - 1}{n_2 + 1}. \tag{2.80}$$

The thickness (L_2) of the substrate is measured with a micrometer and hence its absorption coefficient, $\alpha_2(\lambda)$, obtained from $\mathcal{A}_2(\lambda)$.

2.6.4 Characterizing the Film.

In the case of a transparent substrate ($\mathcal{A}_2 = 1$) the expressions for the envelopes around the transmission spectra [331] are given by

$$\mathcal{T}_{\pm} = \frac{B_1\mathcal{A}_1}{B_2 \pm B_3\mathcal{A}_1 + B_4\mathcal{A}_1^2}, \tag{2.81}$$

where

$$\begin{aligned} B_1 &= 16n_1^2n_2, \\ B_2 &= (n_1+1)^3(n_1^2 - n_2^2), \\ B_3 &= 2(1-n_1^2)(n_1^2 - n_2^2), \\ B_4 &= (n_1-1)^3(n_1 - n_2^3). \end{aligned} \tag{2.82}$$

In the region where both the film and substrate are transparent, the refractive index of the film (n_1) may be calculated from the envelope $\mathcal{T}_-$ as

$$n_1 = \left[\mathcal{M} + (\mathcal{M}^2 - n_2^2)^{1/2}\right]^{1/2}, \tag{2.83}$$

where

$$\mathcal{M} = 2n_2/\mathcal{T}_- - (n_2^2 + 1)/2. \tag{2.84}$$

In the region where the film is absorbing but the substrate is transparent, n_1 may be calculated from equation 2.81 using both envelopes $\mathcal{T}_+$ and $\mathcal{T}_-$:

$$n_1 = \left[\mathcal{N} + (\mathcal{N}^2 - n_2^2)^{1/2}\right]^{1/2}, \tag{2.85}$$

where

$$\mathcal{N} = 2n_2\left((\mathcal{T}_+ - \mathcal{T}_-)/\mathcal{T}_+\mathcal{T}_-\right) + (n_2^2 + 1)/2. \tag{2.86}$$

The thickness of the film (L_1) can be determined from the values of λ_e, wavelength at the extrema, using the standard interferometric equation

$$2n_1L_1 = m\lambda_e, \tag{2.87}$$

where m is the interference order number. The best estimate of L_1 is obtained when the statistical standard deviation from its average value is at a minimum. Once L_1 is known, more accurate values of $n_1(\lambda)$ can be calculated using the values of λ_e and the order numbers, m, of the interference patterns. The values of n_1 can similarly be fitted to the Cauchy relation (equation 2.78) to obtain the values of n_1 in the region of strong absorption. The transmission spectrum can be used to determine $\mathcal{A}_1(\lambda)$ using,

$$\mathcal{A}_1 = \frac{B_5 - B\mathcal{T}_7}{2\mathcal{T}B_8} \pm \left[\left(\frac{B_5 - \mathcal{T}B_7}{2\mathcal{T}B_8}\right) - \frac{B_6}{B_8}\right]^{1/2} \tag{2.88}$$

where

$$B_5 = (1 - \mathcal{R}_{01})(1 - \mathcal{R}_{12})(1 - \mathcal{R}_{20})\mathcal{A}_2,$$

$$
\begin{aligned}
B_6 &= 1 - \mathcal{R}_{12}\mathcal{R}_{20}\mathcal{A}_2^2, \\
B_7 &= 2r_{01}r_{12}(1 - \mathcal{R}_{20}\mathcal{A}_2^2)\cos\delta_1, \\
B_8 &= \mathcal{R}_{01}(\mathcal{R}_{12} - \mathcal{R}_{20}\mathcal{A}_2^2), \\
\mathcal{R}_{01} &= \frac{1 - n_1}{1 + n_1}, \\
\mathcal{R}_{12} &= \frac{n_1 + n_2}{n_1 + n_2}.
\end{aligned} \tag{2.89}
$$

2.7 The Rutherford Backscattering Technique

2.7.1 Introduction

The discussion of the theory of Rutherford Backscattering Spectrometry (RBS) that follows has been summarised from a standard text [5] and the Handbook of Modern Ion Beam Materials Analysis [334]. RBS is a useful technique for an accurate determination of stoichiometry, elemental areal density and impurity distribution in materials. This technique makes use of light ion beams in the MeV energy range. Measurement of the number and energy distribution of backscattered ions from atoms in the surface and near-surface region of the material allows identification of the atomic masses and the depth distribution of the target elements.

Consider an ideal case of a two element (A_mB_n) thin film of uniform composition on a low-mass substrate. The incident ions scatter elastically from the target atoms with energies characteristic of the mass of the latter. The ions also lose energy passing in and out of the material. Energy analysis of the backscattered ions yields a backscattering spectrum in the form of counts per channel versus channel number. The channel number is linearly related to the backscattered ion energy. The peaks A_B and A_A result from the energy loss of the ions in the material (see figure 2.9). The elements *i* in the material may be identified using the *i*th measured energies E_1^i of the high energy sides

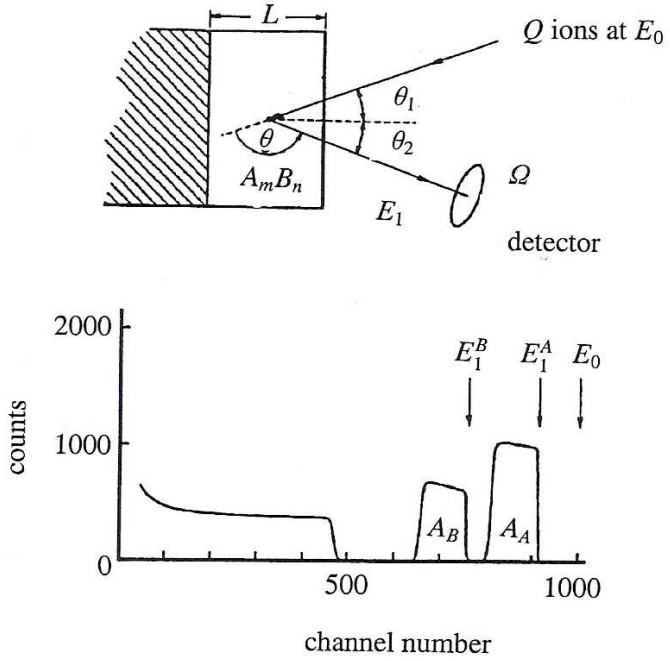


Figure 2.9: The geometry and typical backscattered energy spectrum of a heavy thin film on a lighter substrate. The peaks are due to scattering of the incident ions by the two different elements that constitute the material under investigation. Taken from the Materials Research Society Handbook, 1995 [334].

of the peaks and the kinematic factor for the *i*th element is given by

$$\boldsymbol{k}_i \equiv E_1^i/E_0, \tag{2.90}$$

and has been determined to be

$$\boldsymbol{k}_i = \left[\frac{(M_i^2 - M_1^2 \sin^2\theta)^{1/2} + M_1 \cos\theta}{M_1 + M_i}\right]^2, \tag{2.91}$$

where E_0 is the incident energy and θ the scattering angle in the laboratory frame of reference. M_1 and M_i are the masses of the incident and target particles, respectively. Since M_1, E_0 and θ are known, M_i is determined and the target element identified.

The areal density, $(NL)_i$, defined as the number of atoms per unit area, may be determined for the *i*th element by knowing the detector solid angle, Ω, the integrated

count under peak A_i, for Q incident ions, and the cross section $\sigma_i(E,\theta)$ using

$$(NL)_i = \frac{A_i \cos\theta_1}{Q\Omega\sigma_i(E,\theta)}, \tag{2.92}$$

where N_i is the atomic density (number of atoms per unit volume) of the ith element, Q the number of incident ions, L is the physical film thickness and θ_1 is the angle between the incident beam and the sample normal.

Since the Rutherford backscattering technique was only used investigate the spatial uniformity of the implanted spot, a more detailed discussion than already presented has not been provided but may be found in standard texts on this subject [5, 334].

Chapter 3

Experimental Techniques

3.1 General Introduction

This chapter describes the major equipment used in the present work. They include the ion implanter, and the Cockcroft-Walton and tandem accelerators, which are all located at the Schonland Institute of Nuclear Sciences (SRINS) at the University of the Witwatersrand (Wits) now designated IThemba LABS (North) since the transfer to their ownership. Important items of equipment located at other sites are also described, while specific techniques used for the preparation of samples and experimental procedures may be found in the relevant chapters.

3.2 The Cockcroft-Walton Accelerator

The acceleration potential provided by the Cockcroft-Walton transformer, discussed in the next paragraph under this section, is based on the principle of a voltage multiplier circuit. Figure 3.1 shows such a circuit in which the two capacitors are charged through the rectifiers in different half-cycles by the alternating power supply. Assuming that no current is drawn, the voltage across the output capacitor is the sum of the output alternating voltage and the dc charge of the first capacitor, which becomes essentially twice the peak input voltage after sufficient charging period. The capacitors are therefore charged in parallel to a common potential, but the output voltage is obtained in series.

This facility uses a simple form of acceleration, namely a charged particle moving through a constant potential difference $\mathcal{V}$. If the particle has a charge q, it will

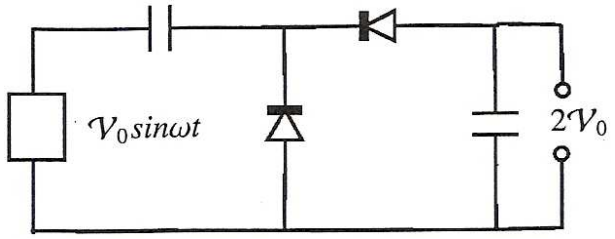


Figure 3.1: Circuit diagram of a voltage multiplier.

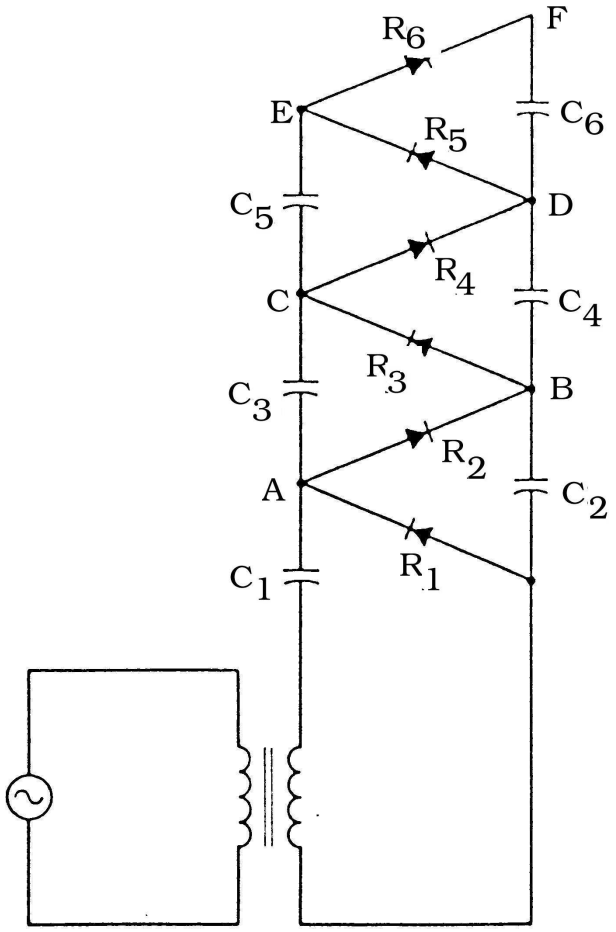


Figure 3.2: Schematic diagram of the Cockcroft-Walton high voltage transformer.

acquire a kinetic energy $q\mathcal{V}$. The potential is provided by a Cockcroft-Walton high voltage transformer (see figure 3.2). The switching between the series and parallel connections is accomplished by means of rectifiers. The secondary voltage from the trans-

former is $\mathcal{V}(t) = \mathcal{V}_0 sin\omega t$, where $\mathcal{V}_0$ in the present case is of the order 100 kV and the capacitor-rectifier array has 14 stages. The charging of the capacitors is done through large resistors (not shown) such that the *RC* time constants are large as compared to the time ω^{-1} that characterizes the variation of the transformer voltage. After sufficiently long time, when the capacitors have become charged, capacitor C_1 is charged to voltage $\mathcal{V}_0$, and thus the voltage at point A varies sinusoidally between 0 and $2\mathcal{V}_0$. With the forward conducting of rectifier R_2, point B eventually reaches a constant potential of $2\mathcal{V}_0$, this same potential of $2\mathcal{V}_0$ is imposed on point C by the rectifier R_3 and thus the AC potential at point C varies between $2\mathcal{V}_0$ and $4\mathcal{V}_0$. The rectifier R_4 then fixes the potential at point D to the constant value of $4\mathcal{V}_0$, as capacitor C_1 charges to a voltage $2\mathcal{V}_0$. This chain can be continued to higher potentials limited only by the ability of the high-voltage terminal to maintain its potential without an electrical discharge to the surroundings. In practice there is a reduction in potential of voltage because some of the charge is drained as current by the beam, and each cycle of the applied voltage $\mathcal{V}(t)$ restores the lost charge in the steady state. The voltage at the end of the chain is applied to the acceleration tube and repels the positively charged gas ions.

Figure 3.3 shows a schematic diagram of the proton accelerator used in this work. The tank is filled, to about 6 atmospheres, with a mixture of dry carbon and nitrogen gases which prevents high voltage electrical discharge in the tank. The beamline has three main vacuum pumps which evacuate three different isolated regions. This ensures that a breakdown in any of the three regions can be handled separately without affecting the other two. A radio frequency ion source near the high voltage end of the tank ionizes the input gas allowing positive ions to be accelerated down the beamline. There are four gas bottles containing hydrogen, deuterium and helium that can be used to produce H_2^+, D^+, $^3He^+$, $^4He^{++}$ ion beams respectively. Accelerated ions are magnetically focused by the vertical quadrupoles to pass through to the analyzing magnet which selects the desired ion mass and energy. The selected ions pass through the image slits and are

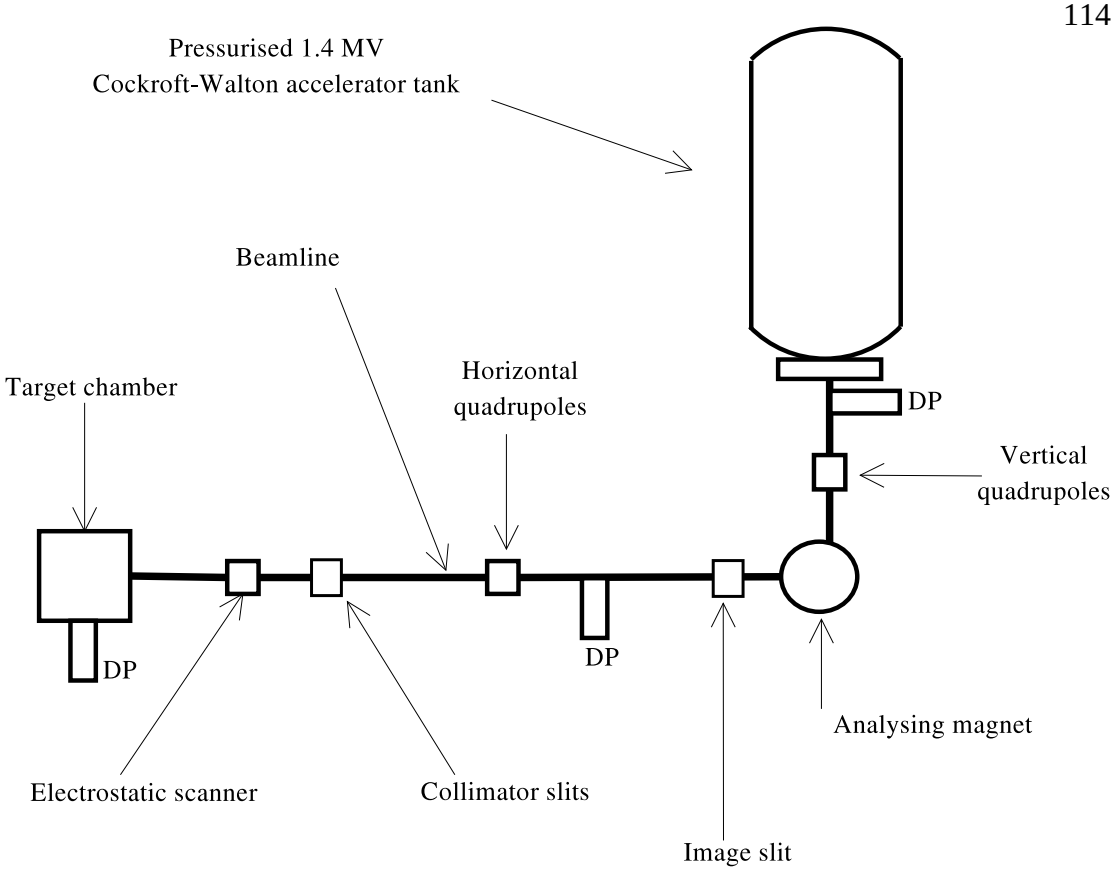


Figure 3.3: Block diagram of main features of the Cockcroft-Walton accelerator (DP stands for diffusion pump).

then focused by the horizontal quadrupoles through to the collimator slits. Electrostatic scanning, available on the beamline after the collimator slits, is used to deflect the beam in two perpendicular directions using two power supplies with variable voltage output giving rise to the desired spatially uniform pattern. The beam is then allowed to pass through a sample collimator in the target chamber and finally onto the target.

The target chamber is electrically isolated from the rest of the beamline. Target current is measured using the leakage current from the target chamber, which acts as a Faraday cage. The sample is held near the centre of the chamber by a holder that can be displaced by up to 2 mm vertically and horizontally from the beam axis. Built in electrical leads are provided, which may be used to connect a heater to a sample holder,

should there be a need to perform experiments at temperatures above ambient.

3.2.1 Production of a Proton Beam

The production of a proton beam begins by producing a specific field by means of the analyzer magnet. The current (35 A for protons) needed to create the field is chosen from an existing calibration that relates the atomic number to the magnetic field that bends the beam through the desired path. Cooling water connected to the analyzer magnet is turned on for protection due to heating that may damage the magnet itself, associated wiring and electronics because of the large currents used. As a precautionary measure, safety interlocks are installed to disable the operation of the high voltage generator in case the cooling water is not turned on. The ionized hydrogen gas supply is turned on and the high voltage is then slowly increased until the required beam energy is attained. The accelerator is then left for about 1 hour to allow stabilization of the electronics and the accelerating voltage.

A fluorescing ceramic sheet located after the electrostatic scanner is used to view the beam spot and hence monitors the adjustment of spatial uniformity and beam area. The beam may then be allowed to fall on the target through the previously selected sample collimator of a suitable size. In the present case a circular sample collimator with a diameter of 6 mm was used. With a known size of the sample collimator (hence the irradiated area) and the target current, the required fluence (D), in ions/cm^2, may be determined by the following equation,

$$D = \frac{it}{\text{Area} \times e \times q}, \tag{3.1}$$

where i, t, e and q are the target current, the time, the electronic charge and the ion charge state, respectively. The Cockcroft-Walton accelerator was used in the present work to implant and irradiate CsI crystals and tin-doped indium oxide films with various fluences of 1 MeV protons as reported in chapters 4 and 7, respectively.

3.3 Higher Energy Accelerators

3.3.1 The Van de Graaff Generator and Accelerator

When a charged inner conductor and a hollow outer conducting shell are placed in electrical contact, all the charge from the inner conductor will flow to the outer one, regardless of how much charge resides there already or how high the potential of the outer conductor (see figure 3.4). The resulting potential ($\mathcal{V}$) on the outer conductor is determined by its capacitance (C) with respect to the grounded surroundings by $\mathcal{V} = Q/C$, and in principle the potential increases without limit as more charge (Q) is added. In practice, a limit is imposed by the electrical breakdown of the insulating column that supports the outer conductor or the surrounding atmosphere. This is the physical basis of operation of a Van de Graaff generator.

Like the Cockcroft-Walton accelerator, a Van de Graaff accelerator is enclosed in a tank pressurized with a dry mixture of carbon dioxide and nitrogen in a suitable ratio to reduce electrical breakdown and sparking and hence increase the high voltage

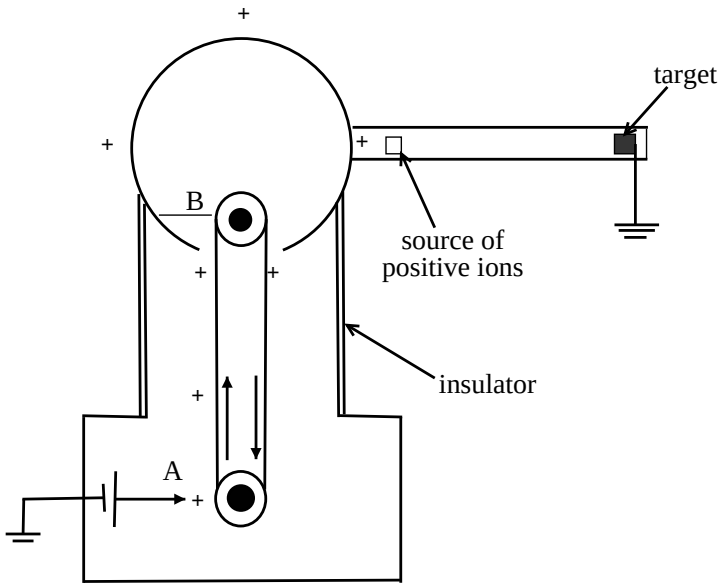


Figure 3.4: Schematic diagram of a Van de Graaff generator and accelerator.

potential. Charge is sprayed onto the belt by a corona discharge at the low voltage side of the accelerator at point A. The charge is transferred to the high voltage terminal by a continuously moving belt, made of insulating material, via a brush at point B. In this type of accelerator the ion source is located inside the pressurized tank. The positive ions from the ion source are repelled towards the target.

The Van de Graaff accelerator provides one important advantage over the Cockcroft-Walton accelerator - the terminal voltage on a Van de Graaff is extremely stable and lacks the AC ripple of the Cockcroft-Walton. The terminal voltages are constant to within 0.1%. The disadvantage of the Van de Graaff accelerator is its low beam current compared to the Cockcroft-Walton.

3.3.2 The Tandem Accelerator

A complete and detailed description of the tandem accelerator is long and therefore the discussion under this section is summarized and limited to the essential features of this facility and in particular to those used in the present work. The tandem accelerator, whose schematic diagram is shown in figure 3.5, is a modification of the standard Van de Graaff. The ion source is placed outside the pressurized tank containing the accelerator. This is an advantage because maintenance and change of source material can be performed without necessarily opening the tank.

The source material is normally embedded in a recess on a specially designed copper cathode in the ion source chamber, from where it is sputtered using a low energy cesium beam. Being the most electropositive element known in the periodic table, cesium readily gives up electrons to the sputtered ions making them negatively charged. The negatively charged ions produced in the ion source chamber are attracted from the low energy (LE) side of the accelerator by the large positive potential at the centre terminal in the tank. Here the ions are passed through a stripper gas that removes electrons and ionizes the ions. The resulting positively charged ions experience a strong

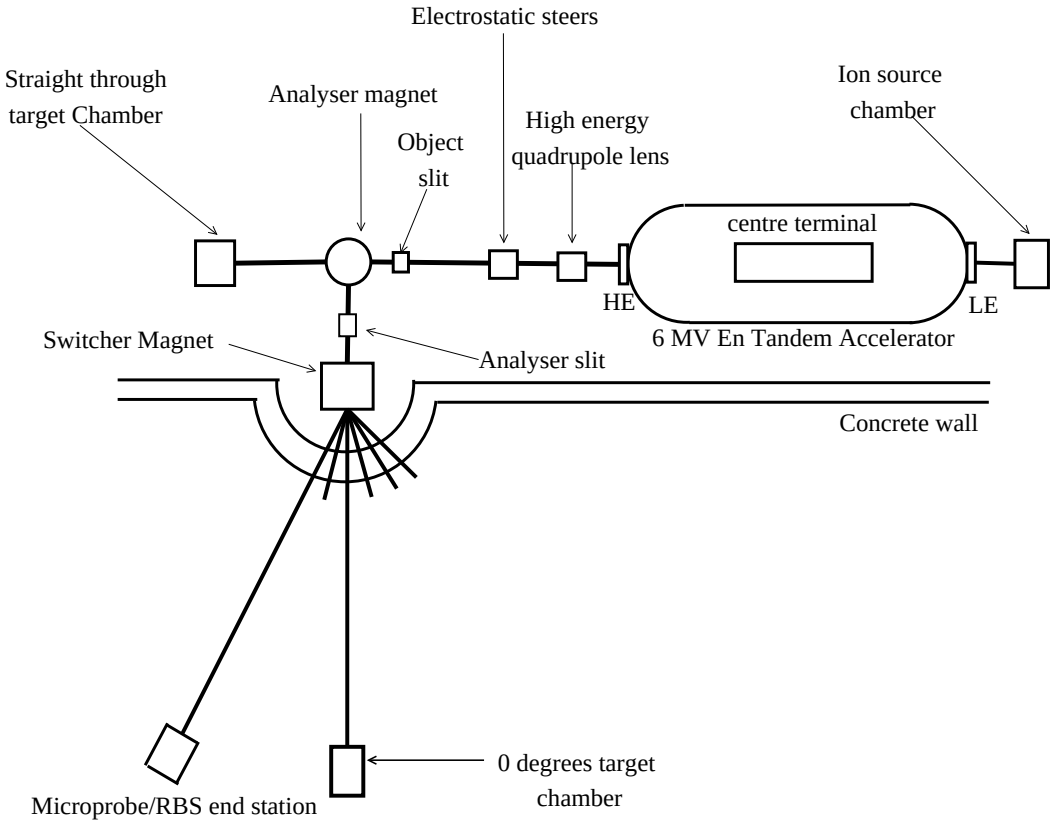


Figure 3.5: Schematic diagram of the main features of the tandem accelerator.

repulsion by the large positive potential at the centre terminal towards the high energy (HE) side of the accelerator. The name tandem accelerator originates from the existence of the two forces experienced by the two different signs of the charge states of the accelerated ions. This principle of the sequential attraction of the negative ions and repulsion of the positive ions is illustrated schematically in figure 3.6. The possibility of the sputtered ions, in the ion source chamber, picking up more than one electron from cesium is small and thus the initial acceleration is the attraction of a singly negatively charged ion by the positive potential, $\mathcal{V}$, at the centre terminal. After emerging from the stripper gas region the net result is a spread of beam energies because of the creation of a variety of different positive charge states by the ionization process. Therefore an ion whose charge state is now $+q$ is repelled by the positive centre terminal and hence

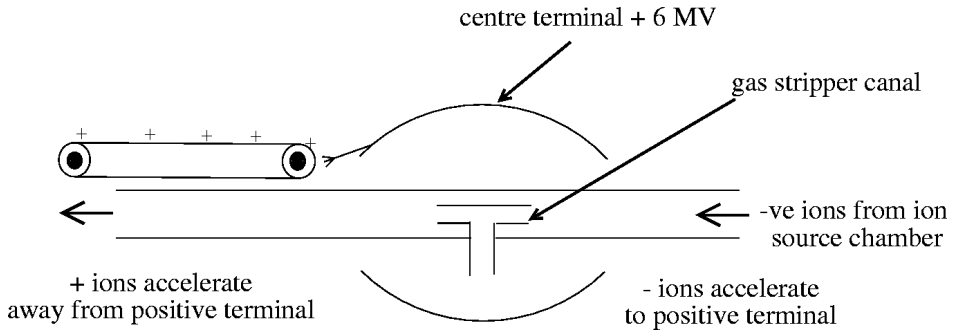


Figure 3.6: Schematic diagram illustrating the attraction and repulsion mechanism at the centre terminal of the tandem accelerator.

acquires a total kinetic energy of $(q + 1)$ eV, where the potential, $\mathcal{V}$, is typically of the order of a few million volts.

3.3.3 Beam Transport

Positive ions have a very short range in matter and therefore the beam lines and the target chamber are maintained under a good clean vacuum to prevent the ions from scattering in collisions with the remnant gas molecules and to prevent the build up of carbon on the sample surface under the irradiated region. The scattering of the ions through large angles would prevent the ions from reaching the target and therefore be removed from the beam. What is also of great significance are small angle deflections, which can lead to the degradation of the beam and thus affect the spatial resolution and divergence of the beam. Ion beams have a natural tendency to diverge and hence the need for focusing devices. Beam transport systems, consisting of a number of electric and/or magnetic devices that focus the beam and bend or deflect it, allow the beam to be transported along the desired path. Such focusing devices are often called lenses. Fig 3.7 above shows an example of a quadrupole lens, which creates magnetic field components in the x and y directions of the form $B_x = by$ and $B_y = bx$, where b is a constant. The beam axis is in the z direction, along which there is no field. The

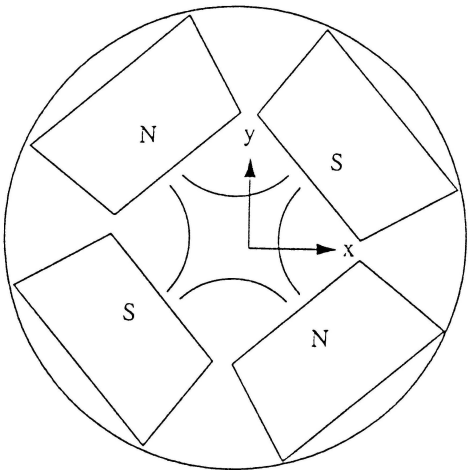


Figure 3.7: Schematic diagram of a quadrupole lens.

components of the Lorentz force $\vec{\mathcal{F}} = q(\vec{v} \times \vec{B})$ are

$$\mathcal{F}_x = -qv_z B_y = -qv_z bx = -kx \tag{3.2}$$

$$\mathcal{F}_y = qv_z B_x = qv_z by = ky, \tag{3.3}$$

Assuming $b > 0$, particles with x displacement experience a strong force toward the x axis and thus deflects the beam along the x direction. In the y direction, the effect is to defocus the beam. If two quadrupole lenses are placed in series, with the second rotated 90^0 relative to the first, then along x and y axes there is both a focusing and defocusing effect but the net effect of the two lenses is to focus the beam.

When the beam leaves the accelerator it is aligned with a set of object slits before entering the analyzer magnet. This magnet is used to select the energy of the beam from the accelerator. This is accomplished in conjunction with an analyzer slit system, which also limit the divergence of the beam, after its exit from the analyzer magnet. The slit edges are oriented so that, at a constant magnetic field, an energy change will deflect the beam onto one slit edge. A suitable feedback circuit maintains the correct terminal potential needed to pass the beam through the analyzer slit system. If the bending capability of the analyzer magnet is not required, the beam can be allowed

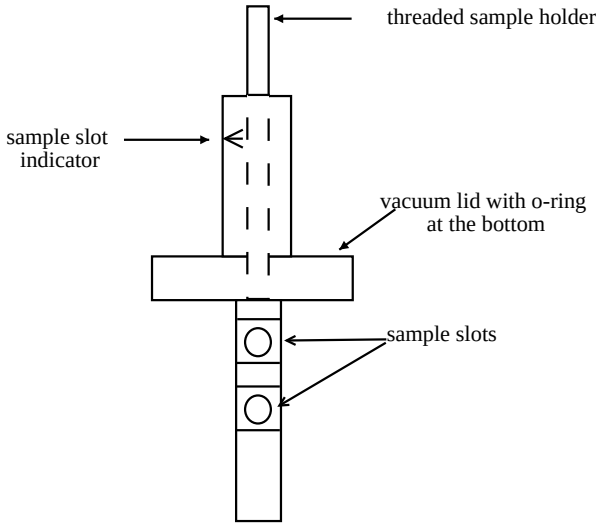


Figure 3.8: A cross-sectional diagram of the sample holder employed in the Au ion implantation using the tandem accelerator.

to enter the straight through target chamber. Otherwise, the beam enters the switcher magnet which is used to select the different beam lines that share the same accelerator. Depending on the experiment being performed, the beam is guided to the appropriate target chamber as shown in figure 3.5.

3.3.4 Target Chamber

For the purposes of the Au implants performed in this work, the straight through chamber of the t accelerator was used to hold the sample. This avoided using the analyzer magnet and increased the beam current so as achieve the required fluence in a realistic period. Electrical connections from this target chamber to the control panel were used to monitor the target current and hence determine of the fluence. Figure 3.8 shows the vacuum compatible sample holder that was used in the present work. This holder has a threaded arm that enables the sample to be lowered or raised relative to the beam axis. The actual position of the sample slot is determined with the aid of an indicator on the threaded arm.

3.4 The Ion Implanter

This discussion is summarized from the manuals of the supplier of model 200-20AF ion implanter. The ion implanter, shown schematically on figure 3.9, is capable of producing high beam currents unlike the accelerators discussed previously. A typical ion implantation period to a fluence of $1x10^{17}$ ions/cm^2, using a scanned beam at a current density of 2 μA/cm^2 over an area of about 28 cm^2, would be less than 4 hours. For the metal ions, used in the present work, a hot tungsten filament was used to vaporize the source material that was placed in a graphite crucible within the ion source chamber. An extraction potential of 20 kV, which is automatically applied when the implanter is switched on, accelerates the ions produced in the ion source chamber towards the analyzer magnet. An atomic mass-current calibration is used to ensure the successful selection of a single or particular species of ions by the analyzer magnet. The analyzer magnet field is maintained at a constant value as the final beam energy is varied over its entire range. This allows very stable magnet operation, minimizing drift and hysteresis effects. The subsequent acceleration potential above the 20 kV extraction potential is provided by the high voltage stack and ions with an energy range of up to 200 kV can be produced.

Following the acceleration, the beam is focused by a quadrupole triplet lens system, before passing through the x, y scanners that sweep the beam across the sample to provide a homogeneous fluence in the following way. The beam is scanned in both the x and y directions by separate voltages with triangular waveforms applied at the deflection plates. The available scanning frequencies, whose ratio is variable, are unsynchronized to prevent path retracing. A beam current integrator, located at the control console, measures the fluence implanted in the sample and closes the beam gate when the desired fluence level is reached. Only when the ion beam is actually required for implantation is it deflected onto the target. When temporarily stopped, the ion beam is

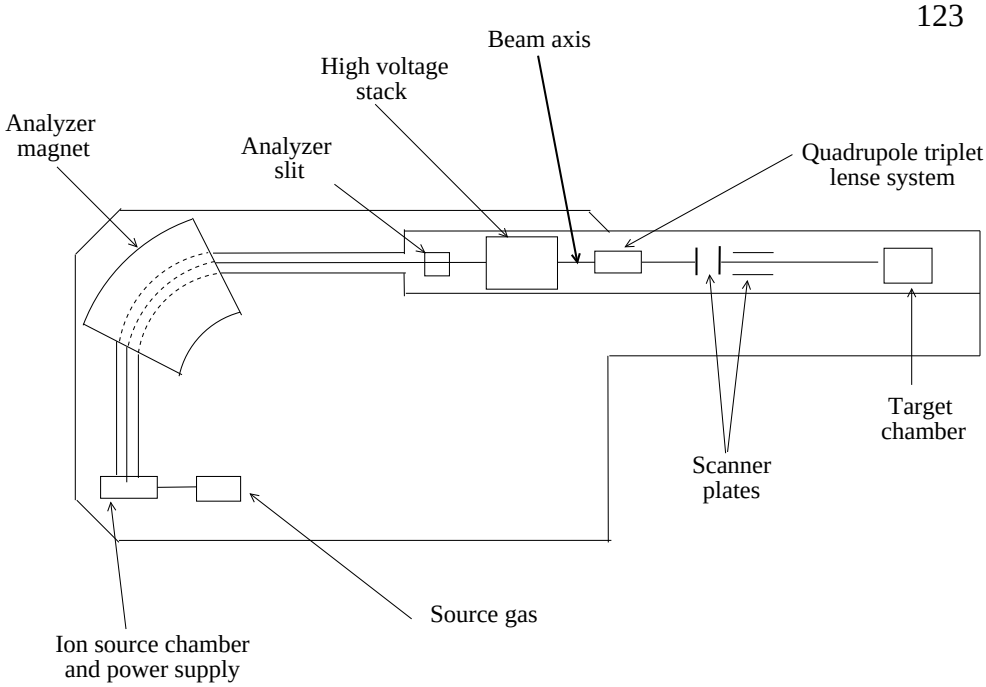


Figure 3.9: Block diagram of the main features of the ion implanter.

deflected off the target by a voltage applied on the scanner plates. Thus, critical beam parameters are unaffected by a constant turning on and off of the beam. Whenever necessary, gases such as carbon tetrachloride, argon or nitrogen were injected into the ion source chamber for stabilization and to assist in the process of ionization of the source atoms.

3.5 Laue X-ray Orientation of the Crystals

The Laue back-reflection X-ray technique was employed to orient certain of the lithium niobate (LN) crystals used in the present work. The spots in the Laue photographic films were matched and interpreted with the aid of standard stereographic projections [335]. Whenever necessary conversion of the (x, y) Cartesian coordinates of a particular symmetry spot to polar angles [336] was made to allow the centering of selected spots.

The X-rays were obtained from a Philips X-ray generator type PW 1008 using a molybdenum anode tube operated at 40 kV and 20 mA. A Laue camera was used to detect and record the diffracted spots. The specimen were mounted on a flat plate of a three stage Anshaw model 3 goniometer using adhesive wax. The goniometer is designed in such a way that it can be transferred from the mounting track on the X-ray machine to a crystal saw (to be discussed shortly), that was used to make vertical cuts on the samples. The 3 arcs of the goniometer were initially set to 0^0 and the goniometer mounted on the appropriate track of the X-ray generator and a Laue back-reflection picture taken. The procedure was to identify the spots corresponding to one of the high symmetry directions i.e. four fold < 100 >; three fold < 111 > and two fold < 110 >. These directions were confirmed with the aid of standard stereographic projections. Once a particular direction was identified, it was centred in the Laue photographic film by the necessary adjustment of the goniometer and a crystal slice was cut. The crystal slice was then checked for misorientation that might have occurred during the cutting process. This was done by mounting one face of the crystal slice on a stainless steel rod with a flat end. Another Laue back-reflection picture was taken to check if the selected plane was still centred. If not, the crystal slice was mounted on a similar brass rod with a face inclined at an angle equal to the correction to be made. The brass rods were made such that they had faces inclined between 1^0 and 3.5^0 in steps of 0.5^0. Once mounted on the appropriate correction rod, polishing (described in section 3.5.2) was carried out to remove the misalignment.

3.5.1 Crystal Sawing

An Anshaw model 7 radial-arm wire saw was used to cut the crystals. It consists of a 0.5 mm diameter diamond impregnated copper wire forming a continuous loop running on two pulleys. The front pulley is designed in such a way that the tension on the wire can be adjusted. The rear pulley is driven by a motor with a variable speed

controller. The pressure of the wire on the sample can be controlled by variable weights mounted on an extension shaft located in the rear pulley. Liquid paraffin was used as the cutting fluid.

3.5.2 Crystal Polishing

The cut crystal slice was mounted using molten BDH wax onto specially prepared brass rods whose faces were either flat or inclined, if a correction was to be made. To attach the crystal slice using the wax, the rods had to be heated to temperatures just sufficient to melt the wax. This was done to prevent the crystals from cracking due to thermal shock. Two stainless steel jigs to hold the brass rods were constructed for polishing crystals; one for hand polishing and the other one for a Kent Mark II polishing machine. Initially, relatively coarse emery paper (grade 360) was used to hand polish the crystal slice to intermediate flatness using the hand jig. Liquid paraffin was used as a lubricant between the emery cloth and the crystal slice. The specimen was subsequently hand polished using various grades of emery paper (360, 400, 600, 800 and 1200). High purity alcohol was used to clean the crystal as it moved from one grade of the emery paper to the next. After polishing with the 1200 emery paper the crystal slice was mounted on the jig on the automatic polishing machine. It was then fine polished in sequence using 6 micron followed by a 1 micron diamond polishing suspension. Once the polishing process was complete, the slice on the polishing rod was slowly brought to the boil in methylated spirit to remove all the wax and polishing fluids and finally cleaned ultrasonically in absolute alcohol.

3.6 Furnaces Used for Annealing

A resistance heated glass tube furnace, at the Physics Department of the University of Zululand (UZ), was used to anneal some of the samples in air. A block diagram of the furnace is shown in figure 3.10a. A typical waiting period of 2 hours was needed

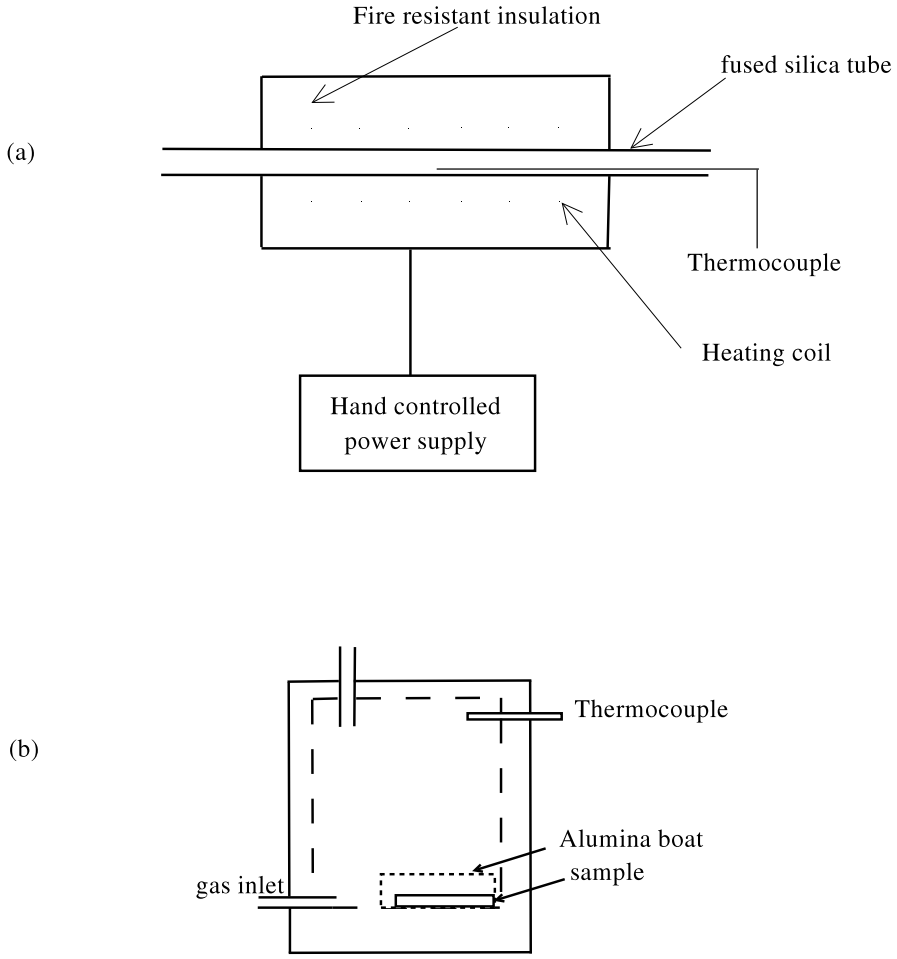


Figure 3.10: (a) Resistance heated tube furnace used in the isochronal annealing process in air. (b) Block diagram of the enclosed Carbolite furnace used in the isochronal anneal under argon gas flow.

to attain temperature stability for this furnace. Another furnace, located at the School of Physics at Wits, was used to perform annealing of other samples. This enclosed Carbolite furnace, fitted with a Eurotherm temperature controller, has the capability of providing an argon gas flow and is shown in figure 3.10b.

Figure 3.11 shows the radiofrequency (RF)-heated fused silica tube furnace [337] used for the annealing of samples under a gentle flow of high purity argon gas. This furnace was employed not only for its capability of heating under argon gas flow but also

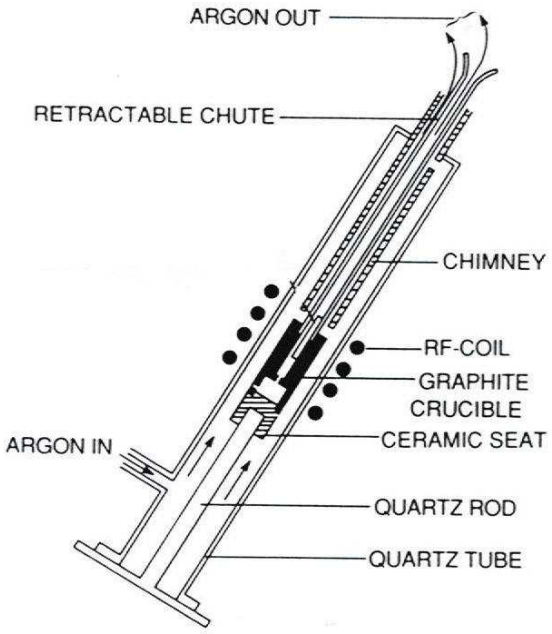


Figure 3.11: Cross-sectional diagram of a RF-heated fused silica tube furnace used in the isochronal sample annealing under gentle argon flow [337].

the possibility of rapidly cooling the sample without exposure to the atmosphere thereafter. This precautions are necessary when dealing with materials composed of reactive elements and the sample temperature has to be brought back to RT in the shortest time. A typical waiting period of 1 hour was required for the furnace to attain temperature stability with the argon flow. The sample was then inserted into the graphite crucible using the retractable chute.

3.7 Optical Absorption Measurements

3.7.1 Introduction

Defects created by the irradiation of crystals have absorption bands that are observed from the near infrared to the ultraviolet range. This makes optical absorption

techniques suitable for the study of such defects. A Cary 500 spectrophotometer in the School of Physics at the University of the Witwatersrand was used to carry out the optical absorption measurements from the 3200 to 175 nm spectral range. A description of its main features is presented in section 3.7.3. A vacuum ultraviolet (VUV) spectrophotometer, whose description is given in subsection 3.7.4 to follow, was employed for measurements in the 330 - 100 nm range. Unless otherwise specified, a virgin crystal or an as-grown thin film was used as a reference in all optical absorption measurements.

3.7.2 The Principle of Optical Absorption

Absorbance (A) and transmittance ($\mathcal{T}$) are defined as

$$A = -log(I/I_0) \tag{3.4}$$

and

$$\mathcal{T} = I/I_0, \tag{3.5}$$

where I_0 is the intensity of the light incident on a sample and I is the transmitted intensity. It is often desirable to compare results from specimens of different thickness and therefore α, the absorption coefficient, is a more useful quantity. It is defined as

$$\alpha = \frac{2.303}{L}A, \tag{3.6}$$

where L is the thickness of the absorber in cm. Therefore α has units of cm^{-1}.

The Smakula equation for a Gaussian absorption band (see equation 2.20) is

$$N = 0.87 \times \frac{10^{17}}{f}\frac{n}{(n^2+2)^2}\alpha_{\max}W, \tag{3.7}$$

where N is the concentration (in cm^{-3}) of the absorbing centres, $\alpha_{\max}$ is the maximum absorption coefficient, n is the refractive index of the medium, W is the full width of the absorption band at half maximum, and f is the oscillator strength. Therefore the

concentration of absorbing centres per cm^3 can be calculated from the maximum absorbance of their associated absorption bands, provided that the defects have a uniform distribution as a function of thickness and the oscillator strength is known.

3.7.3 The Cary 500 Spectrophotometer

The Cary 500 spectrophotometer, located at the School of Physics in Wits, is designed to measure absorption or transmittance and reflectance in the wavelength range 175 - 3300 nm. The schematic details [338] of the design of the instrument are shown in figure 3.12 and a summary of the principles of operation is presented. The light source for the UV region is supplied by a deuterium lamp, while the VIS/NIR region employs a tungsten lamp. The instrument has two detectors. The detector in the UV/VIS region (the range 175-850 nm) is a R928 photomultiplier tube while a Peltier-cooled PbS detector is used in the NIR region (the 800 - 3200 nm range). Light from the tungsten or

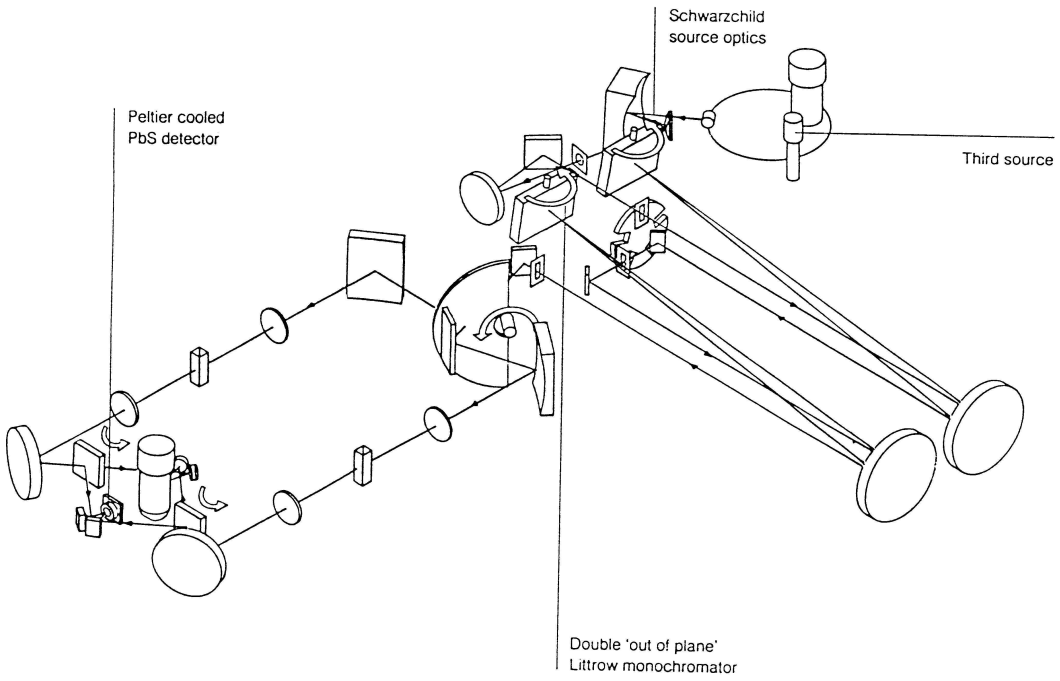


Figure 3.12: Schematic diagram of the main features and the beam path of the Cary 500 Spectrophotometer [338].

halogen lamps is passed through the Schwarzchild source optics (see figure 3.12) from where it is taken through a series of mirrors and then to the double Littrow monochromator, which provides a narrow bandwidth of a selected wavelength. From here the light is passed onto a 50% reflecting mirror and thus split into two equal beams one going to the sample and the other acting as the reference beam. The two beams are then guided by additional optics to the detectors where the signals are electronically compared and using a null-principle, the signal comparison circuitry provides an output voltage such that the ratio (transmittance) or the logarithm of the ratio (absorbance) of the two signals is recorded. The results are displayed on a computer screen using appropriate computer interfacing and software.

3.7.4 The Vacuum UV Spectrophotometer

This is instrument is located at Department of Physics, University of Zululand, South Africa. The essential optical components of the instrument and the sample are all placed in vacuum to eliminate optical absorption from ambient gases in the VUV region. Figure 3.13 [339] shows a schematic cross-sectional diagram of the Rank Hilger E760 single beam vacuum grating monochromator used in the present work. The monochromator is fitted with a sodium salicylate sensitized EMI9558B photomultiplier for use in the VUV region from 330 to 100 nm. The light source for this instrument is a windowless hollow cathode lamp with argon flow. Pressure in the lamp is maintained by differential pumping. The underlying principle of the design is the pivoting of the Rowland circle (designed, by R. W. Ditchburn [339]) about a point O on its circumference, midway between the slits. The entrance X and the exit Y are respectively placed approximately 2 mm in front of and behind the Rowland circle when the instrument is set for zero order. The grating G and the two slits are all on the Rowland circle at one wavelength only. The wavelength drive which moves the grating is manually rotated and the reading of the voltage on the photomultiplier tube control is taken point by point

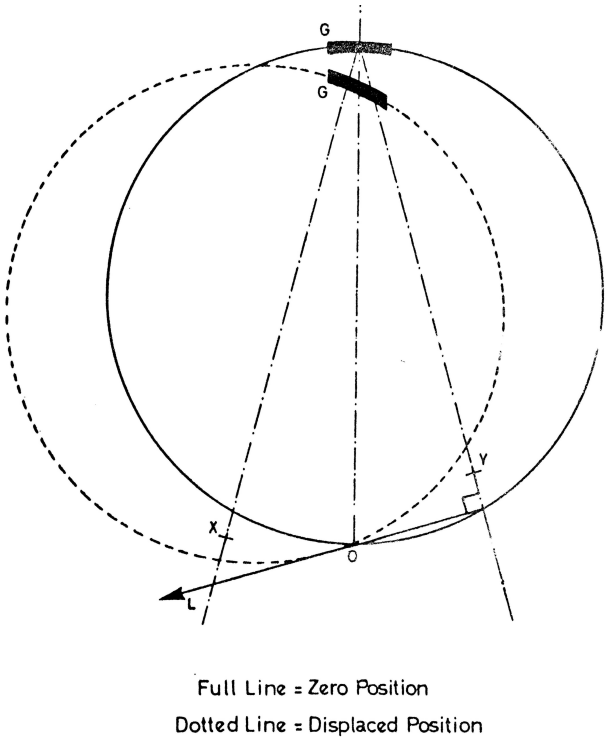


Figure 3.13: Schematic diagram of the monochromator in the VUV Spectrophotometer [339].

for each wavelength individually for the sample and then the reference respectively, as there is only one beam. The two values are then compared using the appropriate formulae and the optical absorption as a function of wavelength for a particular sample is obtained.

3.8 Experimental Setup for the Raman Study

3.8.1 Introduction

This section will provide a description of the Raman spectroscopy system located at the Raman and Luminescence Laboratory at the University of the Witwatersrand. It consists of a Jobin Yvon T64000 Raman triple grating spectrograph, an argon-ion laser used as the excitation source and an optical microscope with a movable stage. A camera

attached to the microscope and the micrometer movements of the stage enable the study of small specimen and analysis on various positions with a single sample.

3.8.2 The Exciting Laser

In the present near-resonance Raman study the laser line of wavelength 488 nm from a Coherent Innova laser was used since its energy sufficiently close to the targeted *V* bands and far away from the *F* band, in the near infrared, to minimise optical bleaching.

3.8.3 The Raman Spectrograph

Grating spectrometers or spectrographs are the standard instruments normally used in analysing the Raman spectra of materials. The major requirements of the spectrometer are good resolution (< 1 cm^{-1}) and a low stray light background. The origin of the stray light background is the internal scattering of the laser excitation light which limits the detection of weak Raman signals close to the intense laser line. The main source of such scattering comes from the gratings. Hence blazed holographic gratings are used due to their low stray light characteristics and the absence of ghosts. The stray light rejection of a single monochromator is not always sufficient for Raman spectroscopy studies. Stray light rejection is improved by using two or more gratings, or by holographic notch filters. A schematic diagram of the Jobin Yvon T64000 spectrograph is shown in figure 3.14.

3.8.4 The Monochromators

The three monochromators of the Jobin Yvon T64000 spectrograph may be used in three different ways : the triple subtractive, triple additive and single modes. Only the first mode, as used in the present work, is discussed. Figure 3.15 shows a schematic

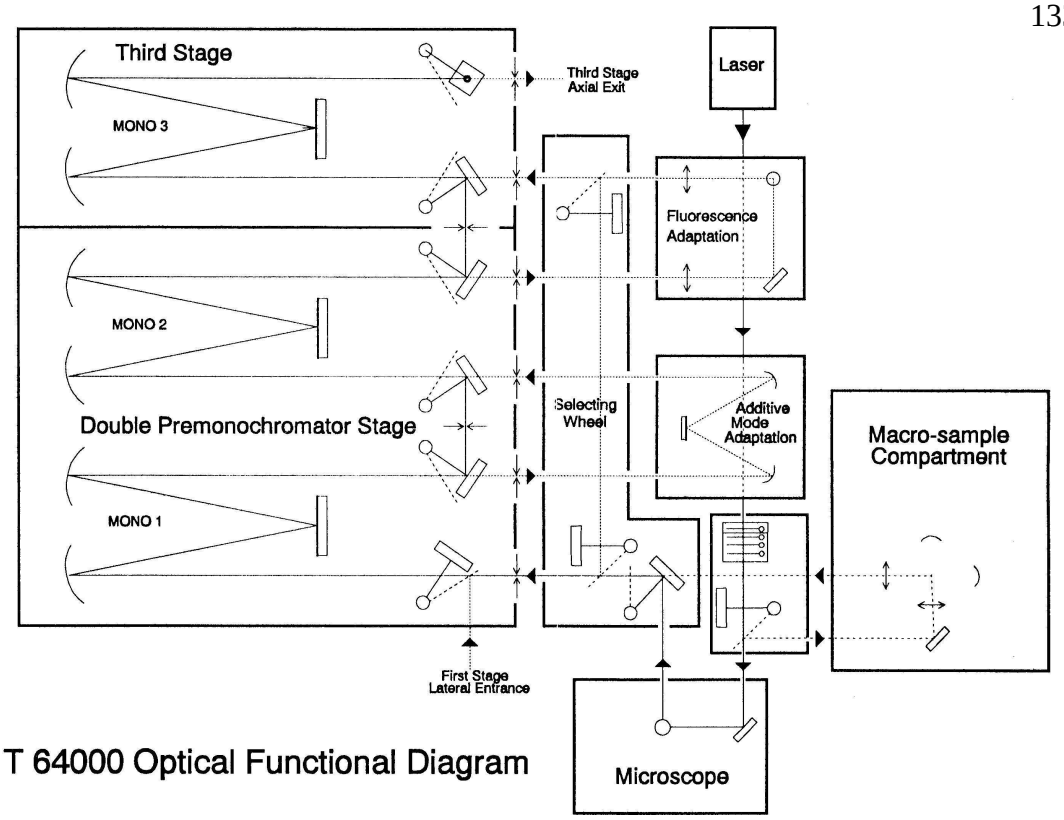


Figure 3.14: Optical diagram of the Jobin Yvon T64000 spectrometer.

of this mode. A polychromatic beam enters the entrance slit (S_1) of the first monochromator and is dispersed by the grating 1. The exit slit of the first monochromator which acts as the entrance slit for the second monochromator selects the bandpass between wavelengths λ_1 and λ_2. All the dispersed beams are recombined by the grating 2 in the second monochromator which is the entrance slit for the third monochromator resulting in a polychromatic beam limited to only the spectral range between λ_1 and λ_2 as shown in this figure. The polychromatic beam selected by the first two monochromators between λ_1 and λ_2 is finally dispersed by the grating 3 in the spectrograph and the spectrum acquired with a multichannel detector which is mounted in the plane of the exit image or with a monochannel detector through an exit slit. This mode rejects the elastically scattered light at the laser wavelength more effectively allowing the measurement

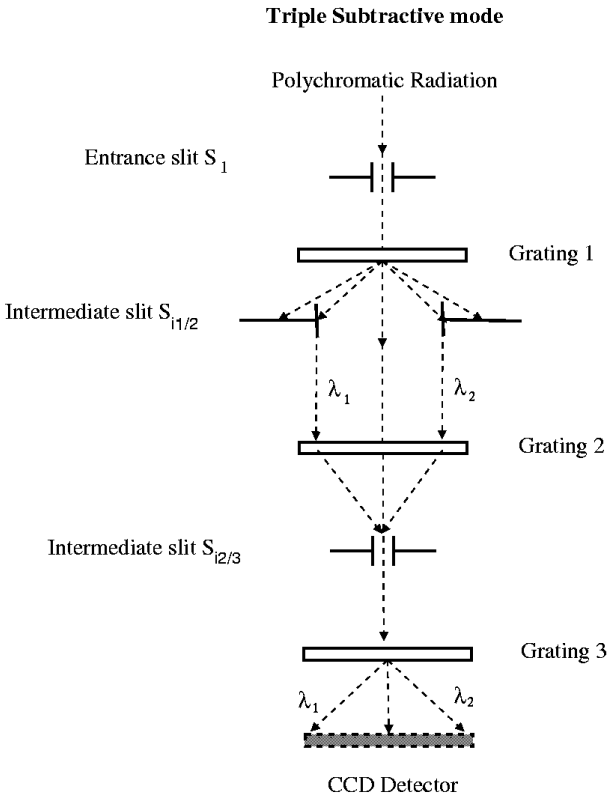


Figure 3.15: The triple subtractive monochromator spectrograph mode. Taken from the manual of the Jobin Yvon model T64000 spectrometer.

of low wavenumber differences.

3.8.5 Gratings

The Jobin Yvon T64000 spectrometer is equipped with two sets of gratings, the 600 grooves (gr)/mm (spectrograph only) and the 1800 gr/mm. The 600 gr/mm and 1800 gr/mm gratings are fixed on a turret in the spectrograph and can be used interchangeably using the software.

3.8.6 Scanning Mechanisms and Spectral Range

The lowest density grating (600 gr/mm) provides the widest spectral range and highest sensitivity, but the lowest resolution. This grating is essential when dealing with samples with weak signals and for large spectral ranges. The 1800 gr/mm grating is more useful in cases where one is looking at narrow ranges and the position of peaks or when the resolution of two adjacent peaks becomes important.

3.8.7 Detectors

The Jobin Yvon T64000 spectrometer employs a multichannel CCD (charge coupled device) detector. The CCD is a rectangular chip with 1024×256 pixels with an active area of 27.64×6.91 mm^2. The spectral resolution of the CCD is limited to one pixel which is about 0.5 cm^{-1} for the 1800 gr/mm grating and 2 cm^{-1} for the 600 gr/mm grating. To provide the best performance to the spectrometer, the CCD is cooled by liquid nitrogen to 140 K. The CCD offers rapid analysis of a spectrum and is ideal for most analytical purposes.

3.8.8 Photon Counting

The output from the detector was analysed by an interfaced PC using software, Spectramax, supplied by Jobin Yvon. This software is used to control all the functions of the spectrometer which includes moving monochromators, changing modes and intermediate slits between the first and second gratings among others. The graphic features of the software enable one to obtain properties such as the peak position, FWHM and the areas under the peaks. It is also possible to export data files in various forms that are compatible with standard commercial software.

3.8.9 Oxford Micro-cryostat

Figure 3.16 shows a cross-sectional view of the Oxford micro-cryostat was used in part of the present work. The specimen under investigation is placed in the sample holder which is aligned with the transparent windows. In normal operation the micro-cryostat is evacuated using a turbo-molecular pump to a vacuum better than 8×10^{-5} Torr before cooling. Further pumping on cooling considerably improves the vacuum to $\approx 2\times10^{-6}$ Torr. Cooling or heating is performed via the heat exchanger and sensor which are connected to an ITC4 temperature controller, from Oxford Instruments, fitted with a digital temperature display. Low temperatures can be attained by the circulation of liquid nitrogen or helium with the help of an external pump unit depending on specific requirements, while those above room temperature require the use of the heater. Intermediate temperatures may be attained by use of both the heater and the circulation of liquid nitrogen or helium. A 10 minute period was always allowed for stabilization after attaining any preset temperature.

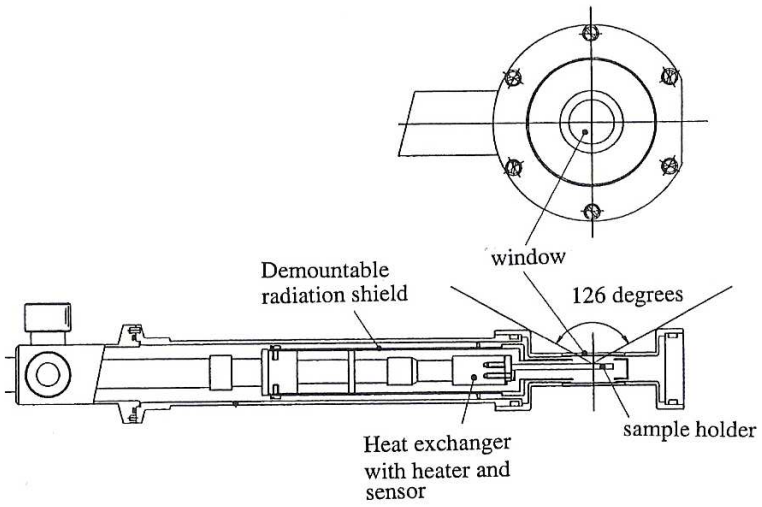


Figure 3.16: Cross-sectional view of the Oxford micro-cryostat. Taken from Oxford Instruments manual.

3.9 The Principles of the X-ray Photoelectron Spectroscopy (XPS)

This section presents an introduction and summary of the X-ray photoelectrons spectroscopy (XPS) technique from the standard texts of Vickerman [340] and Nefedov [341]. This technique is also referred to as Electron Spectroscopy for Chemical Analysis (ESCA). The Quantum 2000 XPS facility used in the present work is located at the Council for Scientific and Industrial Research (CSIR), Pretoria.

In the XPS technique the entire incident photon energy is transferred to an electron bound to an atom leading to ejection from its atomic orbital. The ejection occurs if the energy of the incident photon is larger than the binding energy of the electron to the nucleus. Figure 3.17a schematically illustrates this phenomenon, which is essentially the photoelectric effect [342] and forms the basis of the XPS technique. The core electrons in any atom are obviously more tightly bound in comparison to the valence electrons and an increase in the nuclear charge further increases the binding energy. Therefore all these factors will produce different characteristic electron binding energies for the various atoms in a sample. This means that electron emission from a surface may be traced to a particular atomic species within the solid under investigation.

Figure 3.17b shows the main features of an XPS facility which consists of a monochromatic X-ray source, a detector, magnetic shielding to minimize the effects of external and the earth's fields, and an ultrahigh vacuum chamber. A proper measure of the binding energy of the electrons using the XPS method requires that the sample and detector are at the same potential, normally the ground potential. Accurate values of the energy of the source and work function of the detector also have to be known. Hence

$$KE_{source} = h\nu - BE - \phi_d, \tag{3.8}$$

where BE is the binding energy of the electrons and ϕ_d is the work function of the detector. The XPS technique is therefore an analytical tool that can be used to provide

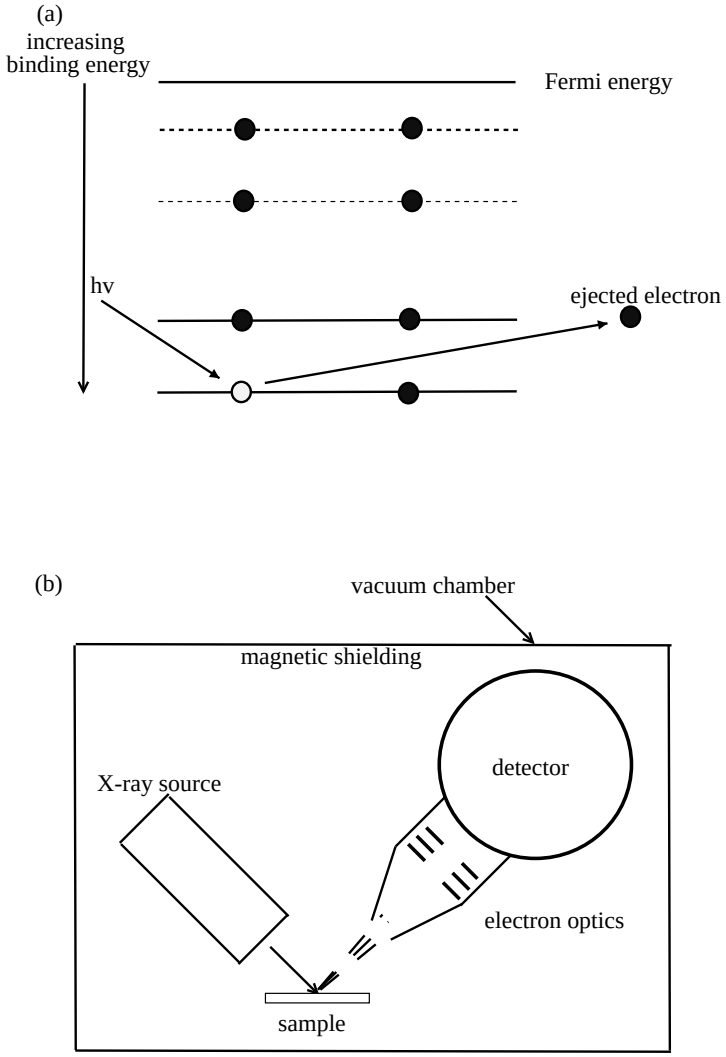


Figure 3.17: (a) Schematic diagram illustrating the removal of a core electron by X-ray photons. (b) Typical XPS technique configuration.

a quantitative elemental analysis of a sample, among other information.

3.10 Transmission Electron Microscopy

3.10.1 Introduction and Principles of Operation

The following general discussion of a transmission electron microscope (TEM) is summarised and some interactions between the incident electron beam and the atoms

within the sample are omitted in order to focus on the description of the interactions relevant to the present work. The Philips CM200 TEM used in the present work is located at the Electron Microscope Unit, Wits. This TEM facility can accelerate electrons to a maximum energy of 197 kV and is equipped with an Oxford ISIS energy dispersive X-ray analyser (EDX) that may be used to determine the elemental composition of a test sample. In an EDX analysis, some of the electrons from the atoms of the sample are removed by an electron beam from the microscope. A position vacated by an inner shell electron is eventually occupied by an outer shell electron via the release of a characteristic X-ray and hence the identification of an atom in the test sample. The crystal structure of a sample may also be investigated by electron diffraction using a focused electron beam.

The samples used in TEM studies are normally made thin enough to enable electrons from the incident beam to pass through them. Figure 3.18 shows a schematic diagram of the interactions employed to study thin samples in TEM. Unscattered electrons are those which pass through the sample without any interaction occurring. The transmission of unscattered electrons is inversely proportional to the sample thickness when the sample is homogeneous. Areas of the sample that are thicker will have fewer transmitted or unscattered electrons and so will appear darker, conversely the thinner areas will have more transmitted electrons and thus will appear lighter on the screen. However, care needs to be taken when heavy impurities are present. The elastically scattered electrons come from the incident electrons that are deflected from their original path by atoms in the sample without loss of energy. They can be used to examine the crystal orientation, atomic arrangements and phases present in the area being examined.

The inelastically scattered electrons are the electrons that interact with atoms in the sample, losing energy during the interaction. They are transmitted through the rest of the specimen and may be used in conjunction with other instrumentation, depending on the type of TEM facility, to obtain information on the composition and bonding state

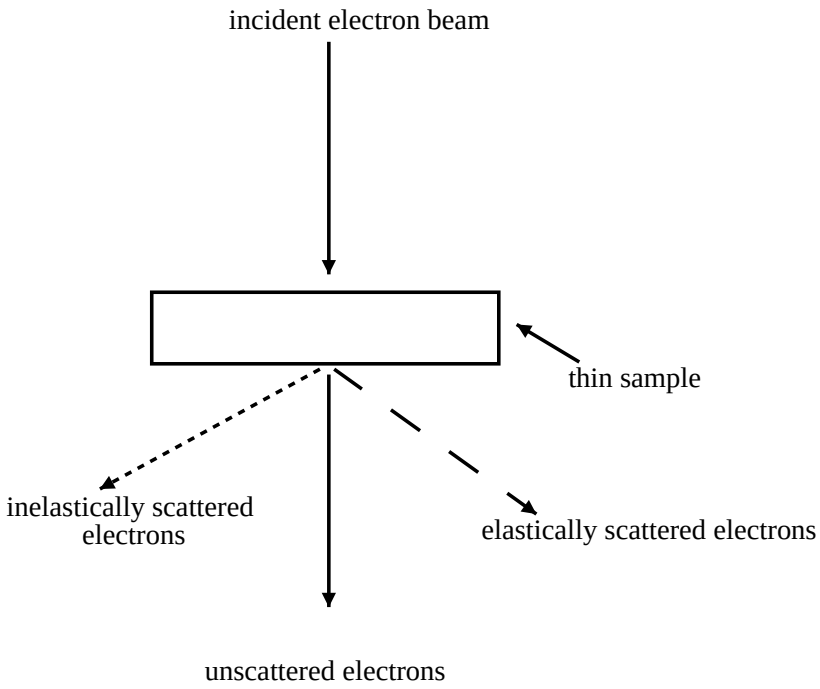


Figure 3.18: Diagram of incident electron-matter interaction.

of each element on the sample area studied.

The main features of a TEM facility are an electron source, normally provided by an electron gun, the necessary optics to focus the electrons and a detector, all in a vacuum chamber. Figure 3.19 [343] shows a typical electronic optical arrangement in a TEM facility used for focusing and other adjustable lenses necessary to obtain good resolution of the images.

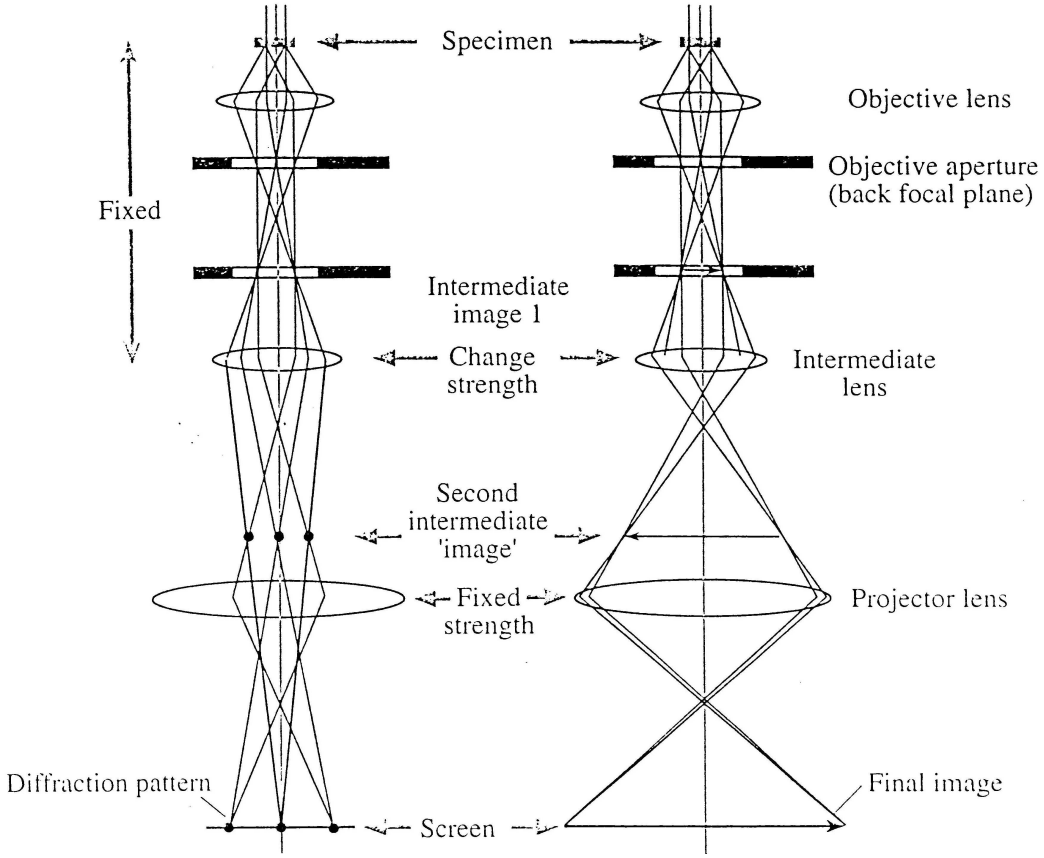


Figure 3.19: Schematic cross-section diagram of the optics used to display an image in a TEM facility [343].

Chapter 4

Optical Properties of Proton Implanted Cesium Iodide Crystals

4.1 Motivation and Scope of Work

A review of the properties and previous work on CsI, section 1.9, indicates that this material has not been widely investigated in as far as irradiation damage is concerned. This could be as a result of the known difficulties encountered in attempting to colour this material. It appears that a high density of electronic excitation is needed to create defects in this material as conventional radiation sources such as X-rays are unsuccessful. With iodides of K and Rb (from the same cation group as Cs in the periodic table) already well studied, the need arises to make comparisons of the nature of the defects as well as the reaction kinetics and activation energy during high temperature annealing of the defects produced by the implantation. This is especially interesting since while the anion remains the same, the size of the cation increases within this group of alkali metals. To the best of the author's knowledge this work represents the first study of the combined use of Raman and optical absorption techniques to investigate defect annealing mechanisms and reaction kinetics in CsI and hence provides new information.

4.1.1 Preparation of the CsI Crystals

A boule of nominally pure CsI crystal was purchased from the Optoelectronics Materials Laboratory, University of Utah, America. CsI crystals are soft and have no known cleavage plane at room temperature. No spots formed on photographic films following the X-ray Laue orientation technique even after several hours of exposure.

Randomly oriented crystal slices of 8×8 mm^2 pieces with thickness of about 2.5 mm were therefore cut from the original crystal boule and polished as described by the techniques discussed in section 3.5. The entire sizing and polishing of the crystal slices had to be done under liquid paraffin because of the high solubility of this material in water and water-based lubricants. Henceforth the future use of the term CsI crystal/sample refers to the crystal slices that have been polished and appropriately sized as described in this subsection.

4.1.2 Implantation and Storage of the Crystals

The CsI crystals have proved difficult to colour after several hours of 60 kV X-ray irradiation and up to 7 days of γ-irradiation by a ^{60}Co source of strength 16.71 TBq, both procedures yielding no discernable radiation-induced optical absorption bands. Other reports of such difficulty have been discussed in section 1.9.1. These radiation sources readily produce irradiation damage in the f.c.c structure alkali iodides [113, 83, 84]. In view of the radiation resistance of CsI to the more conventional sources, 1 MeV proton bombardments were performed at ambient temperature using the Cockcroft-Walton accelerator, described earlier in section 3.2, to implant and colour the crystals. Conducting carbon paste was applied to the sides and one face of the crystals. In each case, the carbon-coated face was in direct contact with the sample holder placed perpendicularly to the beam axis. This ensured that there was good thermal contact hence enabling an accurate determination of the temperature of the crystal and minimising charging effects on the crystal surface. A thermocouple, attached to the crystal surface facing the beam on a region close to the implanted spot, was used to monitor the implantation temperature. The proton beam was collimated by a 4 mm diameter aperture in a thin molybdenum plate. A fluorescing ceramic sheet, normally used for viewing the beam spot, was placed in the beam axis to stop further implantation when the maximum temperature of 300 K was approached. The temperature control

proved to be necessary as it was noted the first run that the crystals would initially show colouration, which would then disappear when the temperature of the crystal rose as result of beam heating.

It was noted that the implanted CsI crystals discolour very rapidly if stored at room temperature, even in a dark desiccator. A glass tube that could be evacuated, filled with high purity argon gas and kept below 273 K was therefore constructed and used to store the crystals whenever the optical and Raman measurements were not being performed. In the experiments, a maximum proton fluence of 6×10^{16} ions/cm^2 was used to ensure that the maximum absorbance achieved remained below 3.5. This ensured that stray light effects arising from very high absorbance values in the optical absorption measurements with the spectrophotometer (see section 4.1.4 below) were avoided.

4.1.3 Annealing of the Crystals

A description of the Oxford micro-cryostat, inside which the annealing was performed, has already been presented in subsection 3.8.9. Special brass plates were constructed to clamp the samples in place to avoid movement during the measurements of the optical absorption, which required the micro-cryostat to be held vertically.

The isochronal annealing cycles were each carried out for 30 minutes at predetermined temperature intervals of 10 K, while the isothermal annealing cycles were performed at 397 K for increasingly varying durations. During a typical isochronal cycle, the crystal was heated to a known temperature for the time indicated and rapidly cooled back to 77 K for measurement. A waiting period of about 10 minutes was allowed for temperature stabilization. Similarly an isothermal annealing cycle involved heating the crystal for predetermined durations at the fixed temperature and thereafter cooled in a similar manner to that for the isochronal cycle.

4.1.4 Optical Absorption and near-Resonance Raman Studies

A Cary 500 spectrophotometer described previously in subsection 3.7.3 was used to perform the optical absorption measurements, while the Raman spectra were measured by the Raman instrument whose features and principle of operation have been discussed in section 3.8. A specially designed holder was constructed to position the Oxford micro-cryostat along the sample beam path in the spectrophotometer. The holder can be translated perpendicular to the beam axis enabling adjustments of position of the micro-cryostat so the spectrophotometer beam passes optimally through the implanted region of the sample. Provisions were also made to allow the holder to be locked onto the base of the spectrophotometer and hence ensure that the force exerted by the bellows of the liquid nitrogen transfer tube did not displace the micro-cryostat away from the sample beam path. One further measure to hold the micro-cryostat included the use of a steel frame placed over the spectrophotometer having arms that clamped the cylindrical part of this cryostat close to be point where transfer tube is connected.

The Oxford micro-cryostat loaded with the sample was placed on a movable stage of the Raman microscope (see section 3.8) for the Raman studies. The reference temperature for the optical absorption and Raman measurements was 77 K unless stated otherwise. From the position of the *V* bands, determined by the optical absorption measurements, the 488 nm laser line was considered suitable as the excitation wavelength, being close to the photon energy range of these bands and hence the near resonance Raman conditions. The laser beam power on the sample was set to 1.5 mW, which was sufficiently low to avoid bleaching of the colour centres. An optical absorption measurement was taken thereafter by transferring the entire setup consisting of the micro-cryostat, temperature controller and the liquid nitrogen circulator onto a movable platform to the location of the Cary 500 spectrophotometer. Subsequent measurements, after annealing to higher temperature and cooling to 77 K, were performed in a similar

manner.

4.2 Discussion of the Results

4.2.1 Typical Optical Absorption and Raman Spectra

Figure 4.1 shows a typical room temperature optical absorption spectrum of a randomly cut CsI sample measured after proton implantation at 77 K. Previous workers [182, 183] have identified the F and F_2 in CsI at 1.68 and 1.1 eV, respectively. It is important to note an unusual feature, namely that the F_2 band is considerably larger than the F band. Several major V bands at 2.7, 3.4 and 4.2 eV are present and will be discussed in more detail in the following sections. The sharp band at 4.2 eV, and

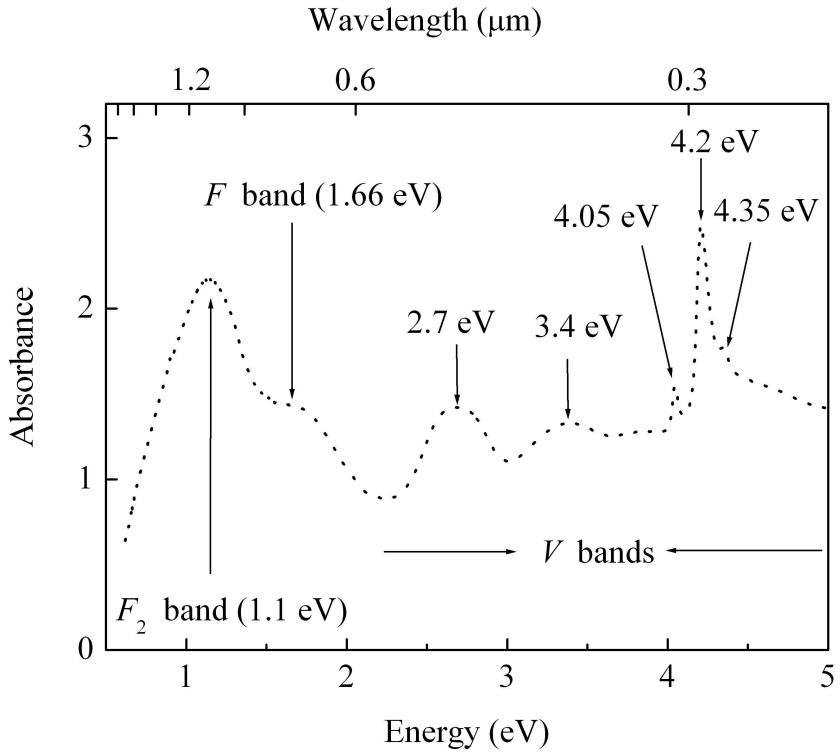


Figure 4.1: Optical absorption spectrum of a CsI sample implanted to a fluence of 6×10^{16} ions/cm^2 at room temperature measured at 77 K. The spectral positions of the F, F_2 and V bands are shown.

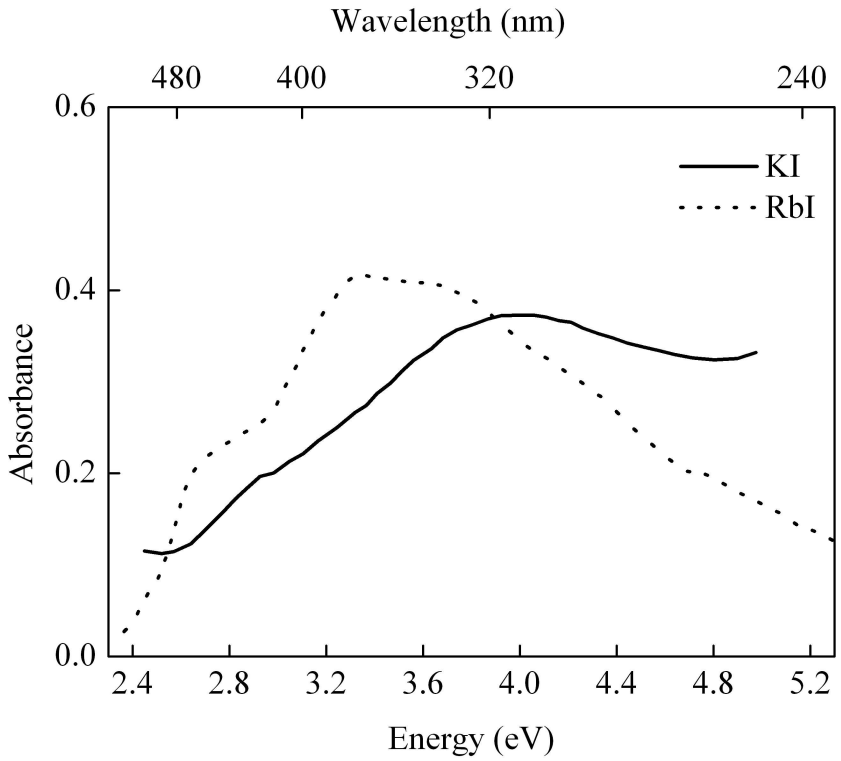


Figure 4.2: Optical absorption spectra in the *V* band region of KI [81] and RbI [112] samples taken near 77 K after annealing at the temperatures indicated. These crystals were subjected to γ-irradiation near room temperature and are shown for comparison purposes to indicate the position of the *V* bands.

its smaller satellites at 4.05 and 4.35 eV, differ significantly in appearance from the 2.7 and 3.4 eV bands, which are broad features. For comparison purposes the optical absorption features in the *V* band region observed after γ-irradiation of KI [82] and RbI [113] are shown in figure 4.2. The optical absorption spectrum of CsI measured at 77 K shows more prominent features, with more structure in the *V* bands observed, that are either absent or relatively weak in the spectra of γ-irradiated KI and RbI.

Figure 4.3a shows the development of the *F*, F_2 and *V* bands with increasing proton fluence. The optical absorption spectrum of the sample with the lowest proton fluence provides an indication of the features near and around the *F* and F_2 bands at an early developmental stage. A closer observation of the spectrum labelled 1 indicates the

existence of a feature near 0.55 eV, which later develops to be the shoulder near the F_2 band on the lower photon energy side. This feature is seen more clearly for the sample (spectrum labelled 3) implanted to a fluence of 3×10^{16} ions/cm^2. The F_2 band is also

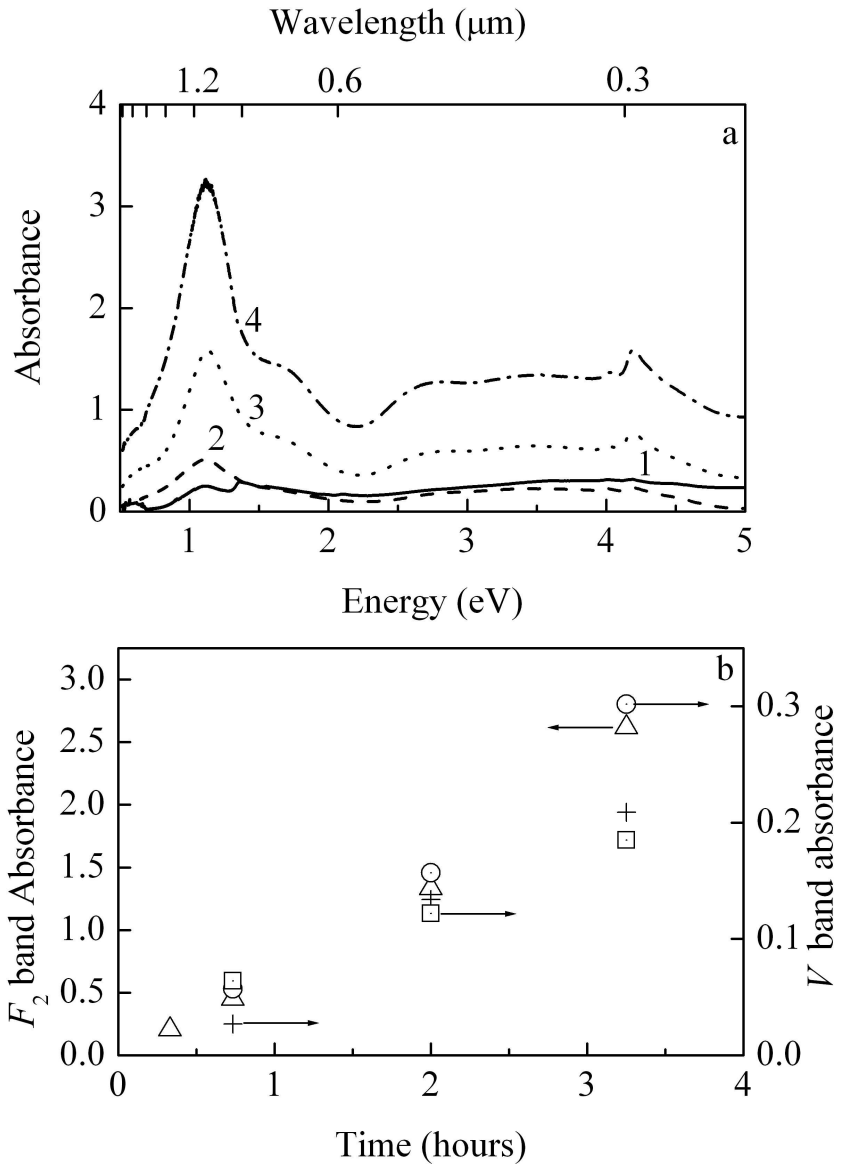


Figure 4.3: (a) Development of the optical absorption features with increasing proton implantation fluence (1 : 5×10^{15}, 2 : 1×10^{16}, 3 : 3×10^{16}, 4 : 6×10^{16} ions/cm^2). (b) Growth of the F_2 band at 1.1 eV (triangles), V bands at 2.7 eV (circles), 3.4 eV (squares) and at 4.2 eV (plus sign) with increasing implantation time. All the implantations and optical absorption measurements (within 30 minutes of the former) were performed near 300 K.

seen at an early development stage, and stays at approximately the same photon energy with increasing proton fluence. A broad band feature observed initially between 1.3 and 2.0 eV and evolving with increasing proton fluence on the higher photon energy side of the F_2 band is identified as the F band [182, 183]. Figure 4.3b shows the change in the absorbance as a function of the implantation time. The absorbance increases indicating accumulation of F and F_2 centres and their complementary defects in a manner that is near linear. This growth curve was useful in estimating the value of the fluence needed to obtain a reasonable value of the absorbance of the F_2 band and thus avoid the stray light effects mentioned earlier in subsection 4.1.2.

Figure 4.4a shows a representative Raman spectrum obtained from a proton implanted CsI sample measured at 77 K without annealing. The intense Raman peak occurring at 113 cm^{-1} is accompanied by other weaker overtones located at wavenumbers that are nearly a multiple of the main peak, i.e. near 224, 336, 447 cm^{-1} and at similar higher wavenumbers with smaller intensities. These peaks are associated with vibrational modes generated by the I_3^- di-interstitial defects which are excited by the near-resonance Raman technique employed (see section 2.3.4). It is justified to make comparisons of the optical properties of defects created by γ- and X-ray irradiation of KI and RbI to the present case of proton implantation of CsI because an excitonic mechanism is considered to be operative. Therefore, for purposes of comparison the Raman spectra for the room temperature γ-irradiation of RbI [113] and KI [82] are shown in parts b and c, respectively, of the figure 4.4. Similar progressive overtones, as in the present case of the proton implanted CsI, are observed for the γ-irradiated RbI sample and are attributed to the proximity of the laser line (488 nm) to the V bands photon energy range. The absorption band near 2.7 eV in RbI has been associated with the occurrence of the Raman feature at 201 cm^{-1}, which is attributed to the I_2^0 monomer (see section 1.4.2). Table 1.2 in the same section of chapter 1 shows that Raman bands near 173 cm^{-1} may be associated with the presence of I_n^-. However, in the present

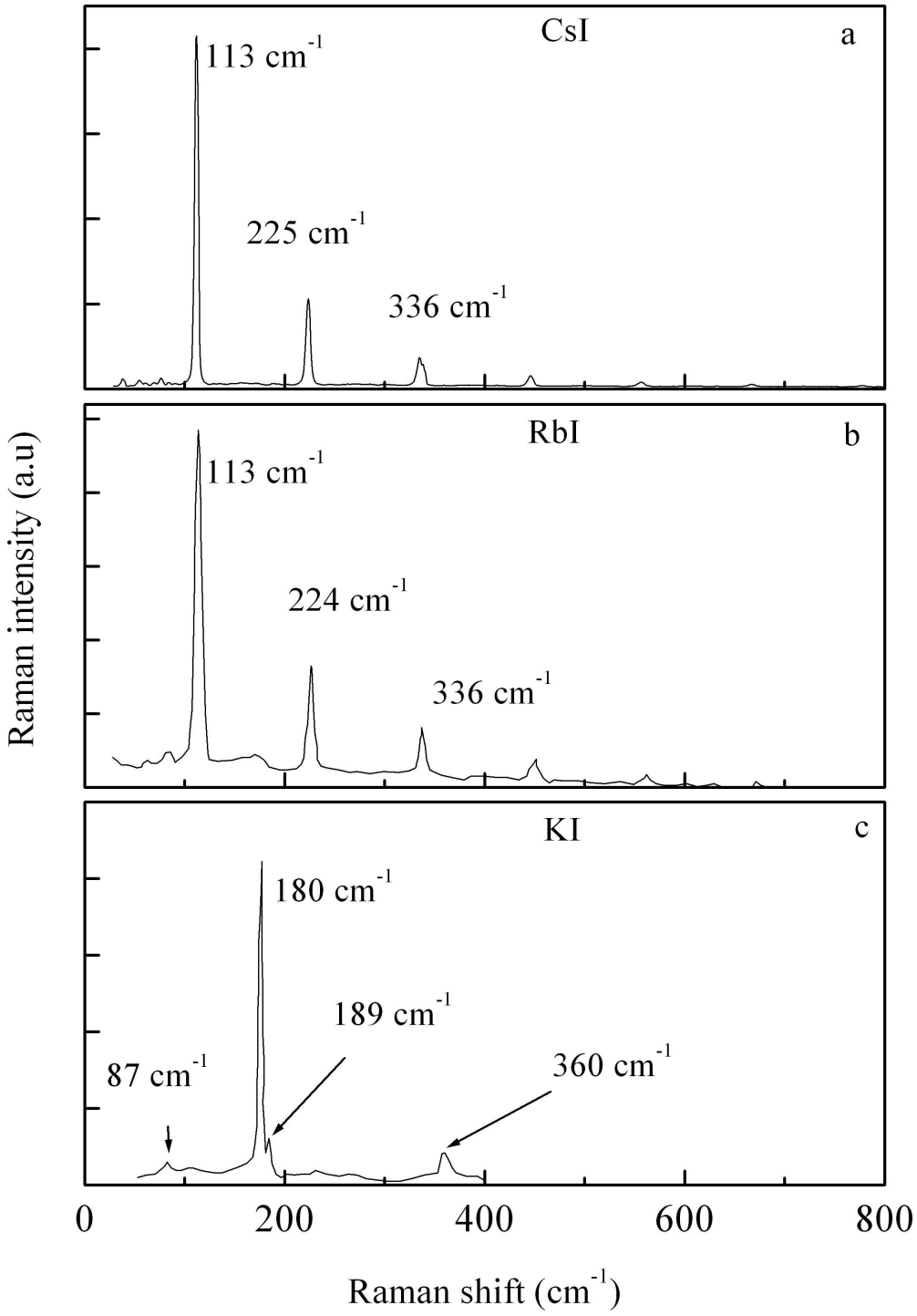
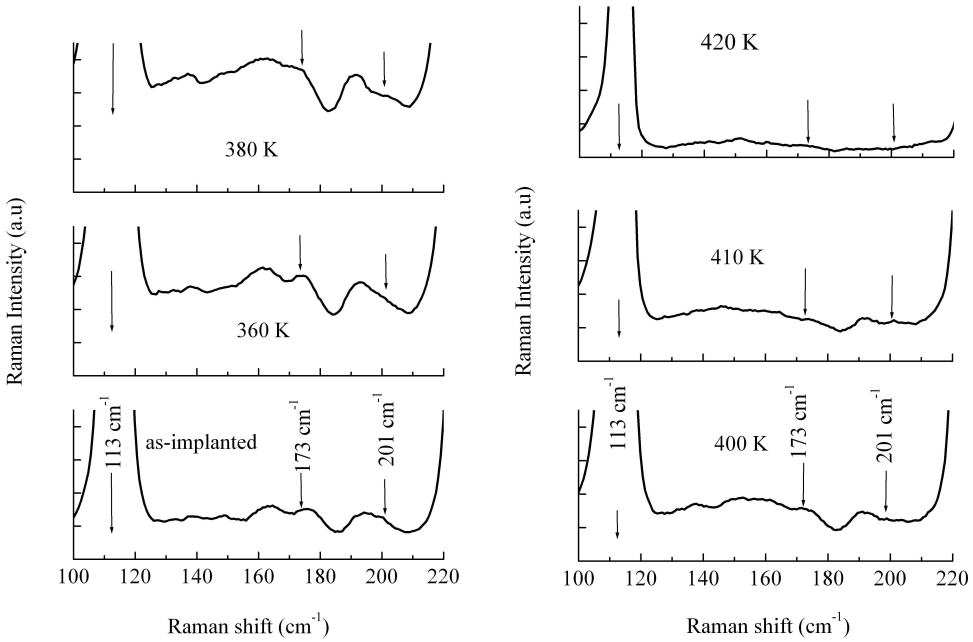


Figure 4.4: Raman spectra of (a) a proton implanted CsI irradiated at 300 K, (b) γ-irradiated RbI [112] and (c) KI [81] samples, shown for comparison purposes. The irradiation of the latter two samples was performed at 295 K. All spectra are measured near 77 K. The Raman excitation wavelength was the 488 nm argon laser line in all cases.



(a) (b)

Figure 4.5: The evolution of very weak Raman features between 130 and 210 cm^{-1} that may be associated with the presence of I_n^- and the I_2 monomer, which are known to occur near 173 and 201 cm^{-1}, respectively. These features are observed following annealing between (a) room temperature - 380 K and (b) 400 - 420 K.

work the Raman spectra of the proton implanted CsI shows only very weak features at 173 and 201 cm^{-1} indicating extremely low concentrations of these defects. These weak features are shown in figure 4.5 and seem to modify slightly with higher annealing temperature before decaying. However, from the ratio of the intensity scales of figures 4.4a to 4.5 of 30 : 1, the evidence of the formation of I_n^- and I_2^0 defects remains inconclusive.

4.3 Isochronal Anneal

Figure 4.6a shows the optical absorption spectra of a complementary randomly oriented CsI crystal, cut from the same boule, following 30 minutes isochronal annealing cycles between 340 and 430 K with the temperature varied in steps of 10 K. A mutual decay of the F_2 (at 1.1 eV) and V bands (at 2.7 and 3.4 eV) occurs. The F_2 and V bands (at 2.7 and 3.4 eV) begin to decay above 350 K and by 410 K they appear to anneal almost completely. There is still a significant residual absorption by the V band at 4.2 eV even when the F_2 band has annealed out and there is no corresponding Raman intensity. Figure 4.6b illustrates the changes in the neighbourhood of the band at 4.2 eV as the annealing temperature is raised. The optical absorption spectra have been vertically displaced to show the optical absorption changes around this band and the complementary F_2 band to an annealing temperature of 400 K. Energy dispersive X-ray analysis performed in a scanning electron microscope facility did not reveal any significant impurity content in the CsI crystals but trace concentrations may be present. The V band at 4.2 eV has at present an undetermined origin. It may be impurity related and appears not to have a measurable Raman signal under the current conditions of study.

Figure 4.7 shows the correlation between the absorbance of the F_2 band and that of the complementary V bands together with the associated Raman intensity. It can be seen from this figure that the F_2 and the V bands at 2.7 and 3.4 eV have a major annealing stage near 385 K, while the band at 4.2 eV remains significant, only decaying at a higher temperature close to 410 K. This indicates that the band at 4.2 eV does not take part in the mutual decay of the anion vacancy and interstitial defects. The activation energy of the decay process, determined from the slope of figure 4.8, was found to be 1.28 eV.

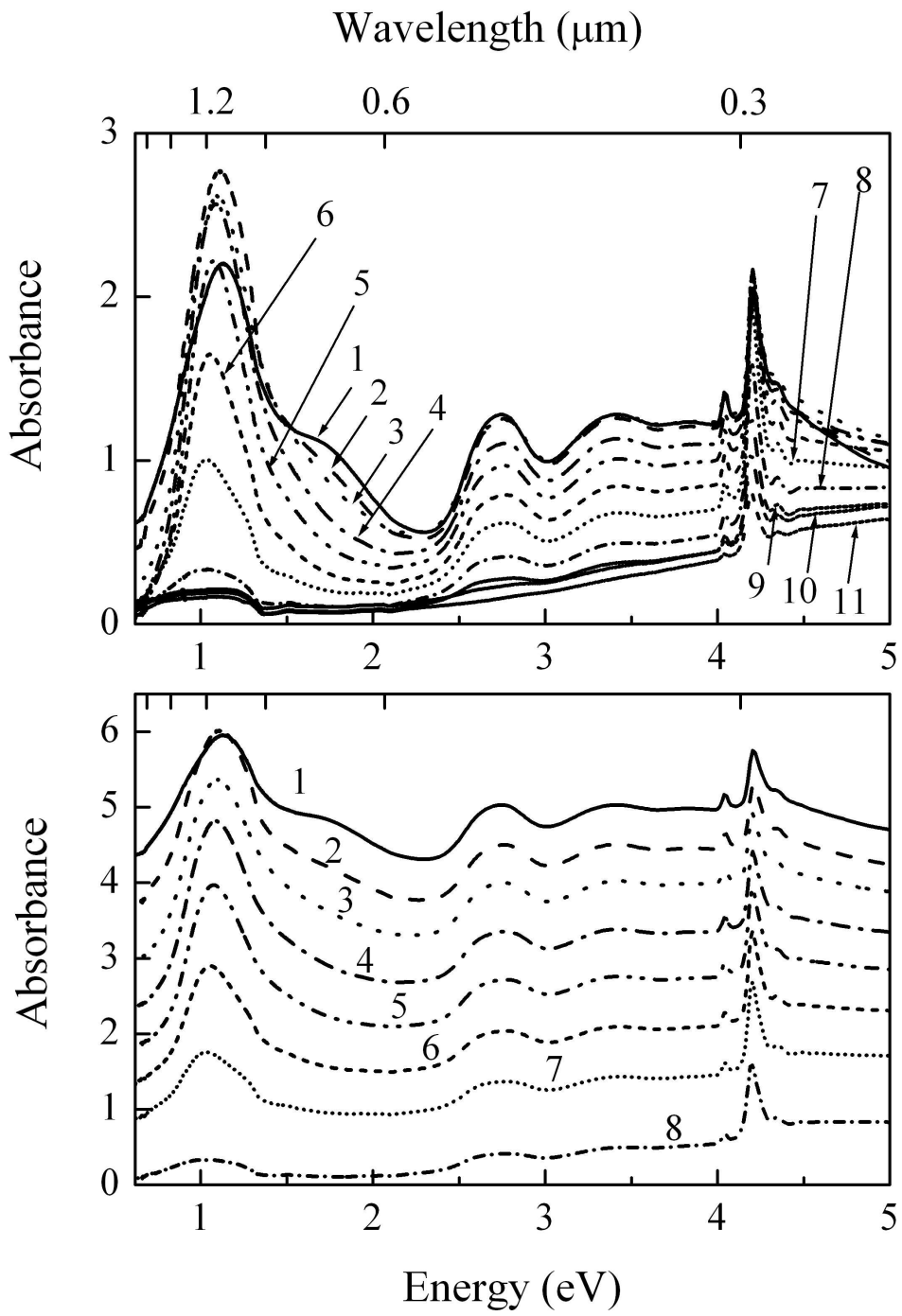


Figure 4.6: (a) Optical absorption spectra measured at 77 K temperature following 30 minutes isochronal annealing cycles (1 : unannealed, 2 : 340 , 3 : 350, 4 : 360, 5 : 370, 6 : 380, 7 : 390, 8 : 400, 9 : 410, 10 : 420 and 11 : 430 K). (b) Similar optical absorption spectra (1-8) as in (a) above shifted to show the development around the *V* band near 4.2 eV. Sample was implanted with 1 MeV protons to a fluence of 6×10^{16} ion/cm^2 near 300 K.

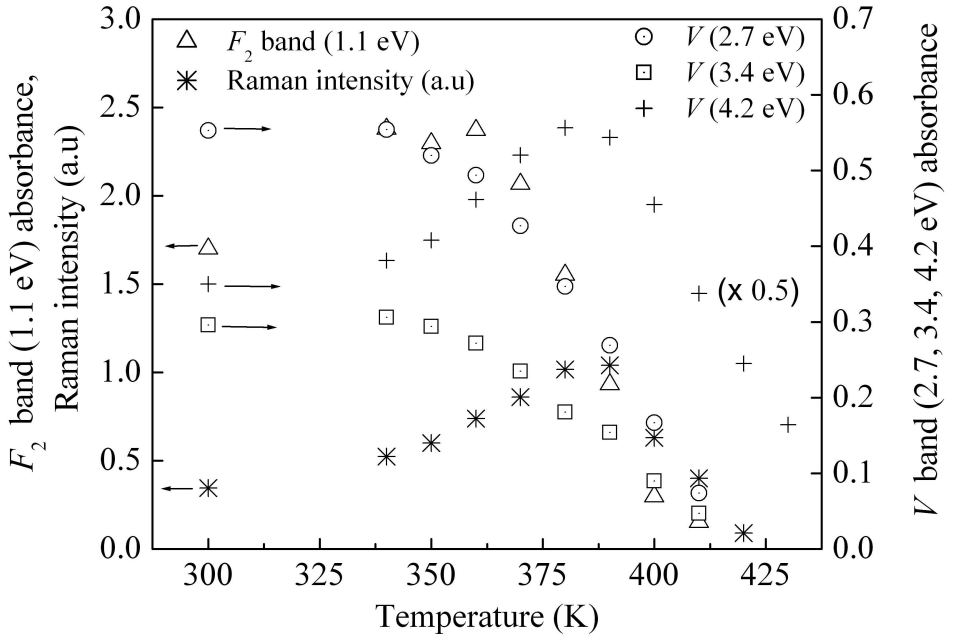


Figure 4.7: (a) Correlation of the F_2 (triangles) and V bands (circles : 2.7 eV, squares : 3.4 eV and plus sign : 4.2 eV) and Raman intensity (asterisk) with increasing annealing temperature, obtained from the isochronal cycles. The absorbance values for the V band at 4.2 eV are reduced by a factor of 0.5.

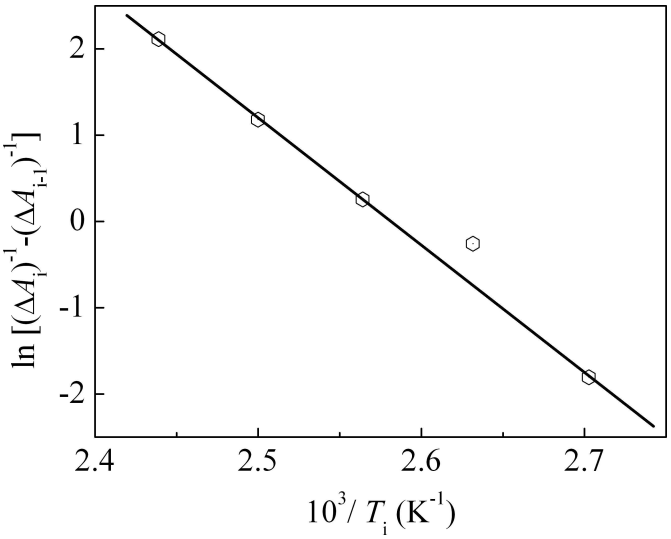


Figure 4.8: Linear plot used for the determination of the activation energy for the interstitial-vacancy recombination from the isochronal annealing of the F_2 or V band (2.7 eV). This plot, as discussed in section 2.4, yields a straight line for $\gamma = 2$ from which the activation energy of 1.28 eV is obtained for the reaction.

4.4 Isothermal Anneal

Figure 4.9 shows the changes in the optical absorption spectra as the implanted sample held at 397 K (determined to be near the midpoint of the annealing stage from the isochronal results in the previous section) is annealed for increasingly longer durations. Whereas the F_2 band absorbance grows before decaying, the V bands at 2.7 and 3.4 eV decay consistently with longer annealing time. The initial growth of the F_2 band (1.1 eV) is attributed to the decay of the F band (1.66 eV) on the higher photon energy side, seen on the spectrum of the as-implanted sample and drawn using the solid line in this figure. The F_2 and V bands (at 2.7 eV and 3.4 eV) appear to anneal out for periods longer than 160 minutes. The correlation between the peak absorbance of the

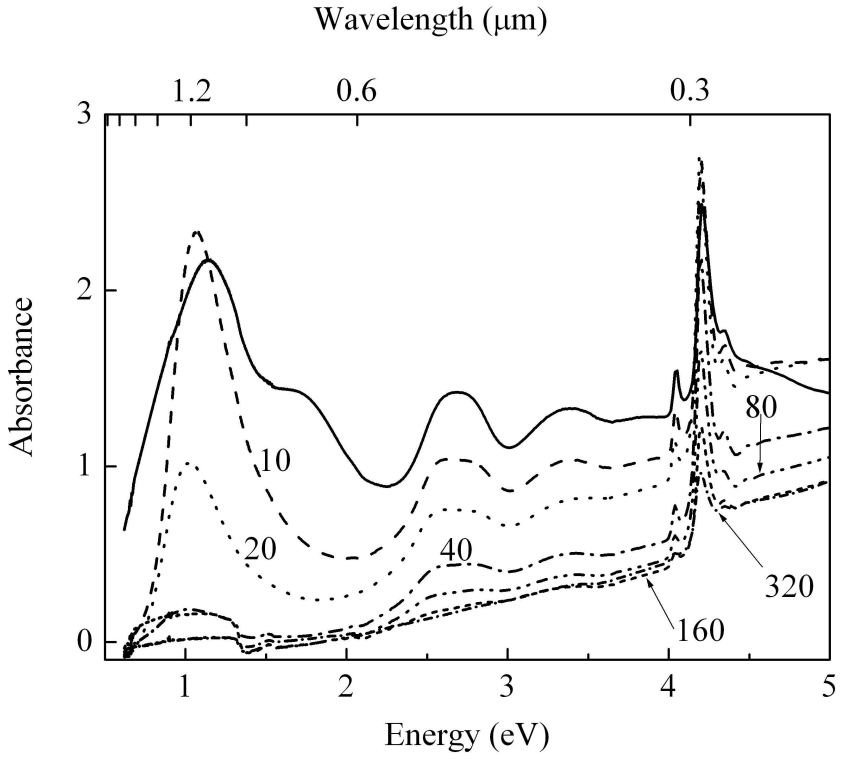
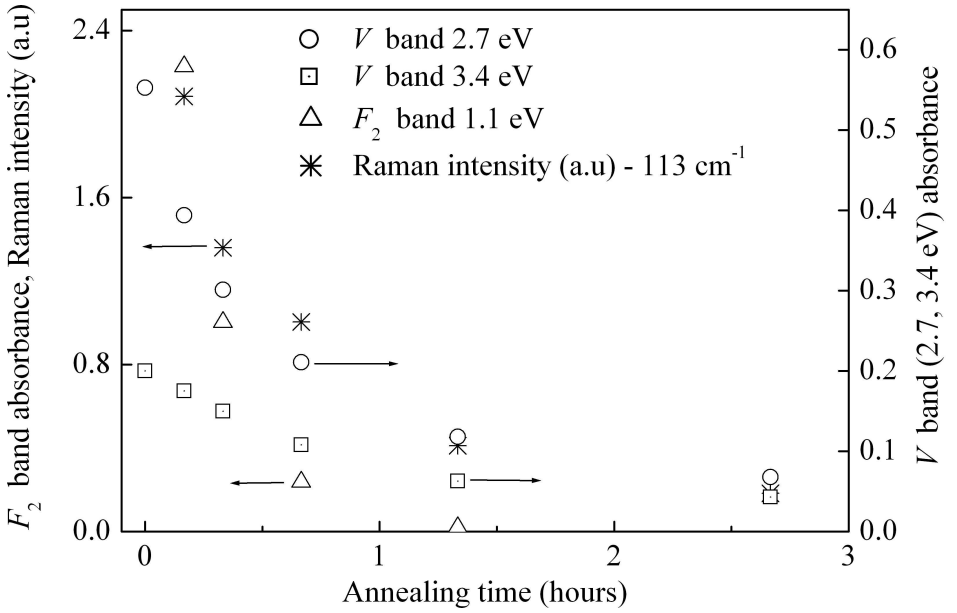
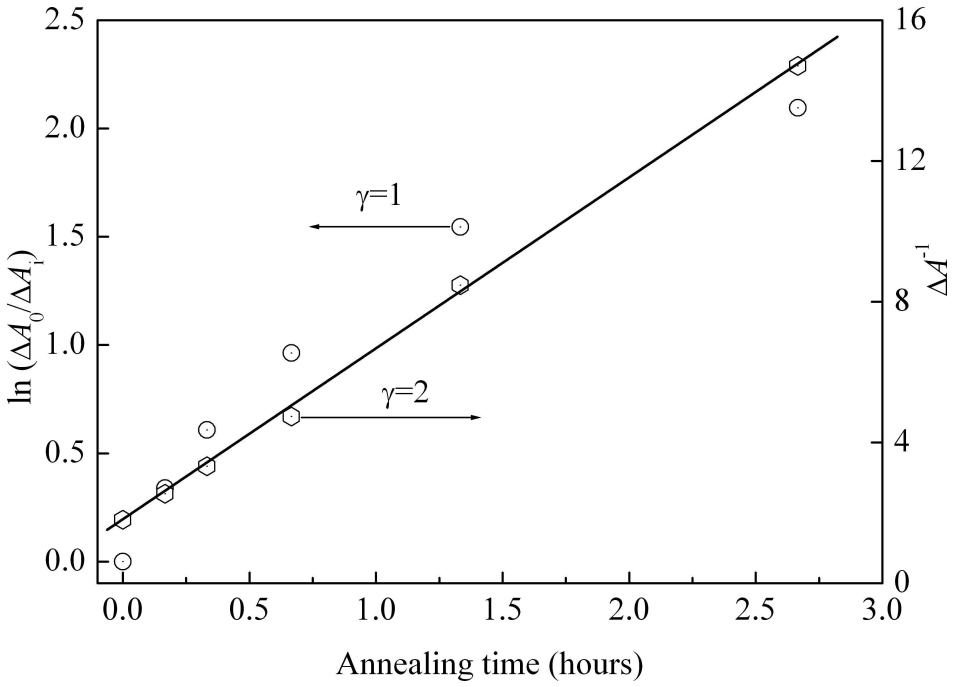


Figure 4.9: Optical absorption spectra measured at 77 K following isothermal annealing at 397 K for the respective total durations (10, 20, 40, 80, 160, 320 minutes). The solid line represents the spectrum obtained from the as-implanted sample, which was implanted with 1 MeV protons to a fluence of 6×10^{16} ions/cm^2 near 300 K.

F_2 and V bands (at 2.7 eV and 3.4 eV) and the intensity of the Raman peak at 113 cm^{-1} is presented in figure 4.10a. This figure shows that the decay, which is due to an interstitial-vacancy recombination process, takes place in a correlated manner and in a single step as shown in the isochronal annealing results in section 4.3. The results of the reaction kinetics (see section 2.4) extracted from the data, represented by the open squares and joined using a solid line, are shown in figure 4.10b. The close agreement between the data and theory indicate that the recombination mechanism occurs via a second order process, suggesting that the I_3^- break up first forming H centres, which later recombine with their complementary anion-vacancy type centres. A probable justification also comes from the isochronal annealing trend, where it is observed that the F centres first decay forming the F_2 centres. It is only then that the F_2 and V bands (2.7 and 3.4 eV), the latter being associated with I_3^- centres, start decaying together on further heating, indicating mutual annihilation. The data plotted assuming a first order reaction, represented by the open circles, is included in the same graph and results in a curve, thus eliminating such a possibility.



(a)



(b)

Figure 4.10: (a) Correlation between the rate of decay of the F_2 and V bands and the Raman intensity obtained from the isothermal annealing performed at 397 K. (b) The associated chemical reaction kinetics graph (see section 2.4) for the determination of the order of the recombination process. The reaction order is 2.

4.4.1 Comparison With Defects Produced in Irradiated KI and RbI

The combination of optical absorption and Raman spectroscopy, in conjunction with isochronal and isothermal annealing experiments has established the nature of the major defects created in 1 MeV proton-bombarded CsI. The anion vacancy defects are *F* and F_2 centres. The *V* centres leading to the bands in the ultraviolet region at 2.7 and 3.4 eV are identified by means of the Raman feature at 113 cm^{-1} and result from I_3^- clusters, which are dimeric defects in which two *H* centres are bonded to a lattice anion. The double peaked structure of the *V* bands is reminiscent of bands at 3.6 and 4.4 eV found in KI for low temperature irradiations in which I_3^- centres are dominant. The work of Okada and Hata [55] accounted for these bands in terms of the spin-orbit interaction in the I_3^- ions in a variety of possible orientations. The *F* type defects and the I_3^- clusters are thus vacancy-interstitial complements. Since these are the same products created by the excitonic mechanism in the f.c.c alkali iodides, at sufficiently low temperatures, it is concluded that a form of the excitonic mechanism is operative in s.c. CsI. This interpretation is consistent with the defect growth under irradiation in which there are linear relationships between the growth of the respective complementary defects. It is also in agreement with the annealing results in which there is a mutual decay of the *F* and *V* centres obeying second order kinetics, being typical of recombination of point-like defects as found in RbI. However, it is quite different for the first order annealing kinetics found in the recombination of *F* centres and large interstitial aggregates of $(I_2)_n$ created in KI during irradiation at room temperature [58, 344, 345].

It is noted that for RbI, irradiated at room temperature, the *V* band envelope consists of three major bands, peaking at 2.7, 3.5 and 4.3 eV. In this case the 2.7 eV band was shown to be associated with the neutral molecule I_2^0 being an alternative di-interstitial structure to the I_3^- defects [113]. The 2.7 eV band annealed in concert with a Raman signal at 201 cm^{-1} at a somewhat lower temperature than the 3.5 and 4.3 eV

bands that decayed with the I_3^- Raman signal at 113 cm^{-1} [113]. In CsI the 2.7 and 3.4 eV features are associated with the I_3^- defects. In the present work careful examination of the Raman spectra show extremely weak signatures at 201 cm^{-1} suggesting that the I_2^0 neutral molecules are present in very small concentrations if at all.

As discussed earlier in subsection 4.1.2, CsI is radiation resistant to the relatively low intensity radiation sources such as X- and γ- rays conventionally used for the colouration of f.c.c. alkali halides. It appears that the radiation damage process in this s.c. compound requires a substantial degree of electronic excitation as provided by high flux γ-irradiation [186], or, as in the present case, by 1 MeV proton bombardment. In spite of these differences, and as already noted above from the forms of the defects created, it is considered that an excitonic defect production mechanism is operative in CsI. It would be most valuable to develop an understanding of the apparent threshold of electronic excitation needed for defect production as well as the geometry of the primary *F-H* pair and the separation process of these primary defects. In this regard the detailed theoretical work that has been so successful in accounting for the creation of defects in the f.c.c. alkali halides [156, 155] could be applied to CsI.

Apart from the challenges posed by the defect formation process in CsI, there are also the issues of the distinctly different iodine clusters formed respectively in RbI (small I_3^-, I_n^- and I_2^0 molecular ions) and CsI (small I_3^- ions), and those formed in KI (large $(I_2)_n$ aggregates). As shown in earlier work [83], the formation of the $(I_2)_n$ aggregates in KI is a thermally activated process as indicated by the increasing proportion of these in the defect inventory as the temperature of irradiation is raised [84]. At low temperatures the $(I_2)_n$ aggregates are absent and the I_3^- and I_n^- defects are present. At room temperature, as shown in figure 4.4c [84], the large $(I_2)_n$ aggregates are absolutely dominant indicated by the characteristic Raman features are 180 and 189 cm^{-1}. It has been suggested [187] that the increasing cation size is a common factor providing a consistent pattern in the f.c.c. alkali halides and bromides. Small cations lead to the $(I_2)_n$

or $(Br_2)_n$ aggregates being formed near or at room temperature under irradiation, but large cations such as Rb do not [113]. This result could now be extended to s.c. alkali halide CsI. In terms of a current model of the formation of *F* and *V* centres under irradiation and their relationship to the formation of perfect dislocation loops, as observed in the electron microscope [76], it is noted that in addition to anion displacements, cation displacements are also necessary. The vacancy pairs thus formed are able to provide sites for the small interstitial clusters such as I_3^-. An extension of this process can therefore provide the necessary void space for large clusters, provided that large numbers of cations can be displaced. Smaller cations such as potassium would be relatively more easily displaced, particularly once sufficiently high temperatures are attained. It would therefore appear that these conditions apply to KI, but not to RbI or presently studied CsI. Electron microscope studies of these latter compounds at high irradiation fluences would therefore be valuable in detecting the presence or not of clusters and dislocation loops in order to test these conclusions.

4.5 Summary and Discussion

CsI crystals have been coloured by implantation with 1 MeV protons near room temperature to fluences of up to 6×10^{16} ions/cm^2. Optical absorption studies performed at 77 K reveal the F_2 band located near 1.1 eV, the *F* band close to 1.66 eV, which appears as a shoulder on the higher photon energy side and several *V* bands located near 2.7, 3.4, 4.05, 4.2 and 4.35 eV. Implantation of the CsI samples with varying proton fluences provides information of the growth curve and the development of the *F*, F_2 and *V* bands from early stages. The *V* band at 4.2 eV is observed to grow linearly with the F_2 and other *V* bands thus suggesting that it is a radiation induced defect. However, this *V* band is fairly sharp making it different from the broad bands normally associated with molecular centres such as those currently observed near 2.7 and 3.4 eV.

The Raman spectra of the proton implanted CsI sample, measured at 77 K, reveal

a peak at 113 cm^{-1} accompanied by more than 5 progressive overtones occurring at higher multiple wavenumbers. These Raman features are associated with the presence of the I_3^- defects. The occurrence of a large number of overtones is attributed to the near resonance conditions of the exciting laser line used. The *V* bands at 2.7 and 3.4 eV, observed by optical absorption studies, are attributed to the I_3^- defects. From the results of the isochronal annealing, the correlation of the optical absorption and Raman intensity confirm that the F_2 and the *V* bands at 2.7 and 3.4 eV decay simultaneously at a major annealing stage close to 385 K. The band at 4.2 eV is still significant at this stage and it is not until near 410 K that signs of major annealing occur. The absorbance values of this band remain relatively large even after the complete decay of the well-correlated F_2 and *V* bands mentioned earlier. Chemical reaction kinetics extracted from the isothermal annealing data show that the interstitial-vacancy recombination process is second order, suggesting that the di-interstitials break up first forming *H* centres which recombine with the F_2 centres. The combined analysis of the optical absorption and Raman studies further shows that the decay occurs in a single step, confirming an interstitial vacancy recombination process. The activation energy of the recombination process determined from the decay of the absorbance of the F_2 band or the *V* band at 2.7 eV was found to be 1.28 eV.

In the Hobbs et al. mechanism [76], the formation of the perfect dislocation loops requires displacement on both the cation and anion sublattices. Such displacements create space in the lattice either as divacancies, larger aggregates and ultimately large voids. The smaller cations, as for the case of KI, are likely to be more easily displaced and hence create more space for large interstitial aggregation. In RbI and CsI, with relatively larger cations, much less space is created and hence result in the formation of smaller aggregates.

The formation of the I_3^- defects in the present work and in KI and RbI, under irradiation certain conditions, suggest that the damage creation mechanism may be similar

in these iodides. However, future investigations should examine the wide range of defects generated and the fundamental defect creation mechanism operative in CsI, as well provide theoretical calculations to back the experimental observables.

Chapter 5

Mg Colloids in Magnesium Fluoride Single Crystals

5.1 Motivation and Scope of Work

As discussed in section 1.10, the interest in ion implantation of single crystals of MgF_2 stems from the fact that reports on the observation of fluorine interstitial defects have been very few and yet it is well documented that the damage creation process in this material is an excitonic mechanism. The implantation of excess Mg^+ ions at low temperature to encourage the growth of colloids, contemporarily known as nanoparticles, has also been undertaken to study the effects of annealing on the optical properties of the fundamental defects created. Implantation at low temperatures is expected to increase the probability of defect retention and hence the density of defects created. The effect of the annealing environment on the growth of the colloids has also been investigated and found to be vital when the constituent elements of the material in which the ions are implanted are reactive.

5.2 Sample Preparation and Implantation of Mg^+ ions into MgF_2

The material used were circular disks of (001) orientated single crystal samples that were purchased from Crystran Ltd (UK). Suitably sized specimens of size 10×10 mm^2 were cut from the disks by means of a diamond impregnated copper wire saw (subsection 3.5.1). After cleaning with alcohol they were attached to the sample holder in the end station of the ion implantation facility and positioned with an offset of a few degrees from the beam axis, to avoid channeling (see section 3.4). The samples

were attached using conducting carbon paste which ensured good thermal contact and minimized charge accumulation. Previous studies [123] had shown significant beam heating effects in MgF_2 crystals when subjected to high fluence ($\approx 10^{17}$ ions/cm^2) ion bombardments at ambient temperature with no temperature control. Accordingly in order to avoid such effects, the samples were maintained at liquid nitrogen temperature (LNT) during this ion implantation.

Just before the sample holder was placed into the vacuum chamber, a gentle stream of nitrogen gas was passed over the samples to remove specks of dust or any foreign substances that may have settled on them. A scanned beam of 100 keV Mg^+ ions from a stable Mg metal source was used at a maximum current density of 2 μA/cm^2 for the implantation of the MgF_2 crystals to a fluence of 10^{17} ions/cm^2. After the implantation, the samples were allowed to warm up to room temperature (RT) in the same way and subsequently cleaned ultrasonically to remove the carbon paste.

5.3 Optical Absorption Measurements and Annealing of the Samples

The Cary 500 and the VUV spectrophotometers, discussed earlier in sections 3.7.3 and 3.7.4, were used to perform optical absorption measurements in the VIS-UV and the VUV regions respectively. These measurements were done on the as-implanted samples and subsequently after predetermined annealing cycles.

Most of the high temperature annealing experiments of MgF_2 samples were carried out in air using the resistance-heated fused silica tube furnace at the University of Zululand (UZ) (see section 3.6). The sample was inserted quickly into the hot zone and after a standard annealing period of 30 minutes was rapidly withdrawn and cooled in air to RT. Isochronal annealing was conducted at selected temperature intervals over the range 373 to 973 K.

A further set of annealing experiments on the MgF_2 samples were carried out in an argon atmosphere in order to investigate the possible effects of oxygen contamina-

tion of the surface of the samples during annealing at the highest temperatures in air. In this case annealing was carried out using the previously described RF-heated silica tube furnace (see section 3.6). High purity argon gas was allowed to flow through the furnace when the RF power was turned on. The sample was inserted into the furnace after temperature stability was attained and annealed for 30 minutes after which the RF power was turned off and the gas kept flowing until the sample was cool enough to be removed. Isochronal annealing was carried out over the 373 to 1073 K temperature range at 100 K intervals.

5.4 Surface Studies of Mg^+ Ion Implanted MgF_2 Sample

An XPS facility, at the Council for Scientific and Industrial Research in Pretoria, whose principle of operation was discussed earlier in section 3.9, was used to probe the surface of the MgF_2 sample following the anneal in air to determine its elemental composition as a function of depth. This was done by sequential sputtering of the material from the surface of the crystal followed by an analysis of the newly exposed surface. The choice of the amount of material to be sputtered away was based on a SRIM2003 simulation (see section 1.2) of the distribution profile of the implanted Mg^+ ions shown in figure 5.1 and ensured that the concentration of the constituent elements were determined in this region.

5.5 Discussion of Results

5.5.1 A SRIM2003 Simulation of Ion Implantation in MgF_2 Crystals

Figure 5.1 shows SRIM 2003 simulation [13] results in which a mean penetration depth of about 150 nm is obtained, while figures 5.2a and b provide information concerning the ionization and vacancy creation profiles over the depth traversed by the accelerated ions. It can be seen from the latter figure that both ionization and vacancy

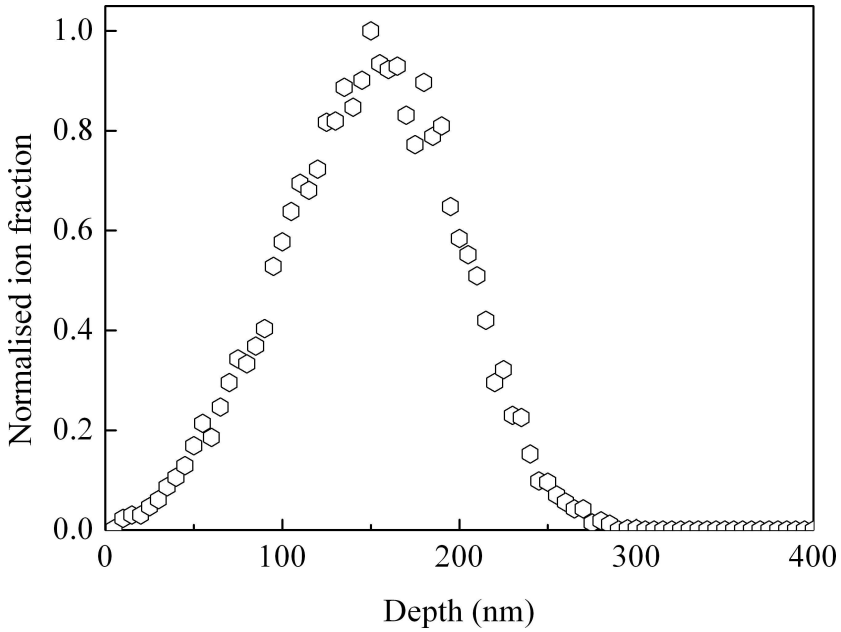


Figure 5.1: Results of a SRIM2003 simulation showing the distribution of the implanted 100 keV Mg^+ ions in a MgF_2 crystal as a function of depth measured from the implanted surface.

creation processes occur via both the incident and recoil ions. For the ionization process, the effect of the incident ions is dominant from the surface becoming comparable to that of the recoil ions just after the mean penetration depth. On entry into the solid the incident ions are still very energetic and will mainly create ionization damage but then start losing energy almost monotonically by the processes discussed earlier (see section 1.1.1). The efficiency of the recoil ions at creating ionization damage will certainly be lower since the primary knock-on ion itself has less energy than the incident ion. This efficiency is also expected to reduce further as the energy of the incident ion diminishes deeper into the solid. In the case of vacancy creation by direct collisional processes, the contribution of the recoil ions dominates over the entire implantation depth. This can be attributed to the relatively lower energies of the recoil ions and hence a larger probability of making elastic collisions. The damage created is therefore essentially within the surface and near surface regions. However, since an excitonic mechanism is

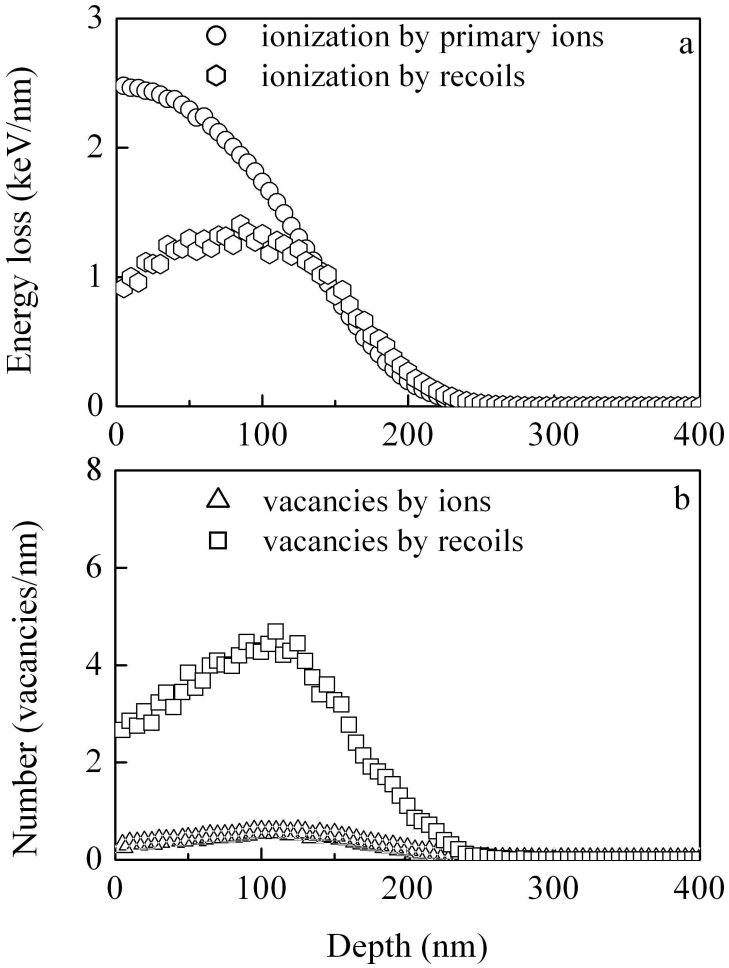


Figure 5.2: Simulations of the (a) energy loss via ionization and (b) vacancy creation as a function of penetration depth following ion implantation with 100 keV Mg^+ ions and the generated recoils in MgF_2 crystals using a SRIM2003 program.

operative in MgF_2, it is the ionization profile that will be related to the *F* centre production. Although this is not exactly what may be expected as the final damage profile, it serves as a useful guide and the accuracy of the mean depth has been shown to be within 10 % of the actual depth [1].

5.5.2 Optical Band Features Observed before Annealing

For purposes of comparison and reference to other work, figure 5.3I shows absorption spectra obtained previously [123] for Mg^+ ion implanted samples at lower fluences than used in the present work. In these room temperature (RT) experiments, the samples were not cooled during the implantation. Five absorption bands are identified, these being the *F* band (4.96 eV, 250 nm) and a cluster of F_2 bands labelled $F_2(1)$ (3.36 eV, 369 nm), $F_2(2)$ (3.91 eV, 317 nm), $F_2(3)$ (3.08 eV, 403 nm). In addition the $F_2(\pi)$ band associated with π-type transitions of the F_2 centres is also observed on the high energy side of the *F* band at 5.66 eV (219 nm). Figure 5.3II shows the spectra of two of the present samples before and immediately after Mg^+ ion implantation at LNT to a fluence of 1×10^{17} ions/cm^2, followed by warming to RT and cleaning as described in subsection 5.2. The spectra are very similar indicating reproducible conditions and defect structures. By comparison with figure 5.3I, the $F_2(3)$ band at 3.08 eV (403 nm) and the $F_2(1)$ band at 3.36 eV (369 nm) are seen to be present. The broad band at 5.25 eV (236 nm) is somewhat different in shape from its counterpart in figure 5.3I. It is considered to be a composite envelope of the *F*, F_2 and $F_2(\pi)$ bands, resulting from the higher fluences, a lower implantation temperature and the subsequent warming to RT.

5.5.3 Air Annealed Samples

Figure 5.4a shows the optical spectra measured at selected temperature intervals during an isochronal annealing run in air from ambient temperature to 973 K. As the temperature is raised, absorption near 3.3 eV (376 nm) and associated with $F_2(1)$ and $F_2(3)$ centres disappears during the 543 K anneal. At the same stage, there are considerable changes in the envelope of the *F*, F_2 and $F(\pi)$ bands with the peak growing and shifting significantly to lower energies, with the peak now being near 4.6 eV (270

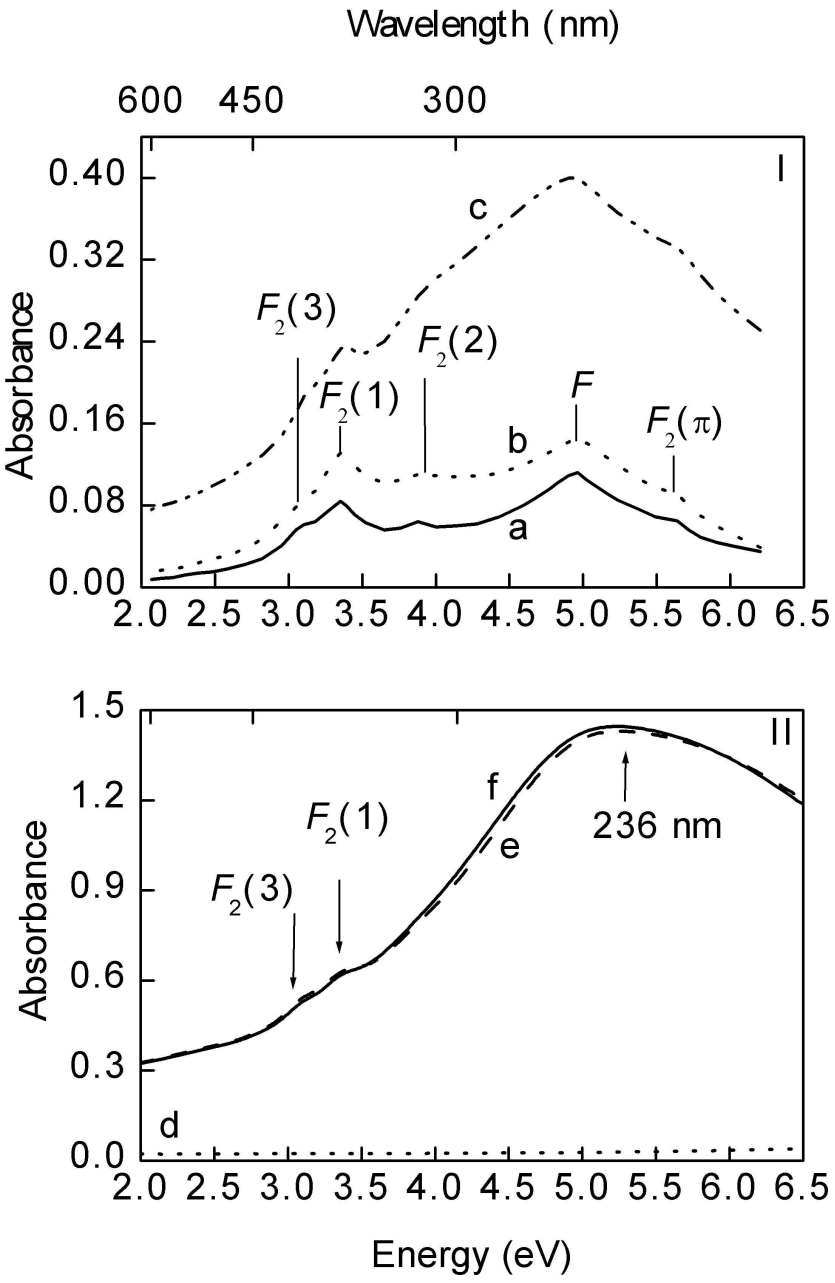


Figure 5.3: I. Optical absorption spectra for VIS and UV photon energy range between 2.0 and 6.5 eV for MgF_2 crystals implanted with 100 keV Mg^+ ions using a dose rate of 2μA/cm^2 at ambient temperature and not actively cooled. The curves correspond to different fluences of implanted ions. (a) 6×10^{15}; (b) 1×10^{16} ; (c) 3×10^{16} ions/cm^2 [123]. II. Optical absorption spectra for (d) a virgin crystal in which the spectrum was measured with air as reference, (e) and (f) after implantation with 100 keV Mg^+ ions to a fluence of 10^{17} ions/cm^2 at LNT and warmed to RT. The spectra for samples (e) and (f) were measured using a virgin crystal as reference. All measurements were done at RT.

nm). After the 633 K anneal a yet more prominent and narrower band has developed near 4.4 eV (282 nm) and reaches a maximum after the 723 K annealing stage. Further annealing reduces this band and by the 903 K anneal absorption in this region has been reduced to a comparatively small magnitude. The entire absorption background below 3.3 eV that is observed in the unannealed spectra and subsequently after annealing at 463 and 543 K diminishes as the temperature is raised. This is attributed to the removal of radiation-induced damage as a result of annealing. However, there is a subsequent increase following the anneal at 973 K.

Figure 5.4b shows the variation of the peak absorbance with annealing temperature for the *V* bands at 7.8 eV (155 nm) and near 6.5 eV (198 nm), the band at 3.3 eV (376 nm) and associated $F_2(1)$ and $F_2(3)$ centres and the Mg colloid band at 4.43 eV (280 nm). It can be seen that the 3.36 eV (369 nm) absorption associated with $F_2(1)$ and $F_2(3)$ centres and the *V* band and F_2 bands decay in unison above 463 K while the Mg colloid band grows with increasing temperature. Figure 5.5 shows the complementary optical absorption measurements performed in the UV and VUV regions revealing the corresponding annealing of the *V* bands. An inspection of figure 5.5a shows that there exists a broad band extending from 5.6 eV (221 nm) to 9.3 eV (133 nm). As seen, the rate of decay of absorption with increasing temperature is not uniform within this spectral region. The processes responsible can be examined in considerably more detail by means of the difference spectra shown in figures 5.5b - d that indicate the presence of at least two *V* bands and clearly identify their respective position. Annealing between 373 and 463 K converts a band at 7.8 eV (159 nm) to the one peaking at 6.5 eV (191 nm), which subsequently decays between 463 and 633 K. Inspection of figures 5.4b and 5.5 clearly shows that the decay of the low energy band near 6.5 eV (191 nm) coincides with the early disappearance during annealing of the $F_2(1)$ and $F_2(3)$ bands and the considerable changes of the *F*, F_2 and $F_2(\pi)$ band envelope. The results strongly suggest that the bands reported in the VUV are complementary to the *F* and *F* aggregate

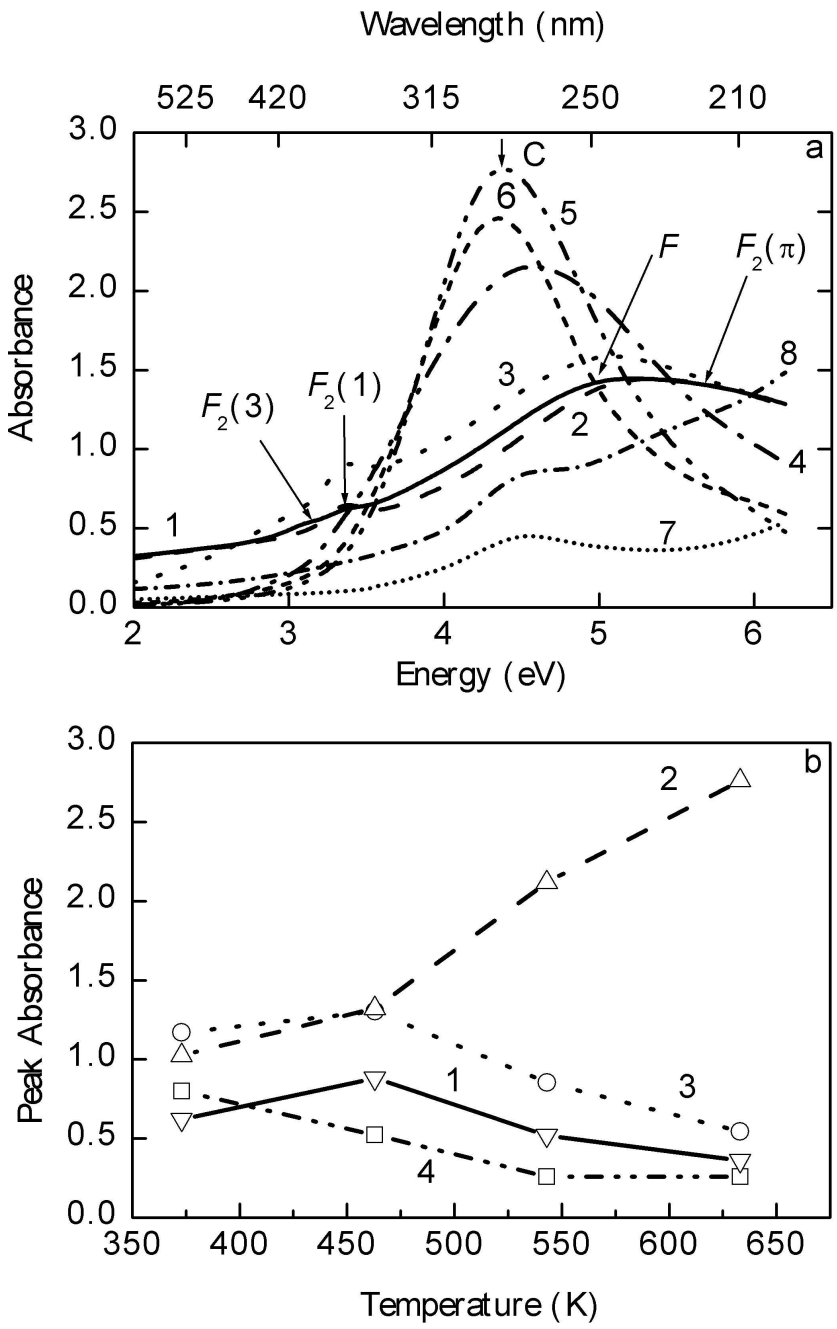


Figure 5.4: (a) Annealing behaviour in air of a MgF_2 crystal after ion implantation with 100 keV Mg^+ ions to a fluence of $10^{17}/cm^2$ at LNT and warmed to RT. The curves show successive optical absorption spectra over the VIS and UV photon energy range (2.0 - 6.5 eV) during an isochronal anneal with annealing stages each of duration 30 minutes (1 : RT, 2 : 373, 3 : 463, 4 : 543, 5 : 633, 6 : 813, 7 : 903, 8 : 973 K). The spectra were measured at RT. (b) Peak absorbance of the various features in (a) above as a function of annealing temperature. Inverted triangles - F_2 band (unresolved combination of the $F_2(1)$ and $F_2(3)$ bands at 3.36 eV (369 nm); triangles - Mg-colloid at 4.43 eV (282 nm); circles - *V* band at 6.5 eV (191 nm); squares - *V* band at 7.8 eV (159 nm).

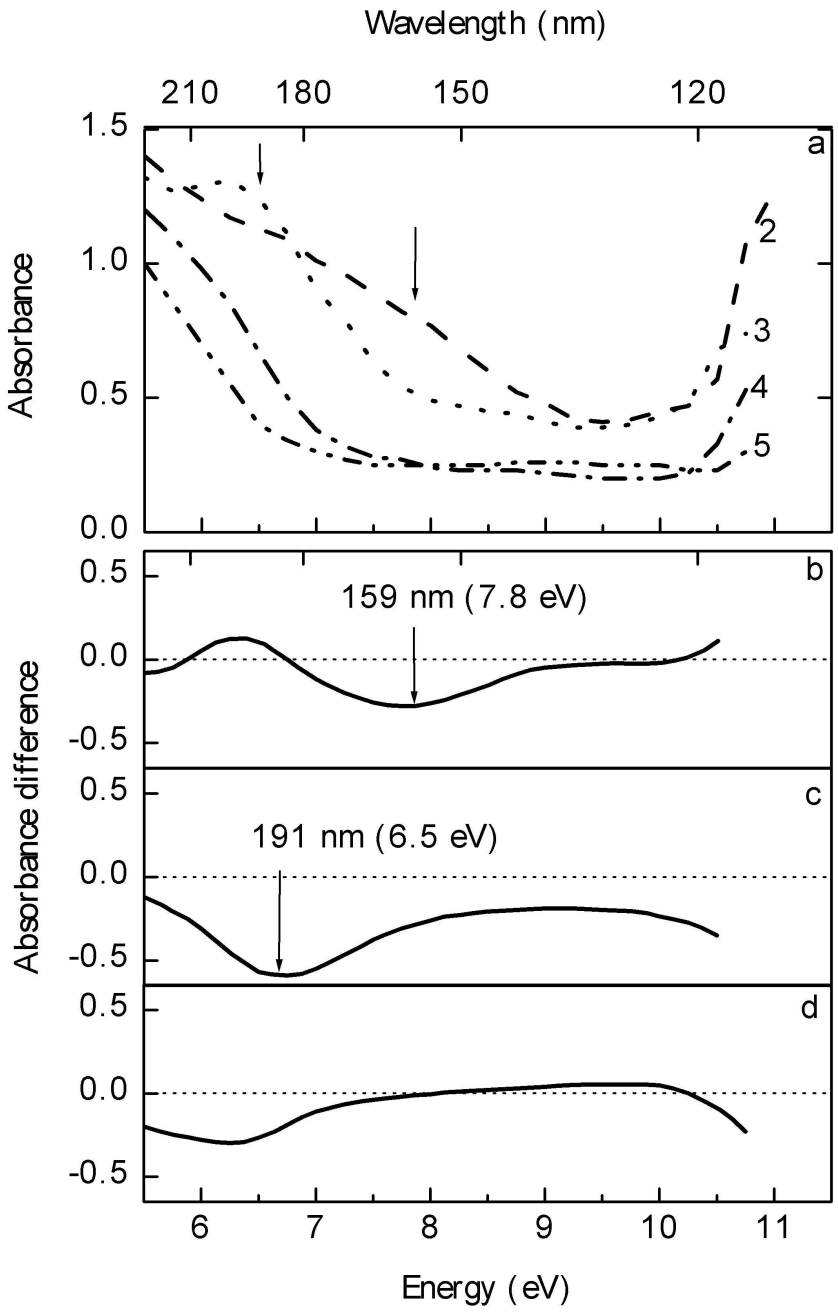


Figure 5.5: (a) Optical absorption spectra in the UV and VUV photon energy range between 5.5 and 11.5 eV for the same MgF_2 crystal as reported in figure 5.4. The spectra were measured at RT and have the same numbering for each annealing temperature as in figure 5.4a (2 : 373, 3 : 463, 4 : 543, 5 : 633 K). (b) - (d) Difference spectra for the UV and VUV photon energy range between 5.5 and 11 eV obtained from the data presented in figure 5.4. The figure identifies two absorption bands peaking at 7.8 eV (159 nm) and near 6.5 eV (191 nm). Spectra b, c and d in this figure represent the difference between spectra 2 and 3, 3 and 4, 4 and 5 in a above, respectively.

bands in the VIS region of the spectrum and by analogy with the alkali halides, should be termed *V* bands. It appears that an interstitial-vacancy recombination process is taking place and the VUV absorption bands are due to fluorine interstitial defects created together with the *F* centres by means of the excitonic mechanism operative in MgF_2.

Examination of the development of the broad and relatively intense band near 4.4 eV (282 nm) shows that it reaches a maximum near 723 K. This is identified as a Mg colloid band from previous work [123]. It is considered that the colloid band is formed by the agglomeration of the excess Mg ions introduced into the MgF_2 crystal by ion implantation. High temperature diffusion leads to Ostwald ripening of the colloids [115] with larger particles growing at the expense of the smaller ones and resulting in a sharper particle size distribution.

5.5.4 Results of Use of the Mie Theory (MT) and Characteristics Emerging from the Variation of the Fit Parameters

Figure 5.6 shows the theoretical results predicted by the application of the Mie theory (MT) to the experimental data for the case of Mg MNP in a MgF_2 medium. Equations 2.61, 2.62 and 2.63 have been used in the simulations. These equations are for the free electron case as an independent experimental value of ϵ_{core} for Mg is currently not available but also considered small. The graphs in this figure are for the same optical spectrum that was obtained after the 723 K anneal. The theoretical spectrum obtained using the best fit parameters (ϵ_h = 2.45, p = 0.08, d = 1.5 nm) reasonably matching the PR peak position, the FWHM and the maximum extinction of the experimental absorption spectra is shown in figure 5.6a. It can be seen from figure 5.6b, that the variation of ϵ_h mainly changes the position of the PR peak and increases the extinction if the theoretical value of ϵ_h, namely 2.0, is less than that of the MT-fit. The FWHM is unchanged. The value, 2.0, used in figure 5.6b is the real part of the linear dielectric constant ϵ_h of unimplanted MgF_2 matrix in the spectral range considered.

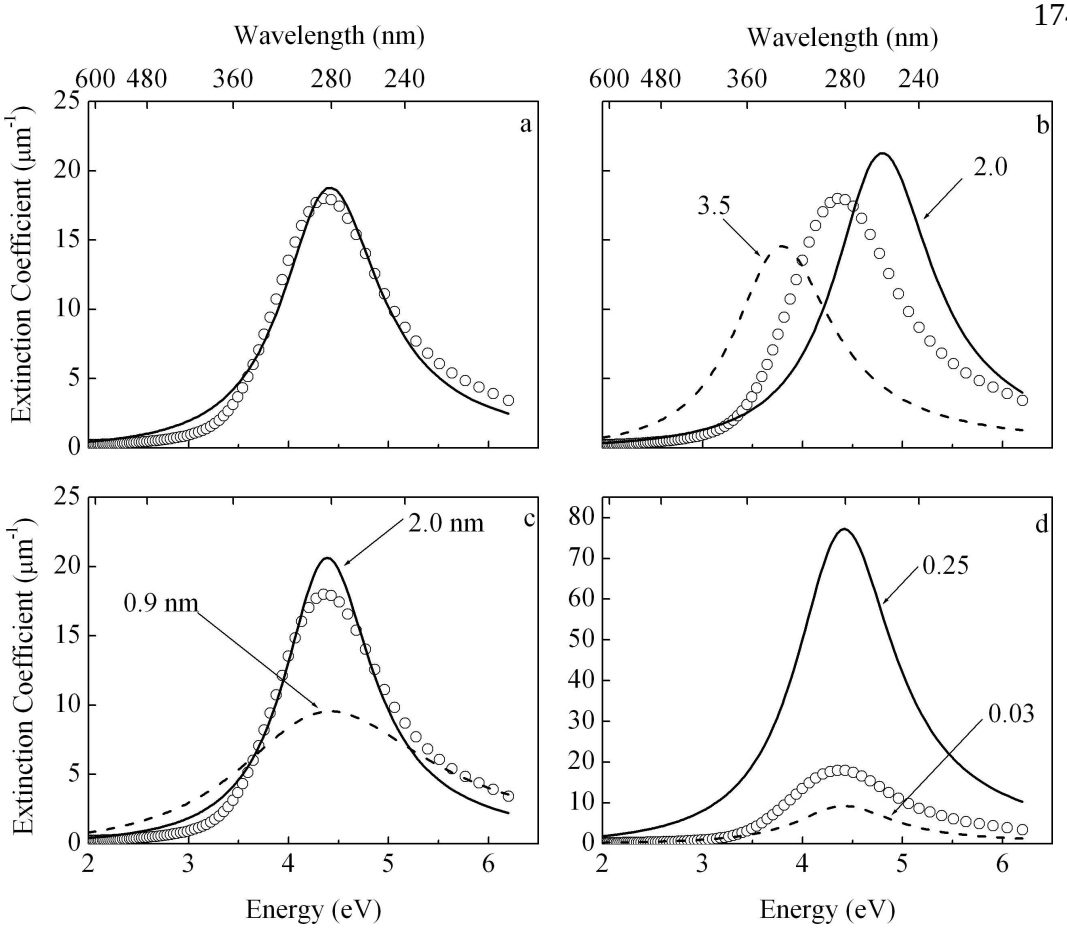


Figure 5.6: Theoretical fitting of the MT to the experimental data after the 723 K anneal. The open circles represent the experimental data while the theoretical curves are drawn in solid and dashed lines. Comparison between experimental data and theoretical spectra when (a) the best fit (ϵ_h = 2.45, d = 1.5 nm, p = 0.08) values, referred to as MT-fit in the text, are used (b) the ϵ_h is changed from the best fit value to 2.0, the real part of the linear dielectric constant of the unimplanted MgF_2, then to 3.5. (c) d is changed from the best fit to 0.9 and 2.0 nm. (d) p is changed from best fit value to 0.03 and 0.25. Note the scale difference in subfigure d.

Raising ϵ_h above 2.45 does the opposite, shifts the PR peak position to lower energy and reduces the intensity, when d and p are kept constant at the best fit values. In figure 5.6c, ϵ_h and p are kept constant at the MT-fit values and increasing the value of d nominally tends to change the intensity without affecting the PR peak position with small changes in the FWHM. Reducing d to values smaller than 1.0 nm, while ϵ_h and p are

constant, has the effect of reducing the extinction intensity and broadening the FWHM with PR peak position remaining practically unchanged. Varying *p* has the effect of broadening the FWHM and increasing the intensity of absorption without altering the PR peak position (see figure 5.6d). The effects of changing *p* and *d* on the extinction spectrum are therefore not independent from a theoretical point of view. The results of fitting the experimental data to the theory are shown in figure 5.7 for the four different annealing temperatures considered : 543, 633, 723 and 813 K labelled as a, b, c and d, respectively. The theory, represented by the solid curve, provides a relatively good fit to the experimental spectra.

The variation of the fit parameters with annealing temperature as extracted from

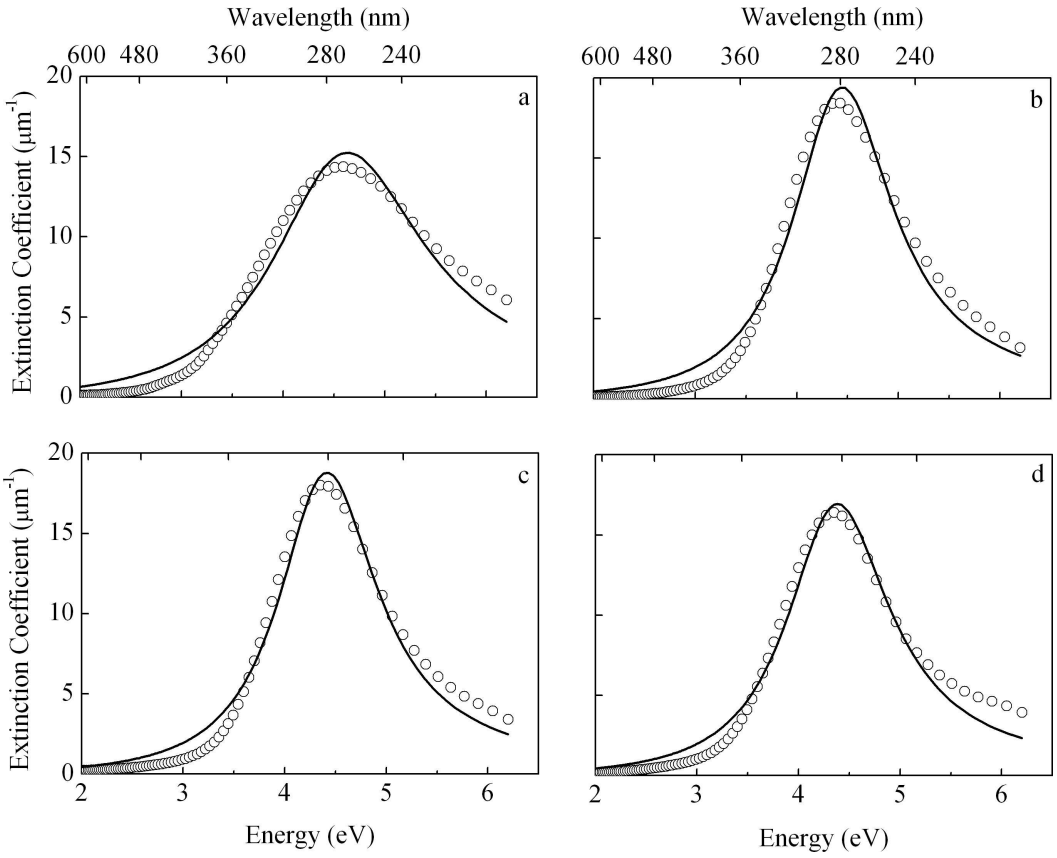


Figure 5.7: MT fit to the experimental data after annealing at a : 543, b : 633, c : 723 and d : 813 K.

Anneal Temp. (K)	543	633	723	813
ϵ_h	2.1	2.4	2.4	2.4
d (nm)	1.2	1.4	1.5	1.5
p	0.17	0.09	0.08	0.07
$(\triangle\omega_{1/2} \times 10^{15})$ (s^{-1})	2.5	1.8	1.8	1.8
$d = 2v_F/\triangle\omega_{1/2}$ (nm)	1.3	1.7	1.7	1.7

Table 5.1: Details of the parameters used to fit the experimental data using MT shown in rows 2 - 4. The data after the double line shows the experimental values of the FWHM ($\triangle\omega_{1/2}$) used to calculate d. The Fermi velocity v_F (Mg) $\approx 1.58\times10^6$ m/s.

the MT model are shown in Table 5.1. The dielectric constant, ϵ_h, after annealing at 543 K is above the value of 2.0, the linear dielectric constant for unimplanted MgF_2, and increases slowly with higher annealing temperature. The mean particle diameter (d) not only increases as expected and seen from the narrowing of the colloid bands with higher annealing temperature but also attains a maximum size in the 723 - 813 K range before decaying on further heating. Estimates of the mean particle diameter obtained from the ratio of the Fermi velocity [329] to the FWHM [346] of the colloid bands are similar to those obtained from the MT model.

The volume fraction, p, decreases after annealing above 543 K and then appears to decrease very slowly with increasing temperature. p has been defined earlier (see section 2.5.2) as the product of the number of particles per unit volume (N/V) and the average volume of a single particle (V_0). The decrease in p following annealing above 543 K is attributed to a lower value of N/V resulting from the growth of larger particles at the expense of the smaller ones by the Ostwald ripening mechanism, as observed in the increase in d. The proximity of the exterior surface of the sample in this low energy implantation is probably also a factor to consider in the variation of p, since the surface may act as a sink to the small particles and the excess atoms. A gradually slow decrease in the value of p, following annealing at higher temperatures, suggests an equilibrium between the two processes of loss of smaller particles and the excess atoms.

5.5.5 Effects at Higher Annealing Temperatures

Samples annealed in air showed unexpected optical absorption features at high annealing temperatures as can be seen in figure 5.8. It is noted that that the measured height of the colloid band of spectrum 6 in figures 5.4 and 5.8 are different. This appears due to stray light effects in the VUV monochromator. As the Mg colloid band decreases in intensity, strong absorption appears near 7.0 eV (177 nm) and extends to higher photon energies. This process became visible after the 813 K anneal and intensified after annealing at higher temperatures. A white coating appeared on the implanted sample at this stage. A possible explanation for this behaviour is as follows.

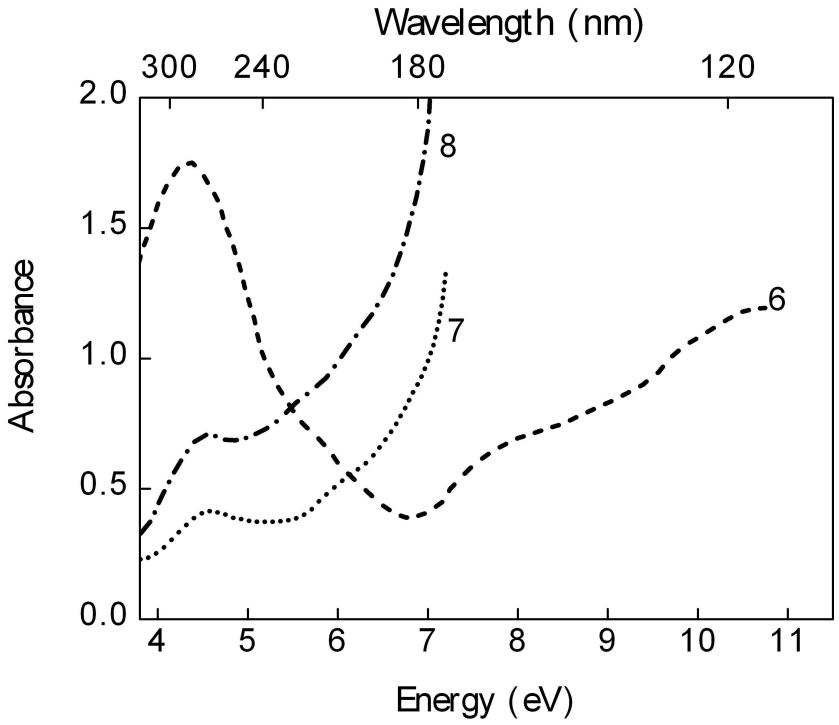


Figure 5.8: High temperature annealing behaviour in air for a MgF_2 crystal after ion implantation with 100 keV Mg^+ ions to a fluence of $10^{17}/cm^2$ at LNT and warmed to RT. The curves show successive optical absorption spectra over the UV and VUV photon energy range (3.8 - 11 eV) during an isochronal anneal consisting of stages each of duration 30 minutes. The spectra were measured at RT. The numbering of the spectra corresponds to that of figure 5.4 (6 : 813, 7 : 903, 8 : 973 K).

Initially, Mg exists in the colloidal form until such a temperature that the colloids break up. This is above 723 K (corresponding curve not shown in figure 5.4) in the present case. Increasing the temperature further enhances the process of disintegration of the colloids into smaller clusters which eventually diffuse into the surface and near surface layer and reacts with other elements forming a sublayer with different optical properties from the host matrix resulting in a red shift of the absorption edge to about 7.5 eV.

It was obvious that a totally independent technique had to be used to probe the elemental constituents of the near surface region (from 0 to 300 nm) including the white coating observed on the surface of the sample annealed in air. The XPS technique was selected and applied to an air annealed sample after the 973 K annealing stage. The results are shown in figure 5.9 and are a clear indication of the existence of oxygen and excess magnesium within the region of the mean projected range of the magnesium ions in the implanted surface layer of the sample. A small broad peak of Mg occurs about 50 nm from the surface in the region of the mean depth of the implanted ions but which has been modified by diffusion during the process of annealing. Oxygen is detected in the near-surface region and has a distribution very similar to that of the excess magnesium.

The value of the bandgap of MgO reported to be between 7 and 9 eV [347, 348] is in agreement with the effects seen in figure 5.8. The absorption background across the entire spectral region observed on spectra 7 and 8 in figure 5.4 is also associated with the formation of this oxide layer. Thus the hypothesis of the formation of near-surface MgO resulting from the diffusion of the implanted magnesium to the surface and combination with oxygen is given strong support. It is seen that the surface itself has a somewhat lower concentration of MgO; presumably there is loss of material to the environs supported by the observation of the white coating on the surface. The XPS results also show a region beyond that near surface in which the elemental constituent ratio of magnesium and fluorine remains constant. This corresponds to bulk MgF_2

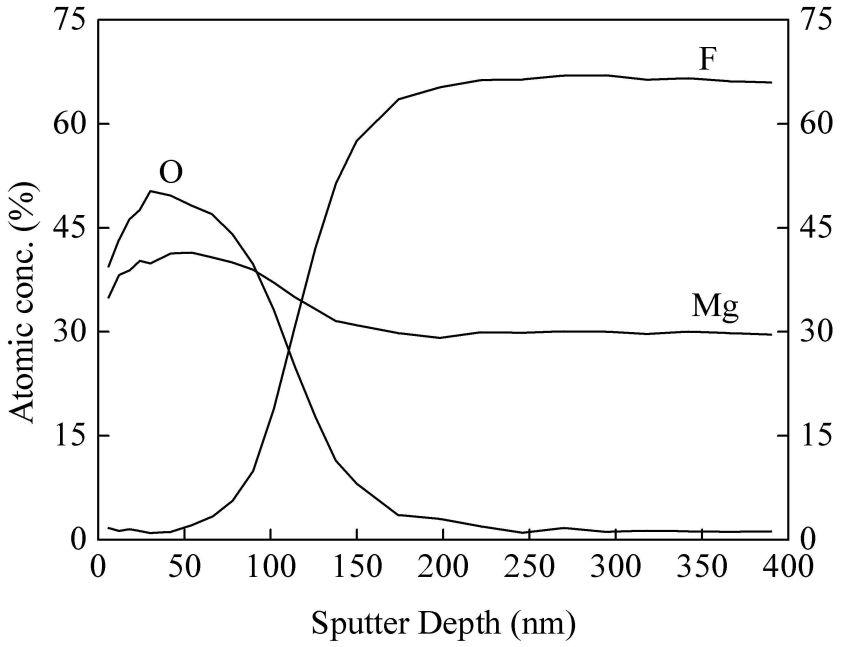


Figure 5.9: Near surface analysis of a MgF_2 sample after implantation of 100 keV Mg^+ ions to a fluence of $10^{17}/cm^2$ at LNT, warmed to RT and subjected to high temperature annealing in air to a temperature of 973 K. The analysis was carried out using XPS and shows the elemental concentration as a function of depth from the implanted surface.

unaffected by the implantation and subsequent annealing processes.

The movement of the excess Mg ions, established by the XPS analysis, towards the surface is hardly surprising because of the existence of vacancies and the general lattice disorder created along the tracks of the implanted ions and subsequent recoil of the target atoms. It is therefore highly probable and also energetically favourable for the excess Mg ions to diffuse into this region than to displace bulk atoms in the region least affected by implantation-induced damage. Diffusion into the bulk would require relatively higher displacement energies like those imparted by accelerated ions which may not be achieved at the annealing temperature range used currently.

5.5.6 Argon Annealed Samples

Having already established that diffusion of oxygen is taking place into the implanted crystal face, an anneal of a similar sample in high purity argon gas was undertaken to examine the behaviour of the colloid band in an environment with minimized oxygen. Figure 5.10 shows the room temperature optical absorption spectra for the sample annealed in an argon atmosphere at 813 and 903 K. Similar behaviour to that shown in figure 5.8, namely increased absorption at photon energies above 7 eV, is observed. However the effect is much less than that observed in the air annealed sample and is attributed to traces of oxygen in the argon gas probably caused by minute leaks

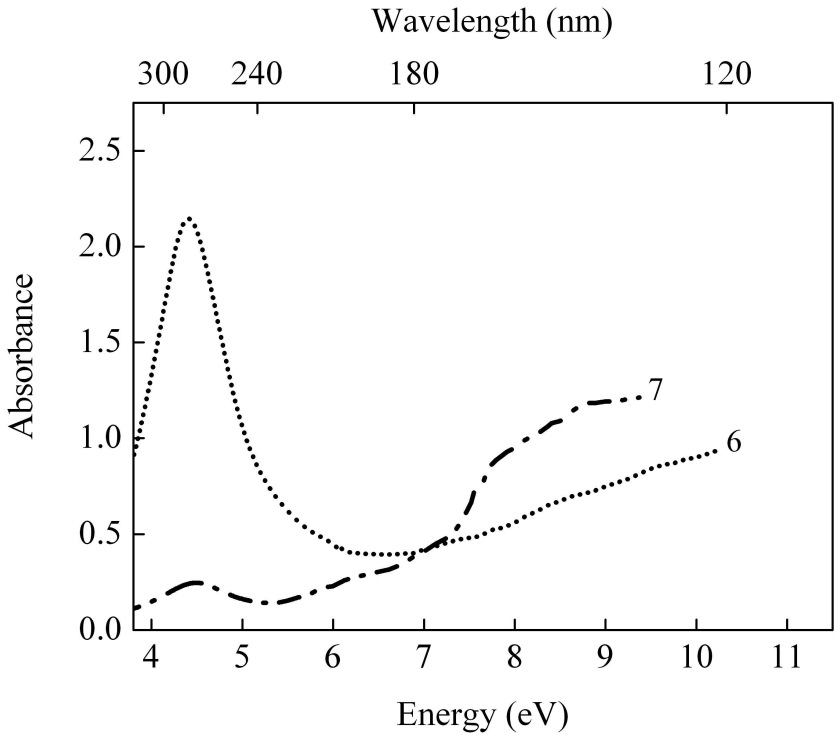


Figure 5.10: High temperature annealing behaviour in argon for a complementary MgF_2 crystal after implantation with 100 keV Mg^+ ions to a fluence of 10^{17}ions/cm^2 at LNT and warmed to RT. The curves show successive optical absorption spectra over the UV and VUV photon energy range (3.8 - 11.5 eV) during an isochronal anneal consisting of stages each of duration 30 minutes The spectra were measured at RT. The numbering of the spectra corresponds to that of figure 5.4 (6 : 813, 7 : 903 K).

in the high temperature furnace and gas delivery system. The decay of the colloid band in the sample annealed under gentle argon flow, from the prominent band observed at lower temperatures, occurs at a similar temperature (903 K) to that measured in the air annealed sample. It is likely that the decay of the colloid band after annealing at 903 K is related to melting of the Mg MNP which is known to occur near 922 K in bulk metal.

5.6 Summary and Discussion

The primary products in a material where the excitonic mechanism is the dominant process of damage creation are vacancies and interstitials. This mechanism is well documented for MgF_2 as being largely responsible for damage creation. Although optical absorption bands due to halogen interstitials defects in the widely studied alkali halides have been observed, the same has not happened for MgF_2. There is, however, a report in which *H* centres have been observed using an electron spin resonance technique following neutron irradiation of MgF_2 [215] at 4 K. The present study reports effects produced in MgF_2 crystals following the implantation at LNT of 100 keV Mg^+ ions to a fluence of 10^{17} ions/cm^2. Optical absorption measurements after warming to RT and subsequent isochronal annealing reveal a broad absorption near 7.5 eV (165 nm) present in the VUV spectra of the as-implanted crystals. By means of the difference spectra, two component *V* bands not previously observed are identified near 7.8 eV (159 nm) and 6.5 eV (191 nm). The composite *V* band absorption is associated with interstitial fluorine defects created during the ion implantation and modified in structure by annealing. Although ion implantation in the present work was done at low temperatures the actual optical measurements were carried out at RT and higher temperatures. It is therefore considered that the centres observed are clusters of halogen interstitials and result in the two absorption bands in the VUV. The conversion of the halogen cluster band at higher energy to the one at lower energy is attributed to

the structural transformations within the cluster types. As discussed in section 1.10.4, earlier work suggested that the band formed near 7.5 eV could be due to fluorine in a molecular form. The present work both confirms this suggestion and provides detailed information on the fluorine interstitial nature of the UV absorption bands in this region.

The development during isochronal annealing of a Mg colloid band near 4.43 eV (280 nm) is discussed. The band is produced by aggregation of the implanted Mg^+ ions. Although the decay of the F, F_2 and V bands coincide with the beginning of the growth and narrowing of the colloid band, which could imply the formation of intrinsic colloids, it is likely that the colloid bands themselves are dominantly formed by the agglomeration of the excess Mg^+ ions introduced by the implantation. The progressive narrowing of the colloid band with increasing annealing temperature is directly linked to the growth of the mean size of the MNP reaching a maximum at the 723 - 813 K range. Beyond this temperature range the particles break up again. The Mie theory (MT) simulations performed to estimate the particle size clearly indicates an increase in the mean Mg MNP diameter with the annealing temperature. Fitting the Mie theory to the experimental spectra also shows that the dielectric constant (ϵ_h) of the host increases with higher annealing temperatures. It is noted that while ϵ_h has been used as a fitting parameter, the dielectric properties of the metal particles have been calculated from theory. Thus all variations will be reflected by changes in ϵ_h.

The diffusion of oxygen into the implanted layer leads to the formation of MgO manifested by the shift in the absorption edge to 7.7 - 7.9 eV. This has been confirmed by the XPS technique used to analyze the elemental constitution of the surface layer of the sample annealed in air at 973 K. The results of the XPS study provide a clear indication that for samples annealed in air, diffusion of oxygen atoms from the environment is a significant factor affecting the disintegration of colloids near the surface. It appears that due consideration of such effects needs to be made in general when annealing ion implanted materials to optimize nano-sized colloids, particularly if potentially reactive

metals are used. Similar optical absorption studies performed in argon gas showed minimized effects of absorption and the shift of the absorption edge to longer wavelength with annealing temperature. The onset of significant decay of the colloid band on annealing in air and under gentle argon flow has been found to occur at a similar temperature, 903 K. This temperature is sufficiently close to the melting point observed in bulk metal, 922 K, suggesting the likelyhood that melting and dispersion of the Mg MNP takes place.

Chapter 6

Optical Studies of Ag and Au Metal Nanoparticles Embedded in Lithium Niobate

6.1 Motivation and Scope of Work

A review of the properties of lithium niobate (LN) has already been presented in subsection 1.11. Certain materials co-evaporated or ion implanted with noble metals and commonly known as nano-composites have optical properties that have recently become a subject of intense investigations [349, 350]. The introduction of silver and gold particles by the use of ion implantation into LN was proposed to study the changes in the optical behaviour of the composite as a whole. The properties observed would then originate from the host material itself and the noble metal nanoparticles (MNP) embedded in it. It is possible that the host dielectric constant changes in the present case where a high fluence ion implantation method has been used. The optical properties of the samples are studied as a function of the annealing temperature as the MNP grow due to agglomeration and as the substrate recovers its crystallinity from implantation-induced damage. It is acknowledged that several workers including Williams et al. [351], Rahmani et al. [245] and Kling et al. [249, 250] have carried out implantations using Au and Ag, Ag^+ and Pt^+ ions, respectively, in LN substrates. The present work goes further not only to point out the effects of higher temperature annealing on the MNP but also on both the implanted and unimplanted host matrix, among other aspects. The Mie theory (MT) in conjunction with the properties of the host matrix has been used [352] to determine the sizes of the Ag MNP in glass using an ion exchange method where the implantation fluence and type of the bombarding ion was varied. The MT, with higher order terms, is extended to a situation where annealing is used to change

the sizes of the implanted MNP and an attempt made to correlate the prediction from the theory and the average particle sizes observed from TEM studies.

6.2 Preparation and Implantation of LN Samples

6.2.1 Introduction

Both a 25×25×1 mm^3 X-cut face of the crystal slice and large crystal boules from which the 10×10×1 mm^3 Y-cut face was prepared (see section 3.5) were donated by Crystran Ltd (UK). These two crystal faces are perpendicular to each other (see figure 1.16). The Ag^+ ion implantations were carried out using the ion implanter, while the Au^{3+} ion implantation was performed using the tandem accelerator. A description of the main features and the principle of operation of both the implanter and the tandem accelerator are given in subsections 3.4 and 3.3.2, respectively.

The study of the optical properties of metal colloids embedded in LN crystals started with investigations in which several metal ions (Ag^+, Au^{3+} and Na^+) were examined as to their suitability to form colloids after ion bombardment and subsequent annealing. It was found that Ag^+ and Au^{3+} ions achieved these requirements.

6.2.2 Implantation of LN Using Ag^+ Ion Beam

In order to study the effect of temperature, ion implantation was done at LNT, RT and 373 K using the ion implanter at an energy of 100 keV with Ag^+ ions to a fluence of 10^{17} ions/cm^2 on X-cut LN samples.

6.2.3 Implantation of LN Crystals Using Au^{3+} Ion Beam

Since the analyser magnet was not used during the implantation of LN crystals with a Au^{3+} ion beam, beam optics simulations were performed to determine the appropriate acceleration and focusing parameters to be applied to the tandem accelerator

thus ensuring that in practice these ions reached the straight through target chamber and limited the presence of the Au^{2+} and Au^{4+} ions. Suitable electrical signals, applied in two perpendicular directions through the magnetic scanners after the high energy (HE) side of the accelerator (see figure 3.5), were used to sweep the ion beam to attain a spatially uniform beam. The implantation of the Au^{3+} ions into the LN samples was then performed on both the X- and Y-cut faces near RT to fluences of 1×10^{17} ions/cm^2.

6.2.4 Optical Absorption Measurements and Annealing of the Samples

All the optical absorption measurements were performed in the visible (VIS) and near infra-red (NIR) regions using the Cary 500 spectrophotometer described earlier in section 3.7.3. The measurements were carried out at room temperature on both as-implanted and annealed X- and Y-cut samples. Unimplanted X- and Y-cut crystals that were annealed in the same way as for the corresponding implanted samples were used as reference samples.

The implanted LN samples were isochronally annealed in an enclosed Carbolite furnace (see section 3.6) under argon flow after a waiting period of 1 hour to allow for temperature stabilization. A standard annealing period of 30 minutes and a 100 K temperature interval were maintained while the annealing temperature range varied from 373 to 1173 K for the Ag^+ implantations and as high as 1373 K for the Au^{3+} implantations.

6.2.5 Rutherford Backscattering Study of the Au^{3+} Implanted LN Sample

In order to estimate the size of the implanted area on the X-cut Au^{3+} ion implanted sample, a Rutherford backscattering (RBS) study (discussed in section 2.7) was carried out, using the tandem accelerator. The study was done because a non-standard magnetic scanning technique was employed on the beam line to spatially spread the beam and it was therefore expected that the shape of the implanted area would not be

regular. The use of Li^{2+} ions, at an energy of 6 MeV, as opposed to the traditional alpha particles was purely on grounds that better mass resolution between the Nb and Au ions would be achieved.

The sample was mounted on the microprobe/RBS end station (see figure 3.5) and the signals in the form of counts as a function of the channel number (energy) from the backscattered ions were collected via a PC interfaced data acquisition system. The data was obtained from various positions of the sample, 5 mm above and below the centre of the Au^{3+} ion implanted region, enabling the presence of Au in the implanted area to be checked. The findings are discussed in subsection 6.5.1 to follow.

6.2.6 TEM Specimen Preparation

Two $4\times3\times1$ mm^3 crystal slices were ultrasonically drilled out from the Ag^+ ion implanted sample, using a hollow rectangular drill bit, and glued with the implanted the faces touching each other. Silicon crystal slices of similar size were attached on either side, as shown in figure 6.1a, such that the whole piece could fit into a 4 mm thick slot of an attachment that could be mounted on the sample holder of an ultrasonic drill. A cylindrical section, 2 mm in diameter, was drilled out of the sandwich-like structure with the drilling running parallel to the length of the ion implanted faces. The cylindrical section was then inserted into a cylindrical brass tube with a slightly larger diameter and the two were held together by a specially prepared mixture of epoxy before being placed in an oven at 513 K for two hours in order to cure the epoxy. Figure 6.1b shows the cross-sectional view of the original cylindrical brass and sandwich-like section from which 0.5 mm thick specimens were cut and thinned down by hand grinding to about 70 μm using a 1 μm diamond suspension. An argon gas ion mill was then used to drill a microscopic hole at the interface of the implanted faces for viewing in the TEM. The preparation of the Au^{3+} ion implanted LN samples were performed in a similar manner

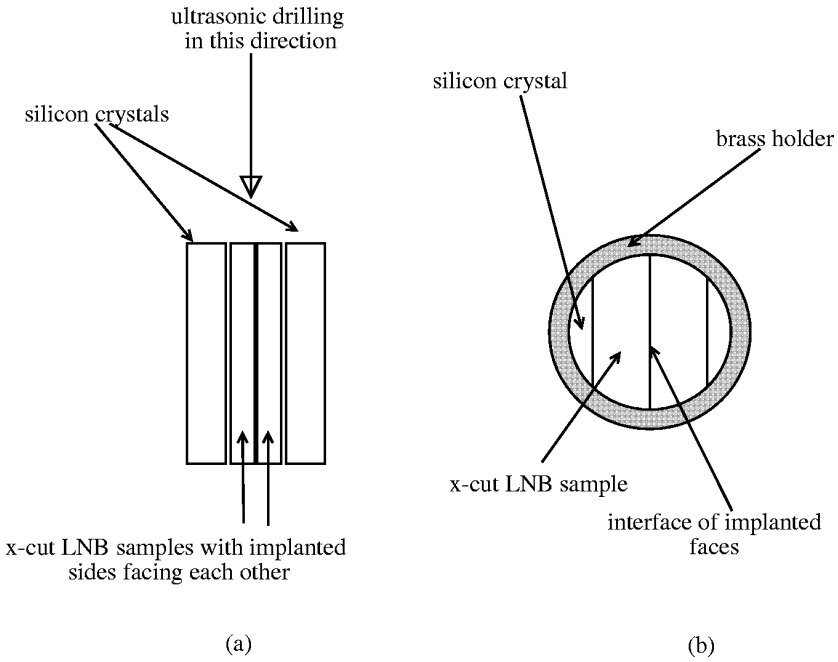


Figure 6.1: Schematic diagram of the main stages of the TEM sample preparation. (a) Two sample slices with the implanted surfaces facing each other sandwiched between silicon crystal slices using epoxy. (b) Cross-sectional view of the cylindrical brass tube and sandwich-like structure.

Sample	Implantation conditions	Comments
1	LNT, 100 keV, 1×10^{17}ions/cm^2	Ag^+, X-cut, annealed, TEM
2	RT, 100 keV, 1×10^{17}ions/cm^2	Ag^+, X-cut
3	373 K, 100 keV, 1×10^{17}ions/cm^2	Ag^+, X-cut, annealed
4	LNT, 100 keV, 1×10^{17}ions/cm^2	Ag^+, X-cut
5	RT, 8 MeV, 1×10^{17}ions/cm^2	Au^{3+}, X-cut, unannealed, RBS
6	RT, 8 MeV, 1×10^{17}ions/cm^2	Au^{3+}, Y-cut, annealed
7	RT, 8 MeV 1×10^{17}ions/cm^2	Au^{3+}, X-cut, annealed
8	RT, 8 MeV 1×10^{17}ions/cm^2	Au^{3+}, X-cut, annealed, TEM

Table 6.1: Details of the LN sample identity, implantation conditions and subsequent analysis after implantation. Ion implantation was performed by the implanter for the case of Ag^+ ions, while the tandem accelerator was used for the higher energy implantation of Au^{3+} ions in LN crystals.

6.2.7 Identity of Implanted Samples

The implantation conditions and other relevant information for the various samples prepared in the present study are supplied in Table 6.1.

6.3 Results and Discussion I: Optical Absorption Effects of Annealing on the Host Matrix

Heating unimplanted X-cut and Y-cut LN was found to have appreciable effects on its optical absorption properties above 973 K. Only small changes were noted between room temperature and 873 K. The results of the changes of the optical absorption of unimplanted X-cut LN as a function of annealing temperature are shown in figure 6.2a. Similar effects are observed for the Y-cut LN in figure 6.2b. These results are in agreement with studies by several workers on thermal reduction of LN [239] and attributed to the introduction of oxygen vacancies during heating. It is likely that the optical absorption spectra of the implanted MNP are actually superimposed on the absorption of the annealed unimplanted part of the host matrix. These optical absorption effects have been corrected in the spectra of the implanted samples (figures 6.5 and 6.11) in order to leave only the effects of the optical absorption of the MNP and defects induced by the implantation. These spectra are therefore presented on the assumption that the annealing behaviour of the virgin crystal is essentially that of the undamaged part of the ion implanted LN samples. Since the SRIM2003 simulations will indicate that the implanted region is a very small part of the effective optical path of the optical absorption measurements, this is a reasonable assumption. It is noted that the effect of the optical absorption changes in the unimplanted part of the host matrix, normally also subjected to high temperature annealing if necessary to encourage development of MNP, is an important aspect that has not been adequately addressed in the large volume of reported literature dealing with this field. Optical absorption effects in LN have been observed, by Kling et al. [249], to occur in annealed Pt^{+} ion implanted LN but not discussed in detail.

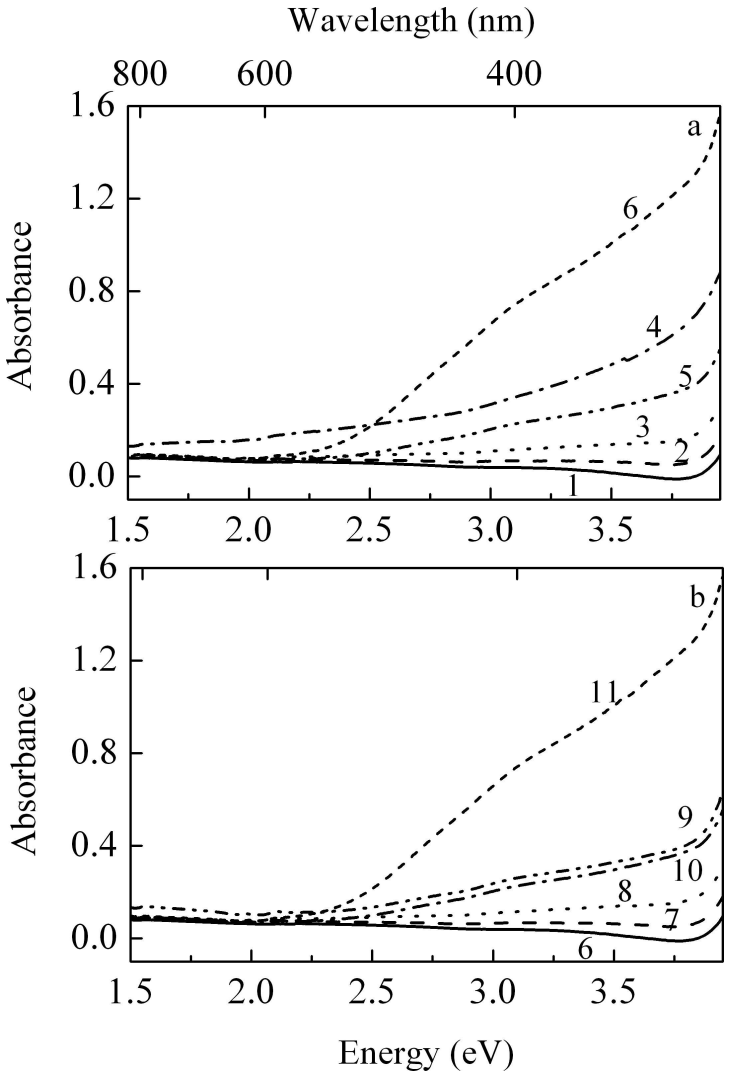


Figure 6.2: Optical absorption spectra of unimplanted (a) X-cut LN (1: unannealed, 2: 973, 3: 1073, 4: 1173, 5: 1273, 6: 1373 K) and (b) Y-cut LN (6: unannealed, 7: 973, 8: 1073, 9: 1173, 10: 1273, 11: 1373 K) following annealing under argon flow. All measurements were performed at RT with a similar virgin and unannealed X- and Y-cut LN crystal, respectively, as reference.

6.4 Results and Discussion II: Ag^+ Ion Implanted LN

6.4.1 Optical Absorption Studies of Ag^+ Ion Implanted LN Samples

Figure 6.3 shows the optical absorption spectra of three similar X-cut LN samples which were all implanted with 100 keV Ag^+ ions at LNT (77 K), RT (300 K) and 373

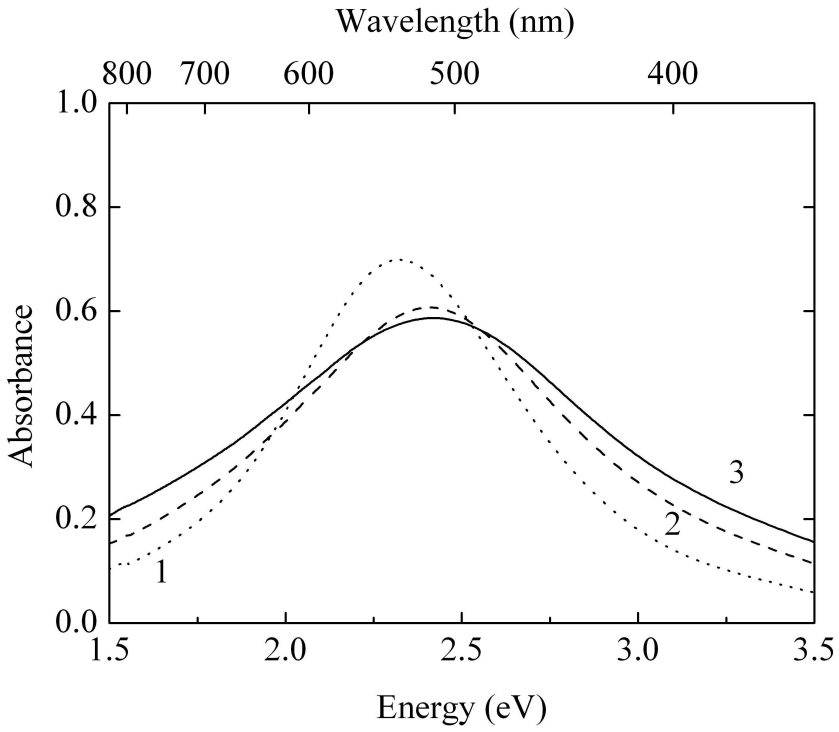


Figure 6.3: Absorption spectra of similar X-cut LN samples implanted at various temperatures with 100 keV Ag^+ ions to a fluence of $10^{17}/cm^2$: 1 (LNT), 2 (RT) and 3 (373 K). All measurements were performed at RT immediately after ion implantation.

K to a fluence of 10^{17} ions/cm^2. The optical absorption bands produced are associated with the formation of metallic colloids in the LN matrix and were rather broad indicating the presence of a significant particle size distribution. The metal colloid bands formed are observed in the visible region of the spectrum and the peaks are located at 2.33, 2.42 and 2.41 eV for these samples namely, 1, 2 and 3, respectively (see Table 6.1). Unlike the case of Mg^+ ion implantation into MgF_2 (chapter 5), the colloid bands are formed in the as-implanted samples 2 and 3 respectively implanted at temperatures of RT and 373 K. This indicates that the implanted Ag^+ ions are mobile in the implantation temperature range used. The discussion of the mobility of the Ag^+ ions is taken up further below.

The characteristics of the optical absorption spectrum of sample 1, implanted

at LNT, are different from those of samples 2 and 3. It has a narrower full width at half maximum (FWHM), the peak absorbance is red shifted and relatively higher compared to the samples implanted at the other two temperatures. This is probably due to the implantation at LNT where retention of defects created is higher due to lower diffusion rates. This sample is also effectively annealed by warming it to RT leading to agglomeration of the existing Ag^+ ions in the LN matrix. A general deduction from these three optical spectra is that the sample implanted at LNT has a smaller particle size distribution.

It is clear that the Ag^+ ions are mobile during and after the ion implantation at RT and above as they become mobile during the warming of sample 1 to RT. A layer of Ag was observed on all the sample surfaces after 1 - 2 days of storage in a dark desiccator at RT. Similar observations have been previously reported elsewhere [247]. The diffusion of the Ag atoms from the implanted layer to the surface may be explained as follows. Implanting the highly polarizable Ag^+ ions to a fluence of 10^{17} ions/cm^2 with an energy of 100 keV (a predicted mean penetration depth of only 34 nm below the surface using SRIM2003 [13], see figure 6.4), creates such a large concentration gradient and high stress levels in the LN matrix that some of the implanted atoms diffuse to the surface readily without the application of extra thermal energy other than that from the ambient. This expulsion of the Ag atoms from the implanted layer is necessary to reduce the stress leading to relaxation of the Ag MNP/matrix. However, this posed a problem because the effective ion fluence for the LN sample would be different from that recorded during implantation making its accurate value uncertain.

Figure 6.5 shows the optical absorption spectra of sample 3 (implanted at 373 K, fluence 1×10^{17} ions/cm^2) taken at RT, after annealing in an argon atmosphere at various temperatures. The spectrum measured at RT after the implantation is included to provide the initial band shape prior to annealing. The rest of the spectra shown start from an anneal at 573 K since there was no noticeable change in the size and

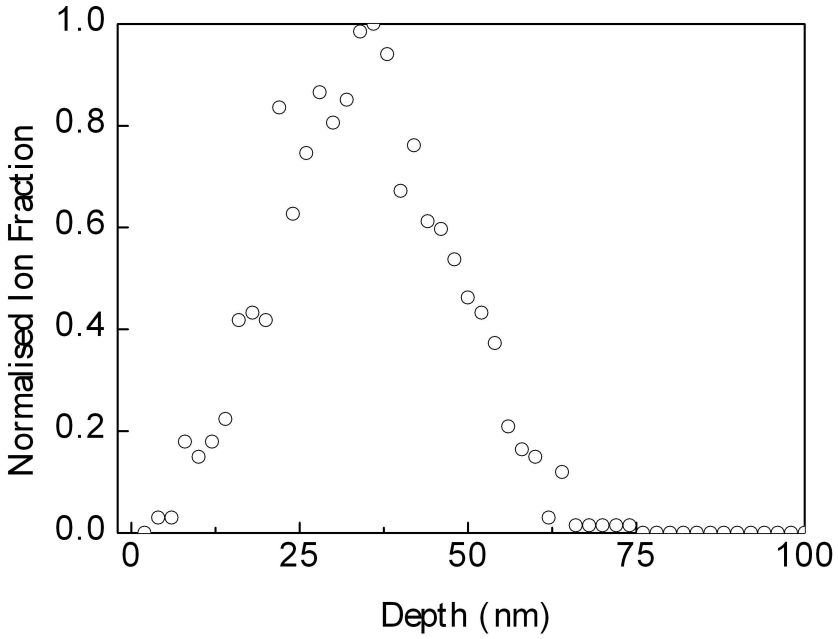


Figure 6.4: Ion distribution versus depth profile obtained from a SRIM2003 simulation of implantation into LN crystals of Ag^{+} ions using energies of 100 keV.

shape of the spectra obtained on annealing at lower temperatures. After annealing at 573 K the colloid band narrows while the PR peak position remains almost unchanged relative to the spectrum obtained at 300 K. From this figure, it can also be seen that the change in the size and shape of the colloid bands was not large below 973 K. There is a small increase in the value of the peak absorbance following annealing between the 573 and 773 K, while the position of the PR peak moves from 2.398 eV to 2.309 eV in the same temperature interval. After the 973 K anneal, there is very little change in terms of the position and intensity of the PR peak but the band broadens on both sides indicating a reduction in the mean particle size of the Ag MNP. Annealing at 1173 K drastically reduces the absorption over the entire region and what appears to be the PR peak approaches an energy (near 2.353 eV) observed after the 573 K anneal. The spectrum obtained after the 1173 K anneal is no longer symmetric and shows more complex structure over the 1.5 - 3.5 eV spectral region. All spectra measured after

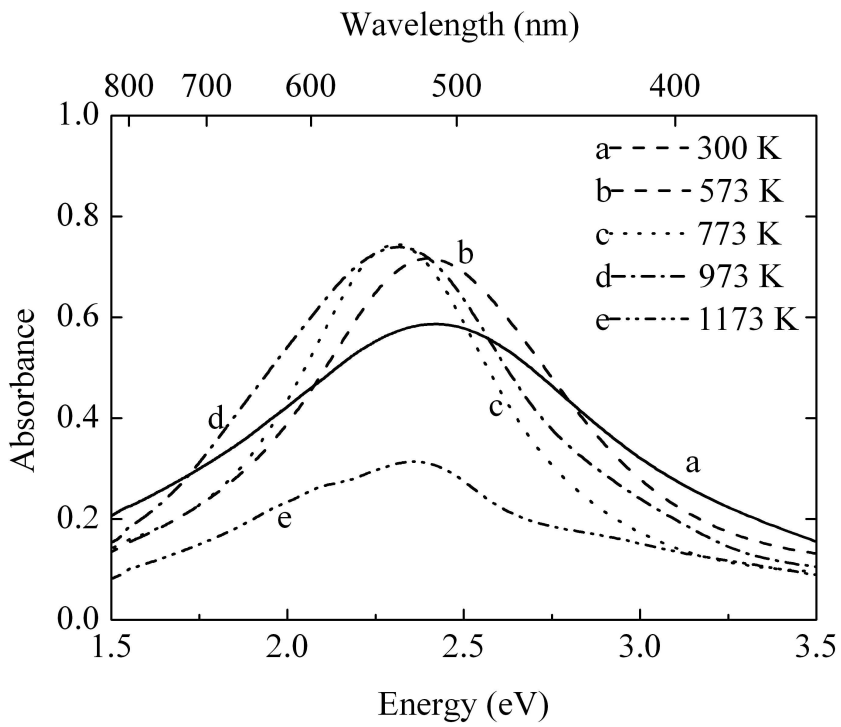


Figure 6.5: Absorption spectra of sample 3 (X-cut LN face), implanted with 100 keV Ag^+ ions to fluence of $1\times10^{17}/cm^2$ at 373 K, obtained at 300 K and after the annealing temperatures indicated. The optical absorption measurements were performed at RT.

annealing at 1173 K have been corrected for optical absorption effects that occur in the host matrix and which were observed to become significant near and above this temperature.

The phenomenon of diffusion of the Ag atoms from the implanted layer to the exterior surface of the sample, described in a previous paragraph in this subsection, tends to limit the growth in size of the Ag MNP indicated by the small change in the intensity and the FWHM of the optical extinction bands below 1173 K. The size of the Ag MNP will not change significantly due to a competing diffusion process of Ag atoms out of the implanted layer to the exterior surface as well as ripening mechanisms [115] which also result in an equilibrium MNP size.

As discussed in subsection 5.5.3 of chapter 5, it is assumed that the colloid band

is formed by the agglomeration of the excess Ag^+ ions introduced into the LN crystal by ion implantation. High temperature diffusion leads to Ostwald ripening of the colloids [115] with larger particles growing at the expense of the smaller ones and resulting in a sharper particle size distribution. Although the systems are different, being Mg in MgF_2 and Ag in LN, the sequence of diffusion of single or clusters of defects leading to annealing of damage, agglomeration of the MNP and finally dispersion of the metal particles in the matrix as the colloid bands decay appear to be similar.

It has been assumed in the overwhelming majority of studies that the refractive index of the medium embedding small metal particles remains unchanged after the process of incorporation the MNP. This may not be true for a preparation method such as ion implantation and perhaps others used to introduce metal ions in a host matrix. It has already been shown in the previous chapter that the best fits to the colloid bands for the Mg^+ ion implantation result in a value of ϵ_h larger than that of virgin MgF_2. In ion implantation, the MNP are located in the same sublayer that is altered by effects such as preferential sputtering of the lighter ions that make up the host matrix. Accordingly the red shift observed is attributed to the changes in the dielectric constant of the host matrix after ion implantation and subsequent annealing. It is noted from figure 6.5 that there is a shift of the PR peak position to higher photon energy after annealing at 1173 K (spectrum e) with the value closer to that observed after the 573 K (spectrum b) anneal, as the Ag MNP sizes become smaller. Annealing at 1173 K is sufficiently close to the melting point of bulk Ag of 1235 K at which temperature the MNP would be likely to disintegrate and hence change the particle distribution size before dispersing.

6.4.2 Correlation between the MT-Fit and the Experimental Data - Ag^+ Implanted LN

Figure 6.6 shows the results obtained on fitting the FWHM, PR peak position and the intensity to the experimental data after the various annealing temperatures for the

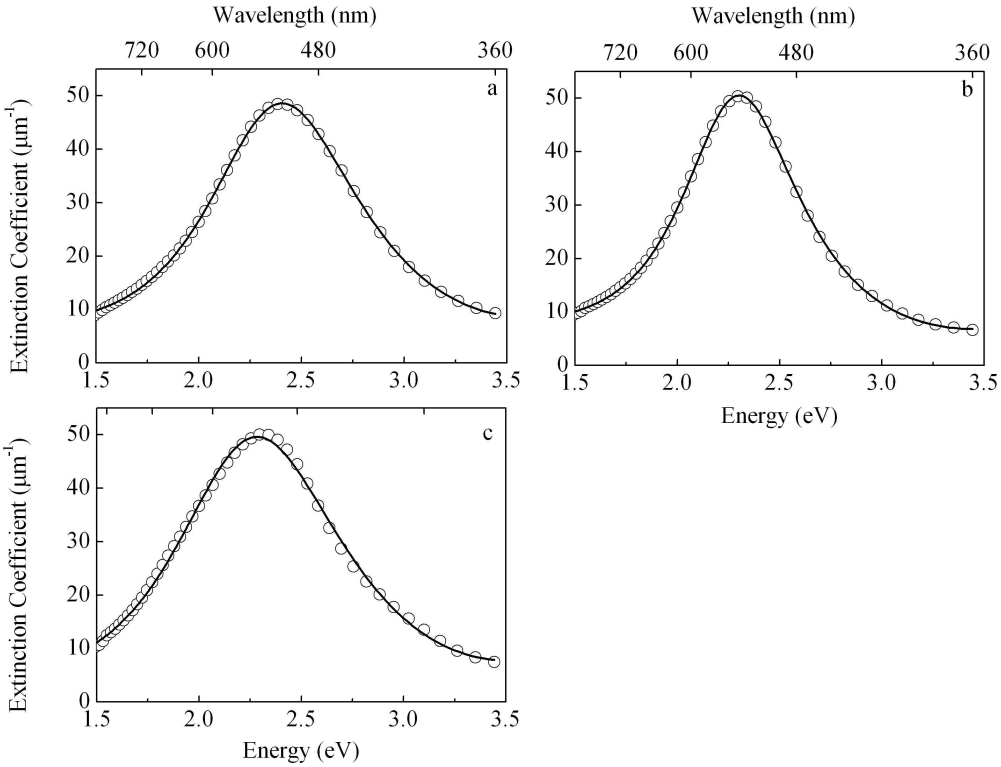


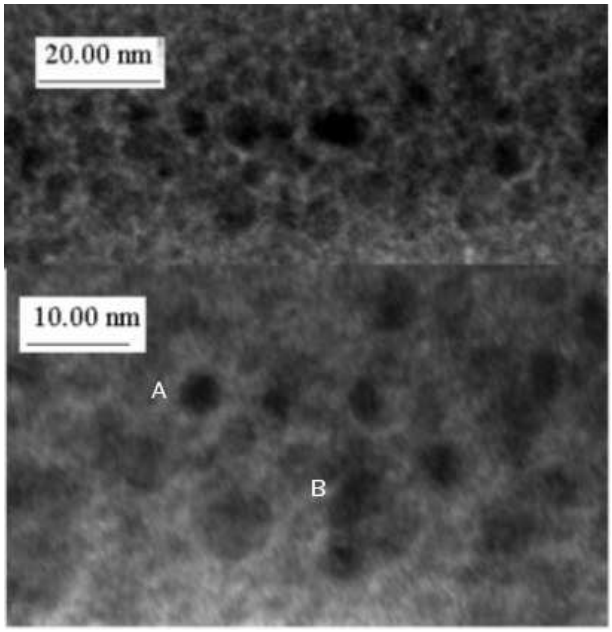
Figure 6.6: Comparison between the experimental data and the MT model, discussed in subsection 2.5.3, of the optical extinction spectra for sample 3 (see Table 6.1) after annealing at 573, 773 and 973 K and labelled a, b, and c, respectively. The X-cut LN sample was implanted with 100 keV Ag^+ ions at 373 K to a fluence of 10^{17} ions/cm^2. The open circles represent the experimental data, while the theory is shown by the solid line.

Ag^+ ion implanted samples (the fitting procedure is discussed in section 2.5.1). Equations 2.61, 2.69, 2.69 and 2.71 are used in the simulations. The correlation between the experimental data and the theory is fair under the assumptions made (see subsection 2.5.3). Table 6.2 presents the details of the fit parameter values namely the host dielectric constant ($\epsilon_h = n^2$, in the optical frequency range), average particle size (d) and volume fraction ($p = (N/V) \times V_0$; see section 2.5.2) with varying annealing temperature. The extracted average value of d increases from about 2.0 nm reaching a maximum near 2.5 nm after the 773 K anneal before decreasing on further heating. The predicted values of d may be compared to figure 6.7 which shows the picture of a

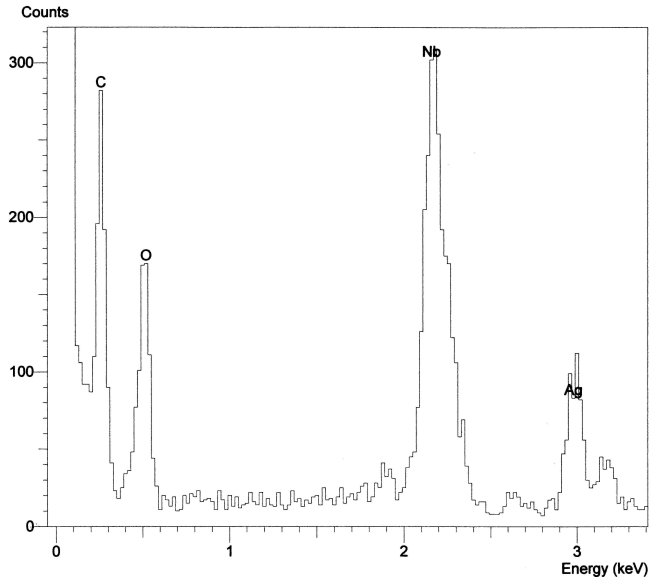
Anneal Temp. (K)	573	773	973
ϵ_h	4.5	5.1	5.1
d (nm)	2.0	2.5	1.7
$p \times 10^{-2}$	1.2	0.89	1.5
$\triangle\omega_{1/2} \times 10^{15}(s^{-1})$	1.38	1.12	1.46
$d = 2v_F/\triangle\omega_{1/2}$	2.00	2.46	1.89

Table 6.2: Details of the fit parameters used to correlate the experimental data to the theory for the Ag^+ ion implanted X-cut LN sample (see rows 2 - 4). For comparison purposes, the data in the row immediately after the double line shows the experimental values of the FWHM ($\triangle\omega_{1/2}$) which can also be used to estimate the values of d.

TEM section from the sample annealed at 513 K indicating a distribution of sizes and shapes. The optical absorption spectrum of this sample would lie between spectra a and b in figure 6.5. The Ag MNP labelled A in this picture looks reasonably spherical and is slightly less than about 5 nm in diameter. Other Ag MNP (for instance B in the same picture) that appear irregular could well be two or more Ag MNP sticking together. It is generally noted, however, that particles do not necessarily have a spherical shape. The comparison between the theoretical values of d and the results of the TEM study is considered fair since the theory used in the present study only predicts an average value whereas in the real case a distribution of particle sizes is observed. The contribution to extinction by scattering for particles with diameter less than 10 nm is small [116] and the current MT simulations confirm that it is negligible. The results of an *in-situ* energy dispersive X-ray (EDX) analysis (see section 3.10) performed during the TEM study is shown in figure 6.7b. The light Li atom which forms part of virgin LN matrix is not detected due to limitation of this instrument but may also be due to depletion by preferential sputtering, while the presence of O, Nb and Ag atoms are attributed to the host matrix and the implanted Ag^+ ions. The C peak arises from aquadag, a quick-set conducting carbon paste commonly used in electron microscopy to prevent charging on the sample surface. Selected area electron diffraction (see section 3.10), performed



(a)



(b)

Figure 6.7: (a) Pictorial results of the TEM cross-section studies of a complementary X-cut LN sample (2, Table 6.1) showing Ag MNP within the embedding host. Lower picture shows a magnified section of the upper one. Ag MNP labelled A appears spherical, while B may be two particles sticking together. (b) EDX spectrum obtained from the implanted region of the TEM section.

to study the nature of the host matrix at selected positions in the implanted sublayer, showed that both amorphous and crystalline regions existed.

Table 6.2, containing the details of the fit parameters from MT model, also shows that both of ϵ_h and d increase after annealing at 773 K. d attains the maximum value at the same temperature before decreasing on further annealing, while ϵ_h increases to about 5.1 after annealing at 973 K. The value of 4.5 obtained for ϵ_h after the 573 K anneal is close to the value of 4.4 quoted for amorphous LN [353]. This is based on the fact that the implantation of the Ag^+ ions causes a significant degree of amorphization of the embedding matrix as suggested by the selected area electron diffraction performed during the TEM study. In the amorphous state the birefringent nature of LN is lost. An increase in the ϵ_h from values obtained for the amorphised host matrix after annealing above 573 K, as in the present work, would be expected as the damage created by ion implantation is removed. Other experiments have reported a decrease of up to 10% in the refractive index on implantation with helium ions [1, 226] and an increase in the refractive index of 5% has been reported in LN implanted with Au ions [351]. Sande et al. [354] have recently reported increases of up to 13 % in the real part of the refractive index, for an alumina matrix containing Ag MNP, above the known value of alumina. This group used an ellipsometric method to determine ϵ_h. It is considered by the present author that the presence of the unaggregated Ag metal is possibly associated with this increase.

The extracted values of p have a minimum value after the 773 K anneal which appears to coincide with the maximum mean particle size of the Ag MNP. A reasonable explanation for this particular observation would be that at maximum particle size, a large fraction of the Ag atoms exist in the colloidal form. The value of p would therefore be relatively low compared to the case when the MNP start to disperse as a result of disintegration indicated by the reduction in d after the next anneal temperature (973 K) or before a larger mean particle size is attained (573 K).

6.5 Results and Discussion III: Au^{3+} Ion Implanted LN

6.5.1 Results of RBS Studies of Unannealed Au^{3+} Ion Implanted LN Sample

Figure 6.8 shows a RBS spectrum of a complementary Au^{3+} ion implanted X-cut LN sample (1, Table 6.1) performed at RT using a 6 MeV Li^{2+} ion beam from the tandem accelerator (section 2.9) and not subject to high temperature annealing. The recoil energy of the Au atoms is well resolved from that of the Nb atoms and the rest of the background, which shows the recoil energy of Li and O atoms as identified in the spectrum. It is assumed that the Au depth distribution profile remains the same for annealing below 973 K as no significant Au MNP bands are observed from optical absorption measurements. RBS studies to estimate the implantation area of the Au

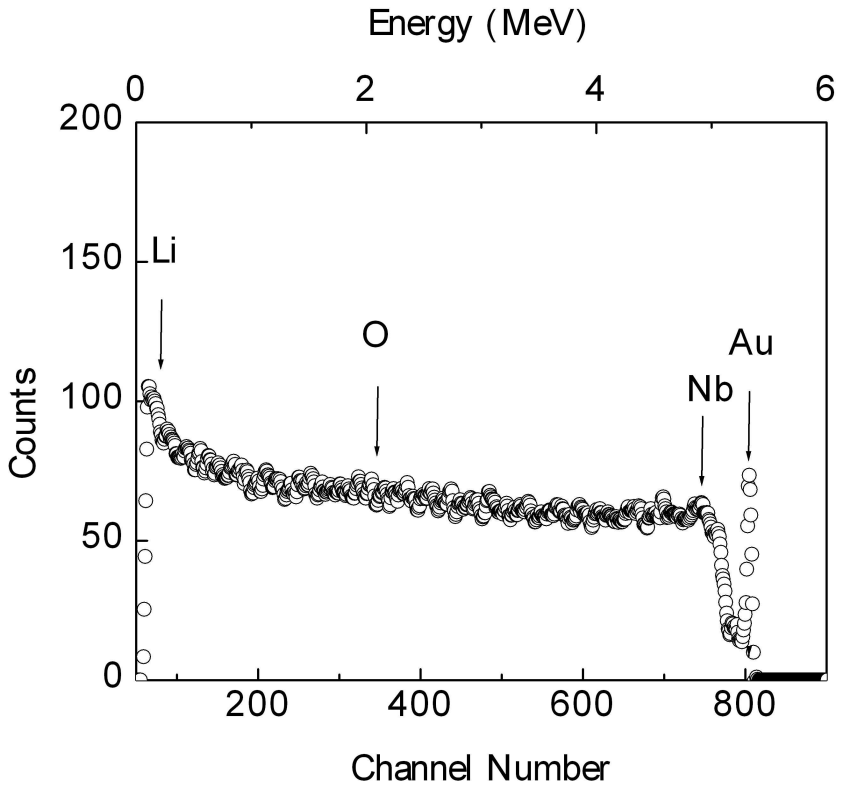


Figure 6.8: RBS spectrum of unannealed Au^{3+} ion implanted X-cut LN sample (7, Table 6.1, section 6.2.7) performed at RT using a 6 MeV Li^{2+} ion beam.

ions at various positions of the sample yield similar features, within a radius of about 3 mm from the centre of the implanted zone. In a related study, Magruder et al. [326] have reported that the position and distribution of the implanted Au^{+} ions in SiO_2 in their RBS spectra remained unchanged during annealing to temperatures as high as 1373 K, in which they used a beam energy of 2.85 MeV for their ion implantation. The use of higher beam energies to create deeper ion penetration in the present case of Au^{3+} ion implantation should therefore lead to more gradual developments in the shape and intensity of the colloid bands with rising annealing temperature compared to the Ag^{+} ion implantation, discussed in section 6.4, where the mean depth is close to the air/sample interface. In the latter case diffusion of the MNP to the surface readily occurs even at temperatures close to RT. Figure 6.9 shows the results of a SRIM2003 simulation [13] of the depth distribution of Au^{3+} ions with an energy of 8 MeV into LN crystals. Since the analyser magnet was not used, there is a possibility of some Au^{2+} and Au^{4+} ions corresponding to energies of 6 and 10 MeV, respectively, also being implanted. The respective mean depths are: 0.9 μm for Au^{2+}, 1.2 μm for Au^{3+} and 1.5 μm for Au^{4+}.

In Figure 6.10 the results of SRIM2003 simulations of the corresponding vacancy distributions are shown. The vacancy distributions are, however, unphysical in the case under consideration. The average number of vacancies per ion is 29781, giving a peak vacancy concentration for the fluence used, of the order of 10^{25} cm^{-3} or about 100 times the atomic density of LN. Thus each atom at the peak of the distribution has been displaced about 100 times. The region of the vacancy distribution between the points at which the tails have fallen to 0.01 of the peak height must therefore be uniformly amorphous. Thus in the region from the surface to the trailing edge of the implanted zone the implanted samples will be of this form. Similar conclusions were drawn Kling et al. [249] in their studies of 50 keV Pt^{+} ions whose atomic mass is close to that of Au implanted into LN with a fluence of 5×10^{15} cm^{-2} using RBS channelling measure-

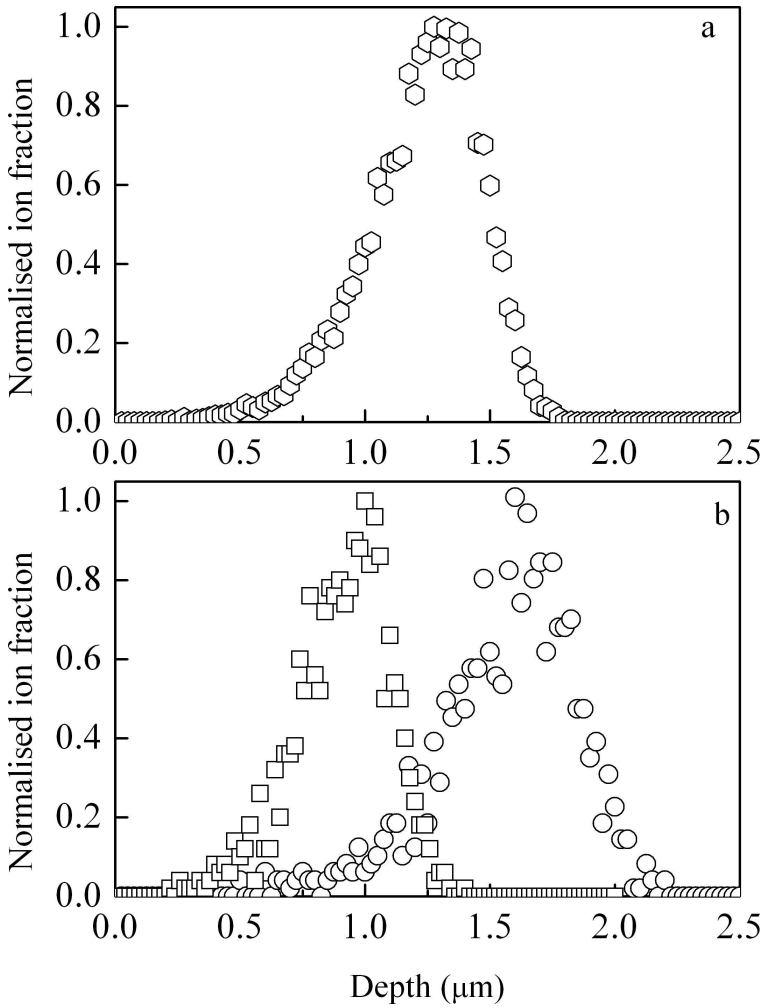


Figure 6.9: Ion distribution versus depth profile obtained from a SRIM2003 simulation of implantation into LN crystals with (a) 8 MeV Au^{3+} ions (open diamonds). (b) 6 MeV Au^{2+} (open squares) and 10 MeV Au^{4+} (open circles). The latter two are included since there is a possibility of these ions finding their way into the target due to lack of use of the analyzer magnet.

ments. Figure 6.10a shows the SRIM2003 results of the electronic stopping power (S_e) for 8 MeV Au^{3+} ions following implantation in LN. These results indicate that only in a limited region does S_e attain the threshold value of 5 keV/nm for amorphization due to electronic excitation by swift heavy ions [353, 355]. Hence the amorphization is expected to arise largely from nuclear stopping in this case.

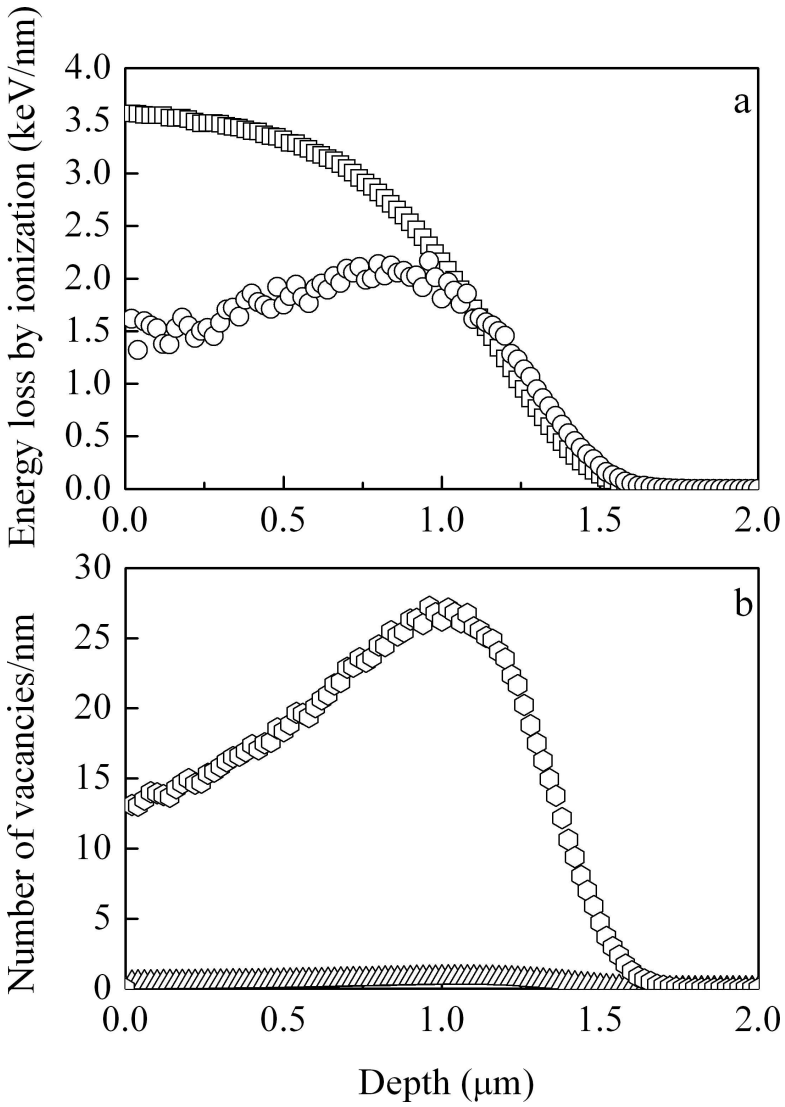


Figure 6.10: The results of a SRIM2003 simulation of implantation into LN crystals with 8 MeV Au^{3+} ions showing the (a) energy loss profile (by primary ions - squares; recoils - circles) and (b) distribution of vacancies (created by primary ions - triangles; recoils - diamonds) as a function of penetration depth.

6.5.2 Optical Absorption Studies of Au^{3+} Ion Implanted LN

Figure 6.11a shows the optical spectra obtained from the Y-cut face of the crystal implanted to a fluence of 10^{17} ions/cm^2 at RT and isochronally annealed in 30 minutes steps at the temperatures indicated. The initial spectrum is shown following anneal-

ing at 673 K because there was no significant change from that recorded immediately after the ion implantation in the optical spectra for lower annealing temperatures. The spectrum displays a broad peak in the neighbourhood of 2.3 eV superimposed on a near linear background increasing towards higher energies. The former feature is considered to arise from Au dimers, trimers and other very small clusters [326]. The near linear background is attributed to defects created during the ion implantation, likely to be oxygen vacancies created by lattice displacements [356] during the initial stages in which the LN maintains its crystallinity to an appreciable degree. Ultimately at the highest fluences massive disorder results in amorphisation and the final background will result from the amorphised region. It is noted that in Pt^+ implanted LN, as discussed earlier, a similar large increasing background was present [249]. The most prominent feature in the spectra obtained after annealing to 773, 973 and 1073 K, respectively, is the extinction band arising from Au MNPs near 2.07 eV (600 nm). The peak energy shifts to lower values with increasing annealing temperature and is accompanied by a reducing full width at half maximum (FWHM).

Figure 6.11b shows the optical spectrum of the X-cut LN sample implanted to the same fluence and under similar conditions as the Y-cut sample whose optical characteristics after annealing are shown in figure 6.11a. Higher annealing temperatures were necessary for the development of the Au MNP and their observation by way of the characteristic prominent optical absorption band in the region of 2.0 eV as in the case of the X-cut sample. Similar optical features and behaviour with increasing annealing temperature are observed at temperatures between ambient and 1173 K, namely a progressive shift of the peak to lower energy and the reduction of the FWHM. At 1273 K there is a more marked shift of the peak to lower energies and a significant reduction in the FWHM. In the final spectrum corresponding to the 1373 K anneal, the peak energy moves slightly to yet lower energy, there is a small increase in the FWHM and a substantial reduction in peak height. While the background absorption increases in anneals

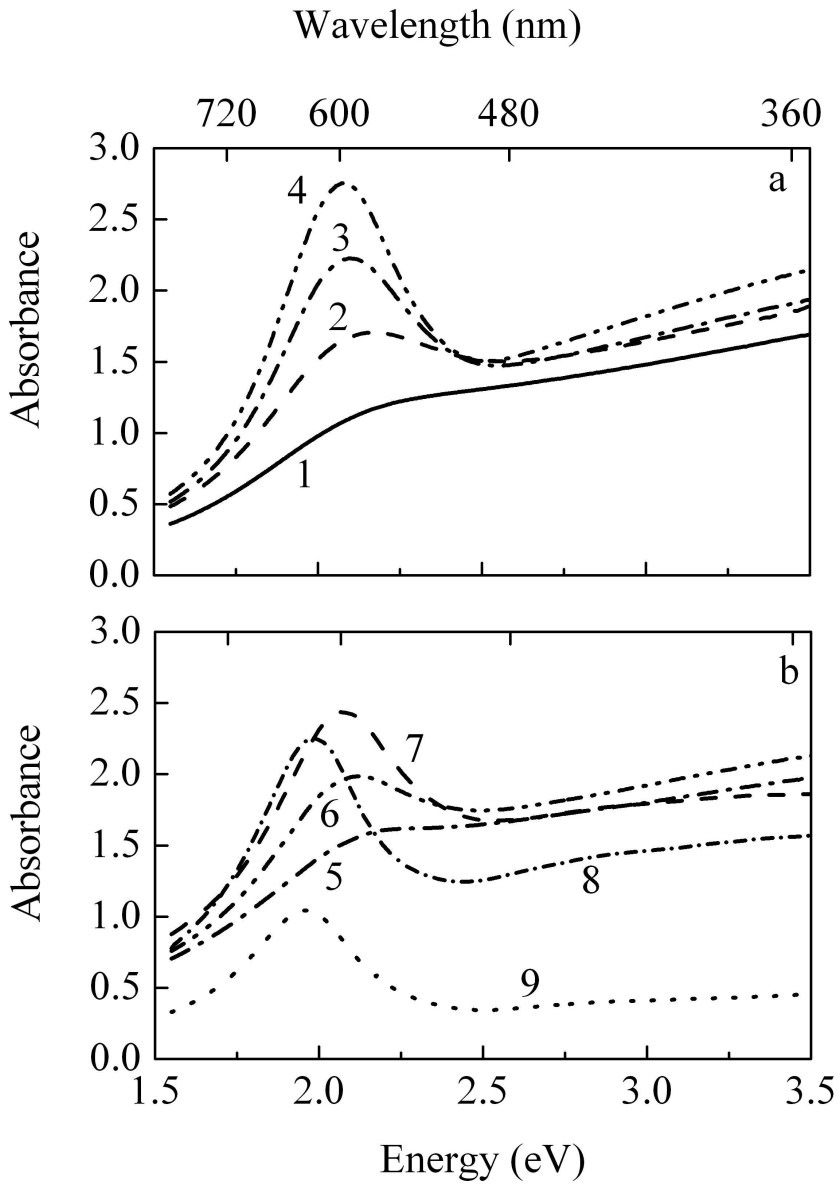


Figure 6.11: Optical absorption spectra after isochronal annealing for 30 minutes for (a) Y-cut sample (1 : 673, 2 : 773, 3 : 973, and 4 : 1073 K). (b) X-cut sample (5 : 973, 6 : 1073, 7 : 1173, and 8 : 1273 and 9: 1373 K). Both the X- and Y-cut LN samples (see Table 6.1) were implanted with Au^{3+} ions at a beam energy of 8 MeV to a fluence of 10^{17} ions/cm^2 at RT. All optical absorption measurements were performed at RT.

from 973 K to 1073 K, the background reduces during anneals from 1173 K to 1373 K, with a major decrease from 1273 to 1373 K.

6.5.3 Correlation Between the MT-Fit and the Experimental Data - Au^{3+} Ion Implanted LN

The fitting (see the theory in section 2.5.1) of the FWHM, PR peak position and intensity of the experimental data to the Mie theory (MT) was performed for the Y- and X-cut Au^{3+} ion implanted LN samples and the results are shown in figures 6.12 and 6.13. Equations 2.61, 2.69, 2.69 and 2.71 are used in the simulations. The fitting parameters used to obtain the theoretical curves are given in the Tables 6.3 and 6.4, respectively. As expected the average particle size increased, inferred from the narrowing of the FWHM of extinction band, with higher annealing temperature for both the X- and Y-cut Au^{3+} ion implanted LN samples. The nanoparticle sizes *d* vary from 3.0 to 5.0 nm over the annealing temperature range from 773 to 1073 K in the case for the Y-cut sample, and from 3.8 to 5.9 nm for the X-cut sample over the range 1073 to 1373 K. In the latter case the maximum particle diameter is 6.3 nm at an annealing temperature of 1273 K. For the Y-cut sample the volume fraction (*p*) of gold in the form of MNPs increases steadily over the temperature range in which the MNP diameter (*d*) is increasing. In the X-cut sample, *p* increases over the range 1073 to 1173 K and decreases at higher temperatures.

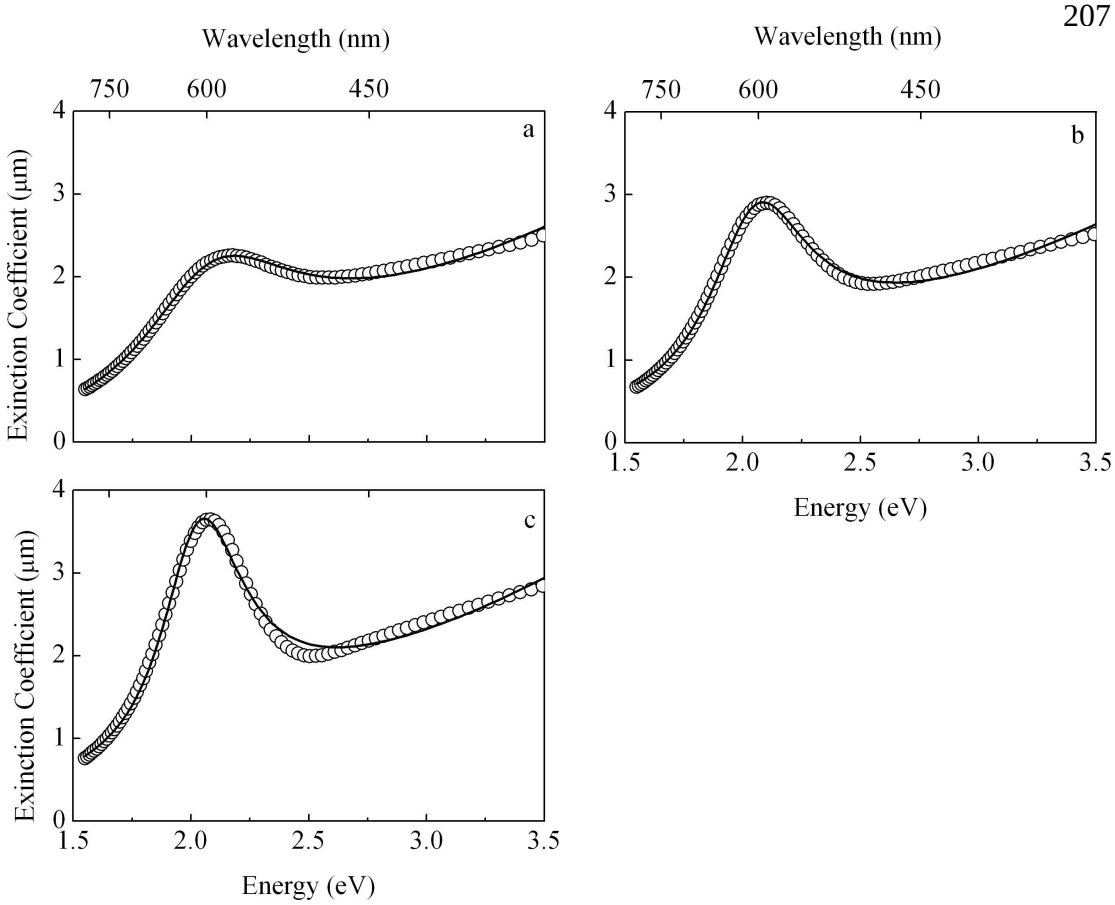


Figure 6.12: Results of the MT fit of the FWHM, PR peak position and intensity of the intensity of the experimental data for the 8 MeV Au^{3+} ion implanted Y-cut LN sample annealed at 773, 973 and 1073 K and labelled a, b, c, and d, respectively. Open circles represent the experimental data and the solid line describes the theory. The implantation done at RT to a fluence of 10^{17} ions/cm^2.

Anneal Temperature. (K)	773	973	1073
ϵ_h	4.2	4.5	4.7
d (nm)	3.0	4.2	5.0
$p \times 10^{-3}$	6.3	7.0	7.9
k_1	-0.7	-0.6	-0.4
$k_2 \times 10^{-6}$	0.9	0.8	0.7
$k_3 \times 10^{-13}$	-1.6	-1.4	-0.9

Table 6.3: Details of the fit parameters used to correlate the experimental data to the theory for the Au^{3+} ion implanted Y-cut LN sample.

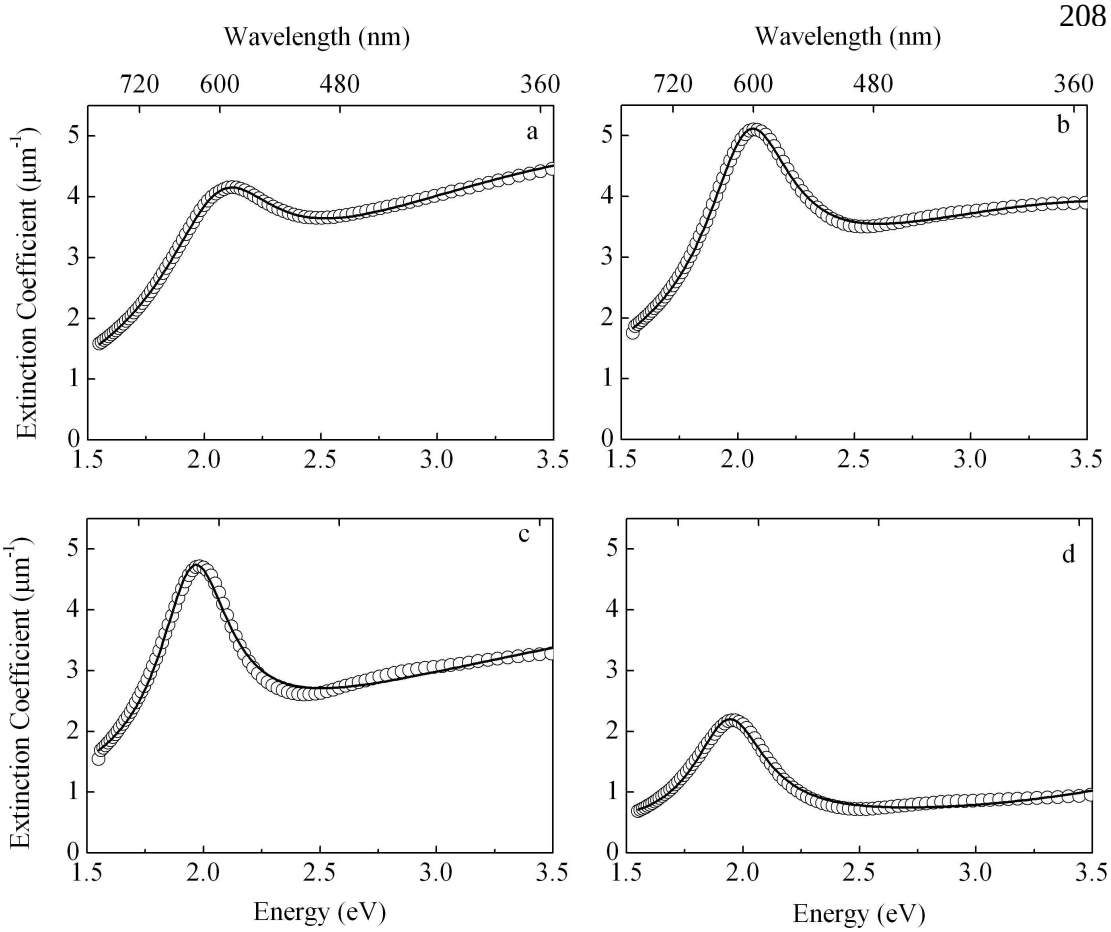


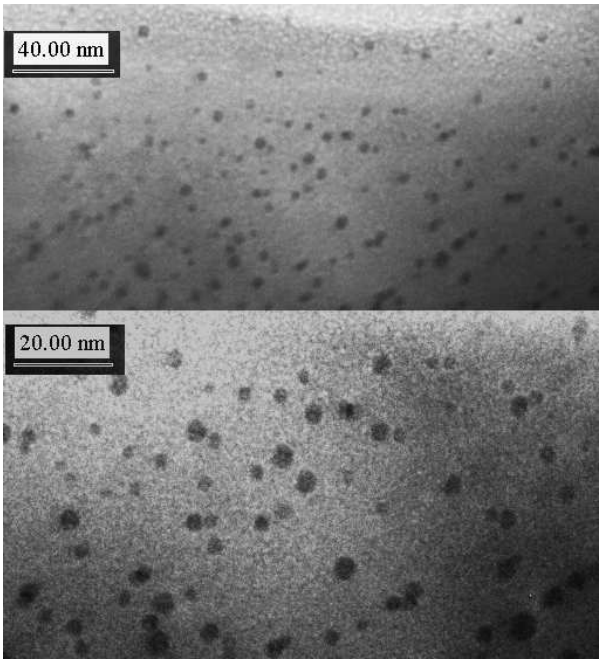
Figure 6.13: Results of the MT fit of the FWHM, PR peak position and intensity of the experimental data for the Au^{3+} ion implanted X-cut LN sample annealed at 1073, 1173, 1273 and 1373 K and labelled a, b, c, and d, respectively. Open circles represent the experimental data and the solid line describes the theory. The X-cut LN sample was implanted with 8 MeV Au^{3+} ions at RT to a fluence of 10^{17} ions/cm^2.

Anneal Temp. (K)	1073	1173	1273	1373
ϵ_h	4.5	4.7	5.6	5.8
d (nm)	3.8	4.8	6.3	5.9
$p \times 10^{-3}$	4.6	5.5	4.2	2.5
k_1	-0.4	0.2	0.3	0.4
$k_2 \times 10^{-7}$	8.4	5.2	1.1	-2.2
$k_3 \times 10^{-13}$	-1.7	-1.0	-0.04	0.52

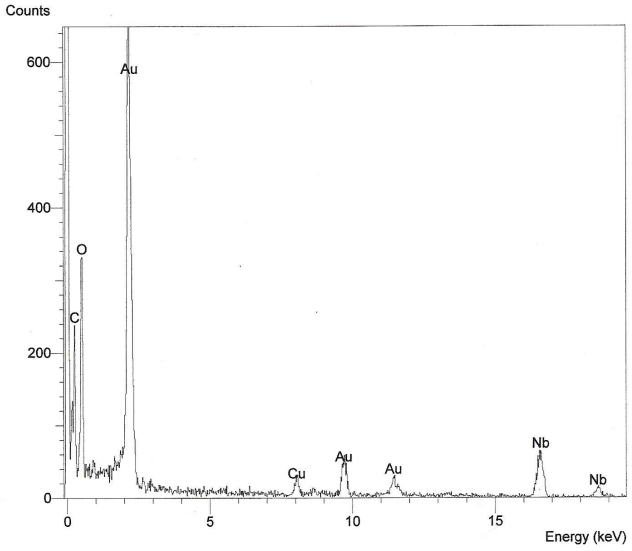
Table 6.4: Details of the fit parameters used to correlate the experimental data to the theory for the Au^{3+} ion implanted X-cut LN sample.

The results of a TEM study done following annealing at 1173 K are shown in figure 6.14a, which reveals the presence of the Au MNP within the host. The assumption that the MNP are spherical appears to be more closely satisfied than for the study of Ag MNP in the same host. The Au MNP are also well separated and the size distribution relatively more uniform. The estimate of the average particle size of 4 - 5 nm is close to the value of 4.8 nm predicted by the Mie theory from the absorption spectrum measured after annealing at this temperature. With the Au^{3+} ions implanted deeper in the LN crystals than in the case of the Ag^{+} ion implantation, the full cycle of growth and the onset of decay of the MNP size for the X-cut sample was observed. A predicted maximum particle average diameter of about 6.2 nm was attained after annealing at 1273 K which reduces slightly to about 5.9 nm after annealing at 1373 for the X-cut LN sample. It is noted that some of the Au MNP have facets exhibiting cubic, octahedron and truncated octahedron geometries, which would agree with the TEM results discussed in a recent review [357] on Au MNP grown under different conditions. As observed in the case of Ag MNP, the reduction in average particle size of the Au MNP observed to occur between 1273 and 1373 K may be related to melting. It is noted that the melting temperature of bulk Au is 1337 K.

Figure 6.14b shows an EDX spectrum taken near a Au MNP, where the peaks associated with the implanted ions are identified. The peaks due to Nb and O atoms originate from the host matrix, while those of Cu and C arises from the brass disc (see figure 6.1) used to hold the LN section and the aquadag used in the TEM preparation process, respectively. The Figure 6.15 shows a representative selected area electron diffraction pattern obtained, *in-situ,* from the TEM study of a number of positions of the host matrix around several randomly chosen Au MNP. The matter surrounding the Au MNP was found to be crystalline in all cases and the electron diffraction pattern reveals spots exhibiting hexagonal symmetry associated with the LN structure.



(a)



(b)

Figure 6.14: (a) Pictorial results of the TEM cross-section studies of a complementary X-cut LN sample (8, Table 6.1) showing Au MNP within the embedding host following annealing at 1173 K. Lower picture shows a magnified section of the upper one. (b) EDX spectrum obtained from the implanted region of the TEM section. This sample was implanted at RT with 8 MeV Au^{3+} ions to a fluence of $1\times10^{17}/cm^2$.

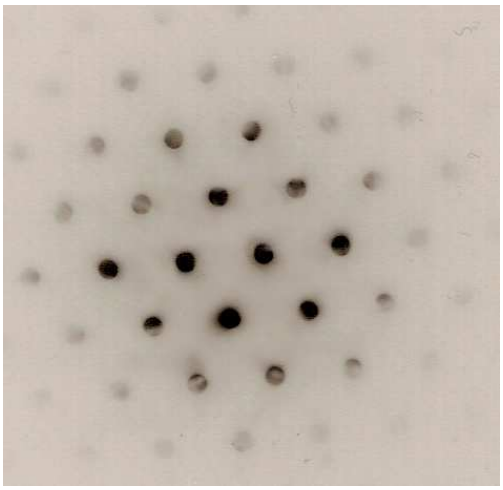


Figure 6.15: Representative selected area electron diffraction pattern of various positions around the Au MNP within the implanted region. The X-cut LN sample investigated was annealed at 1173 K. The electron diffraction pattern shows hexagonal symmetry associated with the LN structure.

6.6 Summary and Discussion

RBS studies of the X-cut LN sample indicate the presence of Au in the implanted region. The ion distribution versus depth profile is assumed to remain unchanged since no Au MNP bands are observed in optical absorption measurements following annealing below 973 K. However a broad pre-colloid band in the neighbourhood of 2.3 eV is present in as-implanted X-and Y-cut specimens and is considered to arise from Au dimers, trimers and other very small clusters [326]; accordingly these must result from statistical formation during ion implantation or radiation enhanced diffusion of the implanted Au in view of the higher temperatures needed for thermally-induced aggregation of the Au atoms.

The growth in the size of the particles by Ostwald ripening and other factors (see subsection 1.5.3) is enhanced by diffusion following higher temperature annealing. Beyond a certain temperature, depending on the metal, there is a decay in the colloid band that is likely to be linked to the melting of the MNP embedded in the LN matrix. In

the case of Ag MNP in X-cut LN, a significant reduction in the optical absorption was noted to occur following annealing at 1173 K. A decrease in the optical absorption and an onset for a reduction average particle size, as determined from the MT results, were also noted following annealing at 1373 K for Au MNP in a similar X-cut LN. These two predetermined annealing temperatures (1173 and 1373 K) were not intentionally set to be close to the bulk melting point of the Ag and Au metals known to occur near 1235 and 1337 K, respectively, as this was not an objective of the study. The melting temperature of the MNP would be expected to be lower than that for the bulk metals since a large fraction of the atoms also constitute part of the surface resulting in lower cohesive forces.

Correcting for the effects of the optical absorption occurring in the unimplanted part of the annealed host matrix has proved to be vital in obtaining mainly the absorption of the MNP and defects induced by the implantation. This correction is necessary because of the simultaneous existence an optical absorption background due defects in the same spectral region, 1.5 - 3.5 eV, which would mask important changes with rising annealing temperature. The optical absorption spectra for the X-cut Au^{3+} ion implanted sample shows that annealing above 1173 K results in the removal of defect induced absorption and by 1373 K the absorption background is relatively flat while the MNP band remains fairly significant. Since the background absorption is only slightly higher than that for the virgin crystal by this stage, it is apparent that the sample has essentially re-crystallized. These results inferred from the optical absorption measurements are given direct support from the selected area electron diffraction study on a complementary X-cut specimen implanted to the same fluence and subsequently annealed in an identical manner at 1173 K in which the hexagonal symmetry associated with the crystalline LN structure is clearly revealed. The decay of the absorption background with rising annealing temperature suggests that the background is mainly associated with the defects created during the implantation.

Because of the birefringent nature of LN, the results of ϵ_h obtained from the fitting are considered to represent an average between the ordinary and extraordinary indices. The average sizes of the MNP predicted by the MT fit are reasonable in the case of Ag and good for Au as observed from the results of the TEM study. The large concentration of Ag metal near the surface, because of the low energy implants, is probably responsible for the wide range of particle sizes compared to the Au metal where the particles are implanted deeper and hence into a larger volume. The volume fraction, p, of the Ag MNP in the X-cut LN matrix is not known accurately for the low energy implantation. In the case of the Ag MNP, the low energy implantation was clearly noted to result in the diffusion of the atoms to the surface of the host matrix. As mentioned earlier in section 6.4.2, the metal volume fraction (p) in the MNP, which are responsible for the observed resonance absorption, is defined as a product of the number of MNP per unit volume (N/V) and their average volume (V_0). During the Ostwald ripening stage the average volume of the MNP increases, a fact observed from the narrowing of the FWHM of the colloid bands as the annealing temperature is raised. p will therefore increase if N/V does not decrease too fast. If both melting and dispersion of the MNP are taking place, the product will be expected to show a monotonic decrease with rising temperature and hence lower values of p.

An intriguing aspect of the present study concerns differences in the MNP development with annealing temperature for the X- and Y-cut crystals. Since the SRIM2003 results in the present and previous work, reported in the literature, show that the implanted region is completely amorphised prior to annealing, it is clear that re-crystallization must have taken place at least in part before the development of the Au MNPs by diffusion of the implanted Au. The findings of Poker and Thomas [358] on Ti, Ag and Pb implanted X-cut LN would support the restoration of crystal properties following annealing in the range 673 - 773 K and above. Using RBS analysis, they noted that both re-crystallization and solid phase epitaxy occurred on annealing the implanted samples.

As shown in the present work by electron diffraction, substantial re-crystallization is present after annealing at 1173 K. The template for re-crystallization thus must be the unimplanted regions of the respective X-and Y-cut LN specimens, acting as a crystalline substrate for epitaxial regrowth of the immediately adjacent amorphised region containing the high concentration of implanted gold atoms in a region parallel to the respective external X- or Y-face. Hence there will occur a directed stress and concentration gradient favoring anisotropic diffusion in directions determined by the original implantation geometry. Thus the ease with which the Au atoms will preferentially diffuse in directions towards the crystalline substrate as well as the now re-crystallized region preceding the original Au atom distribution shown in figure 6.15 will be determined by anisotropic activation energies.

Other observations of differences in colloid development with annealing temperature have previously been reported elsewhere by Rahmani and Townsend [246] where implantation with 385 keV Ag^+ ions was performed in X-, Y- and Z-cut LN samples and have been attributed to anisotropic diffusion of the implanted and displaced ions or vacancies as a result of stress fields induced by ion implantation. However, this group has not considered the effect of annealing which can remove implantation induced damage and thus encourage crystal regrowth.

Chapter 7

Proton Irradiation of Tin Doped Indium Oxide (ITO) Films

7.1 Motivation and Scope of Work

In the work undertaken in this chapter, the intention was to study and identify the irradiation damage mechanism in ITO films, by using a low mass and high energy ion implantation into the ITO medium. The structural, optical and electrical properties of the films are investigated as a function of the irradiation fluence. A literature review of the properties and previous work done on this material has already been presented in section 1.12.

7.2 The Irradiation of the ITO Films

To minimize experimental complexities and the interpretation of results, it was necessary to use samples deposited during a single evaporation run for each irradiation experiment. This ensured that the film thickness was as uniform as possible over the sample. The ITO film samples meeting these conditions were obtained from the Newtech Microlab Ltd. in France and were prepared from a sputter target with a composition of 10 wt % tin oxide and 90 wt % indium oxide. An ITO thin film sample, deposited on a 25 mm wide $\times$ 60 mm long $\times$ 2 mm thick float glass substrate, was mounted and clamped on the end station sample holder of the Cockcroft-Walton accelerator, described earlier in section 3.2. Teflon washers were used in fastening the sample to avoid cracking due to stress resulting from temperature fluctuations induced by possible beam heating especially for large fluences. This was done as a precaution-

ary measure as the temperature rise was expected to be minimal for the irradiations done near RT and 373 K.

The scanned proton beam with an energy of 1 MeV and a diameter of 6 mm was made incident on various regions of the sample by adjustment of the sample height relative to the beam axis. The following fluences were used for irradiation near room temperature and at 373 K : 1×10^{15}, 6×10^{15}, 40×10^{15}, 120×10^{15}, 190×10^{15}, 215×10^{15} and 250×10^{15} protons/cm^2. The irradiation near room temperature was performed without active cooling of the sample. Irradiation of bare float glass similar to that used for the deposition of the ITO films was also performed under similar conditions and fluences. It was found that the change in the absorption of glass was negligible under the current experimental conditions.

In keeping with both the tradition and practice in the area of study of thin transparent conducting films deposited on transparent substrates, optical transmittance rather than optical absorption measurements were emphasised. Unless otherwise stated, all the optical transmittance measurements were thus performed using air as reference at room temperature. However, optical absorption has been used for data analysis in the work and the changes due to irradiation induced effects are corrected by using the unirradiated ITO film and glass substrate. All optical transmittance and absorption measurements were done immediately after the irradiation procedure and at other predetermined intervals.

7.2.1 Measurement of the Sheet Resistance

This description of the dip-stick system is a summary from the work of Albers [359] and highlights those aspects for which it is currently relevant. Sample cooling can be done between 4.5 and 300 K. A typical time period to make a run between these two temperatures is 6 hours at a cooling rate of 1 K/minute. Cooling is achieved by slowly inserting the cryogenic probe, shown in figure 7.1, sealed in an evacuated

stainless steel tube. The probe is filled with small amounts of ^{4}He gas, to act as an exchange gas, before insertion into a dewar filled with liquid ^{4}He. The cryogenic probe is slowly lowered into a dewar filled with liquid ^{4}He using a chain driven by a computer-controlled low gear ratio motor. The rate at which the probe is lowered into the liquid ^{4}He is controlled in such a manner that the computer may stop movement and pause for a period of time if the rate of cooling of the probe is too fast.

Although the sample holder could take two samples at the same time, only one was studied during a particular run. The resistance of the sample, normally being less than 10 MΩ, is determined by measuring the voltage across the sample and the voltage across standard resistors using a Prema model 5000 digital voltmeter (DVM). The temperature of the sample is determined from a Rh/Fe resistance thermometer, whose resistance is obtained by the Prema DVM in the same way as the resistance of the sample.

The samples were cut into suitable sizes so that the implanted area was rectangular with dimensions of about 2.5 mm by 4 mm. To enable the use of the four-point DC technique employed in this work, 4 thin connecting leads were attached on each sample with conducting silver paste. To connect the samples and the Rh/Fe thermometer to room temperature, 40 SWG copper and 42 SWG manganin varnish-insulated wires are used for the current and voltage leads, respectively. All the connections to the sample holder are made via the vacuum feedthroughs. The samples are attached to the Cu sample holder by silicone high vacuum grease to ensure good thermal contact and the four thin leads are soldered onto electrically isolated terminals. Similarly, the four leads for the thermometer are soldered directly to the resistance thermometer. The Rh/Fe resistance thermometer is attached to the copper sample holder on the side opposite of the sample as shown in figure 7.1.

The measurement circuit used for the sample is shown in figure 7.2(a). By adjusting the voltage on the power supply and choosing a suitable buffer resistor (R_b),

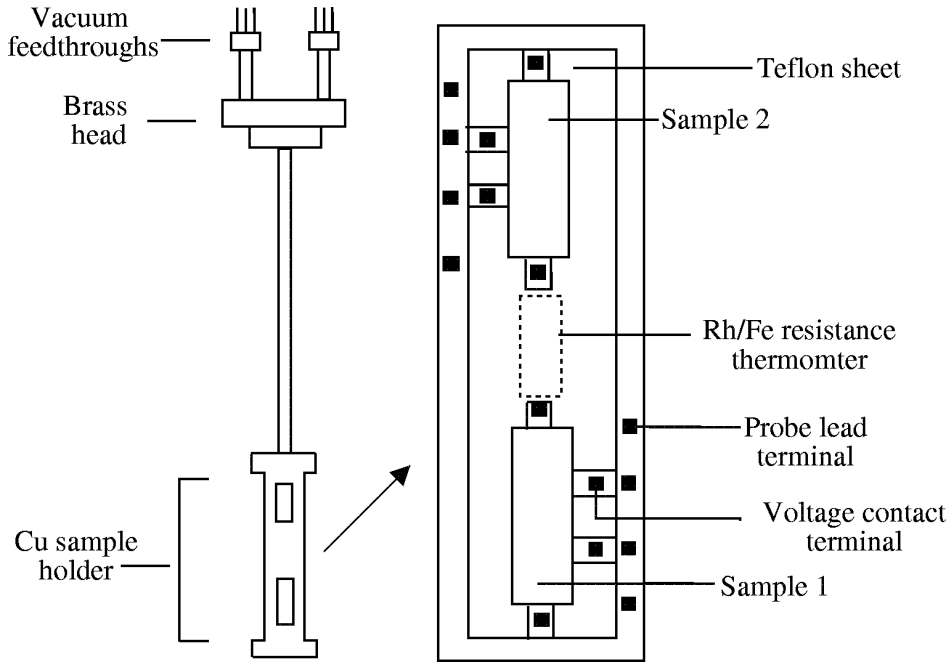


Figure 7.1: Schematic of the cryogenic probe and a cross-sectional diagram of the copper sample holder.

the current in the circuit is set to an appropriate value, such as to obtain a voltage of about 10 mV across the sample. Thermal emfs in the sample are cancelled out from the measured sample voltage (V_{sample}) by measuring the voltage across the sample with the current flowing in the forward and reverse directions. If the voltages across the sample with the current reversed and in the forward direction are V^{r}_{sample} and V^{f}_{sample}, respectively, then

$$V_{sample} = (V^{f}_{sample} - V^{r}_{sample})/2. \tag{7.1}$$

With a known value of V_{std}, the resistance of the sample is calculated to be

$$R_s = \frac{V_{std}}{V_{sample}} R_{std}. \tag{7.2}$$

The circuit used to determine the resistance of the Rh/Fe thermometer is shown in figure 7.2(b). The resistance of the thermometer is measured before (R^{1}_{therm}) and after (R^{2}_{therm}) the measurement of the resistance of the sample. A LakeShore model 120 source was

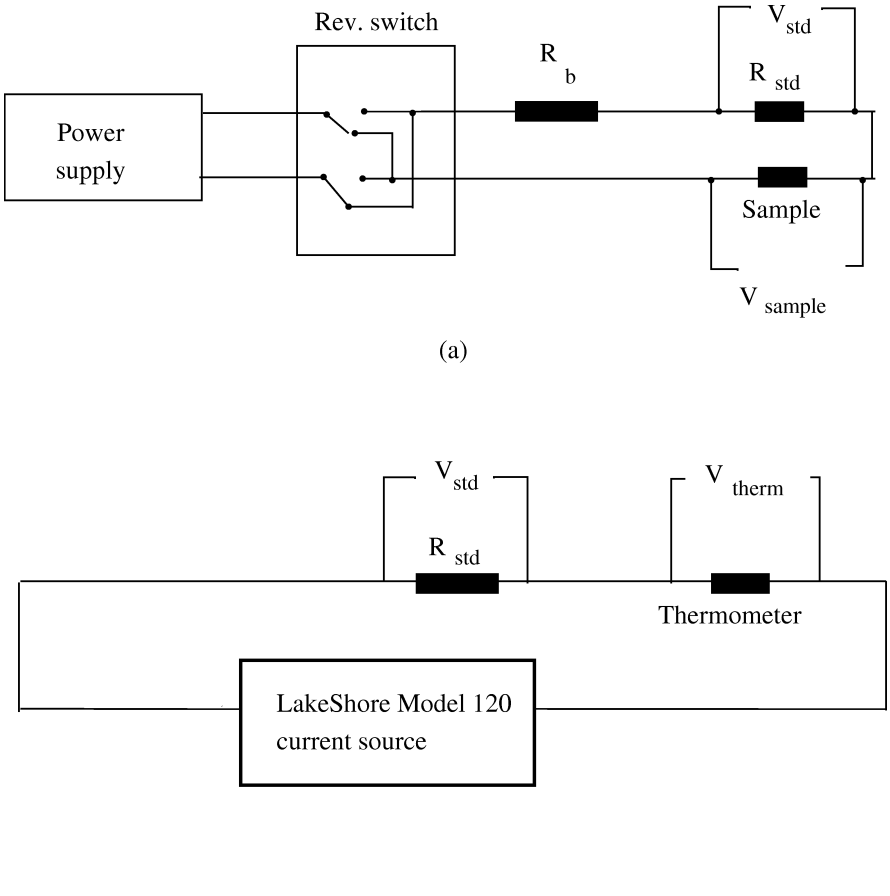


Figure 7.2: Measurement circuit diagrams used for the determination of the resistance of (a) the sample and (b) the thermometer.

used to supply a constant current of 270 μA. Once the voltage across the standard resistance, V_{std}, and that across the thermometer, V_{therm} are known, the resistance of the thermometer is determined by

$$R_{therm} = \frac{V_{std}}{V_{therm}} R_{std}. \tag{7.3}$$

The final resistance of the thermometer, which is an average of the two, is fitted to known thermometer calibration data in order to obtain the temperature. The values of the resistance and temperature are recorded by a PC-based data acquisition system and an X-Y plotter.

7.3 Results and Discussion

7.3.1 Simulations of the Proton Bombardment of ITO Films

Protons are the lightest possible ions and are thus suitable as a low mass probe for various media. In the present case, using an energy of 1 MeV, the accelerated ions are sufficiently energetic when passing through the ITO film to be subject to electronic stopping. This statement is supported by a SRIM2003 simulation (see section 1.2) of 1 MeV protons in ITO whose results are shown in figures 7.3a and b. The actual thickness of the film, about 610 nm, is shown in the figures and is very small in comparison with

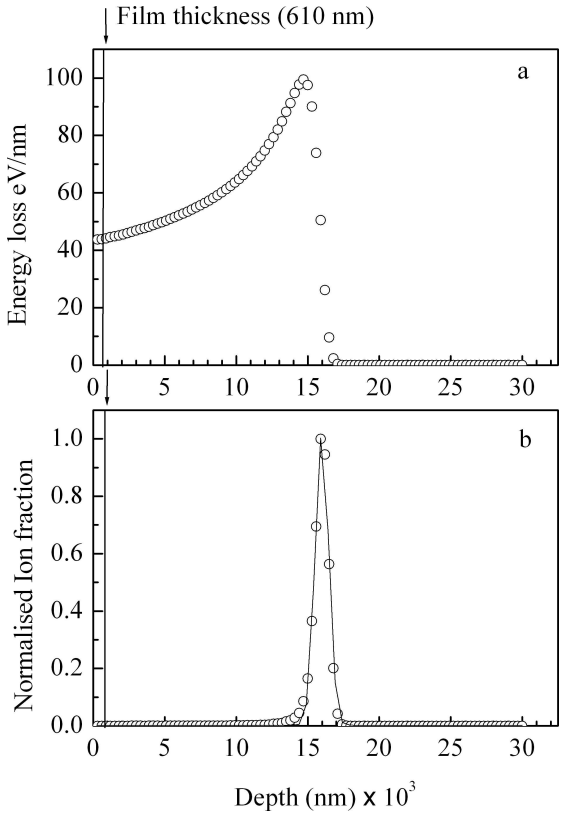


Figure 7.3: Graphical results a of SRIM2003 simulation showing (a) the electronic energy loss profile with distance and (b) the ion range distribution for 1 MeV protons accelerated into an ITO thin film on float glass. The thickness of the film (610 nm) is indicated.

the maximum ion range as shown in figure 7.3b. Thus the protons pass through the ITO film and are brought to rest within the substrate where direct atomic displacements will occur near the end of the ion range.

7.3.2 X-ray Diffraction Studies

Figure 7.4 shows the results of the room temperature X-ray diffraction analysis performed on the polycrystalline thin film samples of ITO. The main X-ray peaks arise from the reflections by the planes (222), (400), (440) and (622) associated with the In_2O_3 lattice. It is evident on examination of spectra 2 to 4 that the crystalline structure of ITO remains unchanged as a result of 1 MeV proton bombardment over a range of fluence from 1 to 40×10^{15} protons/cm^2 and there are no observable signs of a phase transition. In samples 4 (40×10^{15} protons/cm^2) and 5 (250×10^{15} protons/cm^2) the angles at which the four main peaks occur are shifted relative to those of the unirradiated sample. In sample 5, the peaks themselves have lower intensities. A closer examination of the angles at which the characteristic peaks occur and the associated d-spacing for sample 5 is presented in Table 7.1. The details from this Table reveal a small shift to lower peak angles and a corresponding increase in the d-spacing values just after irradiation for each of the peaks. Subsequent X-ray diffraction analysis performed after a month on sample 5 shows recovery of the position of the peak angles and the d-spacing values, which are now almost similar to those of the unirradiated sample. It appears that the irradiation process introduces strain, possibly arising from the presence of defects in the film, without a phase transition or the breakdown of the lattice structure of ITO itself. The position of the peak angles and d-spacing values associated with the reflections from these four planes did not change much for the samples irradiated with lower fluences. It is interesting to note that after storage in a dark desiccator for a period of a month (see figure 7.4b), the first four samples had a similar X-ray diffraction spectra to the unirradiated sample, while there was almost a complete recovery of the

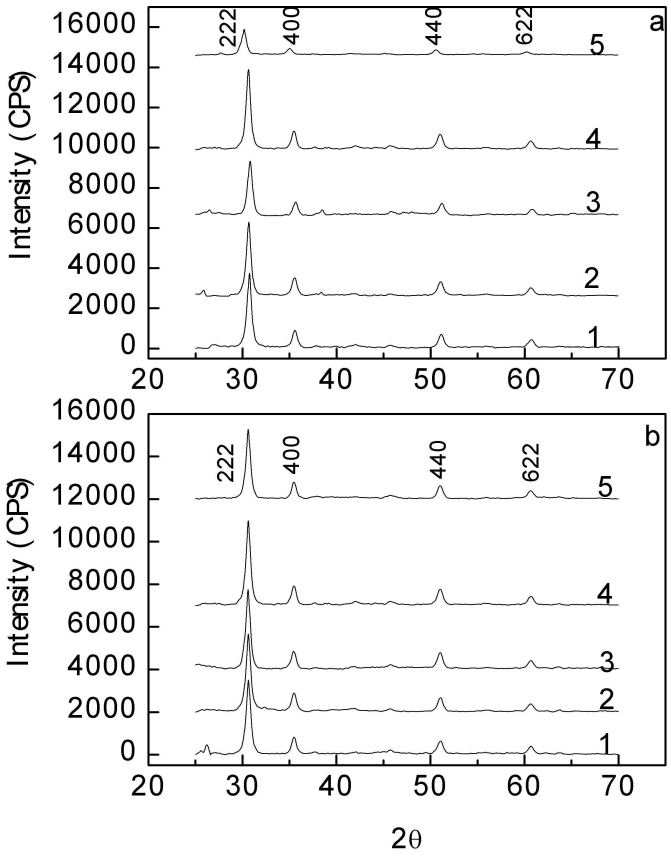


Figure 7.4: Graphs showing the results of room temperature X-ray spectra of selected samples (a) immediately after proton irradiation. They are samples 1, which was unirradiated and 2, 3, 4 and 5 which were irradiated to a fluence of 1, 6, 40 and 250×10^{15} protons/cm^2 at a beam energy of 1 MeV, respectively; (b) after storage for a month.

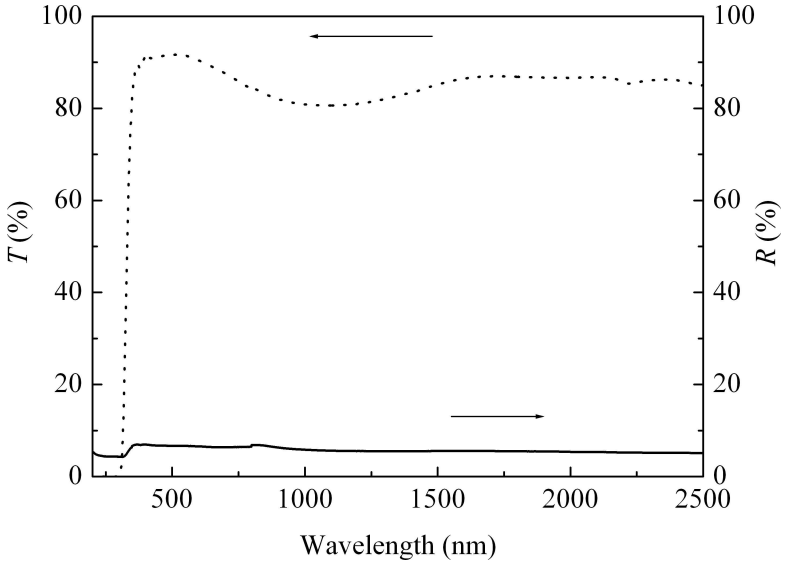
Crystallographic plane	222	400	440	622
Peak angle of unirradiated sample (degrees)	30.73	35.54	51.14	60.72
d-spacing of unirradiated sample ($\mathring{A}$)	2.91	2.52	1.78	1.52
Peak angle just after irradiation (degrees)	30.19	35.01	50.51	60.23
d-spacing of irradiated sample ($\mathring{A}$)	2.96	2.56	1.81	1.54
Peak angle a month after irradiation (degrees)	30.62	35.44	51.03	60.68
d-spacing of irradiated sample after a month ($\mathring{A}$)	2.92	2.53	1.79	1.52

Table 7.1: Details of the peak position, in degrees, arising from X-ray reflections of characteristic crystallographic planes associated with the In_2O_3 lattice before, immediately after and one month following the irradiation of sample 5 (to a fluence of 250×10^{15} protons/cm^2).

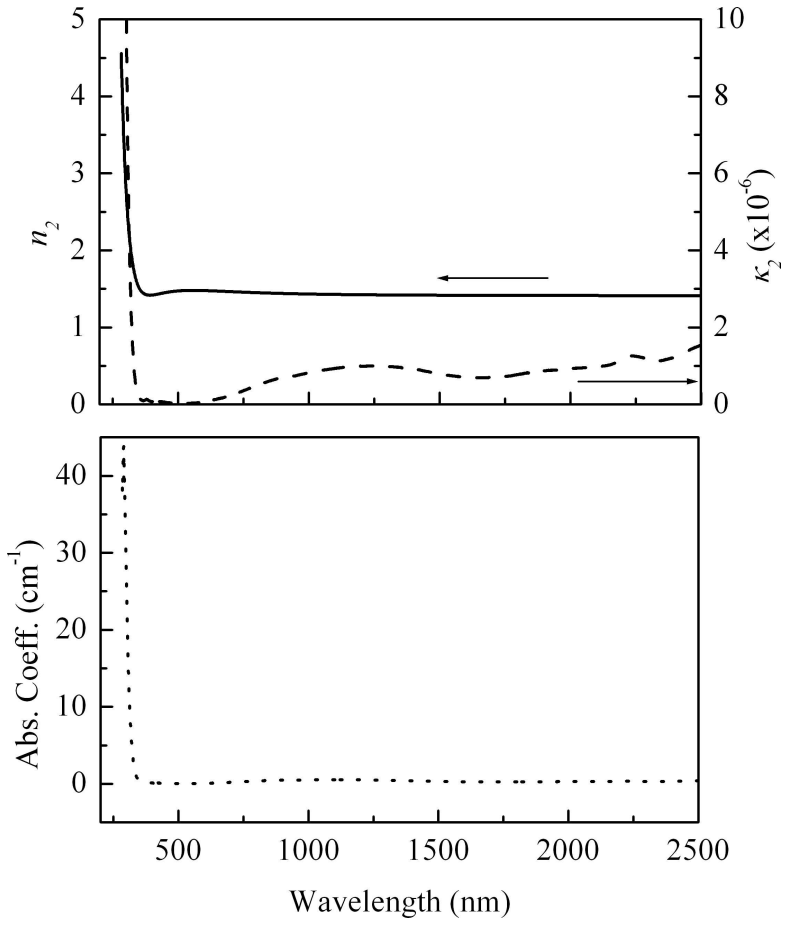
intensity of the X-rays peaks for sample 5, which had received the highest fluence, indicating the existence of a recovery process in a heavily irradiated sample. The period of a month after which the second X-ray diffraction study was carried out on the same samples may not significant. Indeed, while the actual recovery period has not been established, it probably involves a process within the ITO lattice that relieves stresses induced by the irradiation. It has been reported elsewhere that ITO films do undergo an amorphous-crystalline transformation on heating to temperatures as low as 423 K [275, 360]. Structural recovery has also been reported by Shigesato and co-workers [360] in a study where O^+ ions to fluences of 1.3×10^{15} ions/cm^2 at an energy of 80 keV (estimated by the authors result to a mean ion penetration depth of 100 nm from a TRIM simulation) were implanted into ITO films with a thickness of about 196 nm. This group did not however offer an explanation to account for the recovery of the structure of the films after irradiation.

7.3.3 Optical Properties of the Substrate

In order to effectively study the properties of the ITO films on the glass substrate, it was first necessary to examine the optical characteristics of the substrate. Figure 7.5a shows the results of transmittance and reflectance measurements of the unirradiated glass substrate, in the selected spectral region, carried out in preparation for the determination of the optical constants by the method [331] described in section 2.6.3. The real and imaginary parts of the refractive index obtained are shown in figure 7.5b. The real part of the refractive index of float glass (n_2) stays practically constant at 1.4 in the wavelength range 500 - 2000 nm but rises sharply near 350 nm close to the absorption edge of the glass. On the other hand, the imaginary part of the refractive index (κ_2) is negligible over the same wavelength range but similarly rises at the point where the absorption edge of the glass is approached. Figure 7.5c shows the values of the absorption coefficient in a similar spectral region. There is negligibly small absorption in the entire



(a)



(b)

Figure 7.5: (a) Transmittance (T) and reflectance (R) spectra of a 2.5 mm thick float-glass substrate. (b) Calculated values of the real part (n_2) and imaginary part (κ_2) of the refractive index and the absorption coefficient as a function of wavelength from measurement of the transmittance and reflectance of the float glass substrate spectra shown in figure 7.5a.

wavelength region studied, except near the absorption edge of this material where the absorption increases rapidly with reducing wavelength. The optical indices of glass are used in the following subsection to determine the indices of the film and subsequently the film thickness.

7.3.4 Optical Properties of the ITO Films

The thickness of the films obtained by the optical interference method (described in section 2.6.4) before and after the irradiation of the various implanted regions was similar for the low fluence samples. The thickness of the unirradiated film was found to be 610 nm. This differs little (within 1%) from the respective thickness of the films irradiated with 1×10^{15}, 6×10^{15} and 40×10^{15} protons/cm^2, namely, 608, 612 and 617 nm. By contrast, however, the thickness for the sample irradiated with the highest fluence, 250×10^{15} protons/cm^2, was 463 nm indicating that material is lost from the surface by an unknown mechanism. An attempt was made to use profilometry to determine the film thickness. A measurement on an unirradiated sample yielded a result of 480 nm, thus being significantly lower than that of the optical measurement. It is considered that the etching process did not fully remove the film to the substrate owing to its well-known property of excellent adhesion to glass substrates. This method was not attempted further.

The results of the transmittance measurements carried out after the irradiation experiments at ambient and 373 K are shown in figure 7.6. The effect of irradiation by the proton beam is clearly seen as a reduction in the transmittance by inspection of the spectrum of the unirradiated sample relative to the first sample irradiated at both ambient temperature and 373 K. Substantial reductions in the transmittance are observed with increase in fluence for the RT irradiation but considerably smaller effects are observed at 373 K.

The sample irradiated at RT was re-examined a month later. The optical trans-

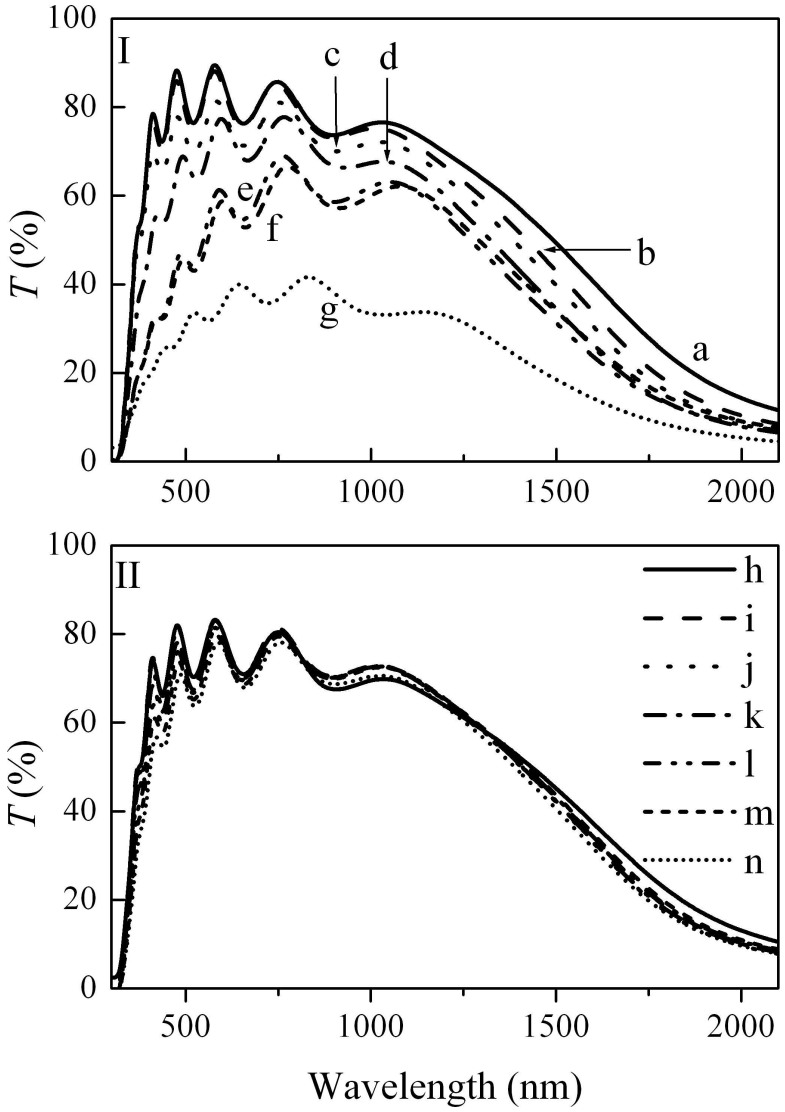


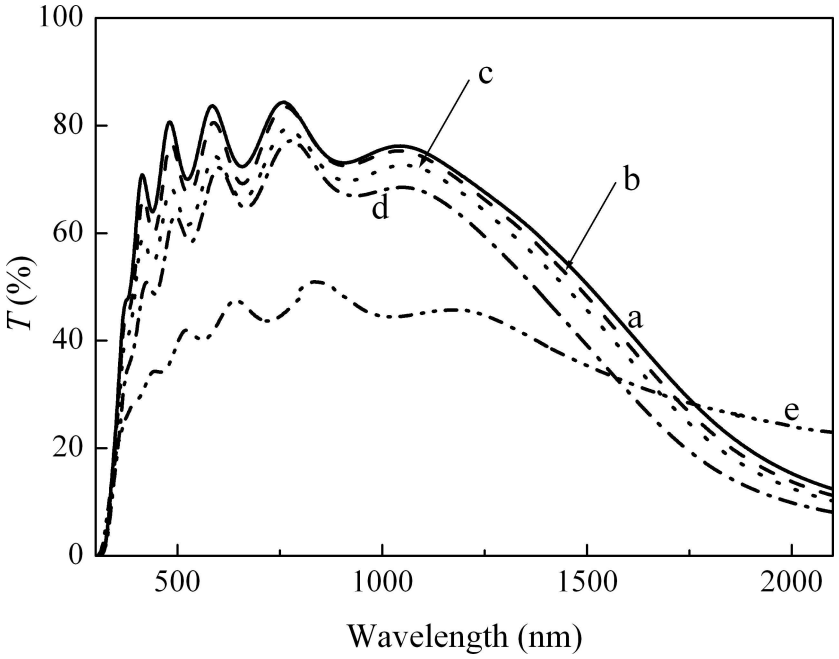
Figure 7.6: Transmission spectra of selected ITO samples with varying proton fluence after irradiation with 1 MeV protons at: I - near RT (a: unirradiated, b: 1×10^{15}, c: 6×10^{15}, d: 40×10^{15}, e: 190×10^{15}, f: 215×10^{15}, g: 250×10^{15} ions/cm^2); II - 373 K (h: unirradiated, i: 6×10^{15}, j: 40×10^{15} k: 120×10^{15}, l: 190×10^{15}, m: 215×10^{15}, n: 250×10^{15} ions/cm^2). Optical spectra measured at RT. The spectrum between that for the unirradiated sample (h) and that for sample i has been omitted in II for better clarity.

mittance studies, figure 7.7a, showed the development of a long tail towards the longer wavelengths for the sample with the largest fluence, spectrum e in this figure. The transmittance in the visible region is higher than that measured immediately after irradiation,

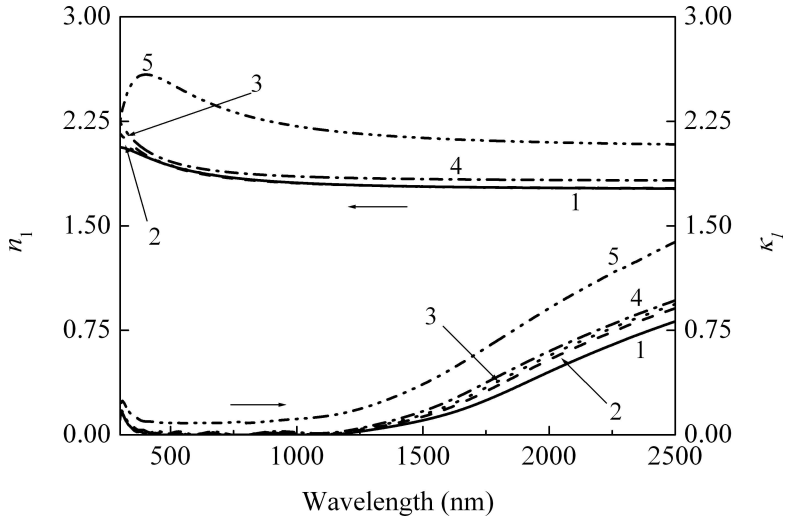
indicating some degree of recovery. This is likely to be related to the recovery in the d-spacing values and the peak angles discussed in the results of the X-ray analysis in subsection 7.3.2. There was no significant change in the spectra of the other samples.

The optical indices of the irradiated films were determined as described in section 7.3.3 using the data presented in figure 7.5. Figure 7.7b shows the real (n_1) and imaginary (κ_1) parts (related by equation 2.72) of the refractive index of the films calculated from the experimental spectra in the transparent region and fitted to the Cauchy relation, equation 2.78, for extrapolation to other regions. The imaginary part of the refractive index (κ_1) and hence the absorption coefficient, α (= $2k\kappa/c$), for the ITO films remains low in the visible region of the spectrum except for the sample which received the highest fluence. This low values of α account for the high optical transmittance in the 400 - 1100 nm spectral range and demonstrates a fairly high tolerance to irradiation damage. However, the absorption coefficient steadily rises towards the infrared spectral range.

Figure 7.8 shows the variation of absorption coefficient, at 550 nm, with irradiation time (fluence) of the ITO films irradiated near RT and at 373 K. A three stage growth mechanism in the absorption coefficient with irradiation time is present for the samples irradiated near RT. There is an initial increase in the absorption coefficient followed by a monotonic growth to a point where it is marked by yet another rise. The absorption coefficient behaviour for the samples irradiated at 373 K, shown in the same figure, has a growth curve with a nearly flat saturation region and the absorption coefficient rises only slightly by the time the highest fluence has been attained. The discussion in taken up further in subsection 7.3.7 where a wider correlation with other observed properties is made.



(a)



(b)

Figure 7.7: (a) The optical transmittance of irradiated ITO thin films after storage for about a month (a : unirradiated, b : 1×10^{15}, c : 6×10^{15}, d : 40×10^{15}, e : 250×10^{15} ions/cm^2). (b) The real (n_1) and imaginary (κ_1) parts of the refractive index as a function of wavelength for selected samples 1 : unirradiated, 2 : 1×10^{15}, 3 : 6×10^{15}, 4 : 40×10^{15} and 5 : 250×10^{15} ions/cm^2. The calculations were performed using the data from I in figure 7.6. The curves for both optical indices are represented by the same type of lines.

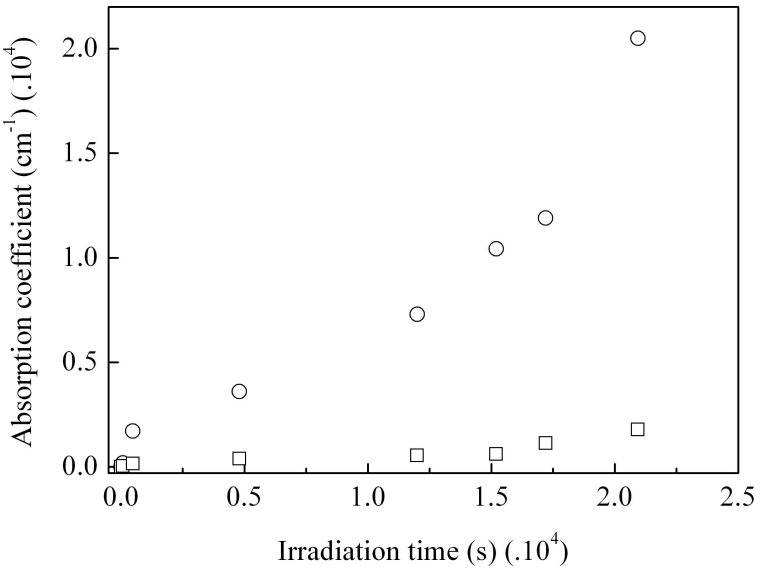


Figure 7.8: The variation of the absorption coefficient in the middle of the visible region (at 550 nm) with irradiation time obtained for two similar samples near RT and at 373 K, represented by circles and squares, respectively.

7.3.5 Model of Defect Growth Behaviour

It has already been mentioned in the previous subsection that the growth of the absorption coefficient with fluence (time) for the ITO films show a three stage growth process. It resembles the well-known behaviour of the *F* centre growth kinetics in irradiated alkali halides near room temperature and can therefore be similarly modelled [95]. A model in which complementary defects *x* and *y* are produced by a primary mechanism, one of which is stable and the other mobile, associated with a mechanism of heterogeneous nucleation of the mobile defects by pre-existing defects or impurities to form clusters was employed to study the growth behaviour.

$$\frac{dx}{dt} = g - \sigma xy, \tag{7.4}$$

$$\frac{dy}{dt} = g - \sigma xy - \sigma y s_0 - \sigma_1 y s_1 - \sigma_2 y s_2 - \sigma_a y a + \sigma_d s_2, \tag{7.5}$$

$$\frac{ds_0}{dt} = -\sigma y s_0, \tag{7.6}$$

$$\frac{ds_1}{dt} = \sigma_d s_2 - \sigma_1 y s_1 + \sigma y s_0, \tag{7.7}$$

$$\frac{ds_2}{dt} = \sigma_1 y s_1 - \sigma_d s_2 - \sigma_2 y s_2, \tag{7.8}$$

$$\frac{da}{dt} = \sigma_2 y s_2. \tag{7.9}$$

x and y represent the concentration of the immobile and mobile defects, respectively. a represents the concentration of immobile aggregates of the mobile defects, g the concentration of defects produced per unit time, s_0 the pre-existing defects. s_1 and s_2 stand for the concentrations of defect centres after capturing one and two mobile defects, respectively. The common capture rate for the mobile with the immobile defects and the s_0 centres is σ. In the present work different capture rates of the mobile defects with the s_1 and s_2 centres, namely, σ_1 and σ_2, respectively, are used. For aggregated centres the capture rate is $\sigma_a = n_a^{2/3}\sigma$, where n_a is the average number of the mobile centres per cluster. σ_d is the detrapping rate for the thermal bleaching of the s_2 centres.

The initial conditions are such that the parameters representing concentrations are set to zero except s_0. However, the formulation of this model does not explicitly include the effects of temperature on the growth kinetics of the defects. Introduction of temperature coefficients brings in the multiplicative factor $\exp(-E_m/K_BT)$ on σ, where E_m is the migration energy of the mobile defects, K_B is the Boltzmann constant and T the temperature in Kelvin. Detrapping is also expected to be temperature dependent, hence $\sigma_d = \sigma_{d0} exp(-E_d/K_BT)$, and is assumed to occur from the s_2 centres with an activation energy of E_d. The inclusion of such temperature coefficients in the defect growth kinetics was successfully done elsewhere by Comins and Carragher [49], which accounted for the transition into the saturation region in the growth curves for alkali halide crystals doped with divalent cations (see section 1.3.11). The next step is then to solve the six ordinary differential equations simultaneously by a numerical method with the prescribed initial conditions. Figure 7.9 shows the results of the simulations, which are in qualitative agreement with the experimental data in figure 7.8. More detail

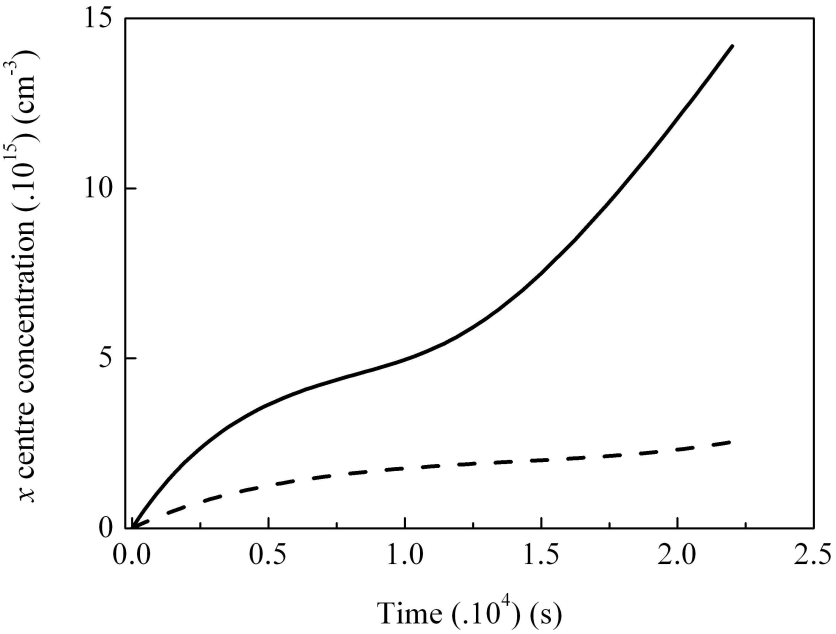


Figure 7.9: Simulation of the variation of the defect concentration of *x* centres with irradiation time at different temperatures, near RT (solid line) and 373 K (dashed line). The following parameter values have been used in the simulation: $\sigma = 1.6 \times 10^{-13}\exp(-E_m/K_BT)$ cm^3 s^{-1}, $E_m = 75$ meV; $g = 10^{16}$cm^{-3} s^{-1}; $\sigma_d = 7.1\times10^5\exp(-E_d/K_BT)$ s^{-1}, where $E_d = 0.12$ eV; $\sigma_1/\sigma = 1.0$, $\sigma_2/\sigma = 0.02$; $s_0(0) = 3\times10^{15}$cm^{-3}, where $s_0(0)$ stands for the density of pre-existing defects at time ($t = 0$).

on the program used to solve the equations is provided in appendix B.

Figure 7.10 shows the behaviour of the variation of the change in absorbance with wavelength for various irradiation fluences. The following discussion is similar to the work carried out by Connell et al. [361] on the implantation of diamond. For present purposes it is necessary to stress some points from the Mie theory [321]. For simplicity, consider the case of spherical particles with average radius *R*, where in the limit of small particles $R \ll \lambda$. If the extinction is dominated by absorption then the absorbance

$$A \propto \frac{1}{\lambda}, \tag{7.10}$$

and if scattering dominates

$$A \propto \frac{1}{\lambda^4}. \tag{7.11}$$

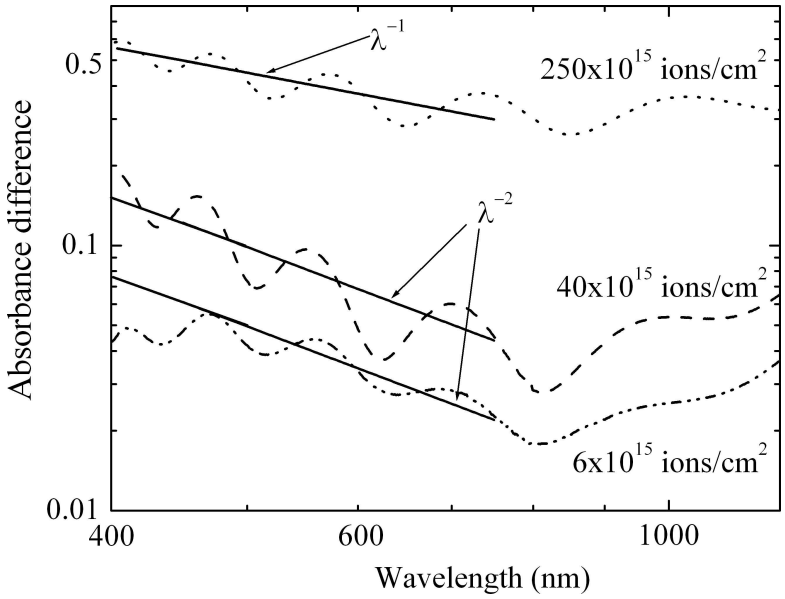


Figure 7.10: Relationship between the irradiation induced absorbance difference (A) and wavelength for various irradiation fluences: 6, 40 and 250×10^{15} protons/cm^2. The $1/\lambda$ dependence is associated with cluster absorption.

The irradiation induced absorbance is obtained by correcting for the absorbance of the unirradiated film. It is observed, if one neglects the interference patterns in the region between 450 - 750 nm, that the irradiation induced absorbance (A) shows a near $1/\lambda^2$ dependence for the samples irradiated with fluences of 6 and 40×10^{15} ions/cm^2. It is not immediately obvious why the $1/\lambda^2$ dependence is observed in the electronically modified film and the most likely explanation is a transition stage between small particle scattering described by equation 7.11, displaying $1/\lambda^4$, and that corresponding to the $1/\lambda$ dependence of equation 7.10 associated with small particle absorption. The change in the absorbance for the lowest fluence, 1×10^{15} ions/cm^2, is relatively small and hence not considered. At the highest fluence, 250×10^{15} ions/cm^2, the radiation induced absorbance-wavelength dependence changes to $1/\lambda$ suggesting that the formation of clusters, predicted by the defect growth model, is now mainly responsible for the darkening of the films within the irradiated spot.

7.3.6 Results of the Resistance-Temperature Measurements

The results of the sheet resistance versus temperature measurements shown in figure 7.11 indicate that the ITO films exhibit a typical metallic behaviour since the resistance of the samples decreases as the temperature is lowered. This is because the decrease in the temperature reduces the phonon component of scattering of the charge carriers. All the samples attain a residual sheet resistance at liquid helium temperature that appears to be dependent on the irradiation fluence and hence the active charge carrier dopant concentration. The residual sheet resistance for samples it000 (unirradiated) and it115 (irradiated with a fluence of 1×10^{15} protons/cm^2) are almost identical below 200 K perhaps due to the small irradiation fluence difference between them. The overall difference in the behaviour of the two samples is considered small and thus not discussed further. The general increase in the sheet resistance of the films with higher proton fluence observed for the samples in this figure is further discussed in the next subsection where all possibly correlated optical and electrical effects are presented.

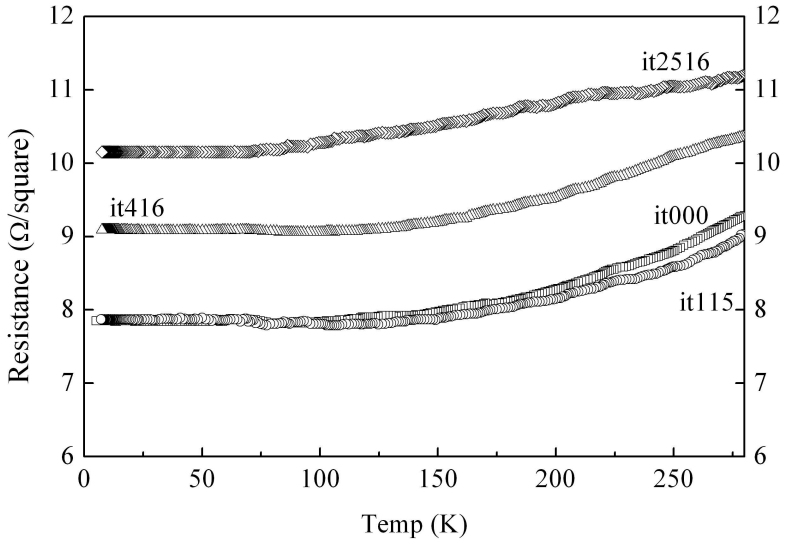


Figure 7.11: Graph showing resistance-temperature behaviour of selected ITO film samples after irradiation. it000 is unirradiated, while it115, it416, it2516 are irradiated with proton fluences of 1, 40 and 250×10^{15}/cm^2, respectively.

7.3.7 Correlation between the Optical, Structural and Electrical Properties

The behaviour of the absorption coefficient curves as a function of irradiation fluence, in figure 7.8, is explained further as follows. The steady increase in the absorption coefficient, at the intermediate stage on the curve obtained for the RT irradiations, could indicate a transition to a different form of dominant defect from the initial type. The growth stabilizes momentarily and likely transforms to a yet higher defect form responsible for the increase in the absorption coefficient curve for the largest fluence region. The relationship between the fluence and absorption coefficient appears similar to the well known *F* centre growth curve seen in the study of alkali halides. It is not entirely unexpected since more damage should be retained on implantation at a lower temperature as shown by the difference in values of absorption coefficient in the results of the irradiation near RT and at 373 K for similar fluence. When the sample is irradiated at a temperature higher than RT, the defects created are perturbed by lattice vibrations from the external thermal source. This leads to diffusion and hence the annihilation of an appreciable number of defects created via recombination with their complements or trapping by other forms of structural defects during the irradiation process. At lower temperature, the effects of lattice vibrations on the defects created are reduced with the result that relatively larger defect densities are retained and hence the absorption coefficient values are higher. The behaviour of the two growth curves and their temperature dependence has been modelled by a set of equations, given earlier in subsection 7.3.5, and shows qualitative agreement with the experimental data of the absorption coefficient. There are three stages of the growth curve. Stage I involves the trapping of the mobile defects, forming the s_1 centres at extrinsic defect points, e.g. at impurities. This stage is considered to be relatively stable. The next stage (II), in which two mobile defects are trapped forming the s_2 centre is unstable compared to the initial stage. Of the three stages, the last one (III), which involves the trapping of more than

two mobile defects culminates into the formation of relatively large clusters assumed to be stable.

X-ray diffraction analysis shows that no structural change occurs following irradiation with low proton fluences and indeed significant recovery from the reduction in peak intensity is observed at the highest fluence. The continued irradiation leads to progressive darkening of the films with higher proton fluence resulting ultimately in the formation of defect clusters. This can be inferred from the results of figure 7.10, where it can be seen that the absorption mechanism displays a $1/\lambda$ dependence linked to the formation of such clusters for the most heavily irradiated sample (250×10^{15} ions/cm^2).

The present measurements although indicating the generation of defect clusters do not provide information on their composition. In this context, darkening effects in ITO films have also been studied by other workers. Fan and Goodenough [362], using XPS, suggested the formation of a Sn_30_4-like phase in as-grown ITO films. This suggestion was later disputed by Wu and Chiou [363] who also studied sputter deposited ITO films using XPS and found no evidence of the presence of this phase. The latter group attributed the darkening of the films to the variation of the content of oxygen during the deposition. Lowering the amount of oxygen was found to result in darker films. The work most relevant to the present study is that of Shigesato et al. [273] involving the implantation of ITO films with 33 keV protons and 80 keV oxygen ions. The energies of the ions were selected to ensure they were embedded within the films thereby causing maximum atomic displacements. Shigesato and co-workers, drawing on the work of Fan and Goodenough, suggested that the presence of the Sn_30_4-like phase was the cause of the darkening effect. However, this conclusion was not substantiated with XPS or other independent techniques.

There are two possible reasons for the increase in the sheet resistance. The first one especially noted in the higher fluence regime and mentioned earlier in subsection 7.3.4, is the loss of material from the surface of the films. The results of such losses

would be enhanced surface roughness [364] leading to an increase in the sheet resistance of the films with rising irradiation fluence. Secondly, additional resistance would occur via carrier scattering by the clusters formed.

7.4 Summary and Discussion

The use of 1 MeV protons to irradiate ITO thin films has been found to dominantly create defect and defect clusters by an electronic mechanism, leaving the basic structure of the ITO films unchanged. These conclusions are supported by a SRIM2003 simulation, which shows that the energy of the proton beam is such that the mean penetration depth is considerably larger than the thickness of the films. Thus nuclear stopping will occur in the glass substrate. This is consistent with the X-ray diffraction analysis of the samples, which show almost no change in the intensity of the peaks that characterize the ITO lattice structure for samples irradiated with proton fluences below $250\times10^{15}/cm^2$. At the highest fluence, namely $250\times10^{15}/cm^2$, the peak angles at which the four characteristic X-ray reflections occur are slightly shifted to lower angles and there is a corresponding increase in the associated d-spacing values and a reduction in the peak intensity. The shift is attributed to strain introduced by the presence of defect clusters arising from the high fluence irradiation of the film. A subsequent check on two irradiated samples, which received fluences of 40 and $250\times10^{15}/cm^2$, showed recovery of the d-spacing values when investigated again by the X-ray diffraction analysis after storage for a month. The intensities of the X-ray peaks for the sample irradiated with 250×10^{15} protons/cm^2 also recovered to a considerable degree. This check suggests that a structural recovery process occurs after the irradiation experiment. The detailed nature of the clusters is not known. Further work is needed to attain a deeper understanding.

The optical indices of the unirradiated float glass substrate supporting the ITO films have been determined. The real part of the refractive index stays practically con-

stant at about 1.4 over the entire spectral region studied, but rises steeply near the absorption edge of glass. The imaginary part is generally very small over a similar spectral region. The absorption coefficient has been found to be much lower than that of the ITO films. This information permitted the optical indices of the films to be determined. The optical indices of the films show fluence dependence and little dispersion over large regions of the infrared and part of the visible spectrum.

Irradiation of the ITO thin films with successively increasing proton fluences at RT leads to a three stage growth of the absorption coefficient. At higher irradiation temperature (373 K), the rate of growth of the absorption coefficient with increasing fluence is significantly diminished and the second stage is lengthened with the third stage barely visible. Using a model previously applied to the growth of *F* centres in alkali halides near room temperature but modified to take into account the effect of temperature, the growth kinetics of the absorption coefficient of the ITO films with fluence (irradiation time) and hence of the defect production processes at the two temperatures are qualitatively reproduced.

An examination of the radiation induced absorbance versus wavelength behaviour with increasing proton fluence reveals a change from a near $1/\lambda^2$ dependence, probably related to a transition stage in the extinction mechanism, to a $1/\lambda$ dependence, where the latter is associated with absorption by clusters. The darkening of the ITO films, an observation made in the present work coinciding with the reduction of transmittance, is thus ultimately linked to the formation of the clusters. The sheet resistance of the unirradiated ITO film sample decreases when the temperature is lowered representing typical metallic behaviour as the effect of phonon scattering on charge carriers is reduced. Selected samples irradiated with higher proton fluences show a similar behaviour but have a higher sheet resistance. Two possible reasons emerge from the current work that could lead to the rise in the sheet resistance. The first one is the creation of disorder introduced by the removal of material from the surface of the films causing roughness

and hence scattering of the charge carriers. The second reason, whose effect would also enhance scattering of charge carriers, is the formation of clusters that form in the high fluence regime.

Chapter 8

Studies of the Properties of Polycrystalline Magnesium Fluoride Films

8.1 Motivation and Scope of Work

The scope of this work is to study the electrical and to some extent optical and structural properties of polycrystalline magnesium fluoride (PMF) films prepared by thermal beam evaporation. The conductivity was increased by implantation with Mg-ions, annealing in a slightly reducing atmosphere and co-deposition with AlF_3. The initial work was motivated by metal-insulator transitions observed in granular materials. The use of ion bombardment and annealing in a reducing atmosphere was therefore proposed to see if the resistivity could be analyzed using the well known theories and formalisms attributed to metal-insulator transitions in granular materials. The product would be useful technologically if successful [161, 164]. The physics aspects of the application were unfortunately hindered by irreproducibility thus preventing a satisfactory analysis of the results. Although the production of films was successful they contained defects such as grain boundaries among others and it is these factors, as will be discussed, that lead to irreproducible results. Further work was therefore terminated and the efforts redirected to other areas. This work was not very successful but has been included for completeness sake because of the investment of time and effort.

8.2 Preparation of PMF Films

8.2.1 Substrate Preparation

Pyrex and fused silica glass substrates were cut to 8×25 mm^2 to enable them fit into slots on the substrate holder of the thermal evaporation unit (see section 8.2.2). The Pyrex glass substrates were subjected to a flame polishing process schematically shown in figure 8.1a to remove scratch and polishing marks. Both types of substrates were then cleaned using suitable solvents in an ultrasonic bath and finally dried in a refluxing ethanol system. All the substrates were then coated with evaporated thin conducting palladium metal film electrodes (see the electrode pattern in figure 8.1b) which, unlike thin gold metal film electrodes, were found not to peel off during annealing at high temperatures.

8.2.2 Thermal Evaporation Unit

Figure 8.2 shows a schematic diagram of the thermal evaporation unit used for the deposition of the polycrystalline magnesium fluoride (PMF) films. The vacuum chamber is evacuated in sequence by the various pumps as shown. Deposition on as many as 16 substrates could be made during one evaporation run. The various substrates are brought into the correct deposition position with the aid of a handle that rotates a circular disk attached to the substrate holder. The substrate temperature was adjusted by a combination of a heater and a liquid nitrogen bath.

This unit can be pumped down to 10^{-7} Torr in 4 - 5 days and a pressure in the region of 10^{-5} Torr is normally maintained during the deposition. There are two separate thermal ovens that can be used in a situation where two materials are to be co-deposited. The ovens are placed opposite each other, positioned and angled so that each thickness monitoring unit only receives the evaporant from one oven at any given time while both beams are deposited on the substrate.

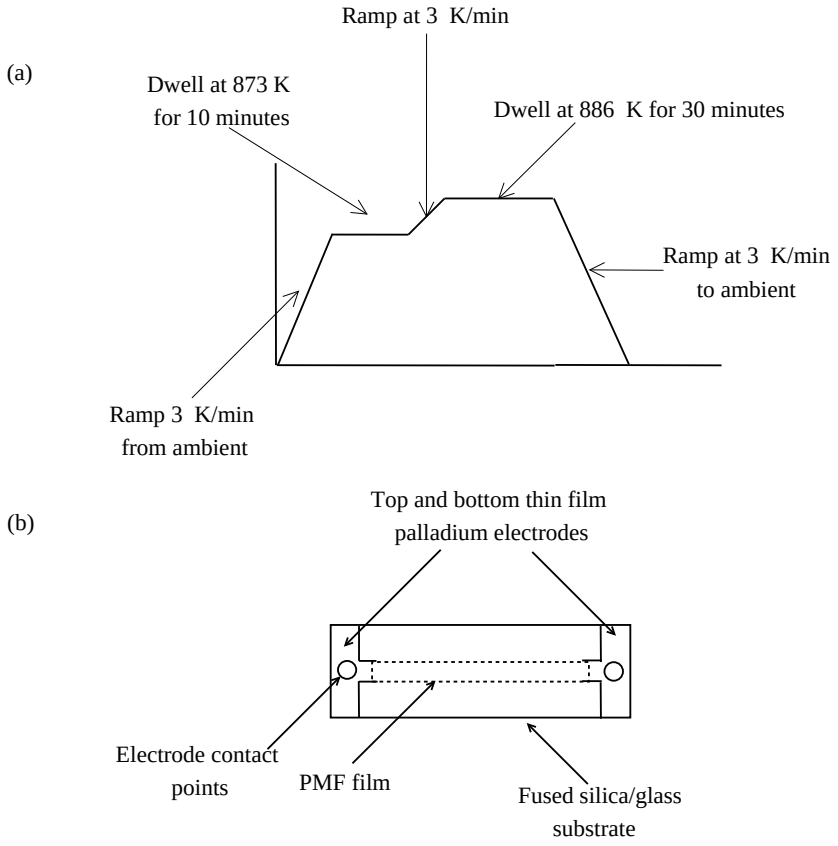


Figure 8.1: (a) Diagram of the flame polishing process applied to the substrates used in PMF film deposition. (b) Top-view diagram of PMF film on pyrex glass/fused silica substrate with palladium electrodes.

In preparation for the deposition of the films, the substrates are cooled or heated to the required temperature. The thermal evaporation ovens and the film thickness control units are turned on about an hour before deposition to allow for the control electronics to stabilize. Water cooling of both the shutters and the oven environment was used to prevent mechanical failure of the former due to excessive heating. The evaporation temperatures are raised slowly to outgas the ovens until the actual deposition rate needed is reached. Finally, with the correct substrates in place, the oven and substrate shutter are opened for the deposition.

The PMF films were deposited onto fused silica or glass substrates, held at liq-

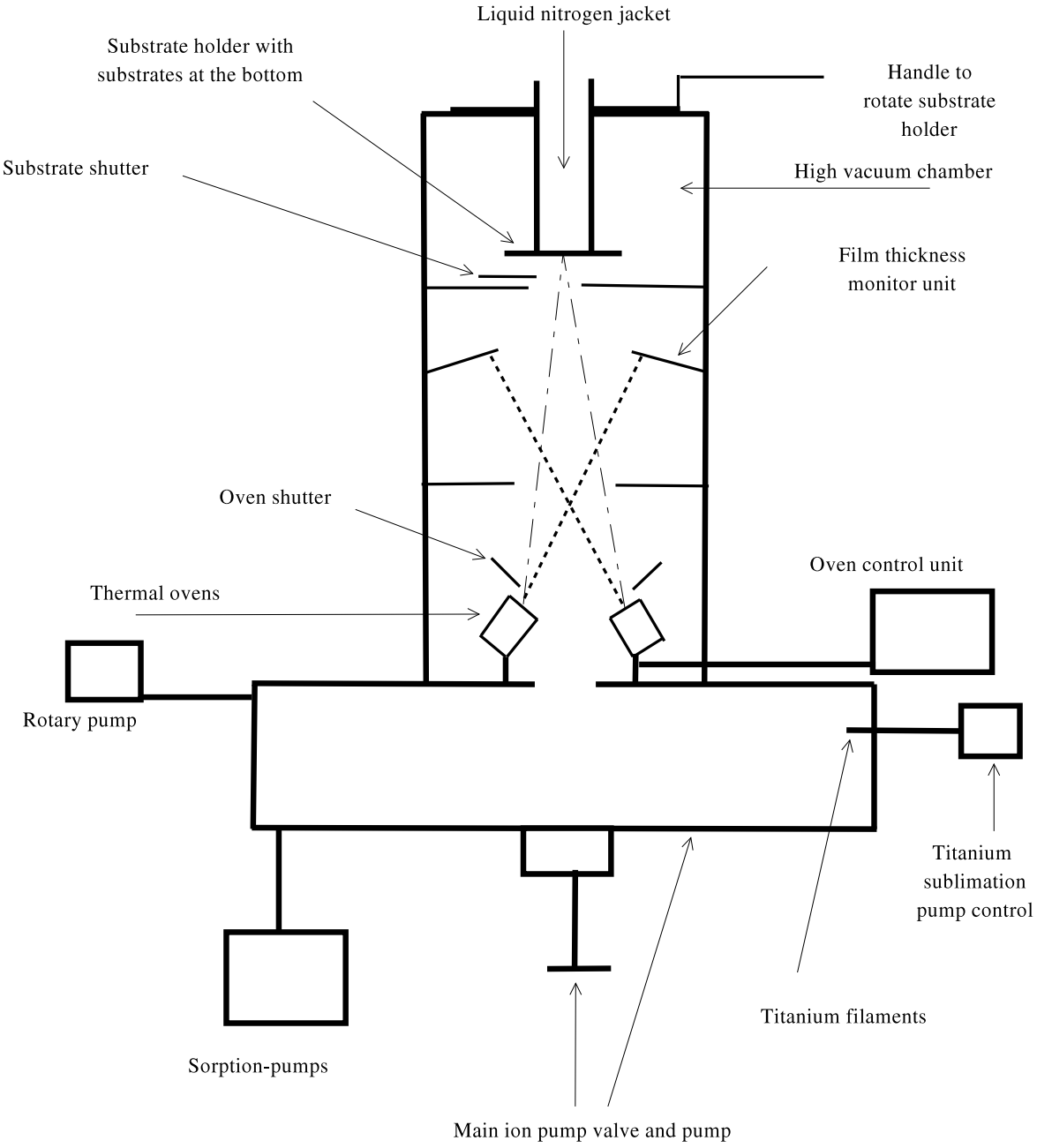


Figure 8.2: Schematic cross-sectional diagram of the thermal evaporation unit used for the deposition of the PMF films on to pyrex and fused silica glass substrates.

uid nitrogen temperature (LNT). Sample thickness was varied from 200 to 1000 nm, depending on the applications for which they were intended, by adjusting both the oven temperature to alter deposition rate or the time. As previously mentioned, thick-

ness monitoring units were employed to check the evaporation rate and measure the thickness during the deposition and the MgF_2 vapour pressure in the chamber was not allowed to exceed 10^{-5} Torr during the entire period of the deposition of the PMF films. A second coating of palladium was then deposited on top of the PMF film in the same pattern as the previous electrodes deposited on the substrate so that the ends of the PMF film were sandwiched (see figure 8.1b), before the resistance measurements were carried out.

MgF_2 and AlF_3 were co-deposited on glass substrates using the two thermal ovens shown in figure 8.2. The composition of the films was varied using different evaporation rates from the thermal ovens. As opposed to ion implantation where the dopant ions were accelerated into the host material leading to radiation damage, thermal co-evaporation and the subsequent quenching of the vapour mixture was expected to produce a relatively defect free mixture of the two materials on the cooled substrate.

8.2.3 Resistance Measurements

A Keithley 617 electrometer capable of measuring very high resistance was used in the two point probe configuration shown schematically in figure 8.3. The film sample was placed on a high resistance teflon block that employed copper contacts coated with indium as the electrodes. All resistance measurements were performed at room temperature between 18 and 25^0C and a correction for the resistance of the substrates was made.

8.2.4 Ion Implantation of the Films

Ion implantation of PMF films, with Mg^+ ions, was carried out at the Schonland Institute of Nuclear Sciences (SRINS) using the ion implanter described previously in section 3.4. In the first instance, various fluences of Mg^+ ions with a fixed energy

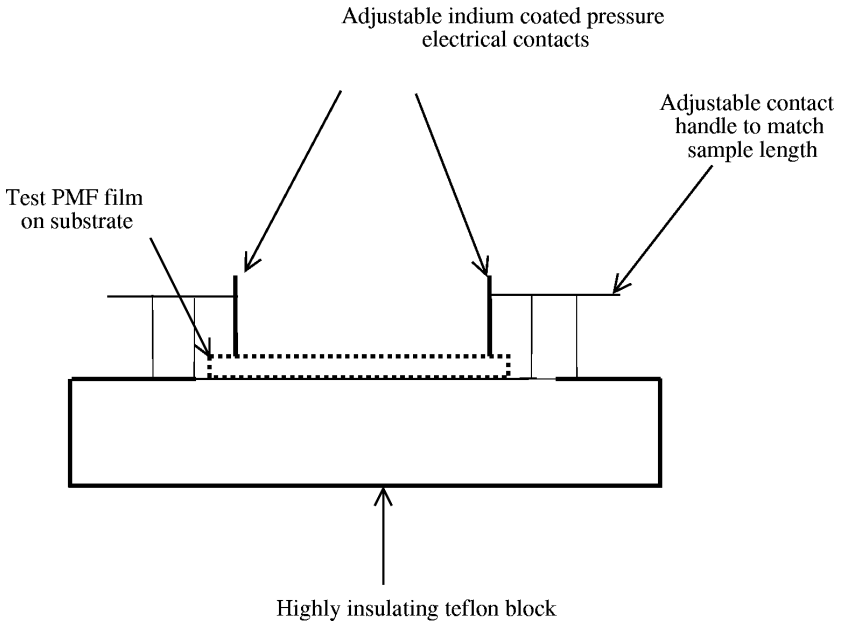


Figure 8.3: Schematic cross-sectional diagram of the resistance measurement setup.

of 100 keV were used, while in the second case the fluence was kept constant and different acceleration energies were employed, in order to attain a range of different mean penetration depths. All the implants were performed at LNT.

8.2.5 Ion Milling of the Films

Ions implanted into the PMF films would normally come to rest below the surface if the ion energy is not sufficiently large to enable them pass right through. To achieve ohmic contact with the implanted ions, a thin layer of surface material of the films has to be removed. Figure 8.4 shows a diagram of the milling unit, which uses argon gas to trim the edges of the films at an angle and hence expose the implanted layer. Silver paste was applied on to the exposed layer, as an electrode, before the resistance measurements were carried out.

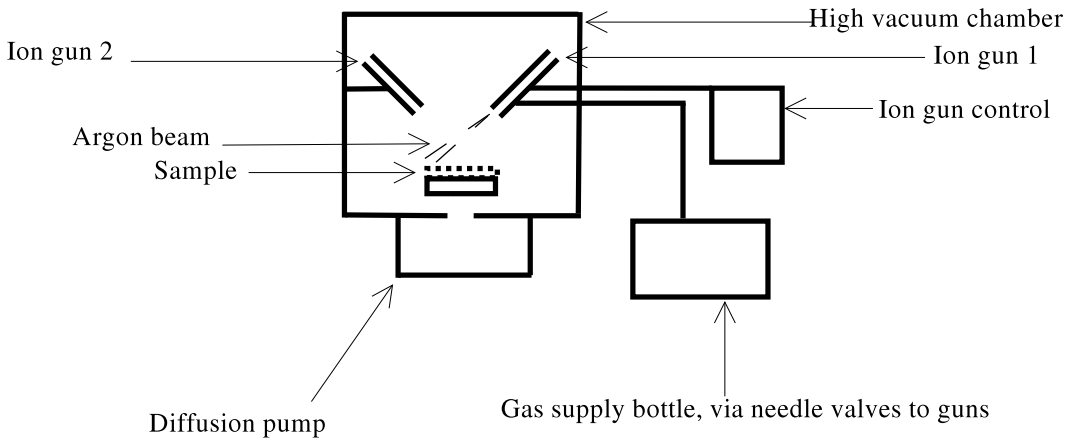


Figure 8.4: Schematic cross-section diagram of the argon gas mill.

8.2.6 Reduction of the Films

Two further approaches were employed in an attempt to reduce the high resistivity of the PMF films of the unimplanted samples. In the first case annealing at various temperatures under an atmosphere of 96% N_2 + 4% H_2, illuminated with a UV light source prior to passage into a standard open ended furnace, was performed. The hydrogen gas was supposed to act as a reducing agent, while the purpose of the UV light was to ionize the gas mixture before passing it over the preheated sample in the range 373 - 773 K. The second case involved the use of potassium pellets that were inserted in a specially made fused silica glass reaction tube together with a PMF film sample in a nitrogen filled glove box. The use this glove box was intended to minimize oxidation of this reactive metal. The fused silica glass tube was then sealed with a stopper before being heated in a standard enclosed box furnace to about 723 K. It was expected that the highly reactive potassium vapour would react with the fluorine and hence introduce free carriers in the PMF matrix, leading to an improvement in the conductivity.

8.3 Results and Discussion

8.3.1 Summary of Prepared Selected Samples and Their Identities

Table 8.1 provides details of selected samples, whose properties are discussed in the subsections that follow.

Sample identity	Thickness (nm)	Comments
1	250	Ion implanted with 100 keV Mg^+ ions
2	500	Ion implanted with 100 keV Mg^+ ions
3	1000	Ion implanted with 100 keV Mg^+ ions
4	500	Analyzed by X-ray diffraction
5	500	Annealed in 96%N_2 + 4%H_2
6	300	Annealed in 96%N_2 + 4%H_2
7	200	Annealed in 96%N_2 + 4%H_2
8	1000	Annealed in 96%N_2 + 4%H_2
9	300	Reduced with potassium ions
10	250	Ion implanted with 50 keV Mg^+ ions
11	500	Ion implanted with 75 keV Mg^+ ions
12	1000	Ion implanted with 100 keV Mg^+ ions
13	250	Ion implanted with 100 keV Mg^+ ions
15	500	Ion implanted with 100 keV Mg^+ ions
16	1000	Ion implanted with 100 keV Mg^+ ions
18	250	Ion implanted with 100 keV Mg^+ ions
19	500	Ion implanted with 100 keV Mg^+ ions
20	1000	Ion implanted with 100 keV Mg^+ ions
21	200	Co-deposited with AlF_3 - 6%
22	200	Co-deposited with AlF_3 - 10%
23	200	Co-deposited with AlF_3 - 16%
24	200	Co-deposited with AlF_3 - 19%
25	500	Co-deposited with AlF_3 - 6%
26	500	Co-deposited with AlF_3 - 10%
27	500	Co-deposited with AlF_3 - 16%
28	500	Co-deposited with AlF_3 - 19%

Table 8.1: Details of selected PMF film samples as-grown, ion implanted, and co-deposited with AlF_3 at LNT. Samples 10 - 13, 15 - 16 and 18 - 20 (deposited during a single evaporation run) were implanted with Mg^+ ions to a fluence of 100×10^{15} ions/cm^2.

8.3.2 Results of SRIM2003 Simulations of the Mean Depth of Ions Implanted into PMF Films

Figure 8.5 shows the results of a SRIM2003 simulation for 50, 75 and 100 keV Mg^+ ions implanted into the PMF films. The expected mean penetration depths for the 50, 75 and 100 keV Mg^+ ions are 72, 107 and 147 nm, respectively. The choice of the energies of the ions was such that the accelerated ions would remain in the films, which could allow the formation of agglomerates during annealing.

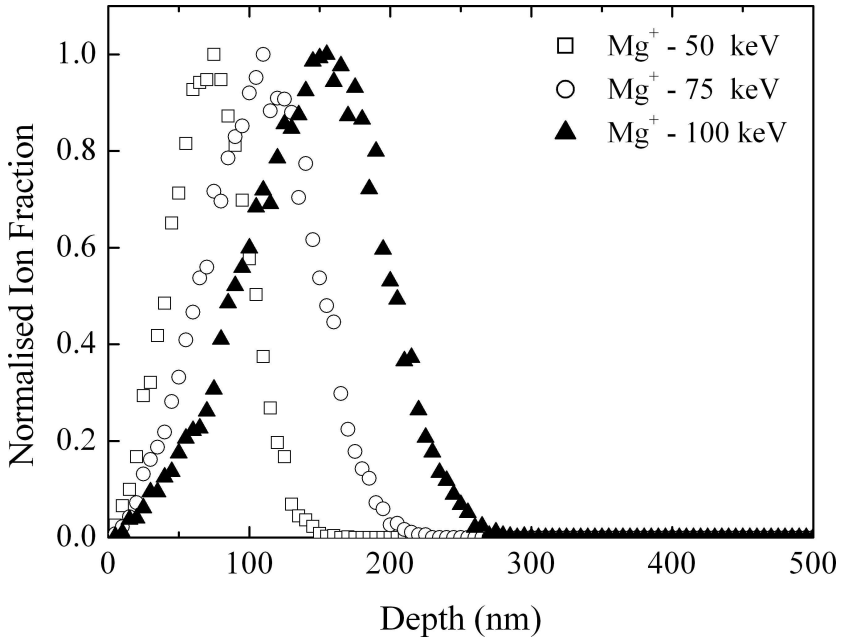
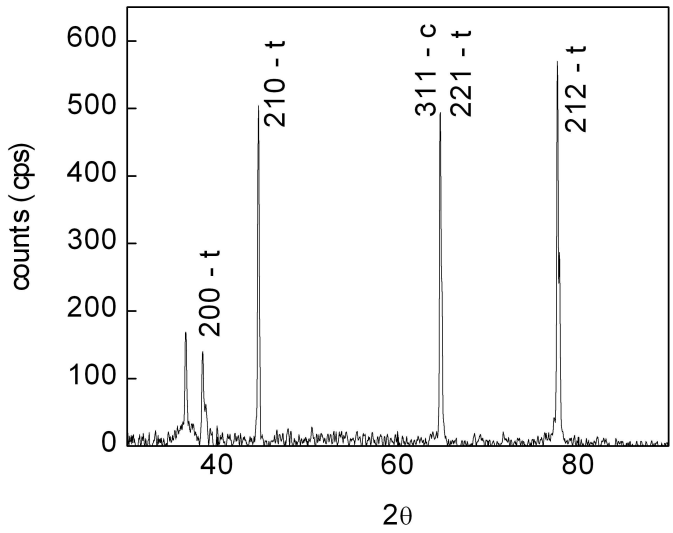


Figure 8.5: Graphical SRIM2003 simulations showing the range of 50, 75 and 100 keV Mg^+ ions used in the implantation of the PMF films plotted on the same scale.

8.3.3 Results of the Structural Analysis

As may be seen from the X-ray spectrum of a 500 nm thick sample in figure 8.6a, the as-grown PMF films are polycrystalline and exhibit preferred orientations. Films of different thicknesses from the same evaporation run showed similar features in the X-ray diffraction spectra. The preferred orientations appearing on the X-ray spectrum



(a)



(b)

Figure 8.6: (a) X-ray diffraction spectrum of a 500 nm (sample 4, Table 8.1) thick PMF film deposited on a pyrex glass substrate at LNT. The symbols t and c stand for tetragonal and cubic phases present in the polycrystalline sample. Measurements were performed at RT. (b) Photograph of a 375×375 μm^2 region of the surface of the PMF film sample on pyrex glass substrate taken at RT using a camera attached to an optical microscope. This is the same sample whose X-ray diffraction spectrum appears in (a) above (1 cm : 34 μm).

are primarily due to reflections from the larger crystallites on the film. Figure 8.6b shows a microphotograph of the surface of the same PMF film sample as analyzed by X-ray diffraction. Crystallite sizes larger than 100 μm in width, together with the grain boundaries separating them, are clearly seen on this picture. The information from this picture confirms the results of the X-ray diffraction studies in establishing that the magnesium fluoride films grown by the thermal evaporation unit are polycrystalline.

8.3.4 Results of the Annealing Studies in a Slightly Reducing Atmosphere

Resistivity-temperature measurements were made, in a slightly reducing atmosphere (96% N_2 + 4% H_2), on several unimplanted samples to determine the best conditions for annealing the PMF films. The oven was set to predetermined temperatures before the samples were inserted. Figure 8.7 shows the results of a typical behaviour of the resistivity as a function of annealing temperature found for the samples, for the same period of 1 hour. The resistivity of a 500 nm PMF film sample (sample 5, Table 8.1), measured at RT, was at its minimum after annealing near 748 K. This temperature was taken as the optimum annealing temperature. The reduction in resistivity occurs due to several reasons. Annealing would basically drive off adsorbed gases and water vapour at low and medium temperatures. A variety of simple defects may start to diffuse in the same temperature range, with their mobility being enhanced as the annealing temperature is raised further. Since the films are grown by vapour quenching there is a possibility of a process such as stress relaxation along adjoining grain boundaries due to lattice vibrations. This process may lead to the removal of the grain boundaries and effectively growth in the crystallite size. All these mechanisms lead to lower values of the resistivity. As the temperature is raised even further, defect aggregation leads to the formation of extended defects which would be responsible for the increase in the resistivity. Three samples of different thicknesses were then held at 748 K in the slightly reducing atmosphere for periods of up to 48 hours. The resistivity

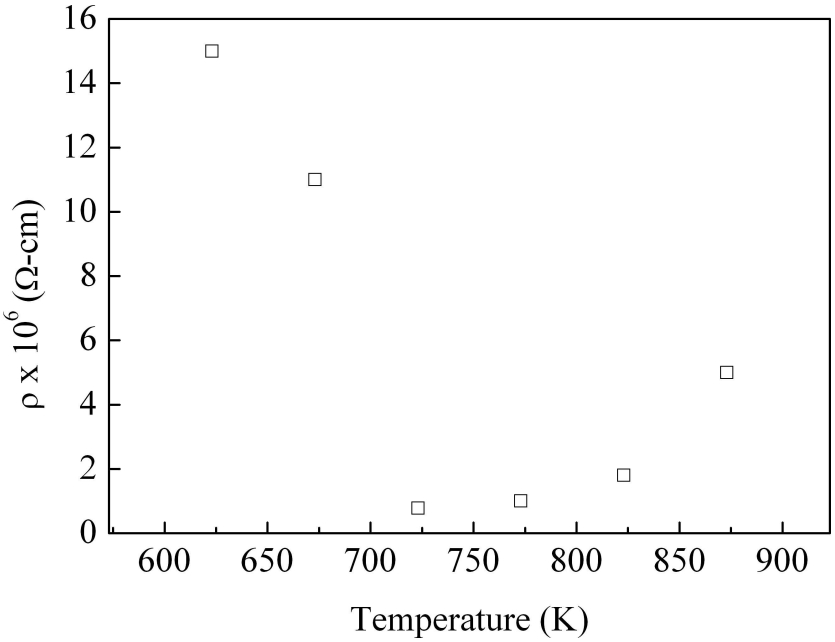


Figure 8.7: Graph showing the variation of resistivity with annealing temperature for a 500 nm thick as-grown PMF film sample (sample 5, Table 8.1). The resistivity measurements were performed around RT.

was again measured after allowing the samples to cool to RT each time, before being heated further. It was observed that the resistivity of all the three samples increased if the annealing was performed beyond 24 hours. The results are shown in figure 8.8. Both the annealing period of 24 hours and the temperature (748 K) at which the lowest resistivity was attained may be specific to the particular experimental conditions during the deposition process. However, because the resistivity of the three randomly selected samples showed similar behaviour on annealing, this presumed optimum anneal period and temperature are considered to be reasonable. Therefore unless otherwise specified, all other annealing experiments were performed at 748 K for 24 hours.

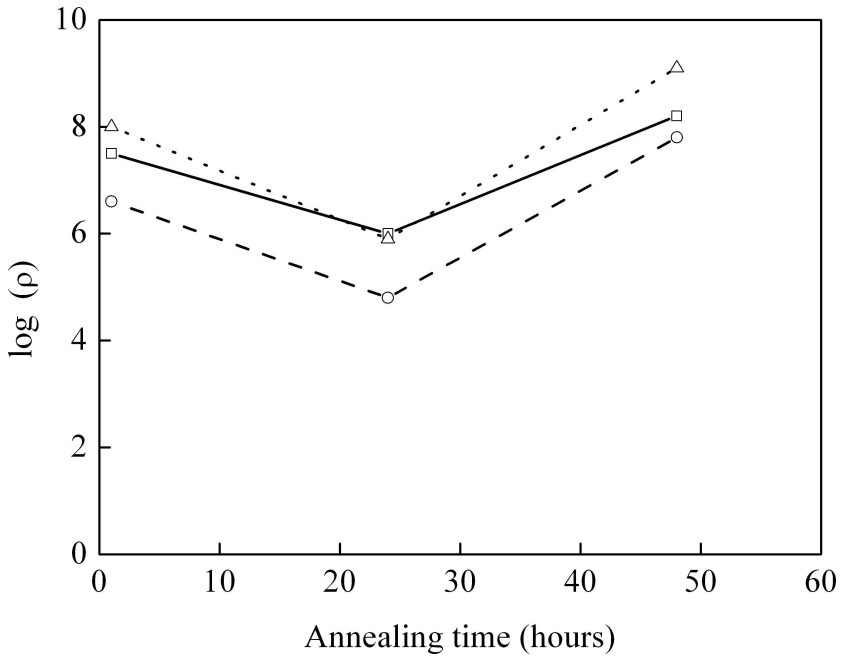


Figure 8.8: Graph of variation of the log of the resistivity with annealing time in a slightly reducing atmosphere (96% nitrogen and 4% hydrogen) performed at 748 K of samples 6, 7 and 8 of thickness 300, 200 and 1000 nm respectively. All resistance measurements were performed between 291 and 298 K.

8.3.5 Results of the Optical Studies

Figure 8.9 shows the transmittance as a function of wavelength for samples 18, 19 and 20 before and after implantation with 100 keV Mg^+ ions to fluences of 10^{17} ions/cm^2 at LNT. These three samples were deposited on fused silica substrates because pyrex glass has a fundamental absorption edge near 350 nm and would therefore mask the absorption of the PMF films, which are expected to show an absorption edge at shorter wavelengths in the UV. It was, however, observed that the absorption edge of the PMF films occurred at longer wavelengths compared to pure single crystals possibly indicating an appreciable density of as-deposited defects. All the three samples analyzed exhibit interference patterns before implantation indicative of a good degree of thickness uniformity (see figure 8.9a). Figure 8.9b shows that the interference pat-

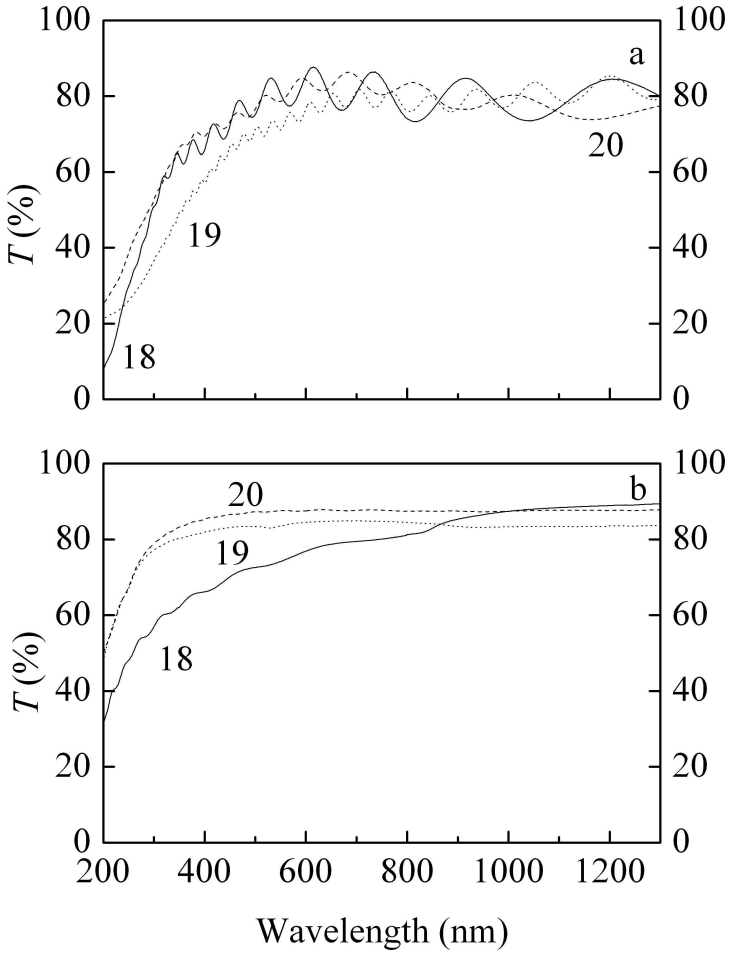


Figure 8.9: Transmission spectra of samples 18, 19 and 20 with thickness of 250, 500 and 1000 nm respectively (a) before and (b) after ion implantation with 100 keV Mg^+ ions to fluences of 10^{17} ions/cm^2 at LNT (see Table 8.1). The transmittance measurements were carried out at RT.

terns are almost completely removed by the specified ion implantation. The explanation for this would be due to sputtering from the surface of the samples, during the implantation process. Sputtering would lead to the removal of surface material in an irregular manner resulting in non-uniform thickness of the films. This is evident as the transmittance of the films, which are now thinner (samples 19 and 20) and have absorption edges that are blue shifted. The periodic nature of the interference patterns can still be observed in the transmittance spectrum of sample 18, but are reduced in intensity and

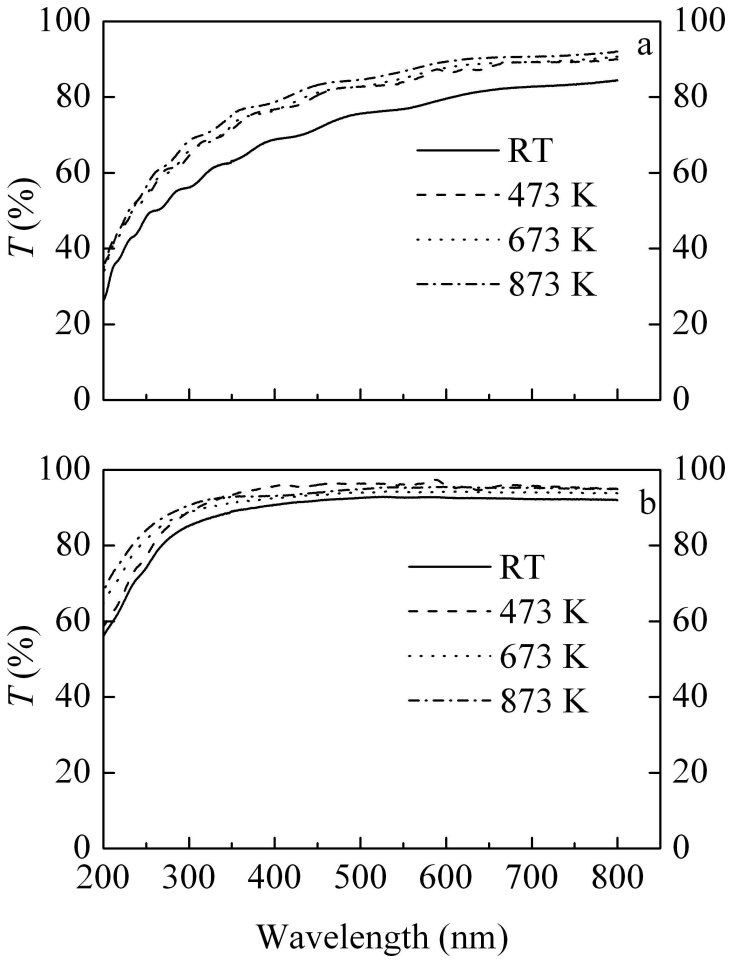


Figure 8.10: Graph showing the changes in transmittance after the 24 hour annealing period for samples (a) 18 and (b) 19 at the temperatures indicated. The transmittance measurements were carried out at RT.

its absorption edge is broadened.

Colloid formation due to the aggregation of the metal ions in the three samples as a function of annealing temperature was expected for sufficiently high annealing temperatures. However, only a small change in the transmittance spectra of the Mg^{+} ion implanted samples was observed on annealing at various temperatures for samples 18 and 19 whose optical transmittance spectra are shown in figure 8.10a and b respectively. In general the small change in transmittance indicated that there was no aggregation leading to the formation of Mg colloids in the PMF films.

Sample ID	Fluence ($\times 10^{15}$ ions/cm^2)	Resistivity ($\times 10^6$ Ohm cm)
1 (250 nm)	10	(61.5)15[9.5]
2 (500 nm)	100	(15)7.7[6.9]
3 (1000 nm)	176	(67.5)110[32.4]
13 (250 nm)	100	(77.5)20[17]
15 (500 nm)	100	(105)17.5 [16.6]
16 (1000 nm)	100	(72.5)120 [75]
18 (250 nm)	100	(65)30[28]
19 (500 nm)	100	(82.5)20[19.5]
20 (1000 nm)	100	(58)83[60]

Table 8.2: Results of resistivity measurements at RT of samples implanted with various fluences of Mg^+ ions at 100 keV at LNT. Samples 13, 15, 16 and 18 - 20 were prepared during a single evaporation run. Values of the resistivity in brackets, unbracketed and in square brackets were measured before, after ion implantation and annealing at standard conditions, respectively.

8.3.6 Results of the Resistivity Measurements

Table 8.2 sums up the results for 100 keV Mg^+ ion fluences used and the resistivity measurements before (in brackets), after ion implantation (unbracketed) and annealing (in square brackets) for the same samples (samples 18 - 20, Table 8.1) whose optical transmittance studies are discussed in section 8.3.5. Samples 13, 15 and 16 with similar thickness, which were implanted under similar conditions during the same experiment are displayed for comparison purposes. Another set of samples (1, 2 and 3) with similar thickness but which received varying fluences of the same energy are also included. It should be noted that the calculations of the values of the resistivity assume that the film thickness are uniform and of the same value as at deposition. There are changes in the values of the resistivity in these three sets of samples that appear to be inconsistent with the fluence. The decrease (for samples 13 and 18) or increase (for samples 16 and 20) in the resistivity, after ion implantation, for samples of similar thickness that were prepared during the same evaporation run is not monotonic. The non-uniform change in the values of the resistivity also applies to first set (samples 1 -

3, Table 8.2), prepared during a different evaporation run. Therefore an increase in the fluence of the implanted ions does not necessarily translate to a decrease in the resistivity of the films. Sputtering, and not ion implantation, is considered to be the main reason for the increase in the resistivity as it leads to the creation of lattice disorder and non-uniformity on the surface of the films. A closer look at this table shows a trend in the two sets of samples from the same evaporation run that indicates that the resistivity of the relatively thinner films generally decreased on ion implantation. This could possibly be explained as follows. The top and bottom contact electrodes (see figure 8.1b) are separated by less material in the case of the 250 and 500 nm films compared to the 1000 nm film and hence an increase in charge carriers is likely to be noticeable in the thinner films. There was however a decrease in the resistivity every time that all the samples (listed in Table 8.2) were annealed at the presumed optimum condition (24 hours at 748 K) in a slightly reducing atmosphere. This is mainly attributed to the removal of grain boundaries on annealing. Other factors such as reduction by the 96% N_2+4% H_2 gas could also play a role.

Substrates (pyrex and fused silica glass) used during the deposition of the virgin samples may in some cases have an effect on the resistivity of the films depending on the lattice mismatch at the film/substrate interface. However, the effect of the two different substrates on the resistivity in the present work is not immediately obvious, probably because the mechanism of the growth of the films during deposition and subsequently the formation of defects as a result of annealing are similar.

The results of reduction with potassium ions on a number of as-grown PMF films produced a lowest resistivity of 9000 Ohm cm (sample 9, Table 8.1) in this work. This study was not taken further as it proved to be very irreproducible.

The results of the resistivity studies involving thermal co-deposition of magnesium fluoride with aluminium fluoride are shown in figure 8.11. The values of the resistivity go through a minimum at a dopant level of about 10% for the samples prepared

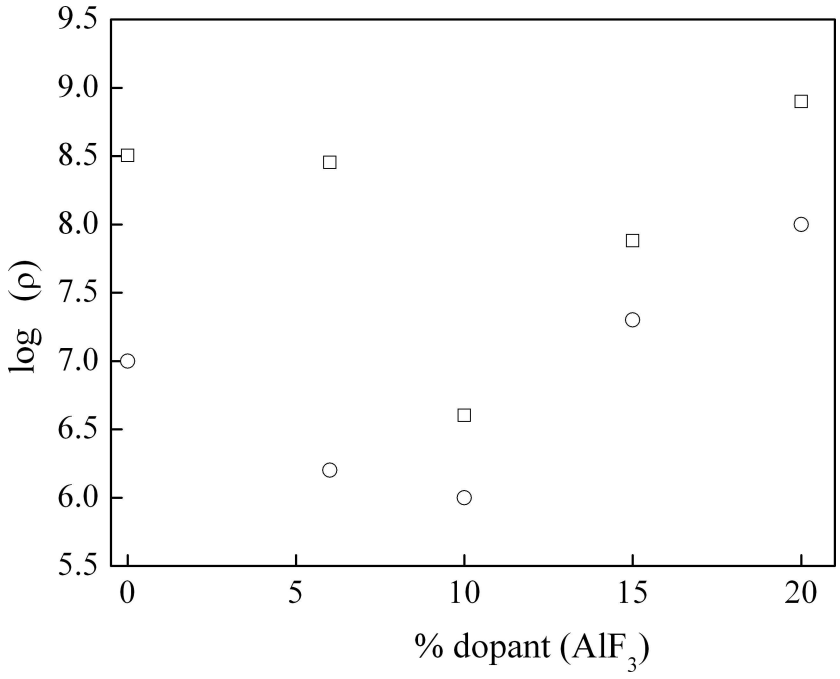


Figure 8.11: Graph showing the logarithm of the resistivity for samples doped with different concentrations of AlF_3. Open squares : thickness 200 nm; open circle : thickness 500 nm.

during two different evaporation runs. However, the results of the change in resistivity were not dramatic. One possible explanation is that may be a tendency for the creation of charge equilibrium on the sites where the dopant ions are situated resulting in few net charge carriers. This could be similar to the well known mechanism of charge compensation in single crystals [15].

8.4 Summary and Correlation with Optical Properties

Uniform PMF films have been deposited on pyrex and fused silica glass substrates held at LNT using a thermal evaporation method. The results presented in this chapter seem difficult to interpret as properties such as resistivity appear to be dependent on the history of preparation of the samples in a complex or irreproducible way. What seemed to be identical evaporation conditions lead to different values of the re-

sistivity of the as-grown films of similar thickness. The difference in the values of the resistivity for samples deposited during the same evaporation run varied by a factor of 7 in the extreme case.

Sputtering during the process of implantation, particularly for large fluences, has a significant effect on the PMF film samples as can be seen on the changes in the optical transmittance spectra after ion implantation. The absence or reduction in the optical interference patterns indicates that thickness uniformity of the samples seems is destroyed. At the same time, the PMF film samples became thinner which in all cases meant larger values of the resistance as the fluence increased. The surface region in which the excess ions are to be embedded could well have been removed during implantation. Using lower fluences brought down the resistivity but not sufficiently to be of scientific interest, while sputtering was a problem when larger fluences were used. Co-deposition of MgF_2 with AlF_3 to dope the PMF films with Al ions produces a minimum resistivity at 10% doping level but has a minimal overall effect. There is also no effect the electrical resistivity in using different the two different substrates (pyrex and fused silica glass), which is attributed to similar film growth mechanisms during the thermal deposition process.

Annealing these films nearly always lowers the resistivity, to a limited degree, probably due to the increase in the size of the crystallites. This decrease in the resistivity is not matched by the expected corresponding change in the optical transmittance since the films could still be classified as highly insulating. There is no certainty that agglomeration of the excess Mg^+ ions in the film or its effects takes place because it is not observed in the optical spectra of the annealed films.

Chapter 9

Summary and Discussion, and Outlook for Further Work

9.1 Optical Studies of Proton Implanted CsI

9.1.1 Summary and Discussion

CsI crystals have been coloured by implantation with 1 MeV protons near room temperature to fluences of up to 6×10^{16} ions/cm^2. Optical absorption studies performed at 77 K reveal the F_2 band located near 1.1 eV, the F band close to 1.66 eV, which appears as a shoulder on the higher photon energy side and several V bands located near 2.7, 3.4, 4.05, 4.2 and 4.35 eV. Implantation of the CsI samples with varying proton fluences provides information of the growth curve and the development of the F, F_2 and V bands from early stages. The V band at 4.2 eV is observed to grow linearly with the F_2 and other V bands thus suggesting that it is a radiation induced defect. However, this V band is fairly sharp making it different from the broad bands normally associated with molecular centres such as those currently observed near 2.7 and 3.4 eV.

The Raman spectra of the proton implanted CsI sample, measured at 77 K, reveal a peak at 113 cm^{-1} accompanied by more than 5 progressive overtones occurring at higher multiple wavenumbers. These Raman features are associated with the presence of the I_3^- defects. The occurrence of a large number of overtones is attributed to the near resonance conditions of the exciting laser line used. The V bands at 2.7 and 3.4 eV, observed by optical absorption studies, are attributed to the I_3^- defects. From the results of the isochronal annealing, the correlation of the optical absorption and Raman intensity confirm that the F_2 and the V bands at 2.7 and 3.4 eV decay simultaneously

at a major annealing stage close to 385 K. The band at 4.2 eV is still significant at this stage and it is not until near 410 K that signs of major annealing occur. The absorbance values of this band remain relatively large even after the complete decay of the well-correlated F_2 and V bands mentioned earlier. Chemical reaction kinetics extracted from the isothermal annealing data show that the interstitial-vacancy recombination process is second order, suggesting that the di-interstitials break up first forming H centres which recombine with the F_2 centres. The combined analysis of the optical absorption and Raman studies further shows that the decay occurs in a single step, confirming an interstitial vacancy recombination process. The activation energy of the recombination process determined from the decay of the absorbance of the F_2 band or the V band at 2.7 eV was found to be 1.28 eV.

In the Hobbs et al. mechanism [76], the formation of the perfect dislocation loops requires displacement on both the cation and anion sublattices. Such displacements create space in the lattice either as divacancies, larger aggregates and ultimately large voids. The smaller cations, as for the case of KI, are likely to be more easily displaced and hence create more space for large interstitial aggregation. In RbI and CsI, with relatively larger cations, much less space is created and hence result in the formation of smaller aggregates.

The formation of the I_3^- defects in present work and in KI and RbI, under irradiation certain conditions, suggest that the damage creation mechanism may be similar in these iodides.

9.1.2 Outlook for Further Work

The damage creation resistance of this material to conventional irradiation techniques, such as the use of γ- and X-ray sources, needs further investigation in regard to the primary mechanism of defect production. The presence of a large number of V bands in proton implanted CsI and particularly prominent ones in comparison to

γ-irradiated KI and RbI is a matter that is worth pursuing, backed by theoretical calculations, to understand the nature of defects and the production mechanism.

9.2 Mg Colloids in Magnesium Fluoride Single Crystals

9.2.1 Summary and Discussion

The primary products in a material where the excitonic mechanism is the dominant process of damage creation are vacancies and interstitials. This mechanism is well documented for MgF_2 as being largely responsible for damage creation. Although optical absorption bands due to halogen interstitials defects in the widely studied alkali halides have been observed, the same has not happened for MgF_2. There is, however, a report in which *H* centres have been observed using an electron spin resonance technique following neutron irradiation of MgF_2 [215] at 4 K. The present study reports effects produced in MgF_2 crystals following the implantation at LNT with 100 keV Mg^+ ions to a fluence of 10^{17} ions/cm^2. Optical absorption measurements after warming to RT and subsequent isochronal annealing reveal a broad absorption near 7.5 eV (165 nm) present in the VUV spectra of the as-implanted crystals. By means of the difference spectra, two component *V* bands are identified near 7.8 eV (159 nm) and 6.5 eV (191 nm), with the one at the lower photon energy not previously observed. The composite *V* band absorption is associated with interstitial fluorine defects created during the ion implantation and modified in structure by annealing. Although ion implantation in the present work was done at low temperatures, the actual optical measurements were carried out at RT and higher temperatures. It is therefore considered that the centres observed are clusters of halogen interstitials and result in the two bands in the VUV. The conversion of one of the bands at the expense of the other with increasing annealing temperature is attributed to the structural transformations within the cluster types. This represents the first report of the annealing behaviour of the fluorine interstitial and

anion vacancy defects in MgF_2 studied by optical absorption spectroscopy.

The development during isochronal annealing of a Mg colloid band near 4.43 eV (280 nm) is discussed. The band is produced by aggregation of the implanted Mg^+ ions. Although the decay of the *F*, F_2 and *V* bands coincide with the beginning of the growth and narrowing of the colloid band which could imply the formation of intrinsic colloids, it is likely that the colloid bands themselves are dominantly formed by the agglomeration of the excess Mg^+ ions introduced by the implantation. The progressive narrowing of the colloid band with increasing annealing temperature is directly linked to the growth of the mean size of the MNP reaching a maximum in the 723 - 813 K range. Annealing above this temperature range leads to a significant decay in the intensity of the colloid band. The Mie theory (MT) simulations performed to fit the experimental data also indicate an increase of the average Mg MNP diameter with the annealing to a maximum value of about 1.5 nm. The fitting also shows that the dielectric constant (ϵ_h) of the host matrix increases with higher annealing temperatures. It is noted that while ϵ_h has been used as a fitting parameter, the dielectric properties of the metal particles have been calculated from theory. Thus all variations will be reflected by changes in ϵ_h.

The diffusion of oxygen into the implanted layer leads to the formation of MgO manifested by the shift in the absorption edge to 7.7 - 7.9 eV. This has been confirmed by the XPS technique used to analyze the elemental constitution of the surface layer of the sample annealed in air at 973 K. The results of the XPS study provide a clear indication that for samples annealed in air, diffusion of oxygen atoms from the environment is a significant factor affecting the disintegration of colloids near the surface. It appears that due consideration of such effects needs to be made in general when annealing ion implanted materials to optimize nano-sized colloids, particularly if potentially reactive metals are used. Similar optical absorption studies performed in argon gas showed minimized effects of absorption and the shift of the absorption edge to longer wave-

length with annealing temperature. The onset of significant decay of the colloid band on annealing in air and under gentle argon flow has been found to occur at a similar temperature, 903 K. This temperature is sufficiently close to the melting point observed in bulk metal, 922 K, suggesting the likelihood that melting and dispersion of the Mg MNP takes place.

9.2.2 Outlook for Further Work

The exact location of the implanted Mg^+ ions in the MgF_2 lattice is not known. It would be desirable to perform channeling experiments in order to establish the actual preferred site of the Mg^+ ion in this lattice. Further studies of the new *V* bands are of interest, possibly using electron spin resonance methods.

9.3 Studies of Ag and Au Metal Nanoparticles Embedded in Lithium Niobate

9.3.1 Summary and Discussion

Optical absorption studies of the X-cut LN samples implanted with 100 keV Ag^+ ions to fluences of 10^{17} ions/cm^2 at LNT, RT and 373 K all show optical extinction bands attributed to the formation of Ag MNP. The implant at LNT has a higher intensity, narrower FWHM and its plasmon resonance (PR) peak position is shifted to longer wavelength. The difference in these three optical spectra is explained in terms of the existence of a narrower particle size distribution as a result of relatively lower diffusion rates for the implant done at LNT.

Annealing the X-cut LN sample implanted with Ag^+ ions at 373 K to higher temperatures results in the movement of the PR peak to longer wavelength and the narrowest FWHM at 773 K. It was also observed that diffusion of Ag atoms from the implanted layer to the surface of the samples occurred after a short period in the present study. This diffusion is attributed to expulsion of excess Ag atoms from the implanted

layer due to a high concentration gradient created by a low energy implant of Ag^+ ions. After the anneal at 1173 K, the optical absorption spectrum develops a complex structure, accompanied by reduction in the intensity and broadening of the Ag colloid band, that is likely to be related to melting of the particles being close to that of the bulk, known to occur near 1235 K.

TEM studies of the Ag^+ ion implanted X-cut LN annealed to 513 K confirm the existence of a distribution of particle sizes and shapes that are formed due to the agglomeration of Ag atoms. A comparison between the predicted average particle size using the Mie theory and those observed in a TEM micrograph is considered to be fair. The implanted region was observed to be partially amorphised, which would be consistent with the results of the Mie theory fitting which show a value of ϵ_h lower than that of the virgin crystal following annealing near 573 K.

Implantation of the X- and Y-cut LN samples with 8 MeV Au^{3+} ions have also been performed and the effect of annealing on the embedded ions investigated by optical absorption measurements. RBS studies of the X-cut LN sample indicate the presence of Au in the implanted region. The ion distribution versus depth profile is assumed to remain unchanged since no Au MNP bands are observed in optical absorption measurements following annealing below 973 K. However a broad pre-colloid band in the neighbourhood of 2.3 eV is present in as-implanted X-and Y-cut specimens and is considered to arise from Au dimers, trimers and other very small clusters. These clusters must therefore result from statistical formation during ion implantation or radiation enhanced diffusion of the implanted Au in view of the higher temperatures needed for thermally-induced aggregation of the Au atoms. The development of a colloid band, observed below 2.0 eV (600 nm) at lower annealing temperatures, has been followed by optical absorption measurements and its peak found to consistently shift to the longer wavelength with higher annealing temperature. The near linear background is attributed to defects created during the ion implantation, likely to be oxygen vacancies created by

lattice displacements during the initial stages in which the LN maintains its crystal structure to an appreciable degree. Ultimately at the highest fluences massive disorder results in amorphisation and the final background will result from the amorphised region.

Differences in the colloid development with annealing temperature have been observed and are likely to be associated with the anisotropic diffusion in X- and Y-cut LN, which would be related to crystal structure. The results of SRIM2003 simulation indicate that only in a limited regions does the electronic stopping attain the threshold value of 5 keV/nm for amorphization due to electronic excitation by swift heavy ions. This suggests that the damage is caused mainly by nuclear collisions. Upon annealing, the crystal structure is restored by both re-crystallization from the amorphous regions and solid phase epitaxy from the interface beyond the end of the ion range, thus accounting for the the observed anisotropic behaviour.

The host dielectric constant value, of about 4.7, obtained from the Mie theory fitting following the anneal at 1173 K is less than 5.1, the average between the two indices for the virgin crystal. At the highest annealing temperatures in the range 1273 to 1373 K used for the X-cut samples it is noted that ϵ_h attains values of 5.6 and 5.8, respectively, being higher than that of the virgin crystal. Although full re-crystallization has been achieved, the implanted region at these temperatures is subject to the development of oxygen vacancies and the presence of a significant fraction of the previously aggregated Au in a dispersed form in a now crystalline but defective host. It appears that these factors lead to the enhanced values of ϵ_h. A comparison between the predicted average particle size using the Mie theory and that observed in the TEM micrograph, following the anneal at the same temperature, is considered to be satisfactory. It is further noted that the reasonably spherical Au MNP are embedded in crystalline matter as shown by a selected area electron diffraction analysis. It is observed that the decrease in the size of the Au MNP following annealing between 1273 and 1373 K may be related

to melting of the Au particles, being close to that of the bulk metal quoted to occur near 1337 K.

9.3.2 Outlook for Further Work

To make further progress beyond the results reported in this work, in order to elucidate the mechanisms leading to a blue or red shift in the extinction peaks associated with the presence of MNP, the following suggestions are proposed. The annealing environment containing the samples embedded with MNP should be carefully controlled. This is because the current work has shown differences in the optical properties of the host matrix on annealing under gentle argon flow and in air. While the Au MNP observed in the TEM studies are approximately spherical, they have facets exhibiting cubic, octahedron and truncated octahedron geometries, among others. Further investigations of the morphology of these particles would be valuable.

9.4 Comparison of the Optical Behaviour of Mg MNP in MgF_2 and Ag or Au MNP in LN Systems

Table 9.1 shows the changes in the PR peak position with rising annealing temperature, which consistently moves to higher photon energies. The melting point of the bulk metal and the temperature at which significant colloid band decay was observed are also included. There is a similar pattern in the optical behaviour of the Mg MNP in MgF_2 and Ag or Au MNP in LN with rising annealing temperature observed in the present work. Heating the samples is expected to generate diffusion of the implanted and displaced ions as well as vacancies. The colloid bands form due to the agglomeration of the implanted cations and develop with higher annealing temperature before decaying at temperatures that are close to the melting points of the bulk metal in two of the three cases. The observed behaviour of the decay of the colloid bands strongly suggests that the reduction of the band intensity following annealing at high tempera-

tures results from melting of the MNP in the systems studied. The lower melting point, observed for the Mg MNP and Ag MNP in MgF_2 and LN matrices, respectively, would be consistent with the established fact that the cohesive energy, being the energy needed to break the metal particles into individual atoms, in MNP is less than that for the bulk metal. For these two cases, where low energy implantation was performed and hence the ions ended relatively close to the surface, melting and dispersion of the MNP would lead to significant decay of the associated colloid bands. For the case of Au MNP, where high energy implantation was done leading to a larger mean penetration depth compared to the previous case, an onset of particle size reduction is observed following annealing between 1273 and 1373 K but the colloid band remains significant. It is noted that the melting temperature of Au nanoparticles does not follow the known monotonic decrease in the melting point with smaller particle sizes. The reason for this deviation has been attributed, in a recent review by Baletto and Ferrando [357], to a change in the structure of the Au MNP as the temperature of the host matrix is raised. The strong presence of the Au colloid band following annealing above the melting point of bulk

System	Annealing Temp. (K)	PR peak position
Mg MNP in MgF_2	543	270 nm (4.59 eV)
Bulk metal m.p (922 K)	633	280 nm (4.43 eV)
MNP decay temp. (903 K)	813	285 nm (4.35 eV)
	903	285 nm (4.35 eV)
Ag MNP in LN	300	517 nm (2.40 eV)
Bulk metal m.p (1235 K)	573	520 nm (2.38 eV)
MNP decay temp. (1173 K)	773	540 nm (2.30 eV)
	973	540 nm (2.30 eV)
Au MNP in LN	1073	585 nm (2.12 eV)
Bulk metal m.p (1337 K)	1173	595 nm (2.08 eV)
MNP decay temp. (1273 - 1373 K)	1273	625 nm (1.98 eV)
	1373	635 nm (1.95 eV)

Table 9.1: PR peak position as a function of the annealing temperature. Bulk metal melting points (m.p) and the observed MNP colloid band decay temperature are also shown.

Au is in agreement with this review. However, the findings of Dick et al. [365], who studied melting in silica-coated Au MNP, show that even particles as large as 20 nm had a melting point lower than the bulk.

It is currently considered, based on the experimental evidence and the qualitative results of the Mie theory used, that the annealing of implantation induced damage in the host matrix is the most significant effect that determines the change in the PR peak position. This effect results in the PR peak position moving to lower photon energies.

9.5 Proton Irradiation of Tin Doped Indium Oxide (ITO) Films

9.5.1 Summary and Discussion

The use of 1 MeV protons to irradiate ITO thin films has been found to dominantly create defect and defect clusters by an electronic mechanism, leaving the basic structure of the ITO films unchanged. These conclusions are supported by a SRIM2003 simulation, which shows that the energy of the proton beam is such that the mean penetration depth is considerably larger than the thickness of the films. Thus nuclear stopping will occur in the glass substrate. This is consistent with the X-ray diffraction analysis of the samples, which show almost no change in the intensity of the peaks that characterize the ITO lattice structure for samples irradiated with proton fluences below $250\times10^{15}/cm^2$. At the highest fluence, namely $250\times10^{15}/cm^2$, the peak angles at which the four characteristic X-ray reflections occur are slightly shifted to lower angles and there is a corresponding increase in the associated d-spacing values, and a reduction in the peak intensity. The shift is attributed to strain introduced by the presence of defect clusters arising from the high fluence irradiation of the film. A subsequent check on two irradiated samples, which received fluences of 40 and $250\times10^{15}/cm^2$, showed recovery of the d-spacing values when investigated again by the X-ray diffraction analysis after storage for a month. The intensities of the X-ray peaks for the sample irradiated with

the $250\times10^{15}/cm^2$ also recovered to a considerable degree. This check suggests that a structural recovery process occurs after the irradiation experiment. The detailed nature of the clusters is not known. Further work is needed to attain a deeper understanding.

The optical indices of the unirradiated float glass substrate supporting the ITO films have been determined. The real part of the refractive index stays practically constant at about 1.4 over the entire spectral region studied, but rises steeply near the absorption edge of glass. The imaginary part is generally very small over a similar spectral region. The absorption coefficient has been found to be much lower than that of the ITO films. This information permitted the optical indices of the films to be determined. The optical indices of the films show fluence dependence and little dispersion over large regions of the infrared and part of the visible spectrum.

Irradiation of the ITO thin films with successively increasing proton fluences at RT leads to a three stage growth of the absorption coefficient. At higher irradiation temperature (373 K), the rate of growth of the absorption coefficient with increasing fluence is significantly diminished and the second stage is lengthened with the third stage barely visible. Use was made of a model previously applied to the growth of *F* centres in alkali halides near room temperature, but modified to include the effect of a higher temperature, to account for the growth kinetics of the absorption coefficient of the ITO films under proton irradiation. The three stage growth kinetics were associated with the heterogeneous nucleation of defect clusters and qualitative agreement was achieved between the experimental results and the predictions of the model.

An examination of the radiation induced absorbance versus wavelength behaviour with increasing proton fluence reveals a change from a near $1/\lambda^2$ dependence, probably related to a transition stage in the extinction mechanism, to a $1/\lambda$ dependence, where the latter is associated with absorption by clusters. The darkening of the ITO films, an observation made in the present work coinciding with the reduction of transmittance, is thus ultimately linked to the formation of the clusters. The sheet resistance of the unir-

radiated ITO film sample decreases when the temperature is lowered representing typical metallic behaviour as the effect of phonon scattering on charge carriers is reduced. Selected samples irradiated with higher proton fluences show a similar behaviour but have a higher sheet resistance. Two possible reasons emerge from the current work that could lead to the rise in the sheet resistance. The first one is the creation of disorder introduced by the removal of material from the surface of the films causing roughness and hence scattering of the charge carriers. The second reason, whose effect would also enhance scattering of charge carriers, is the formation of clusters that form in the high fluence regime.

9.5.2 Outlook for Further Work

More work needs to be done to establish the complex nature of defects responsible for the optical behaviour observed and to study the recovery mechanism by using some kind of *in situ* monitoring of the structure of the films during the irradiation experiment. It may be worthwhile to first study the effects of irradiating indium oxide films to obtain a good understanding and to identify the defects created and defect production processes, before extending the studies to ITO films.

Because of the existence of several cations which may exhibit multivalency oxidation states, the use of facilities such as the X-ray fine structure analysis and the XPS technique could be crucial in providing an understanding of what occurs when the irradiation fluence is increased.

9.6 Studies of the Properties of Polycrystalline Magnesium Fluoride Films

9.6.1 Summary and Discussion

Uniform PMF films have been deposited using a thermal evaporation technique on substrates held at LNT. The results presented in this chapter seem difficult to inter-

pret as properties such as resistivity appear to be dependent on the history of preparation of the samples in a complex or irreproducible way. What seemed to be identical evaporation conditions lead to different values of the resistivity for similar film thickness.

Sputtering during the process of implantation, particularly for large fluences, had a significant effect on the PMF film samples as can be seen on the changes in the optical spectra after ion implantation. The absence or reduction in the optical interference patterns indicates that thickness uniformity of the samples seems to be destroyed. At the same time, the PMF film samples became thinner which in all cases meant larger values of the resistance as the fluence increased. The surface region in which the excess ions should have been embedded could well have been removed during implantation. Using lower fluences did not bring down the resistivity sufficiently, while sputtering was a problem when larger fluences were used. Co-deposition with AlF_3 to dope the PMF films with Al ions produces a minimal effect. The was no effect of using different the two different substrates (Pyrex and fused silica glass) on the electrical resistivity, which is attributed to similar film growth mechanisms during the thermal deposition evaporation process.

Annealing the films nearly always lowers the resistivity probably by increasing the sizes of the crystallites but only to a limited degree. This decrease in the resistivity is not matched by the expected corresponding change in the optical transmittance since the films remained highly insulating. There is no certainty that agglomeration of the excess Mg^+ ions in the film or its effects takes places because it is not observed in optical spectra of the annealed films.

9.6.2 Outlook for Further Work

It is possible that co-deposition performed with metals that are sufficiently inert and hence have minimal interaction with the substrate will give better results. A strict control of the residual gases and deposition rates may be key to attaining reproducible

results of resistances for similar film thickness. The role of water vapour in the deposition chamber was not investigated and may have an effect on the films. It is therefore suggested that further work to gain a deeper understanding of the role of water vapour on the resistivity PMF films should be done.

Bibliography

[1] P. D. Townsend, C. J. Chandler and L. Zhang. Optical Effects of Ion Implantation. New York : Wiley, 1990.

[2] G. Carter and W. A. Grant. Ion Implantation in Semiconductors. Edited by Edward Anorld, 1976.

[3] H. Schiott. Rad. Effects., 6:107, 1970.

[4] F. Agullo-Lopez, C. R. A. Catlow and P. D. Townsend. Point Defects in Materials. Academic Press, London, 1988.

[5] W. K. Chu, J. W. Mayer and M. A. Nicolet. Backscattering Spectrometry. Academic Press, New York, 1978.

[6] H. H. Andersen and J. F. Ziegler. Hydrogen Stopping Powers and Ranges in All Element, vol. 3. Pergamon Press, 1977.

[7] J. W. Mayer, L. Eriksson and J. A. Davies. Ion Implantation in Semiconductors. Academic Press : New York, 1970.

[8] H. H. Andersen, J. F. Bak, H. Knudsen and B. R. Nielsen. Phys. Rev. A, 16:1929, 1977.

[9] G. Gotz and O. Karge. Nucl. Instrum. Methods, 209/210:1079, 1983.

[10] M. W. Thompson. Philos. Mag., 18:377, 1968.

[11] P. Sigmund. Rev. Phys., 184:383, 1969.

[12] J. P. Biersack and L. G. Haggmark. Nucl. Instrum. Methods, 132:647, 1976.

[13] J. F. Ziegler, J. P. Biersack and U. Littmark. Stopping Power and Ranges of Ions in Matter, vol.1. Pergamon Press, New York, 1985.

[14] R. P. Webb, D. E. Harrison and M. M. Jakas. Nucl. Instrum. Methods Phys. Res., B15:1, 1986.

[15] J. H. Schulman and W. D. Compton. Colours Centres in Solids Vol. 2 ed. R. Smoluchowski and N. Kurti. Oxford, Pergamon Press, 1962.

[16] W. Hayes and A. M. Stoneham. Defects and Defect Processes in Non-metallic Solids. New York: Wiley, 1985.

[17] T. G. Castner and W. Kanzig. J. Phys. Chem. Solids, 3:178, 1957.

[18] F. Stockmann. Naturwissenchaften, 39:230, 1952.

[19] C. Z. Van Doorn. Review Sci. Instrum., 32:755, 1961.

[20] H. Seidal and H. C. Wolf. Physics of Colour Centres ed. W B Fowler. New York: Academic Press, 1985.

[21] H. Pick. Annalen. d. Physik (Leipzig), 31:365, 1940.

[22] H. Pick. Nuovo Cimento, VII Ser. X, 1958.

[23] F. Luty. Halbleiterprobleme. Band VI ed. W. Schottky p.238. Berlin : Springer, 1961.

[24] M. Ikezawa, M. Hirai and M. Ueta. J. Phys. Soc. Jpn, 17:1474, 1962.

[25] G. Goldberger and F. J. Owens. Phys. Rev. B., 34:3927, 1971.

[26] T. Todorov, N. Koralov and M. Georgiev. Opt. Commun., 13:439, 1975.

[27] C. J. Delbecq, P. Pringsheim and P. Yuster. J. Chem. Phys., 19:574, 1951.

[28] F. Luty. Physics of Colour Centres ed. W. Beall Fowler. New York: Academic Press pp.181-242, 1968.

[29] C. J. Delbecq. Z. Physik, 171:560, 1963.

[30] F. J. Dudek and L. I. Grossweiner. J. Phys. Chem. Solids, 30:2023, 1969.

[31] F. Jaque and F. Agullo-Lopez. Phys. Rev. B, 2:4225, 1970.

[32] I. Schneider. Solid State Commun., 9:2191, 1971.

[33] M. Georgiev. Lecture Notes in Physics, *F′* Centres in Alkali Halides. Berlin : Spinger Verlag, 1988.

[34] A. Rascon and J. L. Alvarez Rivas. J. Phys. C (Solid State Physics), 169:241, 1983.

[35] N. Itoh. Cryst. Latt. Def. and Amorph. Mat., 3:115, 1972.

[36] M. N. Kabler, M. J. Marrore and W. B. Fowler. Luminescence of Crystals, Molecules and Solutions ed. F. Williams. New York : Plenum, 1973.

[37] D. Pooley and W. A. Runciman. J. Phys. C (Solid State Physics), 3:1815, 1970.

[38] H. N. Hersh. Phys. Rev., 148:928, 1966.

[39] M. J. Marrone, F. W. Patten and M. N. Kabler. Phys. Rev. Lett., 31:467, 1973.

[40] A. Wasiela, G. Ascarelli and Y. Meled' Aubique. Phys. Rev. Lett., 31:993, 1973.

[41] R. B. Murray and F. J. Keller. Phys. Rev. A, 137:942, 1965.

[42] R. B. Murray and F. J. Keller. Phys. Rev., 153:993, 1967.

[43] R. G. Fuller, R. T. Williams and M. N. Kabler. Phys. Rev. Lett., 25:446, 1970.

[44] C. J. Delbecq, B. Smaller and P. H. Yuster. Phys. Rev., 111:1235, 1958.

[45] W. Kanzig and T. O Woodruff. J. Phys. Chem. Solids, 9:1728, 1959.

[46] D. Schoemaker. Defects and their Structure in Nonmetallic Solids, Edited by B. Henderson and A. E. Hughes. New York : Plenum, 1976.

[47] R. Capelleti, R. Fieschi, A. Gainotti, C. Mora, L. Romano and E. Zecchi. International Conference on Defects in Insulating Crystals, Riga, USSR., 1981.

[48] J. D. Comins and B. O. Carragher. J. Phys. (Paris), 41:C6–166, 1980.

[49] J. D. Comins and B. O. Carragher. Phys. Rev. B, 24:283, 1981.

[50] W. Hayes and G. M. Nichols. Phys. Rev., 117:993, 1960.

[51] J. Hoshi, M. Saidoh and N. Itoh. Cryst. Latt. Def. and Amorph. Mat., 6:15, 1975.

[52] J. N. Marat Mendes and J. D. Comins. J. Phys. Chem. Solids, 38:1003, 1977.

[53] J. N. Marat Mendes and J. D. Comins. J. Phys. C, 10:4425, 1977.

[54] T. Okada. J. Phys. Soc. Japan, 50:582, 1981.

[55] T. Okada and J. Hata. Mol. Phys., 43:1151, 1981.

[56] D. R. Wolfe E. M. Winter and R. W. Christy. Phys. Rev., 186, No. 3:949, 1969.

[57] J. D. Konitzer and H. N. Hersh. J. Phys. Chem. Solids, 27:771, 1966.

[58] S. Lefrant and E. Rzepka. J. Phys. C (Solid State Physics), 12:L573, 1979.

[59] C. R. A. Catlow, K. M. Diller and L. W. Hobbs. Philos. Mag. A, 42:no.2, pg 123, 1980.

[60] A. B. Lidiard M. J. Norgett. Computational Solid State Physics. Plenum : New York, 1972.

[61] H. Dorendorf. Z. Physik, 129:317, 1951.

[62] C. J. Delbecq, E. Hutchinson, D. Shoemaker, E. L. Yasaitis and P. H. Yuster. Phys. Rev., 187:1103, 1969.

[63] G. J. Dienes, R. D. Hatcher and R. Smoluchowski. J. Phys. Chem. Solids, 31:701, 1970.

[64] R. W. Christy and D. H. Phelps. Phys. Rev., 124:1053, 1961.

[65] H. N. Hersh. Phys. Rev., 105:1410, 1957.

[66] H. N. Hersh. Phys. Rev., 105:1158, 1957.

[67] A. Okuda, T. Harami, T. Okada, Y. Tanaka and O. Takai. J. Phys. Soc. Japan, 43:993, 1977.

[68] H. L. Forbes and D. W. Lynch. J. Phys. Chem. Solids, 25:261, 1964.

[69] F. Seitz. Phys. Rev., 79:529, 1950.

[70] F. Seitz. Rev. Mod. Phys., 26:7, 1954.

[71] J. H. O. Varley. J. Nuc. Energy, 1:130, 1954.

[72] J. D. Comins. Solid State Commun., 5:709, 1967.

[73] E. Sonder, G. Bassignani and P. Camagni. Phys. Rev., 180:882, 1969.

[74] N. Itoh and M. Saidoh. Phys. Status Solidi, 33:649, 1969.

[75] N. Itoh and M. Saidoh. J. Phys. (Paris), 34:C9–101, 1973.

[76] L. W. Hobbs, A. E. Hughes and D. Pooley. Proc. Roy. Soc.(London), A332:167, 1973.

[77] F. Agullo-Lopez, F. J. Lopez and F. Jaque. Cryst. Latt. Def. and Amorph. Mat., 9:227, 1982.

[78] L. W. Hobbs. J. Phys. (Paris), 37, no. 12:C7–3, 1973.

[79] L. W. Hobbs. J. Phys. (Paris), 34:C9–227, 1976.

[80] J. P. Stott and J. H. Crawford. Phys. Rev. B, 6:4660, 1972.

[81] S. Lefrant E. Rzepka, L. Taurel and A. E. Hughes. J. Phys. C (Solid State Physics), 4:L767, 1981.

[82] J. D. Comins, A. M. T. Allen, P. J. Ford and D. A. Mathews. Rad. Effects, 72:107, 1983.

[83] A. M. T. Allen, J. D. Comins and P. J. Ford. J. Phys. C (Solid State Physics), 18:5783, 1985.

[84] A. M. T. Allen and J. D. Comins. Cryst. Latt. Def. and Amorph. Mat., 17:93, 1987.

[85] F. Agullo-Lopez and F. Jaque. J. Phys. Chem. Solids, 34:1949, 1973.

[86] G. Guiliani. Phys. Rev. B, 2:464, 1970.

[87] A. M. Mdebuka and J. R. Seretlo. S. Afr. J. Phys., 8:40, 1982.

[88] N. Itoh, B. S. Royce and R. Smoluchowski. Phys. Rev., 137 A:1010, 1965.

[89] M. Ikeya, T. Okada and T. Suita. J. Phys. Soc. Jpn, 21, No. 7:1304, 1966.

[90] Y. Farge. J. Phys. Chem. Solids., 30:1375, 1969.

[91] J. N. Marat Mendes and J. D. Comins. Cryst. Latt. Def. and Amorph. Mat., 6:141, 1975.

[92] J. N. Marat Mendes and J. D. Comins. J. Phys. C (Paris), 37:C7–132, 1976.

[93] F. Agullo-Lopez and F. Jaque. J. Phys. Chem. Solids, 32:2009, 1971.

[94] M. Aguilar, F. Jaque and F. Agullo-Lopez. J. Phys. (Paris), 41:C6–341, 1980.

[95] M. Aguilar, F. Jaque and F. Agullo-Lopez. Rad. Effects, 61:215, 1982.

[96] N. Itoh and T. Goto. Rad. Effects, 37:45, 1978.

[97] G. Guillot and A. Nouailhat. Phys. Rev. B, 19:2295, 1979.

[98] S. Ramos, J. Hernandez, A. Murrieta and J. Rubio. Phys. Rev. B, 31:8164, 1985.

[99] J. H. Crawford Jnr. J. Phys. Soc. Jpn, 18:329, 1963.

[100] H. Stammreich. Spectrochim Acta, 8:41, 1956.

[101] R. Forneris H. Stammreich and Y. Tavares. Spectrochim Acta, 17:1173, 1961.

[102] A. G. Maki and R. Forneris. Spectrochemica Acta, 23A:867, 1966.

[103] P. Klaboe. J. Am. Chem. Soc, 89 No. 15:3667, 1967.

[104] K. R. Loos and A. C. Jones. J. Phys. Chem., 78 No. 22:2306, 1974.

[105] L. Andrews. J. Chem. Phys., 57:51, 1972.

[106] W. F. Howard and L. Andrews. J. Raman Spectr., 2:447, 1974.

[107] R. W. G. Wyckoff. Crystals Structures Vol. 1. Interscience Publishers, New York, 1948.

[108] F. Vovelle and G. G. Dumas. Mol. Phys., 34:1661, 1977.

[109] K. Kaya, N. Mikami, Y. Udagawa and M. Ito. Phys. Chem. lett., 16, No. 1:151, 1972.

[110] E. S. Prochaska L. Andrews and A. Lowewenschuss. Inorg. Chem., 19:463, 1980.

[111] B. V. Shanabrook and J. S. Lannin. Sol. State Commun., 38:49, 1981.

[112] A. M. T. Allen and J. D. Comins. Nucl. Instrum. and Methods, 46:240, 1990.

[113] A. M. T. Allen and J. D. Comins. J. Phys. Condens. Matter, 4:2701, 1992.

[114] J. D. Comins, T. P. Nguyen, M-A Pariselle, S. Lefrant and A. M. T. Allen. Radia. Eff. Defects Solids, 134:437, 1995.

[115] A. E. Hughes and U. Jain. Adv. Phys., 28:717, 1979.

[116] U. Kreibig and M. Vollmer. Optical Properties of Metal Clusters. Springer-Verlag, 1995.

[117] M. A. Smithard and M. Q. Tran. Helv. Phys. Acta, 46:869, 1974.

[118] W. D. Compton. Phys. Rev., 107:1271, 1957.

[119] P. V. Sastry and K. A. McCarthy. Phys. Status Solidi, 10:585, 1965.

[120] S. V. Pappu and K. A. McCarthy. J. Phys. Chem. Solids, 32:1287, 1971.

[121] G. Chassagne, D. Serughetti and L. W. Hobbs. Phys. Status Solidi A, 40:629, 1977.

[122] G. Chassagne, D. Serughetti and L. W. Hobbs. Phys. Status Solidi A, 41:183, 1977.

[123] A. T. Davidson, J. D. Comins, T. E. Derry and A. M. J. Raphuthi. Phys. Rev. B, 48:783, 1993.

[124] U. Kreibig. J. Phys. F, 4:999, 1974.

[125] U. Jain and A. B. Lidiard. Philos. Mag., 35:245, 1977.

[126] S. C. Jain and N. D. Arora. J. Phys. Chem. Solids, 35:1231, 1974.

[127] D. Chassagne, D. Serughetti and L. W. Hobbs. J. Phys. Chem., 57:757, 1953.

[128] D. Chassagne, D. Serughetti and L. W. Hobbs. Phys. Rev., 171:1075, 1968.

[129] S. C. Jain and N. D. Arora. Solid State Commun., 16:421, 1975.

[130] A. B. Lidiard. Comments Solid State Phys., 8:no.473, 1978.

[131] D. I. R. Norris. Rad. Effects, 15:1, 1972.

[132] D. I. R. Norris. Phys. Technol., 5:29, 1974.

[133] V. I. Dubinko, A. A. Turkin, D. I. Vainshtein and H. W. den Hartog. J. Nucl. Mater., 289:86, 2001.

[134] G. Chassagne, D. Serughetti and L. W. Hobbs. J. Phys. (Paris), 37:C7–510, 1976.

[135] I. M. Lifshitz, V. V. Slezov. J. Exp. Theor. Phys., 35:479, 1958.

[136] I. M. Lifshitz, V. V. Slezov. Soviet Phys. Solid St., 35:479, 1959.

[137] I. M. Lifshitz, V. V. Slezov. J. Chem. Solids, 19:35, 1961.

[138] C. Wagner. Z. Electrochem, 65:581, 1961.

[139] G. W. Greenwood. Inst. of Metals Monograph, no. 33:105, 1969.

[140] M. Kahlweit. Physical Chemistry. New York : Plenum, 1970.

[141] M. Kahlweit. Adv. Colloid Interface Sci., 5:1, 1975.

[142] A. E. Hughes and S. C. Jain. Phys. Lett. A, 58:61, 1976.

[143] A. E. Hughes and S. C. Jain. J. Mater. Sci., 13:1611, 1978.

[144] J. M. Calleja and F. Agullo-Lopez. Phys. Status Solidi A, 25:473, 1974.

[145] S. C. Jain and A. E. Hughes. J. Phys. Paris (Suppl.), 37:C7–463, 1976.

[146] S. C. Jain and A. E. Hughes. J. Mater. Sci., 13:1611, 1978.

[147] G. Chassagne, D. Durand, J. Serughetti and L. W. Hobbs. Phys. Status Solidi A, 40:629, 1977.

[148] A. J. Ardell. Acta. Metall., 20:61, 1972.

[149] D. J. Cellman and A. J. Ardell. Acta. Metall., 22:577, 1974.

[150] M. Smoluchowski. Z. Phys., 17:557–558, 1916.

[151] M. Smoluchowski. Z. Phys. Chem., 92:129, 1917.

[152] F. T. Goldstein. Phys. Status Solidi, 20:379, 1967.

[153] P. D. Townsend and D. J. Elliot. Phys. Lett., 28 A:587, 1969.

[154] J. N. Bradford, R. T. Williams and W. L. Faust. Phys. Rev. Lett., 35:300, 1975.

[155] N. Itoh and A. M. Stoneham. Materials Modification by Electronic Excitation. Cambridge University Press, 2001.

[156] K. S. Song and R. T. Williams. Self-Trapped Excitons. Springer-Verlag, Berlin, 1993.

[157] H. Raether. Solid State Excitations by Electrons. Springer Verlag, Berlin, 1965.

[158] W. T. Doyle. Phys. Rev., 111:1067, 1958.

[159] G. Mie. Ann. Phys., 25:377, 1908.

[160] J. C. M. Garnett. Philos. Trans. R. Soc. Lond., 203:385, 1904.

[161] J. C. M. Garnett. Philos. Trans. R. Soc. Lond., 205:717, 1906.

[162] P. Debye. Ann. Phys. (Leipz), 30:57, 1909.

[163] A. P. van Gelder, J. Holvast, J. H. M. Stoelinga and P. Wyder. J. Phys. C, 5:2757, 1972.

[164] J. C. M. Garnett. Philos. Trans. R. Soc. Lond., 205:717, 1939.

[165] W. T. Doyle. Proc. Phys. Soc., 75:649, 1960.

[166] W. Hampe. Z. Phys., 152:476, 1958.

[167] C. van Fragstein and H. Romer. Z. Phys., 151:54, 1958.

[168] J. A. A. J. Perenboom, P. W. Wyder and F. Meier. Phys. Rep., 78:173, 1981.

[169] R. Kubo. J. Phys. Soc. Jpn, 17:975, 1962.

[170] L. Genzel, T. P. Martin and U. Kreibig. Z. Phys. B, 21:339, 1975.

[171] R. Ruppin and H. Yatom. Phys. Status Solidi B, 74:647, 1976.

[172] A. Kawabata and R. Kubo. J. Phys. Soc. Jap., 21:1765, 1962.

[173] U. Kreibig. Z. Phys. B, 31:39, 1978.

[174] L. Yang, G. H. Li and L. D. Zhang. Appl. Phys. Lett., 76:1537, 2000.

[175] B. N. J. Persson. Surf. Sci, 153:533, 1993.

[176] H. Hovel, S. Fritz, A. Hilger and U. Kreibig. Phys. Rev. B, 48:18178, 1993.

[177] E. V. Chulkov, L. Sarria, V. M. Silkin, J. M. Pitarke and P. M. Echenique. Phys. Rev. Lett., 80:4947, 1998.

[178] J. B. Pendry. Phys. Rev. Lett., 45:1356, 1980.

[179] K. Giesen, F. J. Himsel, H. J. Riess and W. Steinmann. Phys. Rev. Lett., 55:300, 1985.

[180] M. Wolf, E. Knoesel and T. Hertel. Phys. Rev. B, 54:R5295, 1996.

[181] W. Cai, H. Hofmeister and M. Dubiel. Euro Phys. J. D., 13:13, 2001.

[182] P. Avakian and A. Smakula. Phys. Rev., page 2007, 1960.

[183] D. W. Lynch, A. D. Brother and D. A. Robinson. Phys. Rev., 139:A285, 1965.

[184] T. P. Martin. Phys. Rev. B, 11:875, 1975.

[185] T. P. Martin. Phys. Rev. B, 13:3617, 1976.

[186] M. Bernard E. Rzepka and S. Lefrant. Nucl. Instrum. Methods Phys. Res. B, 32:235, 1988.

[187] E. Rzepka M. Bernard and S. Lefrant. Nucl. Instrum. Methods Phys. Res. B, 46:235, 1990.

[188] T. Lida, Y. Nakaoka, J. P. von der Weid and M. A. Aegerter. J. Phys. C, 13:983, 1980.

[189] L. Falco, J. P. von der Weid, M. A. Aegerter, T. Lida and Y. Nakaoka. J. Phys. C, 13:993, 1980.

[190] J. P. Pellaux, T. Lida, J. P. von der Weid and M. A. Aegerter. J. Phys. C, 13:1009, 1980.

[191] H. Nishimura, M. Sakata, T. Tsujimoto and M. Nakayama. Phys. Rev. B, 51:2167, 1995.

[192] W. Hayes. Crystals with the Fluorite Structure. Clarendon Press, 1974.

[193] W. Hayes and J. P. Stott. Proc. R. Soc., A301:313, 1967.

[194] H. W. den Hartog and J. Arends. ibid, 22:131, 1967.

[195] A. M. Stoneham, W. Hayes, P. H. S. Smith and J. P. Stott. Proc. R. Soc., A306:369, 1968.

[196] J. H. Beaumont, J. H. Gee and W. Hayes. J. Phys. C (Solid State Physics), 3:L152, 1970.

[197] R. F. Lambourn W. Hayes and J. P. Stott. J. Phys. C (Solid State Physics), C7:2429, 1974.

[198] J. H. Beaumont, A. L. Harmer and W. Hayes. J. Phys. C (Solid State Physics), 5:1475, 1972.

[199] W. Hayes and J. W. Twidell. Proc. Phys. Soc. London Sec., 79:1295, 1962.

[200] A. Tzalmona and P. S. Pershan. Phys. Rev., 182:906, 1969.

[201] J. H. Beaumont, D. L. Kirk and G. P. Summers. ibid, A315:69, 1970.

[202] Y. Kazumata. Phys. Status Solidi, 34:377, 1969.

[203] T. P. P. Hall, A. Leggeat and J. W. Twidell. J. Phys. C (Solid State Physics), 2:1590, 1969.

[204] A. H. Harker. J. Phys. C (Solid State Physics), 6:2993, 1973.

[205] W. A. Sibley and O. E. Facey. Phys. Rev., 174:1076, 1968.

[206] R. F. Blunt and M. I. Cohen. Phys. Rev., 153:1031, 1967.

[207] M. R. Buckton and D. Pooley. J. Phys. C, 5:1553, 1972.

[208] J. Becher, R. L. Kernell and C. S. Reft. J. Phys. Chem. Solids, 44:759, 1983.

[209] A. S. El-Said, R. Neumann, K. Schwartz and C. Trautmann. Radia. Eff. Defects Solids, 157:649, 2002.

[210] E. V. Zhukova, V. M. Zolotarev and L. P. Shishatskaya. Optics and Spectroscopy, 81:723, 1995.

[211] K. Tanimura and N. Itoh. J. Appl. Phys., 69:7831, 1991.

[212] N. Itoh. Adv. Phys., 31:491, 1982.

[213] W. A. Sibley. Nucl. Instrum. Methods Phys. Res. B, 1:419, 1984.

[214] R. T. Williams, C. L. Marquardt, J. W. Williams and M. N. Kabler. Phys. Rev. B., 10:5003, 1977.

[215] Y. Ueda. J. Phys. Soc. Jpn, 41:1255, 1976.

[216] O. E. Facey and W. A. Sibley. Phys. Rev., 186:926, 1969.

[217] H. D. Megaw. Crystal Structures : A Working Approach. W. B. Saunders Company : London, 1973.

[218] L. Heping, F. Zhou, X. Zhang and J. Wei. Appl. Phys. B, 64:659, 1997.

[219] K. Kitamura, Y. Furukawa and Y. Ji, M. Zgonik, C. Medrano, G. Montemezzani and P. Gunter. J. Appl. Phys., 82:1006, 1997.

[220] M. M. Abouelleil and F. J. Leonberger. J. Am. Chem. Soc., 72:1311, 1989.

[221] S. C. Abrahams, J. M. Reddy and J. L. Berstein. J. Phys. Chem. Solids, 27:997, 1966.

[222] J. G. Bergam, A. Ashkin, A. A. Ballman, J. M. Dziedzic, H. J. Levinstein and R. G. Smith. Appl. Phys. Lett., 12:92, 1968.

[223] G. Malovichko, V. Grachev and O. Schirmer. Appl. Phys. B, 68:785, 1999.

[224] G. Malovichko, V. Grachev, E. Kokanyan and O. Schirmer. Phys. Rev. B, 59:9113, 1999.

[225] H. C. Schweinler. Phys. Rev., 87:5, 1952.

[226] D. T. Y Wei, W. W. Lee and L. R. Bloom. Appl. Phys. Lett., 25:329, 1974.

[227] G. E. Peterson and A. Carnevale. J. Chem. Phys., 56:4848, 1972.

[228] H. Fay, W. J. Alford and H. M. Dess. Appl. Phys. Lett., 12:89, 1968.

[229] W. Bollman. Cryst. Res. Technol., 18:1147, 1983.

[230] K. L. Sweeney, L. E. Halliburton, D. A. Bryan, R. R. Rice, R. Gerson and H. E. Tomaschke. J. Appl. Phys., 57:1036, 1985.

[231] S. C. Abrahams and P. Marsh. Acta. Crystallogr., Sect. B 42:61, 1986.

[232] R. J. Holmes and W. J. Minford. Ferroelectrics, 75:63, 1987.

[233] P. Lerner, C. Legras and P. J. Dumas. J. Cryst. Growth, 3/4:231, 1968.

[234] Y. Limb, K. W. Cheng and D. M. Smith. Ferroelectrics., 38:813, 1981.

[235] D. M. Smith. Ferroelectrics., 50:93, 1983.

[236] H. Donnerberg, S. M. Tomlinson, C. R. A. Catlow and O. F. Schirmer. Phys. Rev. B, 40:11909, 1989.

[237] K. Kitamura, T. Hayashi, T. Sawada, N. Iyi and S. Kimura. Proceedings of the 8th American Conference on Crystal Growth, abstract No. 40, 1990.

[238] N. Iyi, K. Kitamura, F. Izumi, J. K. Yamamoto, T. Hayashi, H. Asano and S. Kimura. J. Solid. Stat. Chem., 101:340, 1992.

[239] E. R. Hodgson, C. Zaldo and F. Agullo-Lopez. Solid State Commun., 64:965, 1987.

[240] E. R. Hodgson, C. Zaldo and F. Agullo-Lopez. Solid State Commun., 75:351, 1990.

[241] A. I. Popov and E. Balanzat. Nucl. Instrum. Methods Phys. Res. B, 166-167:305, 2000.

[242] P. W. M. Jacobs and E. A. Kotomin. J. Phys., Condens. Mater., 166-167:305, 2000.

[243] O. S. Heavens. Optical Properties of Thin Solid Films. New York : Academic Press, 1955.

[244] J. Rams, J. Olivares, P. J. Chandler and P. D. Townsend. J. Appl. Phys., 84:5180, 1998.

[245] M. Rahmani, L. H. Abu-Hassan, P. D. Townsend, I. H. Wilson and G. L. Destefanis. Nucl. Instrum. Methods Phys. Res., 32:56, 1988.

[246] M. Rahmani and P. D. Townsend. Vacuum, 39:1157, 1989.

[247] D. Y. Shang and Y. Saito, R. Kittaka, S. Taniguchi and A. Kitahara. J. Appl. Phys., 80:6651, 1996.

[248] Y. Saito, D. Y. Shang, R. Kitsutaka, S. Taniguchi and A. Kitahara. J. Appl. Phys., 82:3621, 1997.

[249] A. Kling, J. C. Soares and M. F. da Silva. Nucl. Instrum. Methods Phys. Res. B, 141:436, 1998.

[250] A. Kling, J. C. Soares and M. F. da Silva. Nucl. Instrum. Methods Phys. Res. B, 166-167:280, 2000.

[251] I. Hamberg and C. G. Granqvist. J. Appl. Phys., 60:R123, 1986.

[252] Y. Ikuma, M. Kamiya, N Okumura, I. Sakaguchi, H. Haneda and Y. Sawada. J. Electrochem. Soc., 145:2910, 1998.

[253] R. L. Weiher. J. Appl. Phys., 33:2834, 1962.

[254] Ph. Parent, H. Dexpart, G. Tourlin and J. -M. Grimal. J. Electrochem Soc., 139:282, 1992.

[255] M. Marezio. Acta Crystallogr., 20:723, 1966.

[256] M. Mizuna I. Tanaka and H. Adachi. Phys. Rev. B, 56:3536, 1997.

[257] J. H. W. de Wit. J. Solid State Chem., 8:142, 1973.

[258] J. H. W. de Wit. J. Solid State Chem., 13:192, 1975.

[259] J. H. W. de Wit, G van Unen and M. Lahey. J. Phys. Chem. Solids, 38:819, 1977.

[260] M. Higuchi, M. Sawada and Y Kuronuma. J. Electrochem. Soc.B, 139:282, 1993.

[261] A. K. Kulkani, K. H. Schulz, T. -S. Lim and M. Khan. Thin Solid Films, 308-309:1, 1997.

[262] Ph. Parent, H. Dexpart, G. Tourlin and J. -M. Grimal. J. Electrochem. Soc., 139:276, 1992.

[263] Z. M. Jarbeski. Phys. Status Solidi A, 71:13, 1982.

[264] M. Quaas, C. Eggs and H. Wulff. Thin Solid Films, 332:277, 1998.

[265] N. F. Mott. Metal-Insulator Transitions. Taylor and Francis, London, 1974.

[266] E. Burstein. Phys. Rev., 93:632, 1954.

[267] T. S. Moss. Proc. Phys. Soc. London Sec., 67:775, 1954.

[268] H. Kostlin, R. Jost and W. Lens. Phys. Status Solidi A, 29:87, 1975.

[269] E. Shanti, A. Banerjee, V. Dutta and K. L. Chopra. Thin Solid Films, 71:237, 1980.

[270] Y. Shigesato, S. Takaki and T. Haranoh. J. Appl. Phys., 71:3356, 1992.

[271] S. Muranaka, Y. Bando and T. Takeda. Thin Solid Films, 151:335, 1987.

[272] D. V. Morgan, A. Salehi, Y. H. Aliyu, R. W. Bunce and D. Diskett. Thin Solid Films, 258:283, 1995.

[273] Y. Shigesato, D. C. Paine and T. E. Haynes. J. Appl. Phys., 73:3805, 1993.

[274] T. J. Vink, H. F. Overwijk and W. Walrave. J. Appl. Phys., 80:3734, 1996.

[275] T. Serikawa and S. Shirai. Nucl. Instrum. Methods Phys. Res. B, 37/38:732, 1989.

[276] P. Lissberger and R. G. Nelson. Thin Solid Films, 21:159, 1974.

[277] M. Gajdardziska-Josifovska, R. C. McPhredan, D. R. McKenzie and R. E. Collins. Appl. Opt., 28:2744, 1989.

[278] L. G. Shulz. J. Chem. Phys., 17:1153, 1949.

[279] O. S. Heavens and S. D. Smith. J. Opt. Soc. Amer., 47:469, 1957.

[280] E. Bauer. Z. Kristal, 107:265, 1956.

[281] H. G. Coleman, A. F. Turner and O. A. Ultrich. J. Opt. Amer., 37:521, 1947.

[282] C. Weaver. Adv. Phys., 11:85, 1962.

[283] J. Robillard. Rev. Opt., 28:129, 1949.

[284] H. K. Pulker and E. Jung. Thin Solid Films, 9:57, 1971.

[285] K. L. Chopra. Thin Film Phenomena. New York : McGraw-Hill, 1969.

[286] V. A. Phillips. Philos. Mag., 5:571, 1962.

[287] V. A. Phillips. J. Appl. Phys., 33:712, 1962.

[288] U. J. Gibson and C. M. Kennemore III. Thin Solid Films, 124:27, 1985.

[289] F. Abeles. J. Phys. Radium, 11:310, 1950.

[290] N. Morita. J. Sci. Res. Inst., Tokyo, 46:127, 1952.

[291] S. Ogura. Thin Solid Films, 30:3, 1975.

[292] J. Beynon and L. Olumekor. Thin Solid Films, 41:29, 1976.

[293] K. D. Coonley, G. J. Mehas and C. R. Sullivan. IEEE Trans. on Magn., 36:3463, 2000.

[294] M. Adamov , B. Perovic and T. Nenadovima. Thin Solid Films, 24:89, 1974.

[295] W. B. Fowler. Physics of Colour Centres. Acad. Press, New York, 1968.

[296] W. Martienssen. J. Phys. Chem. Solids, 2:257, 1957.

[297] F. Urbach. Phys. Rev., 78:1324, 1953.

[298] D. Redfield. Phys. Rev, 130:914, 1963.

[299] D. Redfield. Phys. Rev, 130:916, 1963.

[300] T. Skettrup. Phys. Rev. B, 18:2622, 1978.

[301] D. L. Dexter. Solid State Physics, edited by F. Seitz and D. Turnbull. Academic Press, New York, 1958.

[302] A. Smakula. Z. Physik, page 603, 1930.

[303] W. B. Fowler and D. L. Dexter. Phys. Rev., 128:2154, 1962.

[304] W. B. Fowler and D. L. Dexter. J. Chem. Phys., 43:768, 1965.

[305] R. Chang. Basic Principles of Spectroscopy. McGraw-Hill, New York, 1971.

[306] A. M. Stoneham. Theory of Defects in Solids. Clarendom Press, Oxford, 1975.

[307] G. M. Barrow. Physical Chemistry. McGraw-Hill : New York, 1973.

[308] C. V. Raman and K. S. Krishan. Nature, 121:501, 1928.

[309] A. Smekal. Naturwissenschaften, 11:873, 1923.

[310] A. Smekal. Naturwissenschaften, 16:577 and 772, 1928.

[311] D. A. Long. Raman Spectroscopy. McGraw-Hill, New York, 1977.

[312] A. Smekal. Radiologie, Akademische Verlagsgesellschaft, Leipzig, 6:205, 1934.

[313] A. C. Damask and G. J. Dienes. Point Defects in Metals. Gordon and Breach, New York, 1963.

[314] J. R. Seretlo. PhD Thesis, University of Fort Hare. Unpublished, 1972.

[315] R. E. Howard and A. B. Lidiard. Rep. Prog. Phys., 27:161, 1964.

[316] V. Bonacic-Koutecky, P. Fantucci and J. Koutecky. Chem. Rev., 91:1035, 1991.

[317] W. Ekardt. Phys. Rev. Lett., 52:1925, 1984.

[318] W. Ekardt. Phys. Rev. B, 31:6370, 1985.

[319] M. Born. Optik. J. Springer, Berlin, 1933.

[320] H. C. van de Hulst. Light Scattering by Small Particles. J. Wiley and Sons, New York, 1957.

[321] C. F. Bohren and D. R. Huffman. Absorption and Scattering of Light by Small Particles. New York : Wiley, 1983.

[322] U. Kreibig and P. Zacharias. Z. Phys., 231:128, 1970.

[323] R. Ruppin. Proc. Phys. Soc., 87:619, 1978.

[324] P. Mulvaney. Langmuir, 12:788, 1996.

[325] R. Antoine, M. Perllarin, B. Palpant, M. Broyer, B. Prevel, P. Galleto, P. F. Brevet and H. H. Girault. J. Appl. Phys., 84:4532, 1998.

[326] R. H. Magruder III, Li Yang, R. F. Haglund, C. W. White, L. Yang, R. Dorsinville and R. R. Alfano. Appl. Phys. Lett., 62:1730, 1993.

[327] P. B. Johnson and R. W. Christy. Phys. Rev., 6:4370, 1972.

[328] N. W. Ashcroft and N. D. Mermin. Solid State Physics. Holt-Saunders International, Philadelphia, 1976.

[329] C. Kittel. Introduction to Solid State Physics. John Wiley:New York, 7th Edition, 1996.

[330] R. Ruppin. J. Appl. Phys., 59:619, 1986.

[331] R. Swanepoel. S. Afr. J. Sci., 12, no.4:148, 1989.

[332] R. M. A. Azzam and N. M. Bashara. Ellipsometry and Polarised Light. North-Holland Publishing Co., 1977.

[333] J. C. Manifacier, J. Gassiot and J. P. Fillard. J. Phys. E, 9:1002, 1976.

[334] J. R. Tesmer, M. Nastasi, J. C. Barbour, C. J. Maggiore and J. W. Mayer. Handbook of Modern Ion Beam Materials Analysis. Materials Research Society : Pennslyvania, 1995.

[335] A. T. Davenport and A. R. Booth. Stereographic Projections of the Cubic and Closed Packed Hexagonal Lattices. Buttersworth, London, 1970.

[336] E. Preus. Comput. Phys. Commun., 18:261, 1979.

[337] J. F. Prins. Nucl. Instrum. Methods B, 59/60:1387, 1991.

[338] Cary 500 Illustration Chart. Varian, Australia, 1999.

[339] Rank Hilger. Instruction Manual for the One Metre Vacuum Grating Monochromator. 1971.

[340] J. C. Vickerman. Surface Analysis : The Principal Techniques. John Wiley : New York, 1997.

[341] V. I. Nefedov. X-ray Photoelectron Spectroscopy of Solids. VNU Science Press : Utrecht, 1988.

[342] A. Beiser. Concepts of Modern Physics. McGraw-Hill : New York, 1995.

[343] D. B. Williams and C. B. Carter. Transmission Electron Microscopy. Plenum : New York, 1996.

[344] E. Rzepka L. Taurel and S. Lefrant. Rad. Effects, 72:115, 1983.

[345] S. Lefrant and E. Rzepka. J. Physique. Coll., 41:C6–476, 1980.

[346] G. W. Arnold. J. Appl. Phys., 48:1488, 1975.

[347] B. Ulrici, W. Ulrici and N. N. Kovalev. Sov. Phys. Sol. St., 17:2305, 1975.

[348] D. M. Roessler and W. C. Walker. Appl. Phys. Lett., 17:310, 1966.

[349] S. Debrus, J. Lafait, Mr. May, N. Pincon, D. Prot, C. Sella and J. Venturini. J. Appl. Phys., 88:4469, 2000.

[350] R. A. Ganeev, A. I. Ryasnyanski, Sh. R. Kamalov, M. K. Kodirov and T. Usmanov. J. Phys. D, 34:1602, 2001.

[351] E. K. Williams, D. Ila, S. Sarkisov, M. Curley, J. C. Cochrane, D. B. Poker, D. K. Hensley and C. Borel. Nucl. Instrum. Methods Phys. Res. B, 141:268, 1998.

[352] D. P. Peters, C. Strohhofer, M. L. Brongersma, T. van der Elsken and A. Polman. Nucl. Instrum. Methods Phys. Res. B, 168:237, 2000.

[353] J. Olivares, G. Garcia, A. Garcia-Navarro, F. Agullo-Lopez, O. Caballero and A. Garcia-Cabanes. Appl. Phys. Lett., 86:183501, 2005.

[354] J. C. G. de Sande, R. Serna, J. Gonzolo, C. N. Afonso, D. E. Hole and A. Naudon. J. Appl. Phys., 91:1536, 2002.

[355] F. Agullo-Lopez, G. Garcia and J. Olivares. J. Appl. Phys., 97:093514, 2005.

[356] E. R. Hodgson, A. Delgado and J. L. Alvarez Rivas. Rad. Eff., 74:193, 1983.

[357] F. Baletto and R. Ferrando. Rev. Mod. Phys., 77:371, 2005.

[358] D. B. Poker and D. K. Thomas. Nucl. Instrum. Methods Phys. Res. B, 39:716, 1989.

[359] A. Albers. Ph.D Thesis, University of the Witwatersrand, Johannesburg, South Africa. Unpublished, 1995.

[360] Y. Shigesato, S. Takaki, D. C. Paine and T. Haranoh. J. Appl. Phys., 71:3356, 1992.

[361] S. H. Connell, J. D. Comins and J. P. F. Sellschop. Radiation Effects Express, 2:57, 1988.

[362] J. C. C. Fan and J. B. Goodenough. J. Appl. Phys., 48:3524, 1977.

[363] Wen-Fa Wu and Bi-Shiou Chiou. Semicond. Sci. Technol., 11:196, 1996.

[364] H-N Lin, S-H Chen, G-Y Perng and S-A Chen. J. Appl. Phys., 89:3976, 2001.

[365] K. Dick, T. Dhanasekaran, Z. Zhang and D. Meisel. J. Am. Chem. Soc., 124:2312, 2002.

[366] OriginLab Corporation, One Roundhouse Plaza Northampton, MA 01060 USA. 1992.

[367] Micromath Scientific Software, 1710 South Brentwood Blvd Sait Louis,Missouri 63144, USA. 1996.

Appendix A

A.1 Expansion of Some Higher Order Terms of the Mie Equation

The preliminary description of the Mie theory has been presented in section 2.5.1. This appendix summarises the derivation for the higher order terms [168, 320] of the Mie equation that were incorporated in a user constructed simulation program by employing a standard scientific software, Originlab version 6.1 [366].

The extinction efficiency factor, Q_{ext}, may be determined from the amplitude function S(θ), which is given by

$$S(0) = \frac{1}{2}\sum_{l=1}^{\infty}(2l+1)[a_l + b_l] \tag{A.1}$$

for $\theta = 0$ and is related to the extinction cross-section as

$$C_{ext} = \pi\left(\frac{d}{2}\right)^2 Q_{ext} = \frac{4\pi}{k^2}Re[S(0)]. \tag{A.2}$$

Therefore, expressed by the Mie coefficients,

$$Q_{ext} = \frac{2}{x^2}\sum_{l=1}^{\infty}(2l+1)Re\left[a_l + b_l\right]. \tag{A.3}$$

Expansion of Q_{ext} to the second term yields

$$Q_{ext} = \frac{6}{x^2}Re\left[a_1 + b_1\right] + \frac{10}{x^2}Re\left[a_2 + b_2\right] + \frac{2}{x^2}\sum_{l=3}^{\infty}(2l+1)Re\left[a_l + b_l\right]. \tag{A.4}$$

The series expansion of the coefficients leads to the following results :

$$a_1 = -\frac{2}{3}i\left(\frac{n^2 - n_0^2}{n^2 + 2n_0^2}\right)x^3 + -\frac{2}{5}i\frac{(n^2 - n_0^2)(n^2 - 2n_0^2)}{(n^2 + 2n_0^2)^2}x^5 + \frac{4}{9}\left(\frac{n^2 - n_0^2}{n^2 + 2n_0^2}\right)^2 x^6, \tag{A.5}$$

$$b_1 = -\frac{1}{45}i\left(n^2 - n_0^2\right)x^5, \tag{A.6}$$

$$a_2 = -\frac{1}{15}i\left(\frac{n^2 - n_0^2}{2n^2 + 3n_0^2}\right)x^5, \tag{A.7}$$

where $x = kd/2$, $n_0 = \epsilon_h^{1/2}$ and $n^2 = \epsilon_1 - i\epsilon_2$ is the square of the complex index of refraction of the metal particles. The following quantities used in the derivation are defined below as the metal colloid particle volume (V_0), the metal volume fraction (p) and the extinction (Γ),

$$V_0 = \frac{4}{3}\pi\left(\frac{d}{2}\right)^3, \tag{A.8}$$

$$p = \frac{N}{V}V_0, \tag{A.9}$$

and

$$\Gamma = \frac{N}{V}C_{ext}, \tag{A.10}$$

respectively. d is the diameter of the metal colloid particle, N/V is the number of scatterers per unit volume, assumed to be primarily the implanted metal colloid particles, λ and λ_0 are the wavelengths of the incident electromagnetic wave in the medium and in vacuum, respectively. Taking the expression in brackets from the first term of A.5 we have

$$Re\left[i\left(\frac{\epsilon_1 - i\epsilon_2 - \epsilon_h}{\epsilon_1 - i\epsilon_2 + 2\epsilon_h}\right)\right]. \tag{A.11}$$

Multiplying the denominator and numerator by the complex conjugate of the denominator and taking only the real parts yields

$$-\frac{3\epsilon_h\epsilon_2}{(\epsilon_1 + 2\epsilon_h)^2 + \epsilon_2^2}. \tag{A.12}$$

Involving the multiplicative factors, which in this case are $6/x^2$, $-(2/3)x^3$ and $\pi d^2/4$ gives C_{ext} as

$$\frac{6}{x^2}\frac{2x^3}{3}\frac{\pi d^2}{4} \times 3\epsilon_h \times \frac{\epsilon_2}{(\epsilon_1 + 2\epsilon_h)^2 + \epsilon_2^2}, \tag{A.13}$$

which may be re-written as

$$\frac{18\pi}{x^2} \times V_0 \times \epsilon_h \times \frac{\epsilon_2}{(\epsilon_1 + 2\epsilon_h)^2 + \epsilon_2^2}. \tag{A.14}$$

After re-arrangement the final expression is given by

$$\Gamma = \frac{18\pi p\epsilon_h^{3/2}}{\lambda_0}\left\{\frac{\epsilon_2}{(\epsilon_1 + 2\epsilon_h)^2 + \epsilon_2^2}\right\}, \tag{A.15}$$

which is the extinction due to the lowest order electric dipole term.

Expanding the second and third terms in equation A.5, respectively, yields

$$\frac{18\pi^3 pd^2\epsilon_h^{3/2}}{5\lambda_0^3}\left[\frac{(z1\times z4)-(z2\times z3)}{(z3)^2+(z4)^2}\right]. \tag{A.16}$$

and

$$\frac{4\pi^4 pd^3\epsilon_h^2}{\lambda_0^4}\left[\frac{(y1\times z3)+y2}{(z3)^2+(z4)^2}\right], \tag{A.17}$$

where

$$\begin{aligned} y1 &= (\epsilon_1-\epsilon_h)^2-\epsilon_2^2,\\ y2 &= 4\epsilon_h^2(\epsilon_1-\epsilon_h)(\epsilon_1+2\epsilon_h),\\ z1 &= (\epsilon_1-\epsilon_h)(\epsilon_1-2\epsilon_h)-\epsilon_2^2,\\ z2 &= (2\epsilon_1-3\epsilon_h)\epsilon_2,\\ z3 &= (\epsilon_1+2\epsilon_h)^2-\epsilon_2^2,\\ z4 &= 2\epsilon_2(\epsilon_1+2\epsilon_h). \end{aligned} \tag{A.18}$$

The expansion of A.6 and A.7 using a similar procedure as above gives

$$\frac{\pi^3 pd^2}{5\lambda_0^3}\epsilon_2\epsilon_h^{1/2} \tag{A.19}$$

and

$$\frac{5\pi^3 pd^2\epsilon_h^{5/2}}{\lambda_0^3}\left[\frac{\epsilon_2}{(2\epsilon_1+3\epsilon_h)^2+4\epsilon_2^2}\right], \tag{A.20}$$

respectively.

A.2 Mie Theory Simulations Using Originlab 6.1

This section outlines general instructions to create Mie theory simulations using Originlab 6.1 [366]. The program is not limited to the present situation and may be modified to suit other material properties such as the dielectric constant of the host matrix , the core electron contribution to the dielectric constant and the Fermi velocity

of the electrons of the embedded metal particles. The body of the simulation program is taken from equations in the previous section describing the lowest and higher order terms in the Mie theory.

1. A name for the program should be provided on selecting the nonlinear option under the analysis menu in Originlab 6.1.

2. Choice of independent and dependent variables: the user defined option should be selected as a first step. Currently the independent variable is the vacuum wavelength (λ_0). The dependent variables are the host dielectric constant (ϵ_h), the metal volume fraction (p) and the average particle diameter (d). Other dependent variables are k_1, k_2, and k_2, which are needed to provide a suitable background. Parameters: the core electron contribution to the dielectric constant (ϵ_{core}). It is necessary to put constraints on the dependent variables to prevent the simulation and fitting from generating unphysical values. A typical constraint for p and d would be not allowing them to go below 0.

3. Simulations may be performed without having data to familiarise with the program and to study the effects of changing the dependent variables on the shape of the optical extinction curves generated.

4. The experimental data of the optical extinction of established colloid bands may then be opened and plotted, preferably as symbols. Curve fitting should commence once the simulated curves almost match the data by selection of the appropriate iteration option. The iteration is then repeated until there is no change in the fitting function.

A simulation program for Au MNP in lithium niobate is provided below;

$$W = 2 \times \pi \times (3 \times 10^8)/\lambda_0$$

$$W_c = (1.1 \times 10^{14}) + ((2.76 \times 10^6)/d)$$

$$dem1 = \epsilon_{core} - (1.88 \times 10^{32})/((W^2) + (W_c^2))$$

$$dem2 = ((1.88 \times 10^{32})/((W^2) + (W_c^2))) \times (W_c/W)$$

$$S = (((dem1 + ((2 \times \epsilon_h))^2) + (dem2)^2)$$

$$dY1 = ((dem1 - \epsilon_h)^2) - (dem2^2)$$

$$dZ1 = (dem1 - \epsilon_h) \times (dem1 - (2 \times \epsilon_h)) - dem2^2$$

$$dZ2 = ((2 \times dem1) - (3 \times \epsilon_h)) \times dem2$$

$$dZ3 = ((dem1 + (2 \times \epsilon_h))^2) - (dem2)^2$$

$$dY2 = 4 \times (dem2^2) \times (dem1 - \epsilon_h) \times (dem1 + (2 \times \epsilon_h))$$

$$dZ4 = 2 \times dem2 \times (dem1 + (2 \times \epsilon_h))$$

$$S1 = ((dY1 \times dZ3) + dY2)/((dZ3^2) + (dZ4^2))$$

$$S2 = ((dZ1 \times dZ4) - (dZ2 \times dZ3))/((dZ3^2) + (dZ4^2))$$

$$a1 = 18 \times \pi \times p \times (\epsilon_h^{1.5}) \times dem2/(S \times \lambda_0) + (4 \times (\pi^4) \times p \times (d^3) \times (\epsilon_h^2) \times S1/(\lambda_0^4)) + 18 \times (\pi^3) \times (d^2) \times p \times (\epsilon_h^{1.5}) \times (1/(5 \times \lambda_0^3)) \times S2$$

$$b1 = (\pi^3) \times p \times (d^2) \times (dem2) \times (\epsilon_h^{0.5})/(5 \times \lambda_0^3)$$

$$a2 = 5 \times (\pi^3) \times p \times (d^2) \times (\epsilon_h^{2.5}) \times (1/\lambda_0^3) \times ((dem2)/((((2 \times dem1) + (3 \times \epsilon_h))^2) + (4 \times dem2^2)))$$

$$g = a1 + a2 + b1 + k1/\lambda_0 + k2/\lambda_0^2 + k3/\lambda_0^3.$$

Appendix B

B.1 Solving Defect Growth Kinetic Equations Using Micromath Scientist

This appendix provides a summary of the procedure used to solve a set of defect growth kinetic equations described in subsection 7.3.5 of chapter 7, which are repeated below;

$$\frac{dx}{dt} = g - \sigma xy, \tag{B.1}$$

$$\frac{dy}{dt} = g - \sigma xy - \sigma y s_0 - \sigma_1 y s_1 - \sigma_2 y s_2 - \sigma_a y a + \sigma_d s_2, \tag{B.2}$$

$$\frac{ds_0}{dt} = -\sigma y s_0, \tag{B.3}$$

$$\frac{ds_1}{dt} = \sigma_d s_2 - \sigma_1 y s_1 + \sigma y s_0, \tag{B.4}$$

$$\frac{ds_2}{dt} = \sigma_1 y s_1 - \sigma_d s_2 - \sigma_2 y s_2, \tag{B.5}$$

$$\frac{da}{dt} = \sigma_2 y s_2. \tag{B.6}$$

These equations represent the case of heterogeneous nucleation [95] of defects in alkali halides. The numerical method used to obtain the solutions as a function of time is available from Micromath Scientist software [367]. The Episode-Stiff integrator option of the software is used with the time span set to match the experimental conditions. The large differences in the numerical figures such as the rate constant ($\sigma \approx 10^{-14}$ cm^3/s), the defect generation rate ($g \approx 10^{16}$/cm^3/s) and the concentration ($10^{11} - 10^{16}$/cm^3) of the various defects cause computational instabilities that are solved by introducing scaling factors. To manage these instabilities the magnitudes of the concentrations and the defect generation rate (g) are transformed as follows:

$$xp = (\sigma/\sigma_d)x \tag{B.7}$$

$$yp = (\sigma/\sigma_d)y \tag{B.8}$$

$$s_0p = (\sigma/\sigma_d)s_0 \tag{B.9}$$

$$s_1p = (\sigma/\sigma_d)s_1 \tag{B.10}$$

$$s_2p = (\sigma/\sigma_d)s_2 \tag{B.11}$$

$$ap = (\sigma/\sigma_d)a \tag{B.12}$$

$$gp = \sigma \times g. \tag{B.13}$$

xp, yp, s_0p, s_1p, s_2p, ap and gp are the new magnitudes of the concentrations of the immobile centres (x), mobile centres (y), impurities (s_0), impurities that have captured a single mobile centre (s_1), impurities that have captured two mobile centres (s_2), impurities that have captured more than two mobile centres (a or the clusters) and the defect generation rate (g), respectively. σ_d is the detrapping rate for the thermal bleaching of the s_2 centres and has units of s^{-1}. With these transformations the initial set of equations are rewritten as:

$$\frac{d(xp)}{dt} = (gp/\sigma_d^2) - (yp \times xp), \tag{B.14}$$

$$\begin{aligned}\frac{d(yp)}{dt} = (gp/\sigma_d^2) - (yp) \times (xp + s_0p) - ((\sigma_1/\sigma) \times yp \times s_1p) \\ -((\sigma_2/\sigma) \times yp \times s_2p) - ((\sigma_c/\sigma) \times yp \times ap) + (s_2p),\end{aligned} \tag{B.15}$$

$$\frac{d(s_0p)}{dt} = -yp \times s_0p, \tag{B.16}$$

$$\frac{d(s_1p)}{dt} = (s_2p) - ((\sigma_1/\sigma) \times yp \times s_1p) + (yp \times s_0p), \tag{B.17}$$

$$\frac{d(s_2p)}{dt} = ((\sigma_1/\sigma) \times yp \times s_1p) - (s_2p) - ((\sigma_2/\sigma) \times yp \times s_2p), \tag{B.18}$$

$$\frac{d(ap)}{dt} = (\sigma_2/\sigma) \times yp \times s_2p. \tag{B.19}$$

Typical values of magnitudes of the defect generation rate and concentrations after the transformation, with $\sigma = 10^{-14}$ cm^3/s, are for example: g is of the order of 10^{16}/cm^3/s before, and gp is 100 after the transformation; for s_0 with an order 10^{15}/cm^3,

s_0p is $10/\sigma_d$ after the transformation. After the computation, the actual magnitudes of the concentrations and the defect generation rate are obtained by performing the reverse of the initial transformation.

The detrapping rate for S_2 centres (σ_d) and σ have currently been made temperature dependent [48, 49]; $\sigma_d = \sigma_{d0}exp(-E_d/K_BT)$ and $\sigma = \sigma_0 exp(-E_m/K_BT)$, respectively. E_d and E_m are the activation energy for the detrapping of the mobile centres from the S_2 defects and the migration energy for the mobile centres, respectively. The application of different rates as opposed to a single one [95] provides the flexibility to produce and alter various features in the growth curves. While σ_1/σ and σ_2/σ are temperature dependent and can be varied, σ_c/σ, associated with the development of clusters, is both time and temperature dependent. This latter parameter is obtained as follows: subtracting the magnitudes of the concentration of yp, s_1p and s_2p defects from the immobile centres, xp, and dividing the result by the number of clusters (ap) to obtain the average number of mobile centres per cluster (n_a). The rate of change of n_a is then obtained by fitting to a suitable time function and the computation repeated.

The user defined script employed to simultaneously solve the first order ordinary differential equations numerically is provided below:

// Defect Growth

Independent Variable: t

Dependent Variables: $xp, yp, s_0p, s_1p, s_2p, ap, \sigma_c/\sigma$

Parameters: $gp, \sigma_d, \sigma_1/\sigma, \sigma_2/\sigma$

$fp' = (gp/\sigma_d^2) - (yp \times xp)$

$yp' = (gp/\sigma_d^2) - (yp) \times (xp + s_0p) - ((\sigma_1/\sigma) \times yp \times s_1p) - ((\sigma_2/\sigma) \times yp \times s_2p) - ((\sigma_c/\sigma) \times yp \times ap) + (s_2p)$

$s_0p' = -yp \times s_0p$

$s_1p' = (s_2p - ((\sigma_1/\sigma) \times yp \times s_1p) + (yp \times s_0p))$

$s_2p' = ((\sigma_1/\sigma) \times yp \times s_1p - (s_2p) - ((\sigma_2/\sigma) \times yp \times s_2p))$

$ap' = (\sigma_2/\sigma) \times yp \times s_2p$

//Parameter values: ($\sigma = 10^{-14}$)

gp = 100

$\sigma_1/\sigma = 1.0$

$\sigma_2/\sigma = 0.02$

$\sigma_d = 8000$

Initial conditions:

$t = 0$

$xp = 0$

$yp = 0$

$s_0p = 0.00375$

$s_1p = 0$

$s_2p = 0$

$ap = 0$

The primes on the new variables used in the script denote the first order derivative with respect to time. In the present case solutions were obtained for a time scale between 0 and 22000 seconds. It is possible to vary the time scale appropriately to suit specific need.

Appendix C

C.1 Published Refereed Articles and International Conference Proceedings

G. O. Amolo, R. M. Erasmus, J. D. Comins and T. E. Derry, Raman Studies of proton-implanted CsI, NIM B, vol 250, pg 359 (2006).

G. O. Amolo, J. D. Comins, S. R. Naidoo, S. H. Connell, M. J. Witcomb and T. E. Derry, Effects of Ag^{+} and Au^{3+} -ion Implantation of lithium niobate, NIM B, vol 250, pg 233 (2006).

G. O. Amolo, J. D. Comins, A. T. Davidson, A. G. Kozakiewicz, T. E. Derry and D. S. McLachlan, Visible and VUV Optical Absorption Studies of Mg-colloids and Colour Centres in MgF_2 Crystals Implanted by 100 keV Mg^{+} ions, NIM B, vol 218, pg 244 (2004).

G. O. Amolo, J. D. Comins, M. Maaza, T. E. Derry, S. H. Connell, E. S. Haddad and D. S. McLachlan, Optical Studies of Silver- and Gold-Nanoparticles in Lithium Niobate Crystals, *Proceedings of the 2nd International Conference of the African Materials Research Society, Eds. Y. Ballim, A. G. Every, S. Luyckx and D. C. Levendis, pg 222 (2003),* 8 - 10th December 2003, Johannesburg, South Africa.

G. O. Amolo, J. D. Comins, A. T. Davidson, A. G. Kozakiewicz, T. E. Derry and D. S. McLachlan, Optical Absorption Studies of Mg-nanoparticles and Fluorine Interstitial Defects in MgF_2 Crystals Implanted with 100 keV Mg^{+} ions, *Proceedings of the 2nd African International Conference of the African Materials Research Society, Eds. Y. Ballim, A. G. Every, S. Luyckx and D. C. Levendis, pg 203 (2003),* 8 - 10th December 2003, Johannesburg, South Africa.

G. O. Amolo, J. D. Comins, M. Maaza, D. S. McLachlan and T. E Derry, Irra-

diation of Tin doped Indium Oxide Films using 1 MeV protons, Radia. Eff. Defects Solids, vol. 155, pg 183 (2001).

C.2 Articles in Preparation for Publication

G. O. Amolo, J. D. Comins, S. H. Connell and M. J. Witcomb, Optical and TEM Studies of Gold Nanoparticles Implanted in Lithium Niobate.

G. O. Amolo, J. D. Comins and T. E. Derry, Darkening Mechanism in Proton-Irradiated Tin-Doped Indium Oxide (ITO) Films.

C.3 International Conference Presentations

J. D. Comins, G. O. Amolo, A. M. T. Allen, R. M. Erasmus and T. E. Derry, Defect Production in Irradiated Alkali Iodides Studied by Optical Spectroscopy, *3rd International Conference of the African Materials Research Society*, Marakech, Morocco, 7 - 10th December 2005.

J. D. Comins, G. O. Amolo, R. M. Erasmus and T. E. Derry, Raman Studies of proton-implanted CsI, *The 13th International Conference on Radiation Effects in Insulators*, Sante Fe, New Mexico, USA, 28th August - 2nd September 2005.

J. D. Comins, G. O. Amolo, S. R. Naidoo, S. H. Connell, M. J. Witcomb and T. E. Derry, Effects of Ag^{+} and Au^{3+} -ion Implantation of lithium niobate, *The 13th International Conference on Radiation Effects in Insulators*, Sante Fe, New Mexico, USA, 28th August - 2nd September 2005.

G. O. Amolo, J. D. Comins, A. T. Davidson, A. G. Kozakiewicz, T. E. Derry and D. S. McLachlan, Visible and VUV Optical Absorption Studies of Mg-colloids and Colour Centres in MgF_2 Crystals Implanted by 100 keV Mg^{+} ions, *32nd Course of the International School of Solid State Physics : Radiation Effects in Solids*, Sicily, Italy, 16 - 30th July 2004.

G. O. Amolo, J. D. Comins, M. Maaza, T. E. Derry, S. H. Connell, E. S. Haddad and D. S. McLachlan, Optical Studies of Silver- and Gold-Nanoparticles in Lithium Niobate Crystals, *2nd International Conference of the African Materials Research Society*, 8 - 10th December 2003, Johannesburg, South Africa.

G. O. Amolo, J. D. Comins, A. T. Davidson, A. G. Kozakiewicz, T. E. Derry and D. S. McLachlan, Optical Absorption Studies of Mg-nanoparticles and Fluorine Interstitial Defects in MgF_2 Crystals Implanted with 100 keV Mg^+ ions, *2nd African International Conference of the African Materials Research Society*, 8 - 10th December 2003, Johannesburg, South Africa.

J. D. Comins, G. O. Amolo, A. T. Davidson, A. G. Kozakiewicz, T. E. Derry and D. S. McLachlan, Visible and VUV Optical Absorption Studies of Mg-colloids and Colour Centres in MgF_2 Crystals Implanted by 100 keV Mg^+ions, *International Conference on Radiation Effects in Insulators*, Gramado, Brazil, August/September 2003.

G. O. Amolo, J. D. Comins, M. Maaza, D. S. McLachlan and T. E Derry, Irradiation of Tin doped Indium Oxide Films using 1 MeV protons, *Electron Confinement in Nanostructures*, Enrico Fermi School, Milan, Italy, June/July 2002; *International Conference on Defects in Insulating Materials*, Johannesburg, South Africa, June/July 2000.